Bernd Langensteiner, Mag. rer. nat.

Transport processes in ventilated buildings

DISSERTATION

zur Erlangung des akademischen Grades

Doktor der technischen Wissenschaften

eingereicht an der

Technischen Universität Graz

Betreuer

Univ.-Prof. Dr.-Ing.habil. Günter Brenn

Institut für Strömungslehre und Wärmeübertragung

Prof. Dr.-Ing. Dr.h.c. Bodo Ruck (Zweitbegutachter)

Institut für Hydromechanik, Karlsruher Institut für Technologie

Graz, September 2014

EIDESSTATTLICHE ERKLÄRUNG
AFFIDAVIT

Ich erkläre an Eides statt, dass ich die vorliegende Arbeit selbstständig verfasst, andere als die angegebenen Quellen/Hilfsmittel nicht benutzt, und die den benutzten Quellen wörtlich und inhaltlich entnommenen Stellen als solche kenntlich gemacht habe. Das in TUGRAZonline hochgeladene Textdokument ist mit der vorliegenden Dissertation identisch.

I declare that I have authored this thesis independently, that I have not used other than the declared sources/resources, and that I have explicitly indicated all material which has been quoted either literally or by content from the sources used. The text document uploaded to TUGRAZonline is identical to the present doctoral dissertation.

Datum / Date	Unterschrift / Signature

Acknowledgements

The present investigations on natural ventilation of buildings have been accomplished between October 2010 and February 2014 at the Institute of Fluid Mechanics and Heat Transfer at Graz University of Technology. Part of the research was funded by the Österreichische Forschungsförderungsgesellschaft mbH in the frame of the Bridge Project "Native" (Project No. 829657) in cooperation with the AIT Austrian Institute of Technology GmbH, and the Dr. Pfeiler GmbH as an industrial partner.

I would like to express my gratitude to my doctoral adviser Univ.-Prof. Dr.-Ing. habil. Günter Brenn, who was available for me at all times with his professional knowledge and enriched my research project through his ideas, his suggestions and his constructive criticism.

Special thanks I want to address to Ass. Prof. Dipl.-Ing. Dr. Walter Meile, who has, by his many years of experience in aerodynamics and wind tunnel technology, been a great support in the experimental field, and become a valuable and friendly companion by many private talks.

I am grateful to Prof. Dr.-Ing. Dr.h.c. Bodo Ruck from the Institute of Hydromechanics at Karlsruhe Institute of Technology for his valuable suggestions and the review of this doctoral thesis.

Thanks are also due to my colleagues Dipl.-Ing. Christoph Irrenfried and Dipl.-Ing. Emil Baric for their help and fruitful discussions concerning numerical flow simulations.

Furthermore, I would like to thank all my colleagues at the Institute of Fluid Mechanics and Heat Transfer for their helpful support and the fruitful discussions, especially the staff from the workshop, who took a lot of work out of my hands and

endured me even in tense and stressed mood.

Finally, I want to express my deep gratitude to my parents and my girlfriend Nadine for their support and encouragement throughout the duration of my doctoral study.

Abstract

Natural ventilation is the principle most commonly used for the ventilation of buildings. This can be done, on the one hand, through openings in the building envelope and, on the other hand, by active opening and closing of windows and doors. To quantify exemplarily the amount of air flowing through a window, the knowledge of the so-called air exchange rate (ACH) is necessary. The aim of this work was to determine the magnitude of the air exchange rates for different wind velocities and incident angles, both for fully open as well as for tilted windows, and to develop the necessary measurement methods. Furthermore, the influence of temperature differences between indoor and outdoor space to the number of air exchanges should be examined, even for simultaneous action of wind. The experimental investigations were carried out in the two wind tunnels of the Institute of Fluid Mechanics and Heat Transfer at Graz University of Technology. In the boundary layer wind tunnel, the atmospheric wind profile for a given terrain was determined and the pressure distribution modelled on the closed facade. In the aerodynamic wind tunnel this pressure distribution was reproduced and ACH were measured using velocity sensors and tracer gas. Corresponding numerical simulations were partly carried out at the Austrian Institute of Technology (AIT) and later extended by the author in the frame of the present work.

At the beginning of the work, the building geometry to be investigated was specified with all its internal and external dimensions. Models of the whole 10-storey building, of a sample storey and a single room in the scales 1:75, 1:25 and 1:10, respectively, were created. A wind profile typical for a suburban area, was set in the boundary layer wind tunnel and the resulting pressure distribution on the overall building model was measured. The obtained pressure distribution was exemplarily reproduced in the aerodynamic wind tunnel of the institute for the 3^{rd} and 8^{th} floor

to measure the velocities in the open window cross sections and, hence, to calculate the air exchange rates. In order to obtain also information for the case of tilted windows, the air exchange rates were measured on the single room model, on the one hand by measuring the velocities in the gaps of the tilted windows, and on the other hand by measuring the concentration decay carbon dioxide, used as a tracer gas. In addition, the influence of floor heating simulated by heating foils on the air exchange was studied, both with and without simultaneous action of wind. Both, the simulations on the sample storey model as well as those at the single room model, show good agreement with the measured data and clearly point out that the wind induced air exchange rates are significantly larger than the specified values in the Austrian standard ÖNORM B 8110-3 (2012). Furthermore, it can be said that experimental studies using tracer gas are preferable to those using velocity sensors, as they provide local values of the flow velocity in the cross section only, which are not necessarily flow-rate equivalent. On the other hand, the sensors block parts of the cross sections and thereby change the flow field to be measured, which can disturb measurements in small cross sections significantly. Measurements on the thermal influence of the ACH show that a critical Ra number of $\mathcal{O}(10^6)$ must be exceeded so that thermal convection is set in motion at all. From model development of the air exchange rate $ACH(\alpha, U_\infty)$ depending on the incidence angle α and the inflow velocity U_∞, linear proportionality between the ACH and the flow velocity is obtained.

Kurzfassung

Natürliche Lüftung ist das am häufigsten verwendete Prinzip zur Lüftung von Gebäuden. Dies kann einerseits durch Öffnungen in der Gebäudehülle und andererseits durch das aktive Öffnen und Schließen von Fenstern und Türen geschehen. Um die dabei beispielsweise durch ein gekipptes Fenster kommende Luftmenge zu quantifizieren, ist die Kenntnis der so genannten Luftwechselzahl (ACH) notwendig. Ziel dieser Arbeit war es, für unterschiedliche Windgeschwindigkeiten und Anströmwinkel die Größenordnung der Luftwechselzahlen, sowohl für ganz offene als auch für gekippte Fenster, zu bestimmen und die dazu notwendigen Messmethoden zu entwickeln. Des Weiteren sollte auch der Einfluss von Temperaturdifferenzen zwischen Innen- und Außenraum auf die Luftwechselzahl untersucht werden, auch bei gleichzeitigem Einwirken von Wind. Die experimentellen Untersuchungen wurden in den beiden Windkanälen des Institutes für Strömungslehre und Wärmeübertragung der Technischen Universität Graz durchgeführt. Im Grenzschichtwindkanal wurde das atmosphärische Windprofil ermittelt und die Druckverteilung auf die geschlossene Fassade für ein vorgegebenes Terrain nachgebildet. Im aerodynamischen Windkanal wurde diese Druckverteilung nachgebildet und die Luftwechselraten mittels Geschwindigkeitssensoren und Tracergas gemessen. Entsprechende numerische Simulationen wurden teilweise am Austrian Institute of Technology (AIT) durchgeführt und später vom Autor im Rahmen der vorliegenden Arbeit erweitert.

Zu Beginn der Arbeit wurde die zu untersuchende Gebäudegeometrie mit all ihren Innen- und Außenabmessungen charakterisiert. Es wurden Modelle des gesamten 10-stöckigen Gebäudes, eines Geschoßes und eines Einzelraums jeweils in den Maßstäben 1:75, 1:25 und 1:10 erstellt. Ein vorher festgelegtes, für ein Vorstadtgebiet typisches Windprofil wurde im Grenzschichtwindkanal eingestellt und die resultierende Druckverteilung am Gesamtgebäudemodell vermessen. Die erhaltene Druckverteilung

wurde exemplarisch für das 3. bzw. 8. Geschoß zur Messung der Geschwindigkeiten in den offenen Fensterquerschnitten und der daraus berechneten Luftwechselraten im aerodynamischen Windkanal des Instituts nachgebildet. Um auch Daten für den Fall gekippter Fenster zu erhalten, wurden am Einzelraummodell zum einen die Geschwindigkeiten in den Spaltquerschnitten des Kippfensters und zum anderen mithilfe von Kohlendioxid als Tracergas der Konzentrationsabfall gemessen und die entsprechenden Luftwechselzahlen berechnet. Im Einzelraummodell wurde zusätzlich auch der Einfluss einer durch Heizfolien simulierten Fußbodenheizung auf den Luftaustausch untersucht, und das mit und ohne gleichzeitiger Windeinwirkung. Sowohl die Simulationen am Geschoßmodell als auch jene am Einzelraummodell weisen eine gute Übereinstimmung mit den gemessenen Daten auf und machen deutlich, dass die windinduzierten Luftwechselzahlen deutlich größer sind als die in der österreichischen Norm ÖNORM B 8110-3 (2012) angegebenen Werte. Ferner lässt sich sagen, dass experimentelle Untersuchungen mithilfe von Tracergas jenen mit Geschwindigkeitssensoren vorzuziehen sind, da diese nur lokale Werte der Strömungsgeschwindigkeit im Querschnitt liefern, die nicht notwendigerweise dem Durchfluss entsprechen. Andererseits versperren die Sensoren zum Teil die Querschnittsflächen und verändern dadurch das zu messende Strömungsfeld, was Messungen bei kleinen Querschnittsflächen signifikant beeinflussen kann. Messungen der Luftwechselrate, basierend auf thermischen Einflüssen, zeigen, dass ein kritischer Wert der Rayleigh Zahl der Größenordnung 10^6 überschritten werden muss, um überhaupt thermische Konvektion in Gang zu setzen. Aus der Entwicklung eines Modells für die Luftwechselrate $ACH(\alpha, U_\infty)$ in Abhängigkeit von Anströmwinkel α und –geschwindigkeit U_∞ lässt sich ein linearer Zusammenhang zwischen Luftwechselrate und Anströmgeschwindigkeit ableiten.

Contents

Acknowledgements **iv**

Abstract **vii**

Kurzfassung **ix**

List of symbols **xiii**

1 Introduction and outline of the thesis **1**

1.1 General aspects 1

1.2 Objectives of the work 5

2 Theoretical foundations **7**

2.1 Principles of atmospheric flows 14

2.2 The properties of wind and the atmospheric boundary layer 17

The Prandtl layer 24

2.3 Fundamentals of building aerodynamics 30

2.3.1 The flow around buildings 30

2.3.2 Force, moment and pressure coefficients 36

2.3.3 Mechanical similarity and non-dimensional numbers 37

2.3.4 Ventilation – the flow through building openings 40

2.4 Heat transfer through the building envelope 46

3 Experimental and numerical setups, and measurement methods 55

3.1 Models 55

3.2 Wind Tunnels 58

3.2.1 The boundary layer wind tunnel 58

3.2.2 The low-speed aerodynamic wind tunnel 62

3.3 Pressure Measurements 66

3.4 Velocity Measurements 69

3.5 Tracer gas measurements 75

3.6 Determination of the air exchange rate considering thermal influence 80

3.7 Scaling factor of the air exchange rate 85

3.8 Numerical simulations 86

4 Results 91

4.1 Simulation of the atmospheric boundary layer 91

4.1.1 Pressure distributions and force coefficients 94

4.1.2 Validation of the pressure distribution – force coefficients 101

4.2 Determination of the air exchange rate by velocity measurements 103

4.2.1 ACH obtained by velocity measurements for fully open windows 103

4.2.2 ACH obtained by velocity measurements for tilted windows . . 104

4.3 Determination of the air exchange rate by tracer gas measurements for tilted windows . . . 105

4.4 Thermal influence on the air exchange rate . . . 113

4.5 Air exchange rates from numerical simulations . . . 119

4.5.1 Simulations on the storey model . . . 119

4.5.2 Simulations on the single room model . . . 124

4.6 ACH dependencies . . . 133

4.6.1 Comparison of air exchange rates obtained by different methods . . . 133

4.6.2 Comparison of air exchange rates for different wind velocities obtained by tracer gas measurements . . . 142

4.6.3 Comparison of air exchange rates for different temperatures . 150

4.6.4 Impact of wind driven air exchange in thermal building simulations of the sample storey . . . 161

5 Summary and Conclusions **167**

Summary and Conclusions **167**

Bibliography **171**

Appendices **181**

A Pressure distribution **183**

A.1 Distributions of the pressure coefficient . . . 183

A.2 Distribution of the parameters a_i of the multidimensional polynomial function of the pressure distribution . . . 194

B Heat flux table **197**

List of Symbols

Latin symbols

Symbol	Description	Dimension
a	thermal diffusivity	$\mathrm{m^2/s}$
a_i	real coefficient	–
A	area	$\mathrm{m^2}$
A	fitting parameter	1/h
A_{th}	constant	$\mathrm{h^{-1}K^{-1/2}}$
B	integration constant	–
B	fitting parameter	1/h
c_D	drag coefficient	–
c_L	lift coefficient	–
c_P	pitching moment coefficient	–
c_p	specific heat capacity at constant pressure	J/kgK
c_p	pressure coefficient	–
c_R	roll moment coefficient	–
c_S	side force coefficient	–
c_v	specific heat capacity at constant volume	J/kgK
c_Y	yawing moment coefficient	–
C	real constant	–
C_D	discharge coefficient	–
c_∞	sonic velocity	m/s
D_i	door	–
d	path length	m

Symbol	Description	Dimension
e	specific internal energy	J/kg
E	voltage	V
$\mathbf{e}_x, \mathbf{e}_y, \mathbf{e}_z$	unit vectors in $x-, y-, z-$direction	–
Eu	Euler number	–
$\mathbf{F}, F_i, \mathbf{f}$	force	N
f	frequency	1/s
f, f^*	Coriolis parameter	1/s
f_S	calibration factor (nozzle)	–
Fr	Froude number	–
g	gravitational acceleration	m/s^2
Gr	Grashof number	–
H	height	m
H	enthalpy	J
h	specific enthalpy	J/kg
I	electric current	A
Je	Jensen number	–
k	overall heat transfer coefficient	W/m^{2}K
k	wave number	1/m
ℓ	mixing length	m
Δ	Laplacian, defined as $\Delta := \nabla^2$	–
m, M	mass	kg
$\dot{m}$	mass flow rate	kg/s
M_P	pitching moment	Nm
M_R	roll moment	Nm
M_Y	yawing moment	Nm
Ma	Mach number	–
$\mathbf{n}$	normal unit vector	–
∇	gradient	–
Nu	Nusselt number	–
p	pressure	Pa
P	power	W
Pr	Prandtl number	–

Symbol	Description	Dimension
Q	heat transfer rate	W
q	heat flux	W/m^2
q_w	wall heat flux	W/m^2
$\dot{q}_Q$	internal heat source	W/m^3
R	radius	m
$\mathcal{R}$	specific gas constant	J/kgK
$\mathbf{r}$	radial vector	m
R_i	room	–
Ra	Rayleigh number	–
Re, Re_i	Reynolds number	–
Ro	Rossby number	–
RS	rear stagnation point	–
S	separation point	–
t	time	s
T	temperature	K
Δt	time period	s
ΔT	temperature difference	K
T_w	wall temperature	K
Tu	turbulence level	–
Tu_x	longitudinal turbulence level	–
U, V, W, u, v, w	velocity component	m/s
u_τ	friction velocity	m/s
$\overline{\rho u_i' u_j'}$	Reynolds stress tensor	Pa
$\mathbf{v}, \mathbf{v}_i$	velocity	m/s
V	volume	m^3
$\dot{V}$	volume flow rate	m^3/s
W	width	m
W_i	window	–
$\mathbf{x}$	position vector	m
x, y, z	Cartesian coordinates	m
z_0	roughness length	m
z_i	height	m

Greek Symbols

Symbol	Description	Dimension
α	angle	$^\circ$
α	exponent of a power law	–
α	heat transfer coefficient	W/m^2K
β	angle	$^\circ$
β	isobaric expansion coeffcient	$1/K$
δ	velocity boundary-layer thickness	m
δ_t	thermal boundary-layer thickness	m
ε	turbulent kinematic viscosity	m^2/s
ε	jet contraction ratio	–
ζ	loss coefficient	–
η	light absorption coefficient	$1/m$
κ	von Kármán constant	–
κ	adiabatic exponent	–
λ	thermal conductivity	W/mK
λ	wave length	m
μ	dynamic viscosity	kg/ms
ν	kinematic viscosity	m^2/s
ϕ	latitude	$^\circ$
φ_0	blockage ratio	–
Φ_μ	dissipation function	J
$\mathbf{\Phi}$	gravitational potential	m^2/s^2
ρ	density	kg/m^3
σ	stress	Pa
τ	tensor of viscous stresses, shear stress	Pa
τ_{ij}	tensor of viscous stresses in index notation	Pa
τ_w	wall shear stress	Pa
$\mathbf{\Omega}$	rotational vector	rad/s

Symbol	Description	Dimension
Ω	angular velocity of the earth	rad/h

Subscripts

Symbol	Description
0	ambient, atmospheric
$\overline{()}$	averaged quantity
$()'$	fluctuating quantity
$()^\star$	dimensionless quantity
$\underline{()}$	matrix
10	related to a height of 10 m
∞	in undisturbed flow
a	averaged
b	body
$crit$	critical
C	Coriolis
D	drag
dyn	dynamical
eff	effective
el	electrical
F	frictional
g	geostrophic
gr	gradient
h	horizontal
i	non-negative integer for enumerations
i	inside, internal
i	related to an inertial system
in	inflow

Symbol	Description
L	lift
M	model
max	maximal
$mean$	for mean value
min	minimal
N	nature
o	outside, external
out	outflow
p	pressure
P	pitch
R	room
R	roll
r	real
ref	reference
S	side
w	window
W	wall
Y	yawing

Chapter 1

Introduction and outline of the thesis

1.1 General aspects

Natural ventilation of buildings represents a flow which is caused by temperature differences and wind. The desire to improve the indoor air quality concerning comfort and temperature leaded to a strong increase in the use of air conditioners in the last years. The large energy consumption of air conditioners in some cities leads to a situation where the air-conditioning requirements take almost the full capacity of the electricity grid (Linden, 1999). Another disadvantage is the high carbon dioxide emission. On the contrary, natural ventilation uses freely available resources of wind and thermal energy, which are unfortunately difficult to control. Due to increasingly strict environmental and health regulations, the interest in natural ventilation concepts in recent times rises considerably.

The specific type of building ventilation has not only significant influence on the thermal behaviour but also on the quality of the air in the room interior. In most cases, even today, the ventilation is still done via windows, doors or other openings in the building envelope.

Using natural ventilation concepts, the air ventilation is caused by pressure gradients in consequence of wind or temperature differences between inside and

outside the room. The air exchange rate expresses how many times the air within a defined space (normally a room or house) is replaced by the ambient air per unit time, given in the dimension $1/h$. In marked contrast to mechanical ventilation, the air exchange rate on natural ventilation varies in time, with the result that it's numeric value can't be specified in advance, particularly in use of wind.

With mechanically driven ventilation systems an exact adjustment of this numeric value is possible. In the mean time such mechanical ventilation systems belong more or less to the basic equipment of a modern building, although they cause high investment and energy costs, as mentioned above. That's why even the European Union pursues the development and prevalence of natural ventilation strategies, on the one hand to reduce the consumption of energy and on the other hand to minimize the associated carbon dioxide emissions.

The minimum air exchange rates, prescribed from hygienic and building physical reasons, ensure the removal from pollutants in the buildings. These requirements of a minimum air exchange are faced with the limitation of the air exchange regarding energy aspects. In addition to the minimization of transmission heat losses through highly insulated external component constructions, in particular the reduction of ventilation heat losses play a crucial importance. Both the air exchange as well as the ventilation heat losses depend on many different, partly unsteady, factors of influence. These include not only the construction of buildings and the execution concerning joints and air permeability, but also meteorological and topographical conditions of the environment, i.e. thermal or flow-induced pressure gradients acting across the building surface, as well as the usage behaviour of the people.

The flow around a wall-bounded three-dimensional obstacle by the atmospheric boundary layer, results in a complex three-dimensional flow field. On the one hand, a horseshoe vortex near the base of the front edge is formed and on the other hand, extensive recirculation zones develop downstream of the building. Knowledge about the dynamic behaviour of the wake and the separation zones is required to characterize the prevailing transport phenomena. To describe flows of such complex structure, a combined application of experimental investigations and numerical simulations is useful.

The amount of air exchange strongly depends on the incidence angle of the wind as well as on the position and size of the openings in the building envelope

and, in presence of different temperatures inside and outside the building, on thermal buoyancy. The methods for studying natural ventilation are either full scale experiments in real conditions (Heiselberg et al., 2001; Allocca et al., 2003; Larsen and Heiselberg, 2003; Stavrakakis et al., 2008), wind tunnel experiments in full or model scale (Ohba et al., 2001; Larsen et al., 2011; Lo and Novoselac, 2012; Tecle et al., 2013), or Computational Fluid Dynamics (CFD) simulations. CFD results are compared with analytical results or data from wind tunnel measurements (Allocca et al., 2003; Jiang et al., 2003; Nikas et al., 2010; Larsen et al., 2011; Lo and Novoselac, 2012; Tecle et al., 2013). Furthermore, network models (Dascalaki et al., 1995; Schulze and Eicker, 2013) which can be used to predict wind-driven ACH quite accurately, are compared with CFD models in the absence of experimental data (Asfour and Gadi, 2007).

The existing literature reports on various experimental and numerical studies aimed to estimate air flow rates through openings and the resulting indoor air quality. Experimental investigations for single sided natural ventilation on real windows or rectangular openings can be found in Cadloni and Ferrazzini (1997), Heiselberg et al. (2001) and Fracastoro et al. (2002) on real scale under laboratory conditions as well as under real conditions in Daler et al. (1984), Maas (1995), Cadloni and Ferrazzini (1997), Heiselberg et al. (2001) and Assimakopoulos et al. (2002). The driving force within these investigations varies between purely thermally driven under laboratory conditions and a combination of thermally and wind induced effects under real conditions.

Fracastoro et al. (2002) compares the results of a two-dimensional numerical simulation and a simple mass-flow model with measured results for single sided ventilation through a rectangular opening in a real building. Under the assumption of negligible wind velocity, the calculations and experiments show that the incident air causes a rapid temperature decrease in the room until it reaches a steady state. In the area above the opening, a marginally temperature change occurs during the ventilation process, i.e. this area is hardly affected during ventilation. In Heiselberg et al. (2001) measurements on pivoted sash and tilted windows under laboratory conditions are described. The results show a dependence on the discharge coefficient, the opening area, the type of the window, and the temperature difference between inside and outside. Allocca et al. (2003) and Larsen and Heiselberg (2003) investigated both wind driven and thermally induced air exchange. In their studies,

a consistent trend to predict the interaction of the two mechanisms was not found. Schulze and Eicker (2013) investigated three cases under mixed conditions applying local weather data. For a single sided situation they found combined wind and thermally driven natural ventilation to produce ACH between 1 and 5 h^{-1}. Nikas et al. (2010) and Nikolopoulos et al. (2012) studied numerically the impact of the inner topology of buildings on the ACH and compared the results with measurements of Larsen (2006). Both simulation and experiment show that the internal geometry does not alter the overall aerating volume flow rate, but is an important factor for the refreshing rate of inner regions since air exchange does not affect all zones of a room. The results from numerical simulations of Nikolopoulos et al. (2012) revealed a highly unsteady character of the velocity component perpendicular to the openings for incidence angles greater than 60° against the opening normal, which is due to the formation of small but intensive recirculation zones at the openings.

All of the aforementioned studies incorporated experiments or numerical simulations in full scale for single sided window configurations or for windows on opposite walls. The corresponding literature lacks information on configurations with openings in adjacent walls, and especially on the ventilation through tilted windows. The latter is essential to the majority of natural ventilation scenarios in residential buildings during summer periods. Daler et al. (1984) investigated the thermally driven air exchange for ventilation with single sided tilted windows, shafts and other special constructions in 1:1 scale under real meteorological conditions, where only wind velocities below 1.5 m/s were considered. In his studies he found, that the air exchange rate is proportional to the square root of the applied temperature difference. Furthermore, the structure, availability, costs and maintenance of such systems were addressed. Kaczorowski (2009) examined turbulent thermal convection in rectangular containers and cubes and found, however, that a critical temperature difference has to be exceeded to make thermal convection possible at all, which was also observed by Ruck (1993) and the present study. Maas (1995) accounted for the influence of the window reveal, various rotary and tilting positions, as well as differences in temperature and in wind conditions. Pivoted sash windows were found to be more efficient than tilted windows. Since the above approaches for similar boundary conditions yielded significantly different ACH, Hall (2004) formulated a modified model to describe thermally induced ventilation through bottom hung windows for single sided ventilation, accounting for embrasures and heating. A combination of

interior embrasures and heaters reduce the air change potential by approximately 40%. The aforementioned investigations share the fact that only one ventilation opening was considered. A general overview on natural ventilation and appropriate guidelines can be found in the study (ASHRAE, 2009).

The present work investigates natural ventilation concepts for residential buildings where the usual ventilation openings are windows, either fully open or tilted. The driving force is the external wind-induced pressure or a combination of thermally induced and wind-induced forces. The aim is to quantify flow fields responsible for the air exchange and to identify the magnitude of ACH in different rooms of the same storey. The variation of the ACH caused by the relative position of a room and its window openings to the external flow field around the storey is investigated. This work includes both, single sided ventilation and cross ventilation for open and tilted windows. Furthermore, in contrast to the aforementioned studies, the ventilation through tilted windows in adjacent walls is also studied.

1.2 Objectives of the work

The foundations of fluid mechanics important for this work are presented in Chapter 2. This includes the boundary layer equations, the basic principles of atmospheric flows as well as the properties of wind and the atmospheric boundary layer. Furthermore, the fundamentals of building aerodynamics, mechanical similarities and the corresponding coefficients are described. The effects occurring in the flow around buildings are shown and the term flow separation is explained based on a general bluff body, which is characteristic for building aerodynamics. In addition, the ventilation of buildings and the air change rate is explained, and the fundamentals of heat transfer through building envelopes are described.

The metrology applied for the accomplishment of the experiments is described in Chapter 3. This includes the description of the building models, wind tunnels and wind tunnel facilities. The procedure of the pressure, velocity as well as tracer gas measurements are described. Furthermore the superposition of thermal and wind driven air exchange is explained. The measuring instruments as well as the sequence of measurements are described. Finally, the numerical simulations done on a sample storey model in 1:25 scale and on a single room model in 1:10 scale are qualified.

In Chapter 4, the results of all measurements are presented and discussed. A comparison between the different measurement methodes and the numerical simulations is provided and ACH dependences are identified.

The summary in Chapter 5 concludes this work.

Chapter 2

Theoretical foundations

Fluids relevant for building aerodynamics are treated as continua, i.e. as systems of particles without extension and intermediate spaces. A stress tensor of the surface forces and a body force vector can be assigned to each point mass in the continuum. Fluids cannot transfer viscous stresses at rest, but during motion viscous stresses prevail.

Considering the conservation equations for mass and momentum comes to the continuity equation

$$\frac{\partial \rho}{\partial t} + (\nabla \cdot \rho \mathbf{v}) = 0 \tag{2.1}$$

and the momentum equation

$$\rho \left(\frac{\partial \mathbf{v}}{\partial t} + (\mathbf{v} \cdot \nabla)\mathbf{v} \right) = -\nabla p + [\nabla \cdot \underline{\boldsymbol{\tau}}] + \rho \, \mathbf{f}^b \, . \tag{2.2}$$

The energy equation reads

$$\rho \frac{d}{dt} \left(e + \frac{1}{2} |\mathbf{v}|^2 \right) = \rho \left(\mathbf{v} \cdot \mathbf{f}^b \right) - (\nabla \cdot p\mathbf{v}) + (\nabla \cdot [\underline{\boldsymbol{\tau}} \cdot \mathbf{v}]) - (\nabla \cdot \mathbf{q}) + \dot{q}_Q \quad . \tag{2.3}$$

For $\lambda = \text{const.}$ the thermal energy equation in terms of temperature reads

$$\rho c \left(\frac{\partial T}{\partial t} + \mathbf{v} \cdot \nabla T \right) = -p \, (\nabla \cdot \mathbf{v}) + \Phi_\mu + \lambda \Delta T + \dot{q}_Q \ , \tag{2.4}$$

where

$$\frac{1}{\mu}\Phi_\mu = 2\left[\left(\frac{\partial u}{\partial x}\right)^2 + \left(\frac{\partial v}{\partial y}\right)^2 + \left(\frac{\partial w}{\partial z}\right)^2\right] + \left(\frac{\partial v}{\partial x} + \frac{\partial u}{\partial y}\right)^2 + \left(\frac{\partial w}{\partial y} + \frac{\partial v}{\partial z}\right)^2 + \left(\frac{\partial u}{\partial z} + \frac{\partial w}{\partial x}\right)^2 - \frac{2}{3}\left(\frac{\partial u}{\partial x} + \frac{\partial v}{\partial y} + \frac{\partial w}{\partial z}\right)^2 \tag{2.5}$$

is the dissipation function for Newtonian fluids, expressed in Cartesian coordinates.

Materials such as water or gases are so-called *Newtonian Fluids* because the viscous stress $\underline{\boldsymbol{\tau}}$ is proportional to the velocity gradient.

For isotropic Newtonian fluids the Stokes hypothesis yields the following relation between the stress tensor σ_{ij} and the distortion tensor S_{ij}

$$\underline{\boldsymbol{\sigma}} := \sigma_{ij} = -p\delta_{ij} + \tau_{ij} = -p\delta_{ij} + 2\mu S_{ij} - \frac{2}{3}\mu S_{kk}\delta_{ij} \ , \tag{2.6}$$

where δ_{ij} is Kronecker's delta,

$$S_{ij} = \frac{1}{2}\left(\frac{\partial u_i}{\partial x_j} + \frac{\partial u_j}{\partial x_i}\right) \tag{2.7}$$

for $i \neq j$ and

$$S_{kk} = \frac{\partial u_k}{\partial x_k} \tag{2.8}$$

for $i = j$, where the constant of proportionality μ is the dynamic viscosity. The kinematic viscosity is defined as

$$\nu = \frac{\mu}{\rho} \ . \tag{2.9}$$

We assume that the flow is in the $x-$direction. At interfaces, either walls or fluid-fluid boundaries, there is no relative motion due to the no-slip condition. Therefore, the term $\partial u_j/\partial x_i$ in equation (2.7) is zero, which leads to

$$\tau_W = \mu \left.\frac{\mathrm{d}u}{\mathrm{d}y}\right|_W \tag{2.10}$$

for the wall shear stress ($y = 0$). The velocity increases with the distance from the wall until it reaches a local maximum depending on the flow condition. The result is a characteristic velocity profile depending on the flow condition.

But there exist also non-Newtonian fluids, which show a linear relationship between shear stress τ and shear rate $\mathrm{d}u/\mathrm{d}y$. Although a variety of materials meets Eq. (2.6), there are a number of substances which show completely different behaviour, also with respect to the duration of the load. This includes all glassy materials, showing no crystal structure and beginning to flow under long-term exposure to external loads. However, for short-term stress they show the behaviour of solid bodies (Spurk, 2010).

Nondimensionalization of the momentum equation (2.2) and the energy equation (2.3) yields characteristic groups of parameters which influence the velocity and the temperature profiles. Using the characteristic scaling parameters

$$\mathbf{v}^\star = \frac{\mathbf{v}}{U_\infty} \; ; \quad \nabla^\star = L\nabla \; ; \quad t^\star = \frac{tU_\infty}{L}$$

$$\rho^\star = \frac{\rho}{\rho_\infty} \; ; \quad p^\star = \frac{p}{\rho_\infty U_\infty^2} \; ; \quad \underline{\boldsymbol{\tau}}^\star = \frac{L}{\mu U_\infty}\underline{\boldsymbol{\tau}} \; ; \quad \mathbf{f}^{b\star} = \frac{1}{g}\mathbf{f}^b \quad \text{and}$$

$$\Theta = T - T_\infty \; ; \quad \Theta_0 = T_W - T_\infty$$

$$\Rightarrow \quad \Theta^\star = \frac{\Theta}{\Theta_0} \quad \text{and} \quad \mathbf{q}^\star = \frac{L}{\lambda\Theta_0}\mathbf{q}$$

yields for the momentum equation

$$\rho^\star \left(\frac{\partial \mathbf{v}^\star}{\partial t^\star} + (\mathbf{v}^\star \cdot \nabla)\mathbf{v}^\star \right) = -\nabla^\star p^\star + \frac{\mu}{\rho_\infty U_\infty L} \left[\nabla^\star \cdot \underline{\boldsymbol{\tau}}^\star\right] + \frac{Lg}{U_\infty^2}\, \rho^\star\, \mathbf{f}^{b\star} \tag{2.11}$$

or with the non-dimensional groups of reference quantities identified as characteristic numbers

$$\rho^\star \left(\frac{\partial \mathbf{v}^\star}{\partial t^\star} + (\mathbf{v}^\star \cdot \nabla)\mathbf{v}^\star \right) = -\nabla^\star p^\star + \frac{1}{\boldsymbol{Re}} \left[\nabla^\star \cdot \underline{\boldsymbol{\tau}}^\star\right] + \frac{1}{\boldsymbol{Fr^2}}\, \rho^\star\, \mathbf{f}^{b\star} \; . \tag{2.12}$$

For the energy equation (2.3) we get

$$\begin{aligned} \frac{\rho^\star \rho_\infty U_\infty}{L} \frac{\mathrm{d}}{\mathrm{d}t^\star} \left(c_p \Theta_0 \Theta^\star + U_\infty^2 \frac{|\mathbf{v}^\star|^2}{2} \right) = \quad & \rho^\star \rho_\infty U_\infty g \left(\mathbf{v}^\star \cdot \mathbf{f}^{b\star} \right) - \frac{\rho_\infty U_\infty^3}{L} \left(\nabla^\star \cdot p^\star \mathbf{v}^\star \right) + \\ & + \frac{\mu U_\infty^2}{L^2} \left(\nabla^\star \cdot \left[\underline{\boldsymbol{\tau}}^\star \cdot \mathbf{v}^\star \right] \right) - \frac{\lambda \Theta_0}{L^2} \left(\nabla^\star \cdot \mathbf{q}^\star \right) + \dot{q}_Q \end{aligned} \tag{2.13}$$

or in terms of dimensionless numbers

$$\rho^\star \frac{\mathrm{d}}{\mathrm{d}t^\star}\left(\Theta^\star + \boldsymbol{Ec}\,\frac{|\mathbf{v}^\star|^2}{2}\right) = \frac{\boldsymbol{Ec}}{\boldsymbol{Fr^2}}\left(\mathbf{v}^\star\cdot\mathbf{f}^{b\star}\right) - \boldsymbol{Ec}\,\left(\nabla^\star\cdot p^\star\mathbf{v}^\star\right) + \frac{\boldsymbol{Ec}}{\boldsymbol{Re}}\left(\nabla^\star\cdot[\underline{\boldsymbol{\tau}}^\star\cdot\mathbf{v}^\star]\right) - \frac{1}{\boldsymbol{Re}\;\boldsymbol{Pr}}\left(\nabla^\star\cdot\mathbf{q}^\star\right) + \frac{L}{\rho_\infty U_\infty c_p\Theta_0}\,\dot{q}_Q\,. \tag{2.14}$$

Making the thermal energy equation (2.4) dimensionless, we get

$$\rho^\star\left(\frac{\partial\Theta^\star}{\partial t^\star} + \mathbf{v}^\star\cdot\nabla^\star\Theta^\star\right) = \frac{U_\infty^2}{c_p\Theta_0}\,p^\star\left(\nabla^\star\cdot\mathbf{v}^\star\right) + \frac{\mu U_\infty}{\rho_\infty c_p\Theta_0 L}\,\Phi_\mu^\star + \frac{\lambda}{\rho_\infty U_\infty c_p L}\left(\frac{\partial^2\Theta^\star}{\partial x^{\star 2}} + \frac{\partial^2\Theta^\star}{\partial y^{\star 2}}\right) + \frac{L}{\rho_\infty U_\infty c_p\Theta_0}\,\dot{q}_Q \tag{2.15}$$

or in terms of dimensionless numbers

$$\rho^\star\left(\frac{\partial\Theta^\star}{\partial t^\star} + \mathbf{v}^\star\cdot\nabla^\star\Theta^\star\right) = \boldsymbol{Ec}\;p^\star\left(\nabla^\star\cdot\mathbf{v}^\star\right) + \frac{\boldsymbol{Ec}}{\boldsymbol{Re}}\Phi_\mu^\star + \frac{1}{\boldsymbol{Re}\;\boldsymbol{Pr}}\left(\Delta^\star\Theta^\star\right) + \frac{L}{\rho_\infty U_\infty c_p\Theta_0}\,\dot{q}_Q \tag{2.16}$$

with

$$\Phi_\mu^\star = \left\{2\left[\left(\frac{\partial u^\star}{\partial x^\star}\right)^2 + \left(\frac{\partial v^\star}{\partial y^\star}\right)^2\right] + \ldots\right\}.$$

The Reynolds number Re is defined as the ratio of inertial forces to viscous forces and reads

$$Re = \frac{U_\infty L}{\nu}. \tag{2.17}$$

The Froude number

$$Fr = \frac{U_\infty}{\sqrt{gL}} \tag{2.18}$$

represents the influence of gravity on fluid motion by the ratio of inertial and gravitational forces. The Eckert number

$$Ec = \frac{U_\infty^2}{c_p(T_W - T_\infty)} \tag{2.19}$$

expresses the ratio of the kinetic energy to the enthalpy of a flow. The Prandtl

number

$$Pr = \frac{\nu}{a} \tag{2.20}$$

is the ratio of the kinematic viscosity to the thermal diffusivity of the fluid and, therefore, represents the combination of the velocity field with the temperature field of a fluid.

For low flow velocities and not too large temperature differences, the Eckert number is small, so that the importances of dissipation and work by compression are small.

Flows initiated by density differences resulting from temperature differences, i.e. by thermal buoyancy, are summarized under the term *free convection*. The thermal buoyancy is addressed in the momentum equation (2.2) by appropriate mass forces through the isobaric expansion coefficient

$$\beta = -\frac{1}{\rho}\left(\frac{\partial \rho}{\partial T}\right)\bigg|_p \tag{2.21}$$

and yields the momentum equation in the following form

$$\rho\left(\frac{\partial \mathbf{v}}{\partial t} + (\mathbf{v}\cdot\nabla)\mathbf{v}\right) = -\nabla p + [\nabla\cdot\underline{\boldsymbol{\tau}}] - \rho\,\mathbf{g}\,\beta\,(T - T_\infty) \tag{2.22}$$

or in terms of dimensionless numbers

$$\rho^\star\left(\frac{\partial \mathbf{v}^\star}{\partial t^\star} + (\mathbf{v}^\star\cdot\nabla)\mathbf{v}^\star\right) = -\nabla^\star p^\star + \frac{1}{\boldsymbol{Re}}\,[\nabla^\star\cdot\underline{\boldsymbol{\tau}}^\star] + \frac{\boldsymbol{Gr}}{\boldsymbol{Re^2}}\,\rho^\star\,\Theta^\star\,. \tag{2.23}$$

The term Gr/Re^2 in Eq. (2.23) characterizes the ratio of buoyancy forces to inertial forces, and the Grashof number Gr flows with free convection. More precisely Gr specifies the ratio of the buoyancy to the viscous forces acting on a fluid

$$Gr = \frac{g\beta L^3\,(T_W - T_\infty)}{\nu^2}\,. \tag{2.24}$$

According to Incropera and De Witt (2002), combined effects of free and forced convection have to be considered for $Gr/Re^2 \approx 1$, while for $Gr/Re^2 \ll 1$ free convection effects, and for $Gr/Re^2 \gg 1$ forced convection effects may be neglected.

In technical applications, turbulent flows are most important, while laminar flows



(a) laminar (b) turbulent

Figure 2.1: Velocity profiles in (a) laminar and (b) turbulent pipe flow. Referring to Oertel (2012).

are rather an exception. In contrast to laminar flows, in turbulent flows stochastic transverse motions in all directions occur. Due to these fluctuations, energy transport towards the walls takes place, causing a more uniform shape of the time-averaged velocity profile in turbulent flow than in laminar flow (see Fig. 2.1). The much steeper velocity gradient at the wall determines an increase of the shear stress near the wall according to Eq. (2.10). This larger friction causes increased resistance and, thus, losses.

The transition from laminar to turbulent flow is determined by the ratio between inertial and viscous forces. This is expressed by the Reynolds number

$$Re = \frac{UL}{\nu} \,, \tag{2.25}$$

where U and L are characteristic velocity and length scales of the flow problem, respectively. The onset of transition is caused by small disturbances in the flow. In gas flows at small Reynolds numbers the viscous forces dominate and disturbances are damped, so that the flow remains laminar. With increasing Reynolds number the damping is no longer sufficient and transition to turbulent flow occurs.

The flow at larger distances from the body can be approximated as potential flow, i.e. as inviscid and irrotational. This is of course a simplification since viscous forces do not fully vanish in this zone. But experience has shown that even technical flows with high Reynolds numbers outside the near wall region can be described well by assuming inviscid flow.

At high Reynolds numbers, the region near the solid wall is called the boundary layer. This thin region is characterized by the increase of the velocity from zero at the wall ($u = 0$) due to the no-slip condition to the velocity U_∞ in the external flow.

Within this zone, the kinetic energy of the fluid particles is irreversibly converted to heat by friction. The shear stresses acting on the fluid are the physical cause of the viscous drag of a submerged body. The boundary layer, at high Reynolds numbers a very thin zone, is characterized by its thickness δ increasing slowly with the distance along the wall, which depends on the level of turbulence and the behaviour of the static pressure along the wall. The static pressure is independent of the cross stream direction throughout the boundary layer and, therefore, the wall pressure distribution is determined by the outer flow at the edge of the boundary layer. For the boundary layer thickness δ in a laminar flow along a flat plate with zero pressure gradient, the following relation is valid:

$$\delta \sim \sqrt{\frac{\nu x}{U_\infty}} \,, \tag{2.26}$$

and for a turbulent boundary layer

$$\delta \sim \left(\frac{\nu x^4}{U_\infty}\right)^{\frac{1}{5}} \,. \tag{2.27}$$

After Schlichting (1979), transition from laminar to turbulent boundary layer along a flat plate occurs at a critical Reynolds number in a range between $2 \times 10^5 < Re_{crit} < 6 \times 10^5$.

A schematic picture of the boundary layer growth along a flat plate is shown in Fig. (2.2). Near the leading edge, a laminar boundary layer develops for a distance depending on U_∞/ν. The transitional process occurs over a certain distance rather than at a single line. This region extends downstream to the location where the

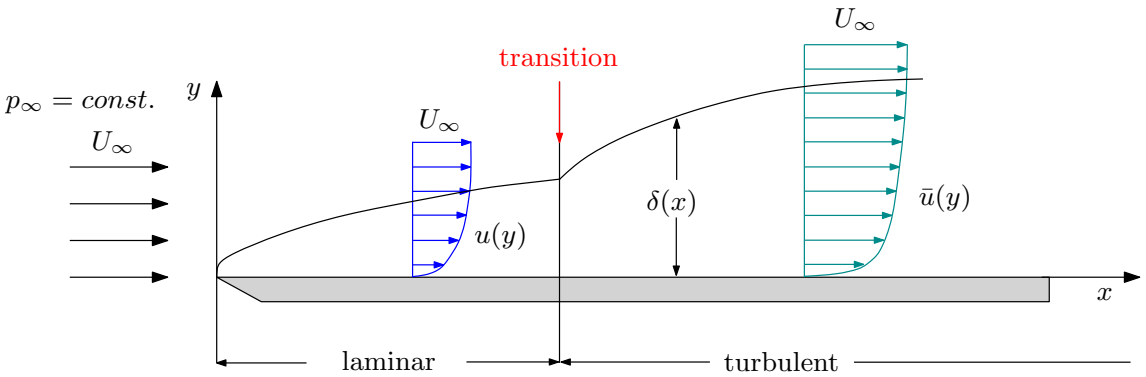


Figure 2.2: Formation of a boundary layer along a flat plate (boundary layer thickness depicted strongly exaggerated). Referring to Fox et al. (2010).

boundary layer flow becomes completely turbulent (Fox et al., 2010).

This concept of the boundary layer was first introduced by L. Prandtl in 1904. By estimating the order of magnitude of several terms in the Navier-Stokes equations Prandtl developed the following boundary layer equations for continuity and momentum (Oertel, 2012):

$$\frac{\partial u}{\partial x} + \frac{\partial v}{\partial y} = 0 \tag{2.28}$$

$$u\frac{\partial u}{\partial x} + v\frac{\partial u}{\partial y} = -\frac{1}{\rho}\frac{\mathrm{d}p}{\mathrm{d}x} + \nu\frac{\partial^2 u}{\partial y^2} \tag{2.29}$$

$$\frac{\partial p}{\partial y} = 0 \tag{2.30}$$

This set of equations is valid for sufficiently large Reynolds numbers, since this is the only way to satisfy the basic requirement in this theory – a very thin boundary layer compared to its characteristic length L:

$$\frac{\delta}{L} \ll 1, \text{ for } Re \gg 1. \tag{2.31}$$

Most of the technical flows satisfy this requirement. With much lower Reynolds number, for example for so-called creeping flows with $Re \leq 1$, as in the case of flow around particles, the boundary layer will not meet this requirement and, therefore, cannot be described with Eqs. (2.28) – (2.30) .

2.1 Principles of atmospheric flows

Atmospheric flows are motions of gases, which are influenced by gravity and determined by pressure and viscous forces. The atmosphere is part of the rotating system of the earth, where Coriolis- and centrifugal forces act. In the following the essential elements of the geophysical flow processes in the atmosphere are explained after Oertel (2012) and Etling (2002).

The basic equations for liquids and gases are valid likewise in the atmosphere, but the rotation of the earth with its atmosphere about the Earth's axis has to be considered. Since it is convenient to describe the processes of motion in an earth-fixed coordinate system, it has become common practice in meteorology to formulate the

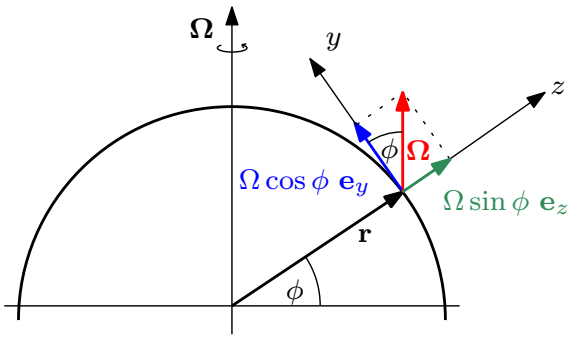


Figure 2.3: Components of the Earth's rotation $\mathbf{\Omega}$ in a tangential plane. Referring to Etling (2002) and Oertel (2012).

basic equations in the rotating coordinate system of the earth. Detailed derivations of the corresponding coordinate transformations can be found e.g. in Etling (2002).

In Fig. 2.3 the Earth's rotation vector $\mathbf{\Omega}$ and the position vector $\mathbf{r}$ of the observed mass point from the rotational axis are shown in a rotating coordinate system. The absolute value of the rotation vector is defined as the angular frequency of the rotation of the earth $\Omega = 2\pi/T$ with the rotation period T of 24 hours.

In the following we observe the rotating earth from an inertial system originating in the center of the earth. A point chosen freely in the Earth's atmosphere, given by the position vector $\mathbf{r}$, has the following velocity with respect to the inertial system (denoted by subscript i)

$$\left(\frac{\mathrm{d}\mathbf{r}}{\mathrm{d}t}\right)_i = \mathbf{v}_f = \mathbf{\Omega} \times \mathbf{r}. \tag{2.32}$$

This velocity $\mathbf{v}_f$ is perpendicular to the vector of the Earth's rotation and the radius vector, and is directed to the east. Assuming that an air particle has the velocity $\mathbf{v}_e$ (subscript e for a coordinate system adjunct to the rotating earth) relative to the Earth's surface, the velocity $\mathbf{v}_i$ of this particle in the inertial system is then given by

$$\mathbf{v}_i = \mathbf{v}_e + \mathbf{v}_f = \mathbf{v}_e + \mathbf{\Omega} \times \mathbf{r}. \tag{2.33}$$

For the temporal change of the velocity vector $\mathbf{v}_e$ in the inertial and the co-rotating system one has

$$\left(\frac{\mathrm{d}\mathbf{v}_e}{\mathrm{d}t}\right)_i = \left(\frac{\mathrm{d}\mathbf{v}_e}{\mathrm{d}t}\right)_e + \mathbf{\Omega} \times \mathbf{v}_e. \tag{2.34}$$

Using the Eqs. (2.32) – (2.34), the relation between the accelerations in the inertial

and the earth-fixed system are obtained as

$$\begin{aligned}\left(\frac{\mathrm{d}\mathbf{v}_i}{\mathrm{d}t}\right)_i &= \left(\frac{\mathrm{d}\mathbf{v}_e}{\mathrm{d}t}\right)_i + \left(\frac{\mathrm{d}}{\mathrm{d}t}\left(\boldsymbol{\Omega}\times\mathbf{r}\right)\right)_i \\ &= \left(\frac{\mathrm{d}\mathbf{v}_e}{\mathrm{d}t}\right)_e + \boldsymbol{\Omega}\times\mathbf{v}_e + \boldsymbol{\Omega}\times\left(\frac{\mathrm{d}\mathbf{r}}{\mathrm{d}t}\right)_e + \boldsymbol{\Omega}\times\boldsymbol{\Omega}\times\mathbf{r}. \end{aligned} \tag{2.35}$$

Omitting the subscript e for the coordinate system rotating with the earth yields

$$\left(\frac{\mathrm{d}\mathbf{v}_i}{\mathrm{d}t}\right)_i = \frac{\mathrm{d}\mathbf{v}}{\mathrm{d}t} + 2\cdot\boldsymbol{\Omega}\times\mathbf{v} + \boldsymbol{\Omega}\times\boldsymbol{\Omega}\times\mathbf{r}. \tag{2.36}$$

The additional terms occurring in Eq. (2.35) are known as the Coriolis acceleration $-(2\cdot\boldsymbol{\Omega}\times\mathbf{v})$ and the centrifugal acceleration $-(\boldsymbol{\Omega}\times\boldsymbol{\Omega}\times\mathbf{r})$.

Finally, the Navier-Stokes equations for incompressible flow specified in a coordinate system rotating with the earth can be written as

$$\rho\left[\frac{\partial\mathbf{v}}{\partial t} + (\mathbf{v}\cdot\nabla)\mathbf{v} + 2\cdot\boldsymbol{\Omega}\times\mathbf{v} + \boldsymbol{\Omega}\times\boldsymbol{\Omega}\times\mathbf{r}\right] = -\nabla p + \mu\cdot\boldsymbol{\Delta}\mathbf{v} + \mathbf{f}. \tag{2.37}$$

To describe geophysical problems usually the description of motions in spherical coordinates is not required. It is rather usual to place a Cartesian coordinate system to the Earth's surface, so that its horizontal coordinates (x and y with their unit vectors $\mathbf{e}_x$ and $\mathbf{e}_y$) form a tangent plane at a given latitude ϕ. The vertical coordinate z (with the unit vector $\mathbf{e}_z$) is then perpendicular to this plane (cf. Fig. 2.3). The rotation vector can be split into its components in this coordinate system as

$$\boldsymbol{\Omega} = \Omega\cdot\cos\phi\cdot\mathbf{e}_y + 2\cdot\Omega\cdot\sin\phi\cdot\mathbf{e}_z = f^*\cdot\mathbf{e}_y + f\cdot\mathbf{e}_z\,, \tag{2.38}$$

where $f^* = \Omega\cdot\cos\phi$ and $f = 2\cdot\Omega\cdot\sin\phi$ are called the Coriolis parameters.

As a conservative force $\mathbf{f}$ in Eq. (2.37) gravity acts in the atmosphere and can be represented using the gravitational potential $\Phi = g\cdot z$ as

$$\mathbf{f} = -\rho\cdot g\cdot\mathbf{e}_z = -\rho\cdot\nabla\boldsymbol{\Phi}. \tag{2.39}$$

While the gravity acts towards the center of the earth and its component $g\cdot\cos\phi$ acts in the direction towards the axis of rotation, the centrifugal force acts away

from the axis of rotation, and is therefore opposite to the appropriate component of gravity force. In meteorology centrifugal acceleration is usually neglected because of its small magnitude compared to gravity.

With these simplifications, the Navier-Stokes equations can be written as

$$\frac{\partial \mathbf{v}}{\partial t} + (\mathbf{v} \cdot \nabla)\mathbf{v} + f \cdot \mathbf{e}_z \times \mathbf{v} = -\frac{1}{\rho} \cdot \nabla p + \nu \cdot \boldsymbol{\Delta}\mathbf{v} + \nabla \boldsymbol{\Phi}. \tag{2.40}$$

The Coriolis force added in the rotating coordinate system should actually occur in all basic equations of fluid mechanics, as all flow processes take place on the rotating earth, even technical flows. For small-scale atmospheric and technical flows, the Coriolis force is irrelevant. For large-scale flows, such as cyclones, however, it has to be taken into account.

As a measure for the influence of the Coriolis force, the Rossby number Ro has been established, which represents the ratio between inertial and Coriolis forces. For flow processes with a characteristic length L and a characteristic velocity U, the Rossby number is defined as

$$Ro = \frac{U}{f\,L}\,. \tag{2.41}$$

The Coriolis parameter f is defined in Eq. (2.38). For large Rossby numbers $Ro \gg 1$, one can neglect the Coriolis force against the inertial force in Eq. (2.40). To the contrary, for $Ro \ll 1$, the Coriolis force plays a dominant role and must not be neglected.

2.2 The properties of wind and the atmospheric boundary layer

According to Hucho (2013), the atmospheric wind has the character of a boundary layer near the ground and is gusty and turbulent. In order to apply the basic concepts of Prandtl's turbulent boundary layer theory to the wind, the roughness and the structure of the terrain and the wind at high altitude have to be considered as boundary conditions. The values of the wind velocity near the ground are usually provided by weather services and measured in a standard height of 10 meters above

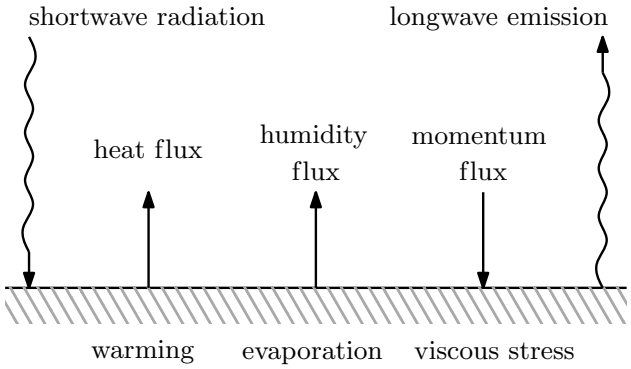


Figure 2.4: Heat and momentum exchange between the Earth's surface and the atmosphere through the boundary layer. Referring to Etling (2002).

ground. From these measurements the wind conditions for a place where, e.g., a building is to be raised, can be determined by the procedure illustrated in the following. Detailed descriptions can be found in Davenport (1963), Counihan (1969), Ruscheweyh (1982), Sockel (1984), Etling (2002), and Hucho (2013).

The basic mechanism initiating all atmospheric motions is the short-wave radiation from the sun. The Earth's surface is heated unequally, which can be traced back on the latitude of the considered location, the different albedo of the Earth's surface (concerning the areas of water and land), the alternation of day and night and on the degree of shading back through clouds. Wind originates as a flow caused by barometric pressure difference between different regions in the atmosphere.

While large-scale pressure differences determine the weather, small-scale pressure differences lead to local winds of limited duration. The air motions are constrained by the viscous stresses generated in the boundary layer which in fact is a momentum transfer to the surface of the earth. On water surfaces this may lead to the formation of waves and in oceans even to drift currents. Fig. 2.4 shows that the heat and momentum fluxes between the earth and atmosphere thus occurring through the boundary layer (Etling, 2002; Hucho, 2013).

Following Etling (2002), the wind flow at high altitudes is virtually unaffected by the viscous effects on the Earth's surface. Assuming a steady flow, the horizontal motion of air in this area is determined by the balance between pressure forces, Coriolis force and centrifugal force. For an inviscid, horizontal flow (subscript h) we

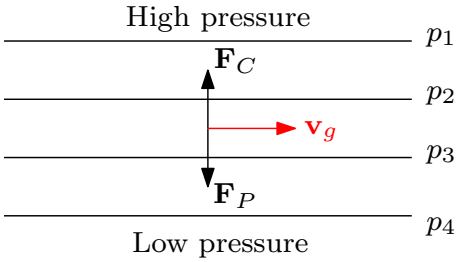


Figure 2.5: Relations between pressure field p, pressure force $\mathbf{F}_P$, Coriolis force $\mathbf{F}_C$ and geostrophic wind velocity $\mathbf{v}_g$. Referring to Oertel (2012).

may deduce from Eq. (2.40)

$$\frac{\mathrm{d}\mathbf{v}_h}{\mathrm{d}t} + f \cdot \mathbf{e}_z \times \mathbf{v}_h = -\frac{1}{\rho} \cdot \nabla_h p. \tag{2.42}$$

A fluid particle can be accelerated in a horizontal direction by the Coriolis force and the pressure force. For an acceleration-free flow, i.e. $\mathrm{d}\mathbf{v}_h/\mathrm{d}t = 0$, the equilibrium of forces requires

$$f \cdot \mathbf{e}_z \times \mathbf{v}_h = -\frac{1}{\rho} \nabla_h p. \tag{2.43}$$

Rearrangement of Eq. (2.43) yields the following expression for the velocity

$$\mathbf{v}_h = \frac{1}{\rho \cdot f} \cdot \mathbf{e}_z \times \nabla_h p, \tag{2.44}$$

which is called the *geostrophic wind velocity* $\mathbf{v}_g$ (usually marked with a subscript g). As can be seen from Eq. (2.44) and Fig. 2.5, the flow is parallel to the isobars and perpendicular to the pressure gradient. The surprising fact that a flow is perpendicular to the acting pressure force is due to the Coriolis force in a rotating coordinate system acting as a compensating force, which can lead to a so-called geostrophic equilibrium. This is possible with $Ro \to 0$ for very large-scale flow phenomena.

Eq. (2.44) is a useful approximation for the real wind in the free atmosphere, but for its derivation $\mathrm{d}\mathbf{v}/\mathrm{d}t = 0$ was assumed. This means that an air particle in geostrophic equilibrium may change neither the absolute value nor the direction of its velocity. Thus, the isobars are straight lines and parallel, since the velocity vectors are parallel to the isobars. This is not true in reality, and all the high-pressure and low-pressure areas in weather maps show a curvature. In order to estimate the

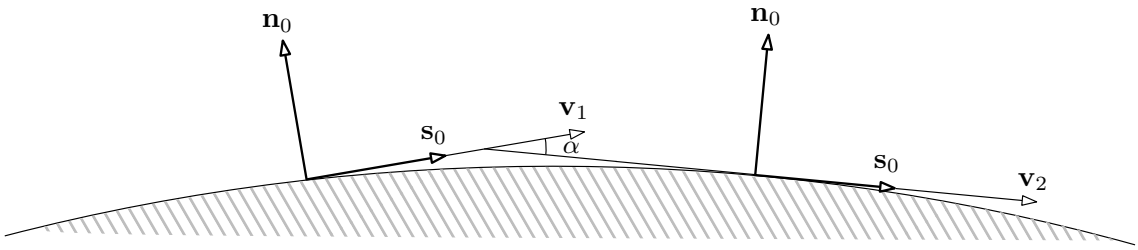


Figure 2.6: Natural coordinate system. Referring to Etling (2002).

effect of the curvature on the geostrophic wind, one introduces a so-called natural coordinate system defined by means of the trajectory of a fluid particle (Fig. 2.6). In Fig. 2.6 the unit vector $\mathbf{s}_0$ indicates the local flow direction, the unit vector $\mathbf{n}_0$ points in a direction normal to the velocity vector, and the angle α denotes the change in direction between the vectors $\mathbf{v}_1$ and $\mathbf{v}_2$. Thus, the velocity vector can be written as

$$\mathbf{v} = |\mathbf{v}|\mathbf{s}_0 \tag{2.45}$$

and the operator ∇ is given as

$$\nabla = \mathbf{s}_0 \frac{\partial}{\partial s} + \mathbf{n}_0 \frac{\partial}{\partial n}. \tag{2.46}$$

Using the so-called Frenet equations from differential geometry (Kühnel, 2010)

$$\frac{\partial \mathbf{s}_0}{\partial s} = \mathbf{n}_0 \frac{\partial \alpha}{\partial s} \quad \text{and} \quad \frac{\partial \mathbf{s}_0}{\partial n} = \mathbf{n}_0 \frac{\partial \alpha}{\partial n} \tag{2.47}$$

the two-dimensional divergence of velocity is calculated as

$$\nabla_2 \cdot \mathbf{v}_2 = \frac{\partial}{\partial s}|\mathbf{v}| + |\mathbf{v}| \frac{\partial \alpha}{\partial n} \,. \tag{2.48}$$

Thus, the equations of motion read (Etling, 2002)

$$\frac{\partial}{\partial t}|\mathbf{v}| + |\mathbf{v}| \frac{\partial |\mathbf{v}|}{\partial s} = -\frac{1}{\rho}\frac{\partial p}{\partial s} \tag{2.49}$$

and

$$\frac{|\mathbf{v}|^2}{R} + f|\mathbf{v}| = -\frac{1}{\rho}\frac{\partial p}{\partial n}\,, \tag{2.50}$$

where R is the radius of curvature of the particle trajectory. Assuming $\partial/\partial t = 0$ and $\partial|\mathbf{v}|/\partial s = 0$, the equilibrium is represented by Eq. (2.50). The first term on the

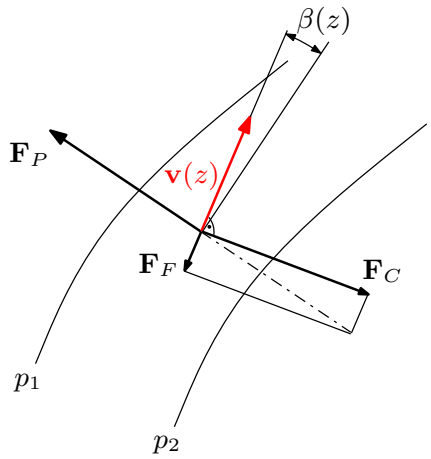


Figure 2.7: Development of an air flow between two curved isobars. Referring to Hucho (2013).

left-hand side of the equation describes the acceleration caused by the curvature of the particle trajectories, i.e. the centrifugal force always pointing in opposition to the curvature. Under steady-state conditions, an equilibrium between pressure force, Coriolis force and centrifugal force exists. In case of a linear particle trajectory, i.e. for $R \to \infty$, the geostrophic equilibrium in natural coordinates is given by

$$|\mathbf{v}| = |\mathbf{v}_g| = -\frac{1}{\rho f}\frac{\partial p}{\partial n}\,. \tag{2.51}$$

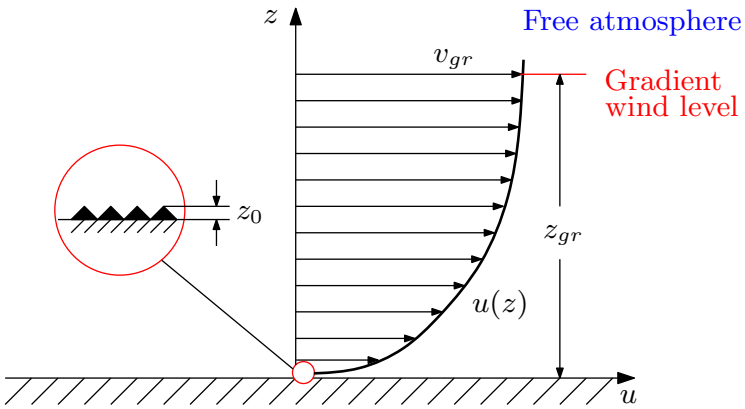


Figure 2.8: Velocity profile of the atmospheric boundary layer and roughnesses on the ground, schematically. Referring to Hucho (2013).

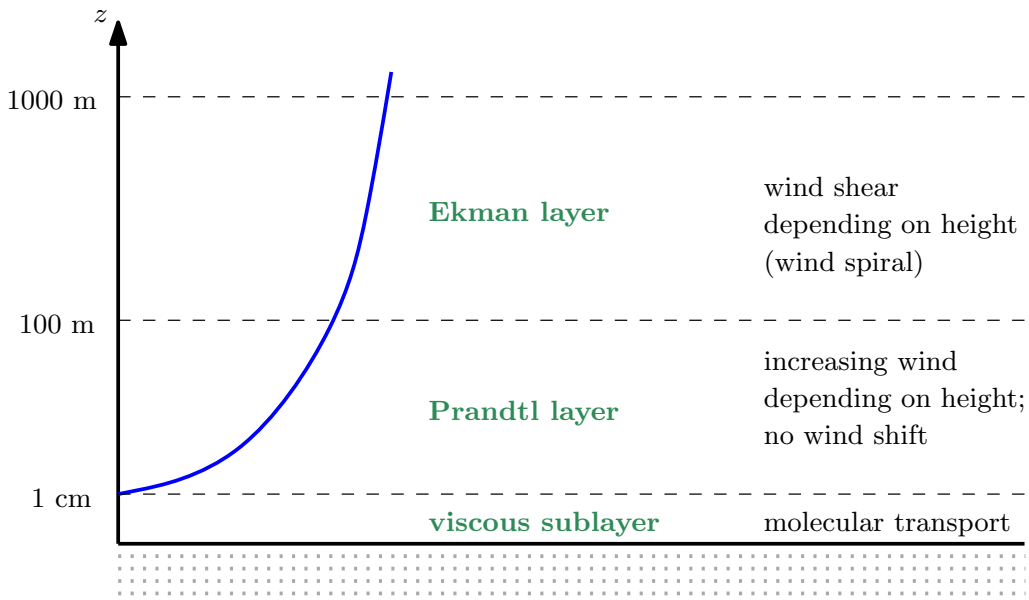


Figure 2.9: Structure of the atmospheric boundary layer. Referring to Etling (2002).

Applied to Eq. (2.50), it follows

$$f(|\mathbf{v}| - |\mathbf{v}_g|) = 0\,. \tag{2.52}$$

From the comparison of Eqs. (2.50) and (2.51) for the same pressure gradients follows, that the wind velocity deviates from the geostrophic value. In case of curved isobars, i.e. for $R \neq \infty$, the geostrophic wind velocity has to be corrected with

$$\frac{|\mathbf{v}_g|}{v_{gr}} = 1 + \frac{v_{gr}}{fR}\,, \tag{2.53}$$

where $v_{gr} := |\mathbf{v}|$ is called the *gradient wind*. With decreasing altitude the frictional influence $\mathbf{F}_F$ becomes more important (Fig. 2.7) and the vector of the wind speed $\mathbf{v}(z)$ is deflected by the angle β towards the region of lower pressure (Hucho, 2013).

The frictional influence from the ground leads to the formation of the so-called atmospheric boundary layer with a thickness δ. Fig. 2.8 shows a typical velocity profile in the atmospheric boundary layer and the zone above, the so-called free atmosphere.

As shown in Fig. 2.9, the atmospheric boundary layer can be divided into three separate layers. The *viscous sublayer* has no immediate influence on the dynamics in

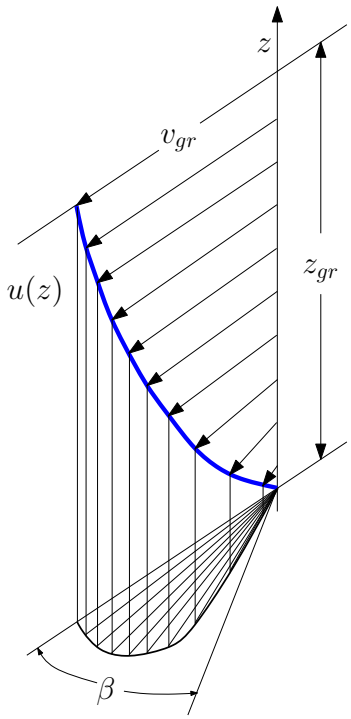


Figure 2.10: Schematic sketch of the twisted velocity profile in the atmospheric boundary layer – the Ekman spiral. Referring to Etling (2002) and Hucho (2013).

the boundary layer, but has to be considered in interactions between the atmosphere and land or sea. It is only a few millimeters thick (Etling, 2002), and the transport of heat or humidity in the absence of turbulence takes place only by molecular processes. The *Prandtl layer* has a vertical extent of about 20 to 150 meters above ground and is therefore known as the ground-level boundary layer. Turbulent fluxes in this layer are constant with height (Etling, 2002; Sockel, 1984), which facilitates the calculation of wind profiles. The influence of the Coriolis force at this height is so small that no rotation of the wind with height takes place. In this layer near the ground, the structure of turbulence is determined by the roughness of the terrain, which is of particular interest in building aerodynamics.

The largest part of the atmospheric boundary layer is formed by the *Ekman layer*, adjacent to the Prandtl layer, which has a vertical extension approximately up to one to two kilometers. Turbulent fluxes in the Ekman layer decrease with height and vanish in the upper boundary. The velocity variation due to friction in the boundary layer causes a deviation of the wind velocity from the direction of the geostrophic wind which depends on the height above ground. In lower regions, the velocity is

smaller and, therefore, the Coriolis force is smaller. The equilibrium of forces yields a larger deflection angle β, reaching its maximum value β_0 on the ground. The Ekman layer is thus also called the spiral layer (Fig. 2.10). The deflection angle β (cf. Fig. 2.7) at the upper boundary has the value $\beta = 0°$ and reaches its maximum value β_0 on the ground. Within the Prandtl layer, an untwisted boundary layer can be assumed, i.e. $\beta = \text{const}$.

Within the Prandtl layer the structure of turbulence is determined solely by the ground roughness. Therefore, we want to expand on this ground-level boundary layer, particularly important in building aerodynamics, in the following section.

The Prandtl layer

Approaching the ground, the level of turbulence in the boundary layer is enhanced which depends on the surface roughness. The rougher the surface, the thicker is the atmospheric boundary layer (Panofsky, 1974; Hucho, 2013). The according velocity profile is sketched in Fig. 2.8.

As mentioned above, the atmospheric wind motions are always turbulent. For the turbulent flow, one approach to a description is to split the actual velocity into a mean value and the fluctuations, which gives for velocity, following Bird et al. (2007), Schlichting (1979), and Hucho (2013):

$$\mathbf{v}(t) = \overline{\mathbf{v}} + \mathbf{v}'(t), \tag{2.54}$$

where the mean value is denoted by an overbar and the fluctuation by a prime (see Fig. 2.11). The velocity $\overline{\mathbf{v}}$ is called the *time-averaged velocity* and Eq. 2.54 is called the *Reynolds decomposition*. Time averaging over periods T of time, the mean value of the velocity $\mathbf{v}(x, y, z, t)$ can be written as

$$\overline{\mathbf{v}} = \frac{1}{T} \int_{t-\frac{T}{2}}^{t+\frac{T}{2}} \mathbf{v}(x, y, z, t)\, \mathrm{d}t \ . \tag{2.55}$$

In turbulent technical tube flows with a constant driving pressure gradient, the quantity $\overline{\mathbf{v}}$ is independent of time, but depends on position. This is called statistically

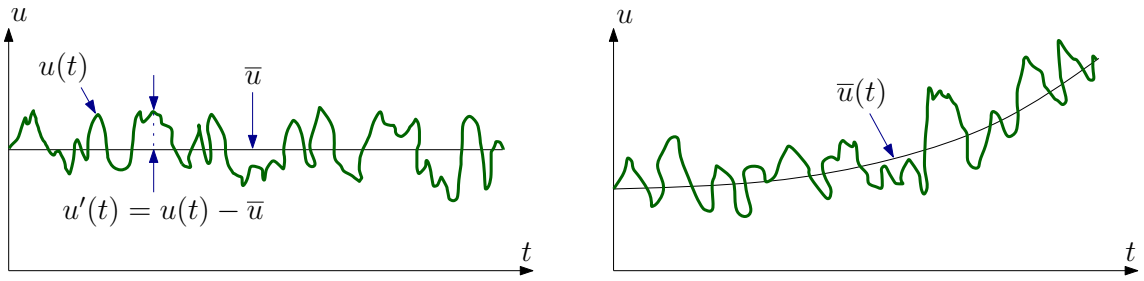


Figure 2.11: The velocity component $u(t)$ at a location in the flow field, its time-averaged value $\overline{u}$ and its fluctuation u' in turbulent flow. Left: constant mean value $\overline{u}$; right: time dependent mean value $\overline{u}(t)$. Based on Bird et al. (2007).

steady turbulence. In natural winds, the mean value of the velocity is dependens on the time period over which the average is formed (Hucho, 2013). This is defined in Fig. 2.11.

The common measure of the magnitude of the fluctuation velocity, e.g. for the $x-$direction, is the root mean square $\sqrt{\overline{u'^2}}$. In dimensionless form with the local mean velocity $\overline{u}$ as the reference, this is expressed as the *turbulence level* for all directions

$$\mathrm{Tu}_x = \frac{\sqrt{\overline{u'^2}}}{\overline{u}} \qquad \mathrm{Tu}_y = \frac{\sqrt{\overline{v'^2}}}{\overline{u}} \qquad \mathrm{Tu}_z = \frac{\sqrt{\overline{w'^2}}}{\overline{u}}\,. \tag{2.56}$$

According to Sockel (1994), the turbulence level in natural winds is approximately constant at a higher altitude and increases when approaching the ground.

For turbulent flows close to the wall, the universal logarithmic law of the wall is valid. The velocity profile of the Prandtl layer can be described like in the boundary layer along the flat plate by a logarithmic distribution. The Reynolds averaged Navier-Stokes equations (RANS) (detailed derivations can be found in Spurk (2010), Oertel (2012), and Etling (2002)) in the rotating system are as follows:

$$\begin{aligned}
\frac{\partial \overline{u}}{\partial t} + \overline{u}\frac{\partial \overline{u}}{\partial x} + \overline{v}\frac{\partial \overline{u}}{\partial y} + \overline{w}\frac{\partial \overline{u}}{\partial z} - f\overline{v} + f^*\overline{w} &= -\frac{1}{\rho}\frac{\partial \overline{p}}{\partial x} + \nu\Delta\overline{u} - \frac{\partial \overline{u'^2}}{\partial x} - \frac{\partial \overline{v'u'}}{\partial y} - \frac{\partial \overline{w'u'}}{\partial z} \\
\frac{\partial \overline{v}}{\partial t} + \overline{u}\frac{\partial \overline{v}}{\partial x} + \overline{v}\frac{\partial \overline{v}}{\partial y} + \overline{w}\frac{\partial \overline{v}}{\partial z} + f\overline{u} &= -\frac{1}{\rho}\frac{\partial \overline{p}}{\partial y} + \nu\Delta\overline{v} - \frac{\partial \overline{u'v'}}{\partial x} - \frac{\partial \overline{v'^2}}{\partial y} - \frac{\partial \overline{w'v'}}{\partial z} \\
\frac{\partial \overline{w}}{\partial t} + \overline{u}\frac{\partial \overline{w}}{\partial x} + \overline{v}\frac{\partial \overline{w}}{\partial y} + \overline{w}\frac{\partial \overline{w}}{\partial z} - f^*\overline{u} + g &= -\frac{1}{\rho}\frac{\partial \overline{p}}{\partial z} + \nu\Delta\overline{w} - \frac{\partial \overline{u'w'}}{\partial x} - \frac{\partial \overline{v'w'}}{\partial y} - \frac{\partial \overline{w'^2}}{\partial z}\,.
\end{aligned} \tag{2.57}$$

According to Allard (2002), within the Prandtl layer effects of thermal stratification on the wind velocity can be neglected, and the flow direction is assumed to be constant in the immediate vicinity of the ground. Assuming the mean flow to point in the $x-$direction, the mean velocity only depends on the height z above ground. Flows of gases with low or moderate Mach numbers ($Ma < 0.3$) can be assumed incompressible, i.e. $\overline{\rho} = \rho$. This applies to air flows around buildings, on which we focus in our study. Assuming a horizontal homogeneous steady flow, neglecting the molecular viscosity term, we obtain from the RANS

$$\frac{\partial \overline{w'u'}}{\partial z} = 0 \tag{2.58}$$

and for the turbulent momentum fluxes $\overline{w'u'}$ or the turbulent shear stress we get

$$\tau'_{zx} = -\rho\overline{w'u'}. \tag{2.59}$$

Thus, the turbulent momentum flux within the Prandtl layer is constant with height, more precisely the magnitude of the shear stress decreases by not more than 10% of its value at the ground. Therefore, the shear stress within the Prandtl layer is equal to the shear stress at the surface of the earth, meaning $\tau = \tau_0$, where τ_0 denotes the shear stress at the ground and depends on the roughness length z_0 as will be shown later. Commonly $\overline{w'u'}$ is defined by the so called friction velocity (Etling, 2002; Allard, 2002)

$$\sqrt{-\overline{w'u'}} = \sqrt{\frac{\tau_0}{\rho}} = u_\tau. \tag{2.60}$$

The turbulent momentum flux $\rho\overline{w'u'}$ points earthwards, i.e. $\overline{w'u'} < 0$, because the mean velocity increases with height from the ground, meaning $\partial\overline{u}/\partial z > 0$ (Etling, 2002). Introducing Prantdl's mixing length $\ell(z) = \kappa \cdot z$, where $\kappa = 0.41$ denotes the Kármán constant, and the turbulent kinematic viscosity

$$\varepsilon = \ell^2 \left| \frac{\partial \overline{u}}{\partial z} \right| \tag{2.61}$$

we have

$$u_\tau^2 = \varepsilon \frac{\partial \overline{u}}{\partial z} = \ell^2 \left(\frac{\partial \overline{u}}{\partial z} \right)^2. \tag{2.62}$$

For the velocity gradient applies $\partial\overline{u}/\partial z = -u_\tau/\ell$. Locally, the fluctuating velocity u'

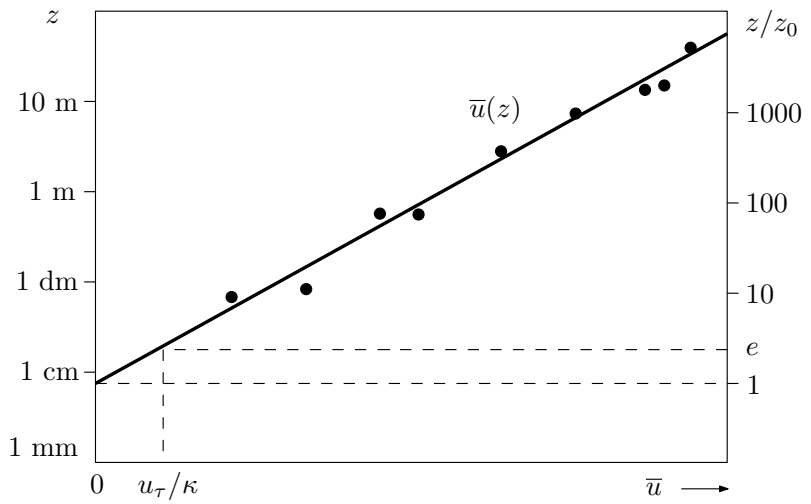


Figure 2.12: Wind velocities depending on height. The height scale is plotted logarithmically and e denotes the Euler number. Schematic diagram referring to Etling (2002).

varies linearly with the distance of displacement ℓ, while w' is of the same order of magnitude as u (Allard, 2002). This is Prandtl's mixing length hypothesis, which is based on the idea that the mixing length is a measure of the size of the eddies causing the mixing within the boundary layer. Prandtl assumed this length proportional to the wall distance. Using Prandtl's hypothesis yields

$$\frac{\mathrm{d}\overline{u}}{\mathrm{d}z} = \frac{u_\tau}{\kappa z} \,. \tag{2.63}$$

Integration of this ordinary differential equation results in

$$\overline{u}(z) = \frac{u_\tau}{\kappa} \ln z + B \,, \tag{2.64}$$

where B is an integration constant. The so-called *roughness length* is the fictitious height above the ground in which the mean velocity $\overline{u}(z)$ is usually set to zero. The reason that the wind velocity does not vanish at $z = 0$ is that the Earth's surface is not smooth but covered with irregularities and obstacles. The level of reference, $z = 0$, is defined as the ground place of the roughness elements. These so-called roughnesses of the ground influence the mean wind profile, thus $\overline{u} = 0$ is already fulfilled at a height z_0. The roughness length z_0 is not identical to the individual height of obstacles but rather a measure of hight and density of the roughness elements. With the boundary condition $\overline{u}(z = z_0) = 0$, we obtain the logarithmic

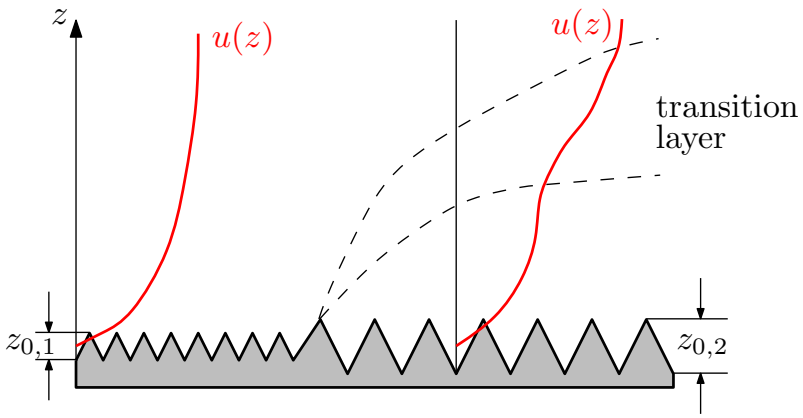


Figure 2.13: Transition of the boundary layer upon change of roughness length z_0. According to Hucho (2013).

wind profile within the Prandtl layer

$$\overline{u}(z) = \frac{u_\tau}{\kappa} \ln \frac{z}{z_0} \,. \tag{2.65}$$

The roughness length z_0 can be determined from measurements of the mean wind profile as a property of the ground, presuming the validity of Eq. (2.65).

In a semi-logarithmic plot of $z(\overline{u})$, the values of the mean velocities $\overline{u}$ must lie on a straight line intersecting the ordinate at z_0. As shown in Fig. 2.12, Eq. (2.65) for $z/z_0 = e$ yields the friction velocity u_τ divided by κ. The turbulent kinematic viscosity $\varepsilon(z)$ for adiabatic conditions increases linearly with height, which can be derived from Eqs. (2.61) and (2.63)

$$\varepsilon(z) = \kappa u_\tau z. \tag{2.66}$$

The application of the logarithmic law of the wall for the calculation of the wind profile is not suitable in practice. Experimental data on the wind velocity in at least two different heights would be required. Meteorological wind data are commonly available in a reference height of 10 m, so that in praxi an empirical law for the mean wind velocity $\overline{u}(z)$, applicable up to the gradient height, was introduced

$$\overline{u}(z) = \overline{u}_{ref} \left(\frac{z}{z_{ref}} \right)^{\alpha} , \tag{2.67}$$

which is called the *power law* (Etling, 2002; Sockel, 1994). With the wind velocity

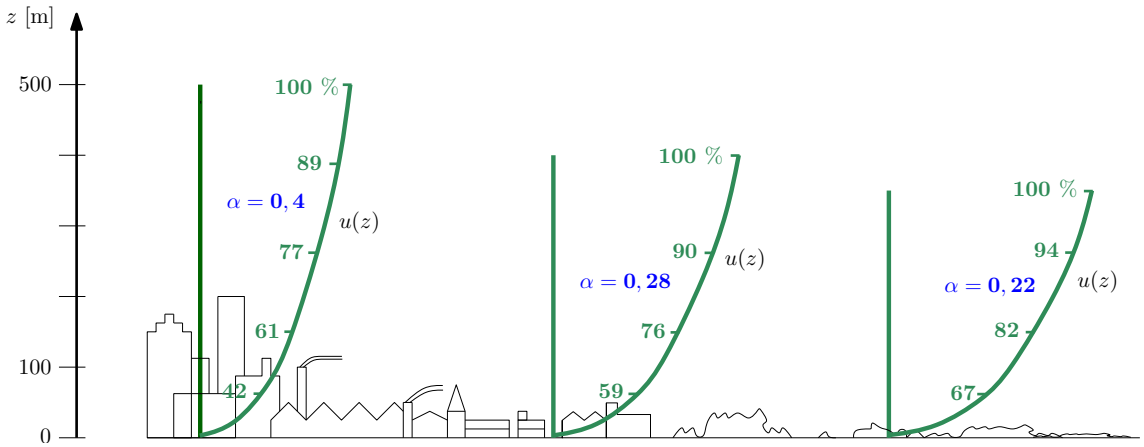


Figure 2.14: Boundary layer height as a function of surface roughness. According to Davenport (1963).

u_{10} measured at 10 m height, this yields (Hucho, 2013)

$$\frac{u(z)}{u_{10}} = \left(\frac{z}{z_{10}}\right)^{\alpha}. \tag{2.68}$$

The exponent α depends on the roughness of the terrain. For smooth ground, the value $\alpha = 0.16$ matches well with the classical $1/7-$power law (Schlichting, 1979). With increasing roughness (plants, buildings, hills), the exponent α and the gradient height z_{gr} increase. In general, the exponent α is estimated for a boundary layer in a state of equilibrium at the considered location. As can be seen in Fig. 2.13, on a change of roughness length z_0 it takes a certain distance until a state of equilibrium is reached again (Hucho, 2013).

An empirical relation between roughness length z_0 and the exponent α was determined by Counihan (1969). For typical types of terrain, Davenport (1963) has specified the velocity profiles and the corresponding values for the exponent α, as shown schematically in Fig. 2.14.

In general, the natural wind is highly non-uniform. On the one hand, the strength and direction of the wind change with season and weather conditions. On the other hand, short-term fluctuations, so-called gusts, superimpose the quasi-steady wind. These gusts have different spatial extent in horizontal and vertical directions. The properties of the unsteady wind can be described well by the RANS. A detailed description of wind statistics can be found in Lawson (2001).

2.3 Fundamentals of building aerodynamics

In the following, some general principles and most important effects of wind loads on buildings are described. This is particularly concerning general aspects of the flow around bluff bodies with sharp edges, i.e. of buildings. The terms boundary layer (cf. the previous section) and flow separation are discussed with respect to the particular problems investigated in the present work. Pressure, force and moment coefficients will be explained, and the laws of similarity as well as dimensionless parameters will be discussed.

2.3.1 The flow around buildings

The characteristic of bluff bodies, particularly buildings, is flow separation, which can lead to large acting forces. For a simple two-dimensional case, boundary layer separation is shown in Fig. 2.15. The condition for the separation of the boundary layer from a wall is an increase of pressure in the flow direction. This can be shown for the two-dimensional case using the comparison of the curvatures of the velocity profile close to the wall and at the edge of the boundary layer. In presence of a separated flow there has to be a point of inflection and an associated inversion of the curvature in the velocity profile. At the edge of the boundary layer, the velocity profile $u(y)$ is always like the velocity reaches a maximum there. The curvature is therefore negative. Evaluating Prandtl's boundary layer equations close to the wall for a negative pressure gradient leads to a negative curvature:

$$\underbrace{u\frac{\partial u}{\partial x}}_{=0}+\underbrace{v\frac{\partial u}{\partial y}}_{=0}=-\frac{1}{\rho}\underbrace{\frac{\mathrm{d}p}{\mathrm{d}x}}_{<0}+\nu\underbrace{\frac{\partial^2 u}{\partial y^2}}_{\Rightarrow 0} \tag{2.69}$$

$$\frac{\mathrm{d}p}{\mathrm{d}x}<0 \Longrightarrow \left.\frac{\partial^2 u}{\partial y^2}\right|_{y=0}<0\,. \tag{2.70}$$

Therefore, the curvature is negative everywhere and there is no point of inflection in the velocity profile. For the case of a pressure gradient counteracting the flow, a positive curvature prevails near the wall:

$$\frac{\mathrm{d}p}{\mathrm{d}x}>0 \Rightarrow \left.\frac{\partial^2 u}{\partial y^2}\right|_{y=0}>0. \tag{2.71}$$

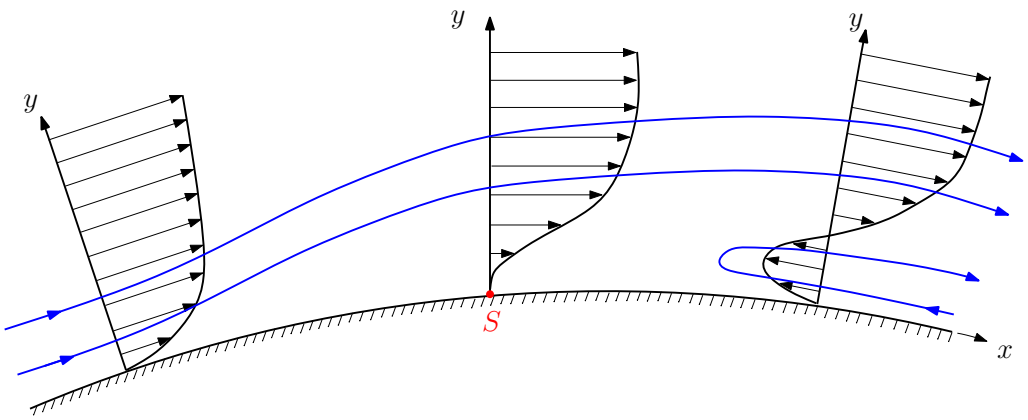


Figure 2.15: The separation of the boundary layer from a body contour, schematically. Referring to Hucho (2013).

This can lead to separation. Since the pressure is imposed from the external flow to the boundary layer, separation is possible in regions where a delayed external flow, and thus a conversion of the kinetic energy in pressure energy takes place (Hucho, 2013). The two-dimensional flow along the wall in Fig. 2.15 is influenced by an eventually adverse pressure gradient. The velocity gradient at the wall is reduced to zero in the separation point S, which means zero shear stress. This is the criterion for beginning separation in two-dimensional flow. In the three-dimensional case, the requirement of disappearing wall shear stress is no longer valid. Separation lines are formed there, along which the wall shear stress does not vanish (Hucho, 2013). In contrast to the above described separation from the surface of bodies caused by an adverse pressure gradient, the flow may also separate at sharp edges due to inertia. This is sketched in Fig. 2.16.

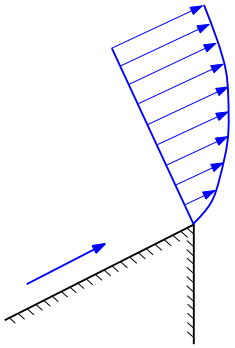


Figure 2.16: The separation of the flow on a sharp edge, schematically. Referring to Hucho (2013).

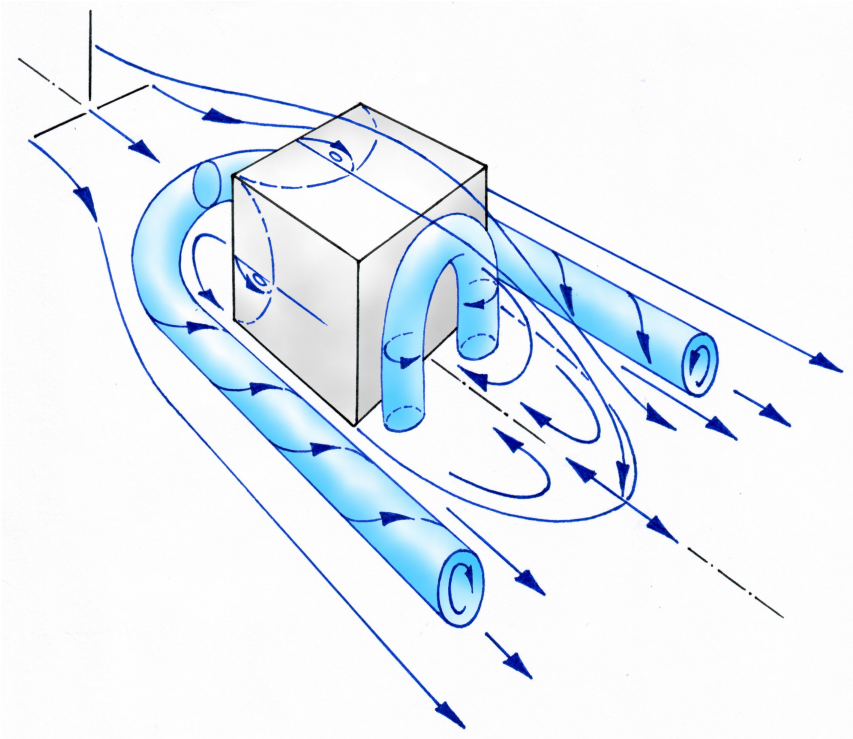


Figure 2.17: Schematic illustration of the flow around a cuboid seated on the ground. Referring to Martinuzzi (1992).

The pressure distribution on a building exposed to wind flow is determined by the geometry of the building. Fig. 2.17 sketches the complex flow structure around a cuboidal body attached to a wall.

In front of the vertically oriented upstream face of the body, the flow is slowed down, and kinetic energy is converted into static pressure, resulting in positive pressure coefficients c_p at that surface. The maximum value of $c_p = 1$ is reached in the stagnation point whose location is determined by the specific geometry.

Fig. 2.17 depicts a so-called *horseshoe vortex* near the front surface and an arc-shaped one near the rear face. On the side walls and on the top, so-called *separation bubbles* may exist.

Immediately behind the body, the near-wake with two counter-rotating vortices is formed, which is delimited by a dividing streamline (see Fig 2.18 (a)). The size of the near-wake and the prevailing under pressure within this zone are essentially responsible for the forces on the body. The flow around the "closed" near-wake is similar to the flow around a rigid body. In the rear part, again an adverse pressure

gradient occurs, leading to separation (sometimes called separation of the second kind). The fluid outside the separating streamline forms the so-called *far-wake* with the outgoing eddies (Hucho, 2013).

According to Hucho (2013), Fig. 2.18 exemplarily shows the behaviour of the flow around a bluff body with a steady adjacent wake. Here (a) shows the streamlines, (b) the profile of the pressure coefficient c_p in the symmetry plane of the body contour, and (c) the velocity profiles. The flow is from left to right with the incoming velocity U_∞. In the stagnation point, the pressure coefficient $c_p = 1$ because all of the kinetic energy of the fluid is converted into static pressure. The pressure coefficient

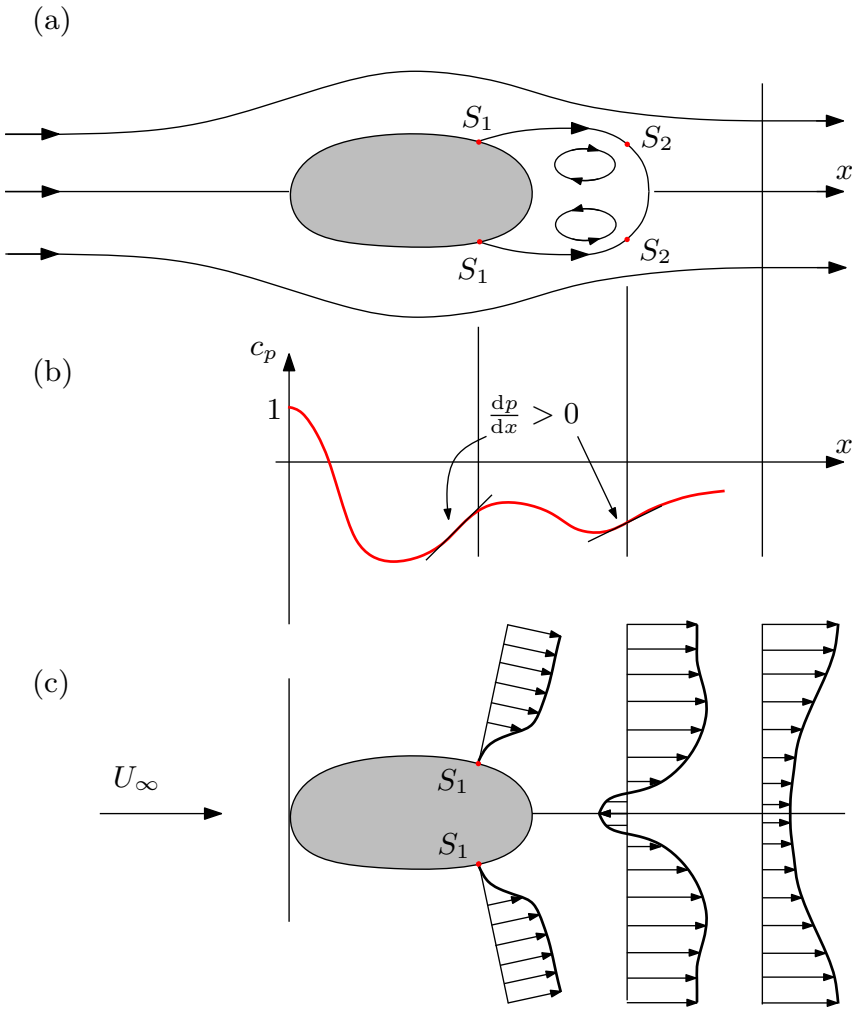


Figure 2.18: Schematic illustration of the flow around a bluff body. (a) Streamlines, (b) pressure distribution, (c) velocity profiles. S denotes separation. Referring to Hucho (2013).

decreases in the upstream region of the body until in the rear part a minimum is reached at the maximum thickness of the body. Due to the body contour, the pressure increases, resulting in the separation of the boundary layer at the points S_1. Here, the fluid is accelerated and the kinetic energy of the fluid particles increases (Hucho, 2013).

The boundary between near- and far-wake at the ground is sketched in Fig. 2.19 following the separation streamline from the windward facade through the horseshoe vortex to the rear stagnation point RS, where the flow is divided either to return upward or to escape downwind. At the rear of the body, two vertical vortical structures occur, driven by the flow from the horseshoe vortex through the shear layers on each side of the body. Those are marked with an A and are connected in a horseshoe like manner as sketched in Fig. 2.17. The pressure coefficient at the upwind edge of the lateral surface reaches a large negative value and becomes less negative downstream. B indicates a circulation driven by the shear layer over the roof tending to draw the flow in the vortices A upwards. The flow escaping in the far-wake is marked with C (Cook, 1985). Drag and lift essentially depend on the behaviour of the boundary layer, the flow separation and the size of the resulting near-wake space. Laminar boundary layers tend to separate sooner than turbulent ones. Considering the velocity profile in Fig. 2.1 it can be seen that higher velocities close to the wall prevail in turbulent boundary layers. Since the flow is more energetic, the turbulent boundary layer may follow an adverse pressure gradient

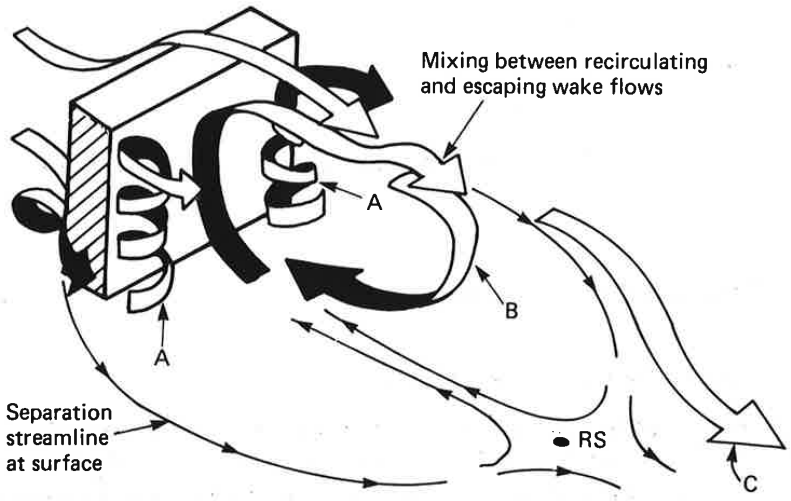


Figure 2.19: Wake circulation behind a cuboidal body, schematically. From Cook (1985).

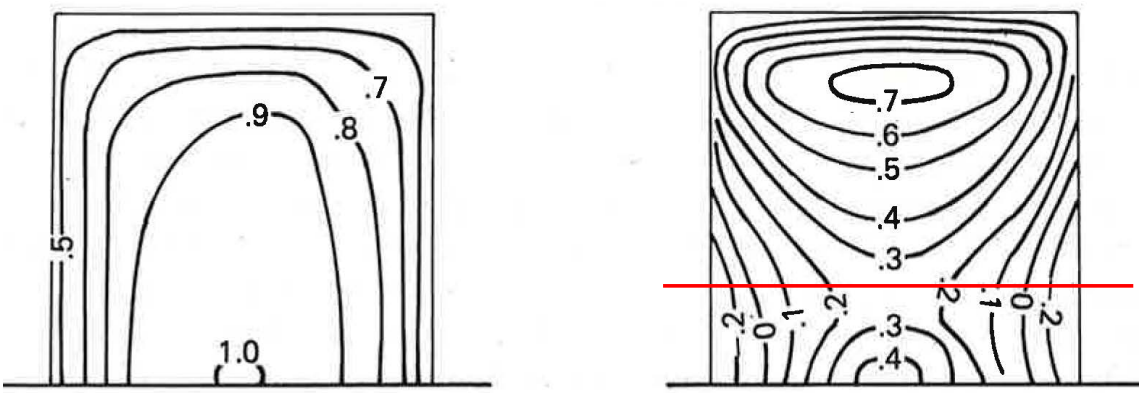


Figure 2.20: Schematical illustration of the distribution of the pressure coefficient on the windward face: (a) for uniform inlet flow, (b) for non-uniform inlet flow. From Cook (1985).

over longer distances until separation occurs.

For sharp-edged bodies, the force and moment coefficients are fairly constant over wide ranges of the Reynolds number. The largest local negative pressure coefficients in the flow around a building usually arise on the roof of the building. In particular, this is caused by so-called *delta-wing like vortices* under yawing inflow conditions. However, this was not investigated in this work, so that it is not discussed here. Detailed descriptions can be found in Cook (1985).

Fig. 2.20 exemplarily shows the different distributions of time-averaged pressure coefficient $c_{p,mean}$ on the windward facade of a cuboidal body (a) for a uniform low-turbulence flow and (b) for a boundary layer flow with corresponding velocity profile and turbulence intensity. Depending on the particular parameters of the velocity profile, these can be very different. For boundary layer flow, the depicted pressure coefficient increases with the height according to the increasing dynamic pressure. According to Fig. 2.17, the stagnation point is approximately located at three-quarters of the height of the building. In the height marked by a red line in Fig. 2.20 a typical corner vortex is formed, which continues laterally around the building so that the horseshoe vortex developes (Cook, 1985).

2.3.2 Force, moment and pressure coefficients

The forces acting on a body can be determined by measurements in wind tunnels, either in original size or using models in appropriate scales. To draw the correct conclusions from such experiments, the results are represented in terms of dimensionless coefficients, since these physical quantities are independent from functional dependencies on scaling factors. If models are applied in measurements, attention to the transferability of the results by similarity laws is required (Hucho, 2013).

The dimensionless coefficients are deduced from dimensional analytical considerations. The relevant forces are related to the dynamic pressure p_{dyn} of the incoming flow, a characteristic reference area A – exemplarily the face of the body in the free stream area – and a characteristic length L of the body. The dynamic pressure is calculated as

$$p_{\mathrm{dyn}} = \frac{\rho}{2} U_\infty^2 \, . \tag{2.72}$$

The momentum equation (2.2), neglecting body forces, in integral form reads

$$\int_V \left[\frac{\partial \rho \mathbf{v}}{\partial t} + \nabla \cdot (\rho \mathbf{v}\mathbf{v}) \right] \mathrm{d}V = \underbrace{\int_V \nabla \cdot \underline{\boldsymbol{\sigma}} \; dV}_{= \oint_S \underline{\boldsymbol{\sigma}} \cdot \mathrm{d}\mathbf{S}} \, . \tag{2.73}$$

Nondimensionalization by characteristic scaling parameters

$$\underline{\boldsymbol{\sigma}}^\star = \frac{\underline{\boldsymbol{\sigma}}}{\frac{\rho}{2} U_\infty^2} \quad \text{and} \quad \mathrm{d}\mathbf{S}^\star = \frac{\mathrm{d}\mathbf{S}}{\mathbf{A}}$$

yields

$$F = \oint_{A^\star} \frac{\rho}{2} U_\infty^2 \; \underline{\boldsymbol{\sigma}}^\star \cdot A \; \mathrm{d}\mathbf{S}^\star \tag{2.74}$$

and, thus

$$\frac{F}{\frac{\rho}{2} U_\infty^2 A} = \oint_{A^\star} \underline{\boldsymbol{\sigma}}^\star \cdot \mathrm{d}\mathbf{S}^\star =: c \, . \tag{2.75}$$

Since $\underline{\boldsymbol{\sigma}}^\star$ is a solution of the Navier Stokes equations, it only depends on the boundary conditions and the Reynolds number Re. Analogously the dimensionless moment

coefficient $M/((AL\rho U_\infty^2)$ can be deduced. The dimensional analysis yields the following relations for the dimensionless coefficients:

$$c_D = \frac{F_D}{\frac{\rho}{2}U_\infty^2 A} \qquad c_L = \frac{F_L}{\frac{\rho}{2}U_\infty^2 A} \qquad c_S = \frac{F_S}{\frac{\rho}{2}U_\infty^2 A}$$
$$c_R = \frac{M_R}{\frac{\rho}{2}U_\infty^2 AL} \qquad c_P = \frac{M_P}{\frac{\rho}{2}U_\infty^2 AL} \qquad c_Y = \frac{M_Y}{\frac{\rho}{2}U_\infty^2 AL}\,. \tag{2.76}$$

The flow around buildings in natural wind causes pressure forces $p\,\mathrm{d}S$ perpendicular to the surface and viscous forces $\tau_W\,\mathrm{d}S$ on the surface element $\mathrm{d}S$. The direction of the shear stress τ_W is aligned with the direction of flow. Friction forces are in many cases relatively small and, thus, the resulting wind forces on the structure can be calculated by integration of the pressure distribution (Kiefer, 2003).

The difference between the static pressure p on the building surface and the ambient pressure p_a is related to the dynamic pressure, yielding the pressure coefficient

$$c_p = \frac{p - p_a}{\frac{\rho}{2}U_\infty^2}\,. \tag{2.77}$$

This coefficient allows for a non-dimensional representation of the static pressure distribution induced by the flow, deviating from p_a.

2.3.3 Mechanical similarity and non-dimensional numbers

An adequate method for the investigation of the flow around buildings are experiments with models in a wind tunnel. To ensure the transferability of the results from the model tests to nature, the relevant similarity laws with regard to the building have to be considered. The physical principles for modeling the flow around buildings in accordance with the similarity laws, are considered in detail in Plate (1982a) and Cermak (1982).

The following section discusses the geometrical similarity between original and model, as well as the kinematic and dynamic similarity.

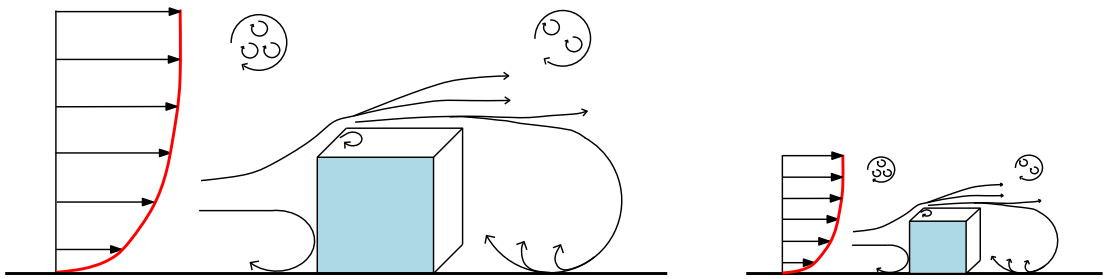


Figure 2.21: Geometrical similarity of a wall-mounted obstacle in nature and in model size.

Geometrical similarity

To ensure geometrical similarity, the scaling down of the building under investigation is not sufficient. The requirement of geometrical similarity may seem trivial, but in general this is not applicable in full detail, the stronger the model is downscaled. Therefore, in each individual test the details to be considered and to be neglected must be decided carefully (Hucho, 2013).

Rather, the turbulence structure and their characteristic eddy sizes in the same scale have to be reproduced as a model of natural wind flow in the wind tunnel (see Fig. 2.21). This can be achieved by downsizing the scale to the similarity numbers of the turbulent wind flow (Hucho, 2013; Kiefer, 2003).

Dynamic similarity

To ensure a similar flow around two geometrically similar models, the forces have to be in the same ratio. Concerning the flow of an incompressible fluid, the inertial and frictional forces are most important. Their ratio is expressed by the Reynolds number (cf. Eq. (2.25)):

$$Re = \frac{U\,L}{\nu}. \tag{2.78}$$

According to Plate (1982a) due to large surface roughnesses, the roughness Reynolds number of natural terrain is always within the aerodynamically rough regime. If the roughness length z_0 and the friction velocity u_τ are chosen as the characteristic length and the characteristic velocity, respectively, the according regime can be expressed

by (Plate, 1982a)

$$Re = \frac{u_\tau \, z_0}{\nu} > 5. \tag{2.79}$$

For dynamic similarity, the Reynolds number must be equal in the two systems. Since the kinematic viscosity of air in nature and in the model experiment is the same, and the characteristic length has to be reduced to model scale, the velocity needs to be increased in the wind tunnel by the same extent to ensure compliance with the Reynolds number similarity. However, this cannot be satisfied in wind tunnel investigations for building models on a smaller scale, since in both cases the same fluid is applied. This would lead to velocity ranges in which the flow would be compressible.

According to Zierep and Bühler (2013), in the case of prismatic bodies, a Reynolds number independence of the flow is reached at much lower velocities than determined by the dynamic similarities. A typical value is given, e.g., by Plate (1982a) with

$$Re = \frac{U_\infty \, W}{\nu} > 5 \cdot 10^4 \,, \tag{2.80}$$

where W denotes the width of the building. In flows over sharp-edged objects, as common for buildings, the error due to non-compliance with the Reynolds number, is reduced since the separation points or lines are predetermined (Kiefer, 2003).

In the lower part of the boundary layer, the roughness length z_0 is the only characteristic length affecting the turbulent motion. After Cook (1986), pressure and force coefficients on models of wall-mounted buildings are equal for both full and model scale only when the roughness length z_0 is in scale with the building size. So for buildings with a height much smaller than the boundary layer thickness ($H \ll \delta$), the ratio of the building height to the roughness length, the so-called *Jensen number*, must be equal in both systems:

$$Je = \frac{H}{z_0}. \tag{2.81}$$

Wherever flows are influenced by gravity, the ratio of inertial forces to the gravitational force is important and represented by the Froude number Fr (cf. Eq. (2.18)). After Sockel (1984), the influence of the Froude number in building aerodynamics is low and therefore not further considered in this context.

The Euler number represents the ratio between pressure and inertial forces

$$Eu = \frac{\Delta p}{\rho\, U^2}. \tag{2.82}$$

An important number for unsteady flows is the Strouhal number Sr, which is the ratio of inertial forces caused by the unsteadiness of the flow and by the convective transport at a characteristic velocity

$$Sr = \frac{U\, f_v}{U^2/L} = \frac{f_v\, L}{U}\,, \tag{2.83}$$

where $f_v = 1/T$ is the frequency of the unsteady phenomena.

According to Counihan (1971), the exponent α of the wind profile in Eqs. (2.67) and (2.68) in nature is proportional to z_0 and therefore a measure for the influence of roughness. From Eq. (2.67) it can be deduced that

$$\alpha_N = \alpha_M\,, \tag{2.84}$$

where the subscripts N and M denote the exponent α in nature and in model scale, respectively.

2.3.4 Ventilation – the flow through building openings

The flow through a building requires a pressure difference between the indoor and outdoor areas and various openings such as windows or doors. Additionally, all leaks act as openings, too.

The pressure difference necessary for the natural ventilation is caused by the local flow conditions in the external flow, by buoyancy due to temperature differences between the inside and outside areas, or from a superposition of both effects (Fitzner, 2013). The resulting over and under pressure regions on a building are represented by profiles of the pressure coefficient c_p (cf. Eq. (2.77) and Fig. 2.20).

Due to the pressure differences across the openings and passages of buildings, often significant air flows occur, which can be characterised by measuring the mean velocities in the cross-sectional areas of the openings, and the equation of continuity.

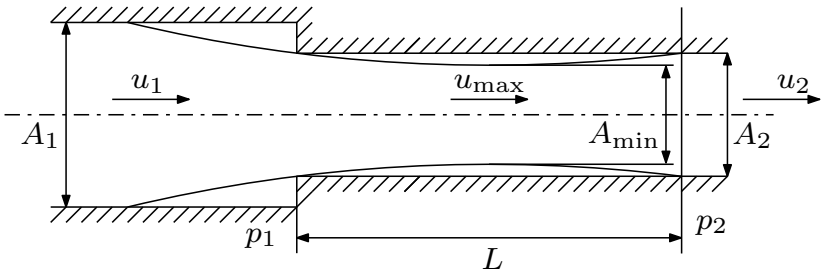


Figure 2.22: Sudden constriction of the flow cross section. Referring to Sockel (1984).

The pressure-driven flow through windows in a facade of a building is much like the flow through a sudden constriction with cross sections $A_1 > A_2$ causing a contraction of the flow cross section and formation of a jet as shown in Fig. 2.22 (according to Sockel (1984)). A detailed derivation can be found in Sockel (1984).

In discontinuous contractions, losses due to separation and jet formation occur. The jet contraction ratio ε is defined as

$$\varepsilon = \frac{A_{\min}}{A_2} = \frac{u_2}{u_{\max}}\,, \tag{2.85}$$

where $A_{\min}$, A_2, u_2, and $u_{\max}$ are depicted in Fig. 2.22. The contraction ratio ε depends on the ratio A_2/A_1 and the cross-sectional shape. A_1 diverges to infinity as u_1 goes to zero in the case of windows in building facades subject to natural wind. The quantity ε enables the calculation of the velocity $u_{\max}$ in the cross section $A_{\min}$ from the measured value u_2, and vice versa.

The particular case to which this consideration can be applied is the flow into a building through a wall opening (e.g. a window), where the constriction is short as shown in Fig. 2.23.

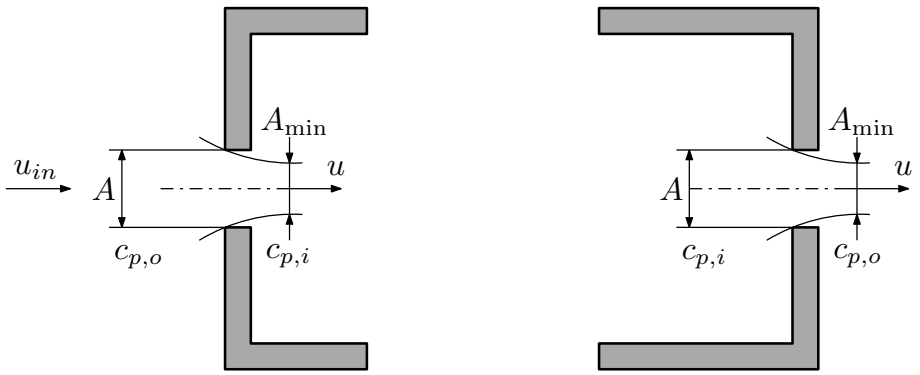
Redefining the quantities

$$A_2 \to A, \qquad u_2 \to u_{in}, \qquad u_{\max} \to u \tag{2.86}$$

for the particular situation and rewriting Eq. (2.85) yields

$$\varepsilon = \frac{A_{\min}}{A} = \frac{u_{in}}{u}\,. \tag{2.87}$$

For this specific case with $A_1 \to \infty$ Sockel (1984) suggests the value $\varepsilon = 0.59$.



(a) (b)

Figure 2.23: Flow through openings and passages: (a) Inflow, (b) outflow. The subscripts i and o denote inside and outside, respectively. Referring to Sockel (1984). Reprinted from Teppner et al. (2014a), with permission from Elsevier.

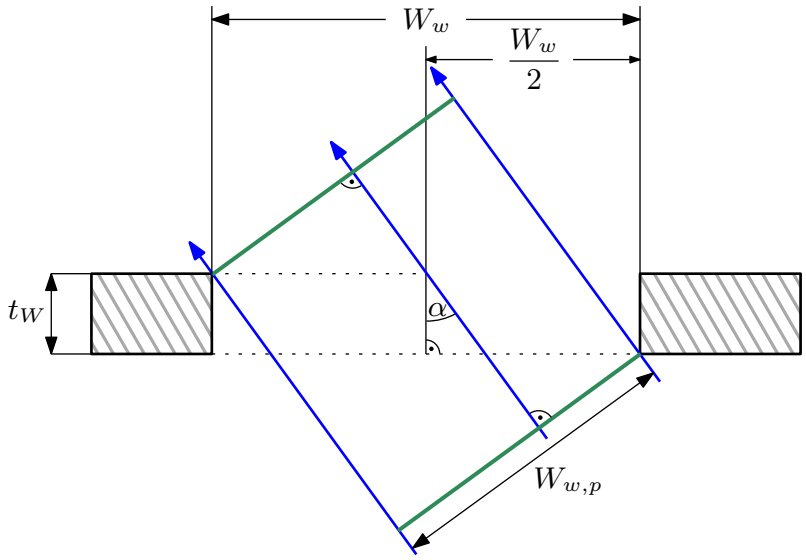


Figure 2.24: Flow through a window at an incidence angle of α.

For a non perpendicular flow to the facade of the building, the projected cross sectional area resulting from different incidence angles α has to be taken into account for the calculation of the volumetric flow rates (Teppner et al., 2014a).

Fig. 2.24 demonstrates the flow through an area depending on the geometry and the incidence angle α, where W_w denotes the width of the window and t_W the thickness of the wall. The projected width $W_{w,p}$ of the window is determined using trigonometric relations by

$$W_{w,p} = \cos\alpha \left(W_w - t_W \tan\alpha\right) . \tag{2.88}$$

The cross sectional area and, hence, the volumetric flow rate $\dot{V}$ through the window can be calculated from the measured velocity applying this projected width $W_{w,p}$.

According to Maas (1995), the type of ventilation has significant influence on the thermal behaviour of buildings as well as the indoor air quality. Even today, most of the buildings are ventilated through windows and doors. If this happens exclusively driven by wind or temperature differences, this is termed *natural ventilation*.

The air exchange achievable by opening windows and doors is described by the so-called air exchange rate (ACH). The ACH is defined as the ratio of the total hourly volumetric air flow rate to a room or building volume, i.e.

$$\mathrm{ACH} = \frac{\dot{V}}{V_R} , \tag{2.89}$$

where V_R denotes the room volume. Following the description in VDI 4300 Part 7 VDI (2001), the result is the number of room volume exchanges per unit time (usually one hour). In general, the existing air exchange through all openings and leakages in the building envelope is taken into account.

The equation for the volume flow rate through an opening with an arbitrary cross section A in a structure is called the *orifice equation* in many textbooks and given as

$$\dot{V} = C_D A \sqrt{\frac{2\Delta p}{\rho}} . \tag{2.90}$$

This expression represents the flow rate as a cross section multiplied by a velocity derived from a pressure difference across the opening, times a factor C_D called the

discharge coefficient. In Eq. (2.90), ρ is the air density.

The discharge coefficient C_D and its specific numerical value for different applications were determined for various configurations in Heiselberg et al. (2001), Iqbal et al. (2012), Karava et al. (2004, 2007), Seifert et al. (2006), Wetter (2006), and Chu and Chiang (2013). The flow across fully open windows as sketched in Fig. 2.23 is captured by a discharge coefficient $C_D \approx 1$ (Sockel, 1984). In the case of partially

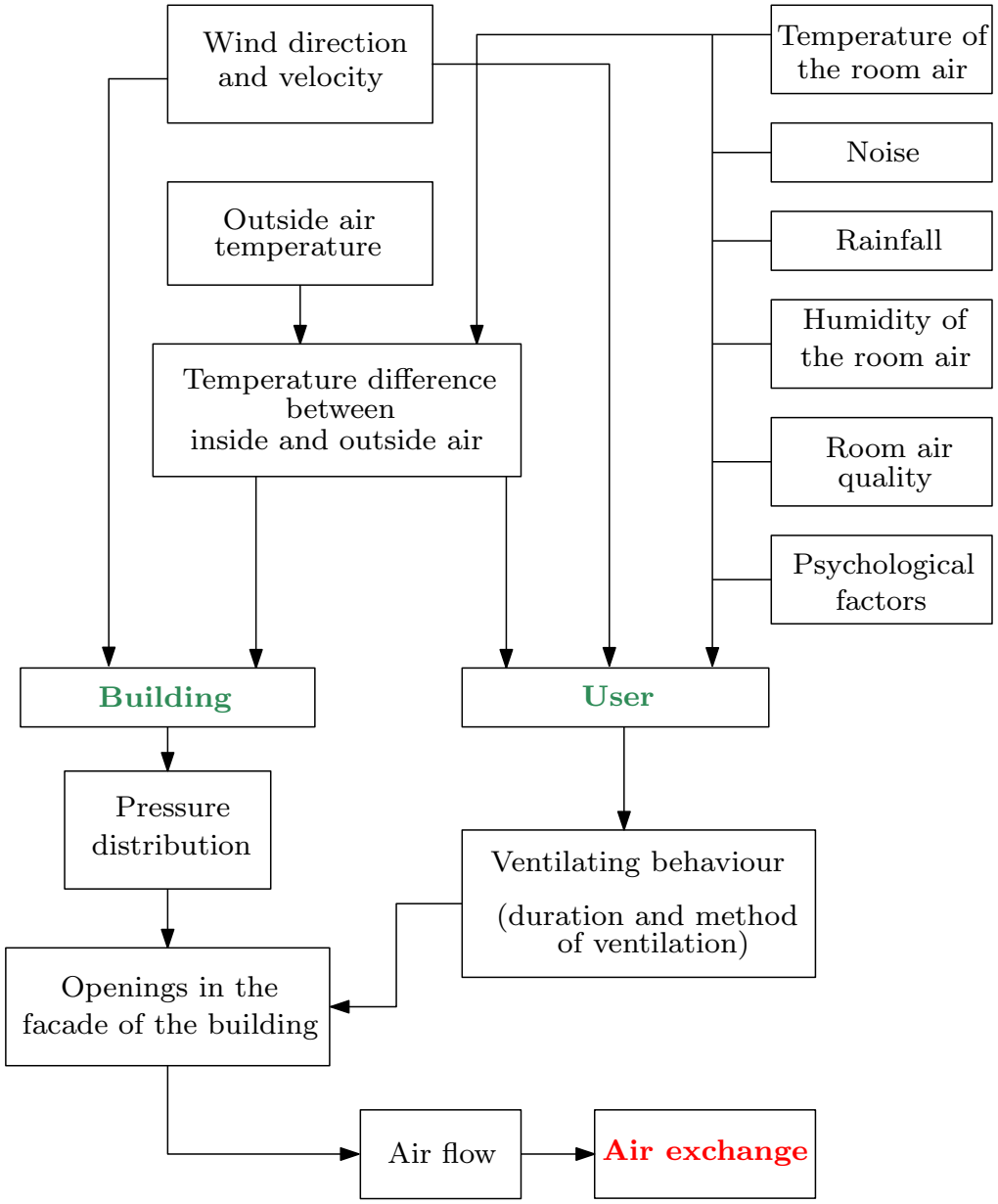


Figure 2.25: Factors influencing the ACH. Referring to Maas (1995).

blocked openings like tilted windows the losses can be taken into account by a loss coefficient ζ. The corresponding discharge coefficient can be calculated as

$$C_D = \frac{1}{\sqrt{1 + \zeta \left(A_G/A\right)^2}} \,, \tag{2.91}$$

where A is the whole cross section of the window and A_G is the cross section of the free gaps. The ACH, which is the air volume flow rate divided by the room volume, can therefore be expressed as

$$\mathrm{ACH} = \frac{A_G}{V_R} \sqrt{\frac{2\Delta p}{\rho \left(1 + \zeta \left(A_G/A\right)^2\right)}} \,. \tag{2.92}$$

Using C_v , the *effectiveness of openings*, the expression for the wind induced air flow rate into a room with a free inlet area A can be formulated as (ASHRAE, 2009)

$$\dot{V} = C_v A U_\infty \,, \tag{2.93}$$

where U_∞ is the wind velocity. C_v is assumed to be 0.5 to 0.6 for perpendicular winds and corresponds to the contraction ratio $\varepsilon = 0.59$ after Sockel (1984) (cf. Eq. (4)).

As can be seen in Fig. 2.25, the air exchange is influenced by many different factors. These include not only driving forces due to thermal and wind-induced influences, but also the usage behaviour of the user. The description of mechanical ventilation systems is avoided, since this was not a part of the present work.

An adequate air exchange is essential to ensure the supply of fresh air for all people in a building, as well as the removal of humidity. The air exchange rate is therefore one of the most important variables for the maintenance of a comfortable indoor climate, even referring to the concentration of harmful substances that must not exceed certain limits (Maas, 1995; VDI, 2001).

The following parameters have important influence on thermal comfort: air temperature and average inner surface temperature of the space-enclosing surfaces. The space-enclosing surfaces in this context include the exterior and interior walls of a room, its floor and its ceiling as well as furniture, heaters and window surfaces.

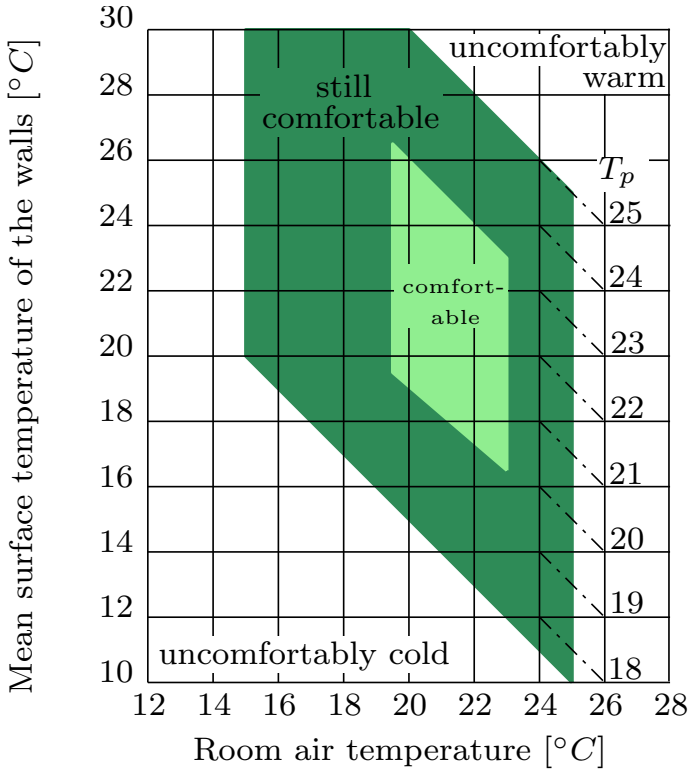


Figure 2.26: Comfort zone, dependent on room air and surface temperatures, schematically. T_p denotes the temperature perceived by people. Referring to Reiher (1975) and Lohmeyer and Post (2013).

The respective surface temperature is proportionally attributed to the mean surface temperature of the space-enclosing surfaces. The greater the distance of the space-enclosing surfaces from a local position in the room, the lower the influence of their surface temperatures on thermal comfort. Fig. 2.26 shows the relationship of comfort and perceived temperature in sitting work to moderate activity and appropriately adapted clothing (Reiher, 1975; Lohmeyer and Post, 2013).

2.4 Heat transfer through the building envelope

Various heat exchange processes occur between a building and the external environment. On the one hand, this happens by heat conduction through various building elements, such as walls, roofs or floors. On the other hand, heat transfer by radiation or convection takes place. In practically all cases, heat conduction occurs in combination with convection. The reason is that the bodies under consideration

are in contact with fluid media and, thus, heat transfer from the solid body to the gaseous or liquid environment or vice versa takes place.

Using the total stress tensor $\underline{\boldsymbol{\sigma}}$, the energy equation in integral form is given by

$$\int_V \frac{\partial}{\partial t}\left[\rho\left(e+\frac{\mathbf{v}^2}{2}\right)\right]\mathrm{d}V + \int_V \nabla\cdot\left[\rho\mathbf{v}\left(e+\frac{\mathbf{v}^2}{2}\right)\right]\mathrm{d}V \tag{2.94}$$
$$= \int_V \left[\mathbf{v}\cdot\left(\nabla\cdot\underline{\boldsymbol{\sigma}}+\rho\,\mathbf{f}^B\right)+\left(\nabla\cdot\mathbf{q}+\dot{q}_Q\right)\right]\mathrm{d}V\ ,$$

where $(\nabla\cdot\mathbf{q})$ is the rate of resultant internal energy transport by heat conduction, and $\dot{q}_Q$ represents the supplied power per unit volume by energy sources. In terms of specific enthalpy h, Eq. (2.94) in differential form reads (Bird et al., 2007):

$$\rho\frac{\mathrm{d}h}{\mathrm{d}t} = \frac{\mathrm{d}p}{\mathrm{d}t} + (\tau:\nabla\mathbf{v}) - (\nabla\cdot\mathbf{q}) + \dot{q}_Q\ , \tag{2.95}$$

where $(\tau:\nabla\mathbf{v})$ is called the dissipation function and represents the irreversible transformation of mechanical energy into thermal energy by dissipation. Assuming vanishing velocities and $\mathrm{d}p/\mathrm{d}t = 0$ for quiescent fluids or solid bodies results in the heat conduction equation

$$\rho\frac{\partial h}{\partial t} = -\left(\nabla\cdot\mathbf{q}\right)+\dot{q}_Q\ . \tag{2.96}$$

Using $\mathrm{d}h = c_p\mathrm{d}T$ for a differential change of the enthalpy, and Fourier's law for heat conduction

$$\mathbf{q} = -\lambda\nabla T\ , \tag{2.97}$$

leads to the heat conduction equation in terms of temperature

$$\frac{\partial T}{\partial t} = \frac{\lambda}{\rho c_p}\Delta T + \frac{\dot{q}_Q}{\rho c_p}\ . \tag{2.98}$$

Here, λ denotes the thermal conductivity. Using the thermal diffusivity $a := \lambda/\rho c_p$, Eq. (2.98) can be rewritten to

$$\frac{\partial T}{\partial t} = a\Delta T + \frac{\dot{q}_Q}{\rho c_p}\ . \tag{2.99}$$

Referring to Fig. 2.27, the steady heat conduction through a plane wall without

energy sources can be described by the following simple equation:

$$\frac{\mathrm{d}^2T}{\mathrm{d}x^2} = 0 \; . \tag{2.100}$$

Solving this differential equation subject to the boundary conditions $T(x = 0) = T_{w_1}$ and $T(x = L) = T_{w_2}$, yields

$$T(x) = T_{w_1} + \frac{x}{L}\left(T_{w_2} - T_{w_1}\right) \; . \tag{2.101}$$

Applying Fourier's law, the heat flux may be expressed as

$$q = \lambda \frac{T_{w_1} - T_{w_2}}{L} \; , \tag{2.102}$$

and the total heat transfer rate as

$$Q = A\lambda \frac{T_{w_1} - T_{w_2}}{L} \; . \tag{2.103}$$

Considering the temperature profile in a moving fluid near a body surface with a temperature T_w diferring from the fluid temperature T_F, the heat flux q is described as the product of the temperature difference between the wall and the undisturbed

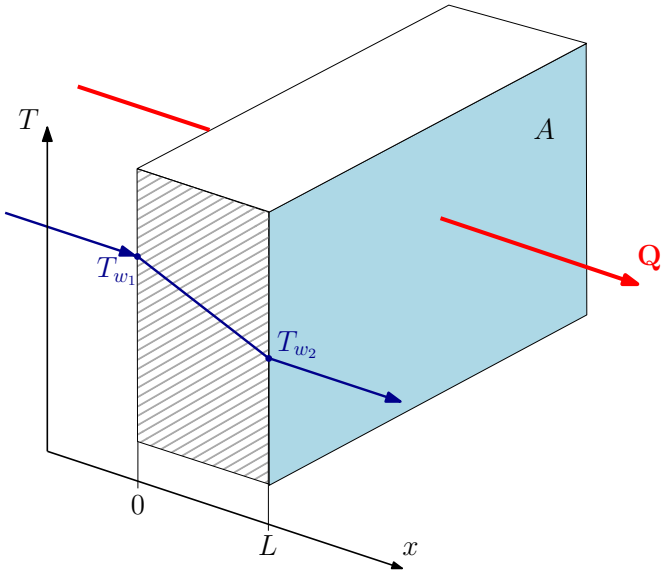


Figure 2.27: Steady-state heat conduction through a wall without sources of energy.

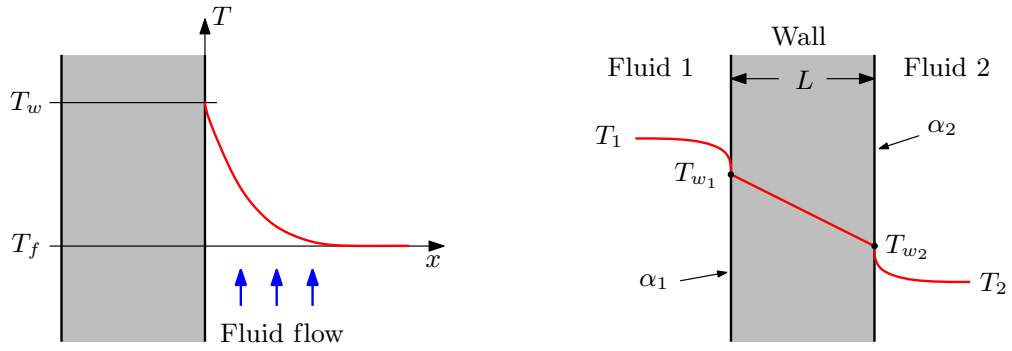


Figure 2.28: (a) Temperature profile in a moving fluid near a body surface. (b) Heat transfer through a plane wall.

fluid and the heat transfer coefficient α through

$$q = \alpha \, (T_w - T_f) \ , \tag{2.104}$$

called *Newton's law of cooling* (cf. Fig. 2.28(a)). The heat transfer coefficient α is a function of the flow conditions, the physical properties of the fluid, and the body geometry.

Fig. 2.28(b) sketches a typical problem in building aerodynamics. We consider the heat transfer from a heated room through an exterior wall of a building to the environment. The heat transfer through a solid wall may be described as follows, if the inner room temperature is assumed to be higher than the outside air temperature: heat is transferred by convection from fluid 1 with temperature T_1 to the wall, transferred through the wall by conduction, and transferred by convection to the outer fluid 2 with the lower temperature T_2. The total heat transfer rate Q for this case is given by

$$Q = \frac{A}{\dfrac{1}{\alpha_1} + \dfrac{L}{\lambda} + \dfrac{1}{\alpha_2}} \, (T_1 - T_2) \ . \tag{2.105}$$

This may be expressed as $Q = k \, A \, (T_1 - T_2)$, where k denotes the overall heat transfer coefficient. The detailed derivation can be found in Bird et al. (2007).

Convective heat transport is actually thermal conduction by a temperature gradient influenced by fluid flow. In the field of building aerodynamics, heat transfer between solid walls and a fluid is of particular interest. In order to determine the

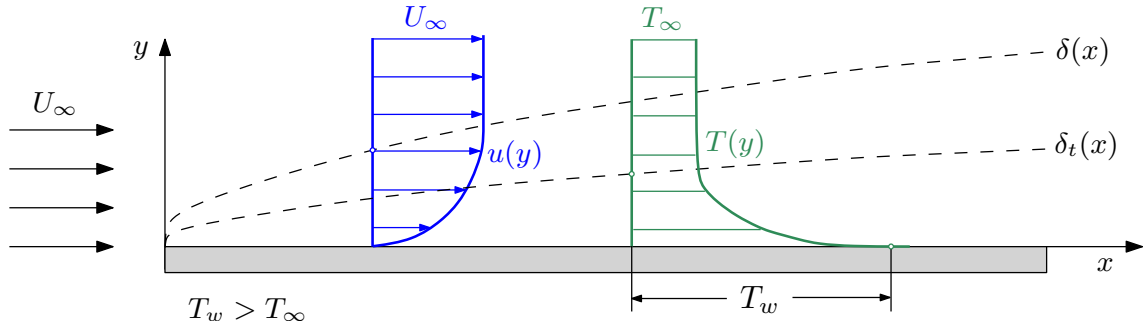


Figure 2.29: Velocity profile for a laminar dynamic boundary layer with thickness $\delta(x)$ and temperature profile in the according thermal boundary layer with thickness $\delta_t(x)$.

temperature distribution in the fluid and in the solid body, knowledge of the flow conditions is necessary.

In analogy to the flow behaviour of fluids along solid walls it can be concluded that the temperature of the fluid changes noticeably only in a thin layer near the solid wall, but is unaffected at larger distances. As already mentioned, in a flow around a body the boundary layer thickness δ changes with the coordinate x along the body contour. Similarly, in case of heat transfer a thermal boundary layer of thickness δ_t develops, as can be seen in Fig. 2.29. The transfer of heat between a solid body and the surrounding fluid is determined by the behaviour in the near-wall region. This may be described by the Nusselt number Nu as the dimensionless temperature gradient at a surface. The heat flux results from the gradient of the temperature profile directly on the wall ($y = 0$). The Nusselt number is then obtained from the dimensionless representation of the boundary condition

$$\alpha(T_W - T_\infty) = -\lambda_f \left.\frac{\partial T}{\partial y}\right|_{y=0} , \tag{2.106}$$

where λ_f is the thermal conductivity of the fluid. Introducing the dimensionless quantities

$$y^\star = \frac{y}{L} , \quad \Theta^\star = \frac{\Theta}{\Theta_0} \text{ with } \Theta = T - T_\infty \text{ and } \Theta_0 = T_W - T_\infty , \tag{2.107}$$

where L is a measure of length, yields

$$\frac{\alpha}{\lambda_f} = -\frac{1}{L} \left.\frac{\partial \Theta^\star}{\partial y^\star}\right|_{y^\star=0} , \tag{2.108}$$

which finally results in

$$\frac{\alpha L}{\lambda_f} = -\frac{\partial \Theta^\star}{\partial y^\star}\bigg|_{y^\star=0} =: Nu \; . \tag{2.109}$$

Physically, the Nusselt number Nu is the ratio of convective heat transfer at a solid surface to the heat transfer due to pure heat conduction.

In order to distinguish whether the heat transfer within a fluid takes place mainly by thermal conduction or by convection, the dimensionless Rayleigh number Ra, which can be derived by nondimensionalization of the equation of momentum, is used. Considering the equations of change for $\rho = const.$ and without heat sources $\dot{q}_Q$ in the form

$$\begin{gathered}
(\nabla \cdot \mathbf{v}) = 0 \\
\frac{\partial \mathbf{v}}{\partial t} + (\mathbf{v} \cdot \nabla)\, \mathbf{v} = -\frac{1}{\rho}\nabla p + \nu \nabla^2 \mathbf{v} - \mathbf{g}\, \beta\, (T - T_\infty) \\
\rho c_p \left(\frac{\partial T}{\partial t} + \mathbf{v} \cdot \nabla T \right) = \lambda \nabla^2 T + \Phi_\mu
\end{gathered} \tag{2.110}$$

and introducing the dimensionless quantities

$$\begin{gathered}
\mathbf{v}^\star = \frac{\mathbf{v}}{U_\infty} \; ; \quad \mathbf{x}^\star = \frac{\mathbf{x}}{L} \; ; \\
p^\star = \frac{pL}{\mu U_\infty} \; ; \quad t^\star = \frac{t U_\infty}{L} \\
\nabla^\star = L\, \nabla \; ; \quad \mathbf{g}^\star = \frac{1}{g}\mathbf{g} \; ; \quad \Phi_\mu^\star = \left(\frac{L}{U_\infty} \right)^2 \Phi_\mu \quad \text{and} \\
\Theta = T - T_\infty \; ; \quad \Theta_0 = T_W - T_\infty \\
\Rightarrow \quad \Theta^\star = \frac{\Theta}{\Theta_0}
\end{gathered}$$

yields

$$\begin{gathered}
(\nabla^\star \cdot \mathbf{v}^\star) = 0 \\
\frac{\partial \mathbf{v}^\star}{\partial t^\star} + (\mathbf{v}^\star \cdot \nabla^\star)\, \mathbf{v}^\star = -\frac{1}{Re}\nabla^\star p^\star + \frac{1}{Re}\nabla^{\star 2}\mathbf{v}^\star - \frac{Gr}{Re^2}\, \mathbf{g}^\star \Theta^\star \\
\frac{\partial \Theta^\star}{\partial t^\star} + \mathbf{v}^\star \cdot \nabla^\star \Theta^\star = \frac{1}{Re\; Pr}\nabla^{\star 2}\Theta^\star + \frac{Ec}{Re}\, \Phi_\mu^\star \; .
\end{gathered} \tag{2.111}$$

Following Bird et al. (2007) the assumption of a creeping flow is appropriate, so that the left hand side of the momentum equation can be neglected. Since no

imprinted velocity is available in this case, it proves convenient to define $U_\infty = a/L$ and, so that the division of the equation of motion by Pr leads to only one dimensionless group $Gr\ Pr$ appearing in the equation:

$$0 = -Pr\ \nabla^\star p^\star + Pr\ \nabla^{\star 2}\mathbf{v}^\star - Gr\ Pr^2\ \mathbf{g}^\star\,\Theta^\star \quad \text{or}$$

$$0 = -\nabla^\star p^\star + \nabla^{\star 2}\mathbf{v}^\star - \boldsymbol{Gr\ Pr}\ \mathbf{g}^\star\,\Theta^\star\ . \tag{2.112}$$

After Bird et al. (2007) neglecting Ec/Re results in an equation of energy, in which no dimensionless groups appear:

$$\frac{\partial\Theta^\star}{\partial t^\star} + \mathbf{v}^\star\cdot\nabla^\star\Theta^\star = \nabla^{\star 2}\,\Theta^\star\ . \tag{2.113}$$

The product of the Grashof and the Prandtl number describes the transfer of heat in a fluid and is called the Rayleigh number

$$Ra = Gr\cdot Pr = \frac{g\beta}{\nu a}\,(T - T_\infty)\,L^3\ . \tag{2.114}$$

For Rayleigh numbers exceeding a critical value of 10^9 the flow changes from laminar to turbulent.

In most practical cases of heat transfer, the mechanical work and the changes of kinetic and potential energies are negligible, which can be directly deduced from Eq. (2.14) for small Eckert numbers Ec. Rewriting the Eckert number in terms of the sound speed $c_\infty = \sqrt{\kappa\mathcal{R}T_\infty}$ yields

$$Ec = \frac{u_\infty^2\,c_\infty^2}{c_p(T_W - T_\infty)\,c_\infty^2} = (\kappa - 1)\underbrace{\left(\frac{u_\infty}{c_\infty}\right)^2}_{Ma^2}\frac{T_\infty}{T_W - T_\infty}\ , \tag{2.115}$$

where κ is the adiabatic exponent. Hence, all the terms in Eq. (2.14) containing the Eckert number Ec only have to be taken into account for transonic velocities and strong wall superheats, which is not the case with us. This applied, results in

$$\rho V\,\frac{\partial h}{\partial t} = \sum_{in} q_{in}A_{in} - \sum_{out} q_{out}A_{out} + \dot{q}_Q V + \sum_{in}\dot{m}_{in}h_{in} - \sum_{out}\dot{m}_{out}h_{out}\ . \tag{2.116}$$

Using the specific heat capacity c_p and a vector $\mathbf{n}$ perpendicular to the surface, gives

$$\rho\, c_p\, V\, \frac{\partial T}{\partial t} = \sum_i \mathbf{q}_i A_i \mathbf{n}_i + \dot{q}_Q V + \sum_i \rho\, \mathbf{v}_i \mathbf{n}_i A_i h_i \;, \tag{2.117}$$

where the last term represents the convective transport of energy through a control volume V. This may be expressed as

$$\sum_i \rho\, \mathbf{v}_i \mathbf{n}_i A_i h_i = \dot{m}\, c_p\, (T_1 - T_2) \;. \tag{2.118}$$

The foregoing relations will be further evaluated for specific applications in the next chapters.

Chapter 3

Experimental and numerical setups, and measurement methods

3.1 Models

The experiments of the present study were carried out with the aim to quantify the air exchange rate of rooms of a residential building model and to identify the magnitude of ACH in different rooms of the same storey. This work includes both single-sided ventilation and cross ventilation for open and tilted windows. For this purpose, three different models were developed and investigated in two different wind tunnels in order to measure (1) the pressure distribution from the atmospheric boundary layer flow on the full building facade, (2) the air exchange rate as derived from air velocities in open window cross sections and indoor cross sections in case of tilted windows, and (3) the air exchange rate with special account for tilted windows in a single room model. Some descriptions in this chapter were published in Teppner et al. (2013) and Teppner et al. (2014a). The corresponding texts were adopted here.

In this work, a 10-storey building with the dimensions of 21 m $\times$14 m and a height of 30 m was investigated. Within the building, the storeys under consideration differ in the positioning above ground only. The representative storey has a floor plan comprising typical natural ventilation scenarios for rooms with open and tilted windows. Fig. 3.1 shows the floor plan of the storey, including the window and room numbers, and the geometry of a tilted window. In the storey model, the dimensions

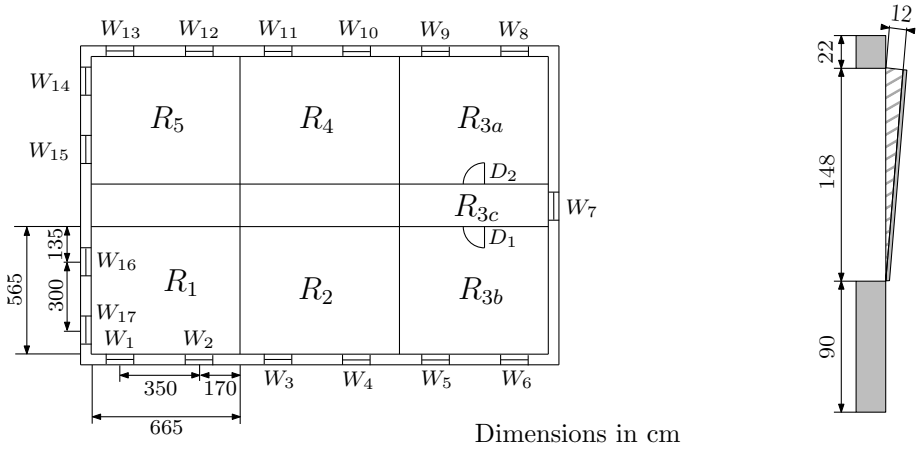


Figure 3.1: (a) Floor plan and notation of the investigated representative storey. Windows are denoted W_1 through W_{17}, rooms R_1 through R_5, doors D_1 and D_2. (b) Detailed sketch of a tilted window. Reprinted from Teppner et al. (2014a), with permission from Elsevier.

of the windows represent the dimensions of 1.48 m height and 1.23 m width on real scale. In case of a tilted window, an opening gap of 12 cm is adopted, as can be seen in Fig. 3.1. The ceiling height per storey is 2.6 m, and the ceiling structure is 0.4 m thick. For the purpose of pressure measurements in a boundary layer wind tunnel, a model of the complete building was established in 1:75 scale. This model was manufactured in the institute's workshop and is shown in Fig. 3.2.

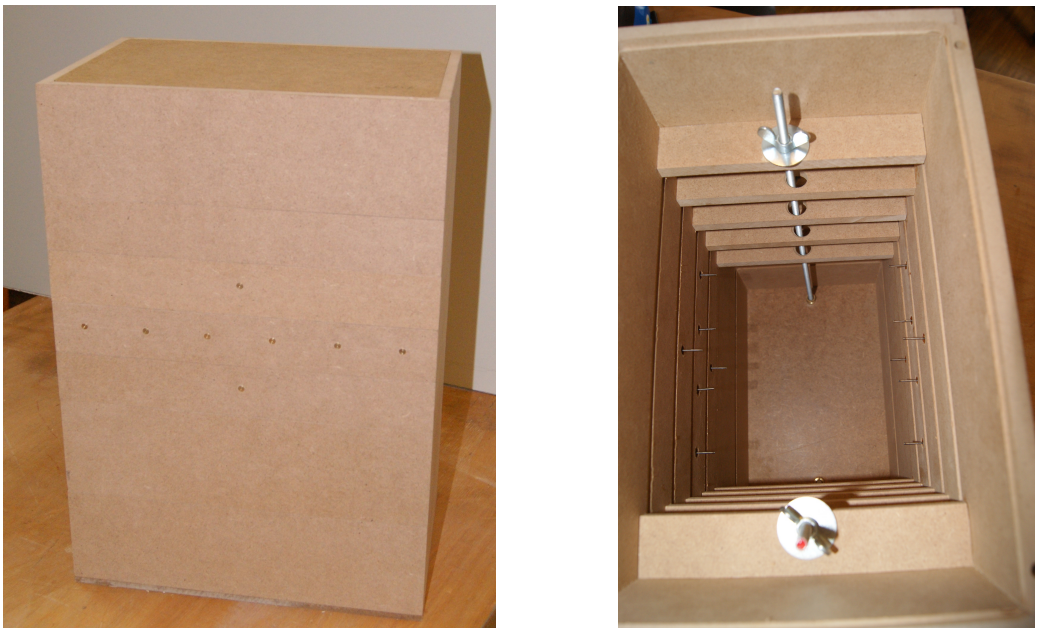
The individual floors are designed to be mounted modularly, so that the storey equipped with measurement units, consisting of 17 pressure sensors positioned in the centres of the closed rectangular window area, can be positioned at any height of the building model. However, this small model scale does not allow for velocity measurements in tiny openings like windows. These measurements were, therefore, carried out in a sample storey model of larger scale (1:25) in an aerodynamic wind tunnel, where the pressure distributions in different heights above ground in the boundary layer were reproduced. Fig. 3.1 shows the floor plan of the storey, including the window and room numbers, and the geometry of a tilted window.

Additionally, for investigating of the situation with tilted windows, a sample single room of again larger scale (1:10) representing the geometry of room R_1 (see Fig. 3.1) was established. Measurements with a storey separated from the rest of the building seem appropriate when parts of the neighbouring storeys below and above are attached as in the present case. Since the incidence angle of the wind and, therefore, the driving forces of the external flow field around the storey are nearly

horizontal, the influence of the building parts above and below can be captured by the adoption of smaller dummy sections. This procedure is equivalent to the use of so-called section models applied in bridge investigations (Teppner et al., 2014a).

Photographs of the two larger models in the test section of the aerodynamic wind tunnel are shown in Fig. 3.3. Due to measurement requirements, a modification of the window dimensions for the single room model was necessary, i.e. the windows have a height of 1.28 m, a width of 1.23 m, and the opening gap for the tilted window is 20 cm on real scale. The same inflow velocities as for the storey model were adopted.

The flow around the single room model does not fully represent the external flow around the storey model. The removal of the single room from the storey structure, and thus the possible upscaling of the model enables the metrological realization of velocity and tracer gas measurements for the case of natural ventilation through tilted windows.



(a) **(b)**

Figure 3.2: The building model on a scale of 1:75: (a) Exterior side and (b) interior top views of the model equipped with pressure holes, with modular constructed storeys.



(a) **(b)**

Figure 3.3: (a) Scaled storey model (1:25), and (b) scaled single room model (1:10) in the aerodynamic wind tunnel. Reprinted from Teppner et al. (2014a), with permission from Elsevier.

3.2 Wind Tunnels

3.2.1 The boundary layer wind tunnel

The first part of the wind tunnel investigations was carried out in the boundary layer wind tunnel of the Institute of Fluid Mechanics and Heat Transfer of Graz University of Technology, which is shown in Figure 3.4. This wind tunnel is a closed tunnel of Göttingen type and specifically designed for investigations within the scope of building aerodynamics when the simulation of atmospheric boundary layers is necessary.

The closed test section, devided in the fetch length and the working section, is 8.6 m long, with a cross section of a 2 m × 1 m at the nozzle exit, which can be changed by an adjustable roof plate to keep the static pressure approximately constant. The maximum uniform flow velocity is about 40 m/s.

This section is too short for the natural growth of thick boundary layers usually necessary for simulations at reasonable model scales. In the present application, artificial stimulation of suitable velocity profiles is achieved via the grid of cylindrical rods with variable spacing at the nozzle exit. The test section floor may be covered with roughness elements of various size and spacing (Lego or Duplo bricks). Thus, the exponential wind profiles (Eq. 2.68) representative for atmospheric boundary layers may be simulated over most of the test section height by using proper combinations of



Figure 3.4: The boundary layer wind tunnel of the Institute of Fluid Mechanics and Heat Transfer at Graz University of Technology.

velocity profile stimulation and roughness. Furthermore, a turntable allows rotation of the tested area in the test section in order to investigate the effects of varying incidence angles. The aim of this work was to investigate buildings in regions of uniform vegetation or suburban development, i.e. $z_0 = 0.15$ m for the logarithmic profile Eq. (2.65) or $\alpha = 0.22$ and $z_{gr} = 250$ m for the power law (Eq. 2.67) are predefined (in both cases related to u_{10}).

The spacing between the cylindrical rods of the grid, as well as the required height and the density of the roughness elements, were determined experimentally. The selected setting of the grid of rods is specified in Fig. 3.5. The test section floor of the wind tunnel, equipped with Lego base plates, was covered with Duplo bricks (19 mm high) or Lego bricks (9.5 mm high), as can be seen in Fig. 3.6. The surface coverage of the ground within the fetch length is 3.59% of the area at an areal extent of the fetch length of 6 m$\times$ 2 m (cf. Fig. 3.7).

The arrangement of saw tooth edges serves to shorten the distance for establishment of a nearly equilibrium boundary layer flow. Enlarging of the tripping devices leads to an increase of the boundary layer thickness and the turbulence intensity

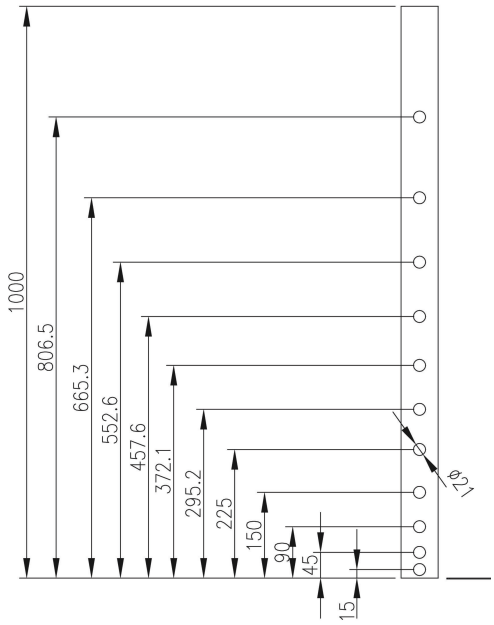


Figure 3.5: Selected setting of the grid of cylindrical rods. Dimensions in mm.

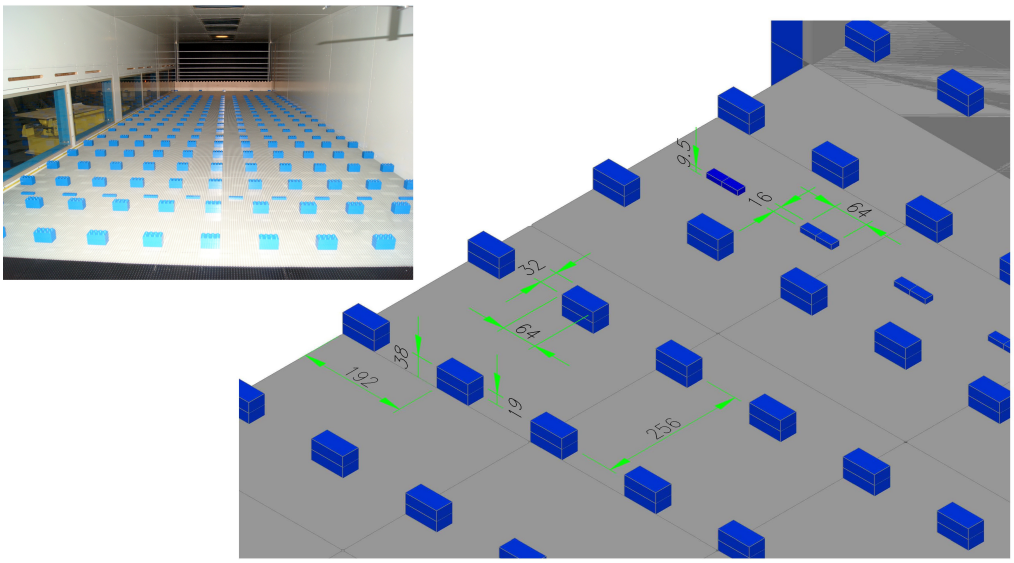


Figure 3.6: Photograph of the test section floor and detailed positioning of the roughness elements in the test section. Dimensions in mm.

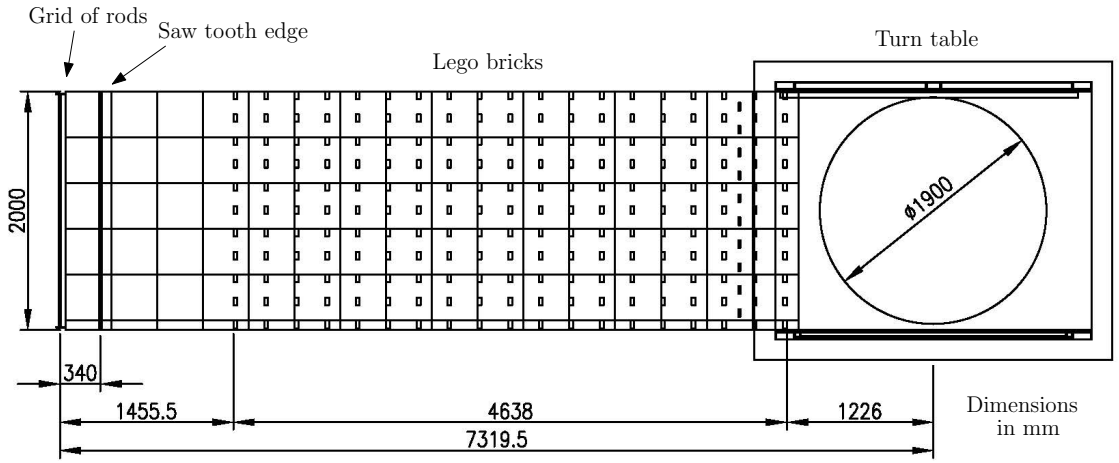


Figure 3.7: Plan view of the boundary layer wind tunnel with the positioning of the grid of rods, the saw tooth edge and the Duplo / Lego bricks.

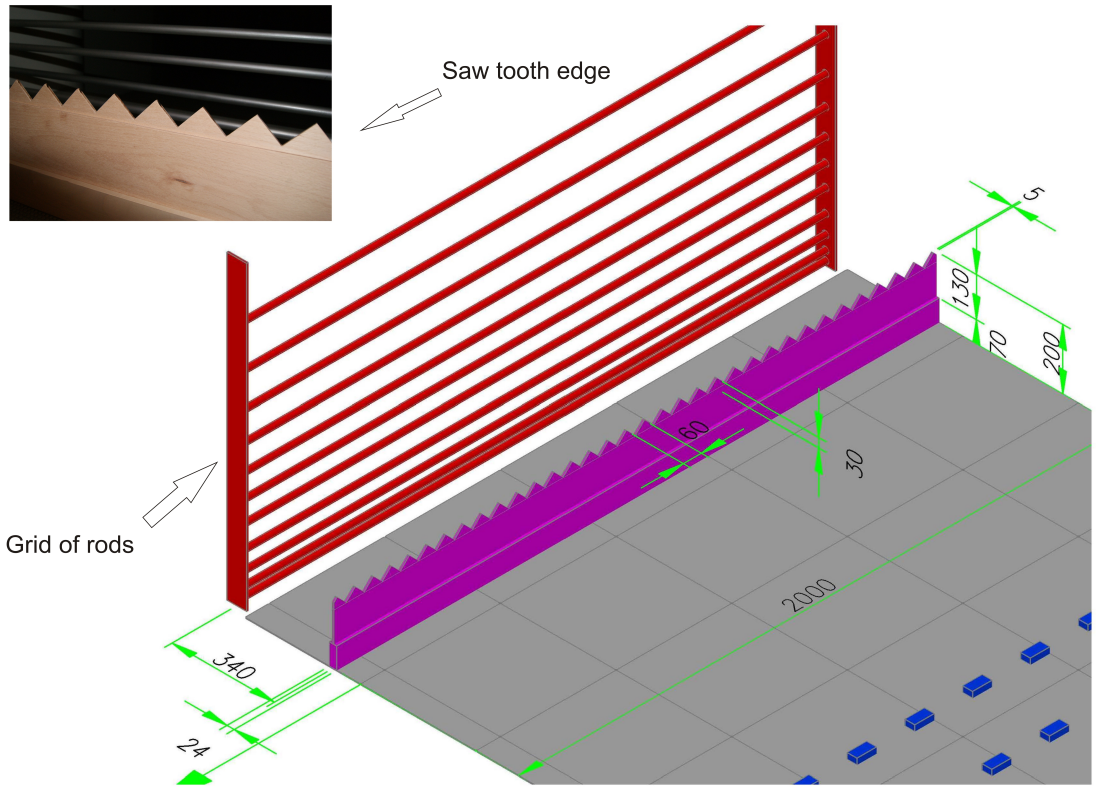


Figure 3.8: Detail sketch and positioning of the saw tooth edge in the test section. Dimensions in mm.

(Counihan, 1969, 1971; Kemper, 2004; Plate, 1982b). According to Gromke and Ruck (2005) and Gromke (2008), a saw tooth edge of 0.2 m height was mounted 0.34 m downstream of the grid of rods (see Fig. 3.8). In combination with the roughness elements on the floor, the desired velocity profile and turbulence structure could be achieved. To set the default velocity profile, a Multichannel CTA System 54N82 with a transmitter 54N95 for comfort sense probes, a reference velocity sensor 54T29, and a thermistor probe 90P10, all from Dantec Dynamics, were used.

3.2.2 The low-speed aerodynamic wind tunnel

The low-speed aerodynamic wind tunnel is of the Göttingen type with closed return. This tunnel is designed for automotive aerodynamics and general purpose applications like studying the aerodynamics of buildings in regions of nearly constant velocity or the aerodynamics of air planes, vehicles and objects in sports. Due to special requirements, the return section had to be divided into three identical parts with a 50 kW powered axial fan in each string.

The entire construction is of a composite nature, consisting of steel profiles and wooden walls with carefully smoothed surfaces (cf. Fig. 3.9). The tunnel has a rectangular cross-section and can be operated with four different nozzles, of which the standard nozzle has an outlet cross section of $2\,\mathrm{m} \times 1.46\,\mathrm{m}$, which permits wind speeds up to 45 m/s. The settling chamber preceding the nozzle is equipped with four screens to provide uniform flow with a low turbulence level. The test section is 3.20 m long and may be run as a free jet or as an open jet with a bottom plate or fully closed.

The main dimensions of the wind tunnel are 16 m in length, 7.7 m in height and 6 m in width. To achieve a low degree of turbulence, four turbulence screens with a relative aperture of 0.61, a wire diameter of 0.3 mm, and a mesh length of 1.1 mm are mounted in the settling chamber. The longitudinal turbulence intensity $Tu_x = \sqrt{u'^2}/U_\infty$, measured in the test section centre, at jet velocities $U_\infty < 10$ m/s is around 0.13% (Gretler and Meile, 1993). Specific modifications at the nozzle exit and correct adjustment of the collector allow a constant pressure over most of the test section length. Effectively, the pressure p_∞ of the jet is equivalent to the ambient pressure p_0 in the wind tunnel hall. Fig. 3.9 shows a schematic illustration

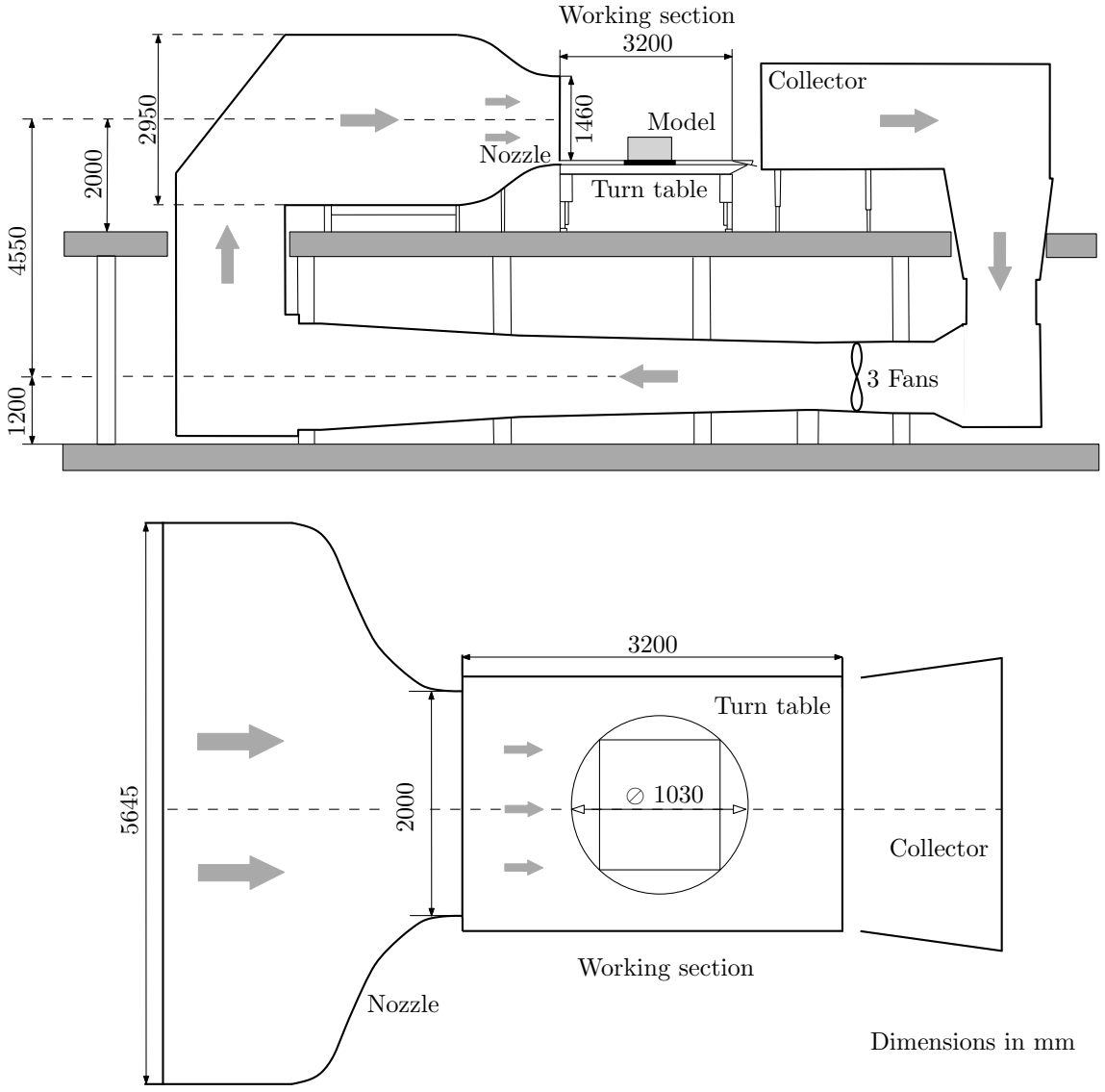


Figure 3.9: Sketch of the low-speed aerodynamic wind tunnel of the Institute of Fluid Mechanics and Heat Transfer at Graz University of Technology. Reprinted from Teppner et al. (2014a), with permission from Elsevier.

of the whole low-speed aerodynamic wind tunnel. Fig. 3.10 shows (a) the nozzle exit of the 2m–wind tunnel and (b) the collector.

To determine the undisturbed velocity U_∞ of the jet, the so-called plenums method is used. The static overpressure in the settling chamber against the ambient pressure in the plenum is proportional to the dynamic pressure in the jet. Furthermore, the pressure measuring points are nearly independent of any configuration change within

the test section.

Applying Bernoulli's equation from the settling chamber to any point in the test section, we get

$$p_\mathrm{s} + \frac{\rho}{2} v_\mathrm{s}^2 = p_0 + \frac{\rho}{2} v_\mathrm{jet}^2 \ , \tag{3.1}$$

where the subscript s denotes the settling chamber and losses are neglected. According to the equation of continuity

$$u_\mathrm{s} \cdot A_\mathrm{s} = U_\infty \cdot A_\mathrm{jet} \tag{3.2}$$

the pressure difference Δp_m between settling chamber and plenum may be expressed as

$$\Delta p_\mathrm{m} = \frac{\rho}{2} U_\infty^2 \left[1 - \left(\frac{A_\mathrm{jet}}{A_\mathrm{s}} \right)^2 \right] \ . \tag{3.3}$$

Because of the high contraction ratio of $A_\mathrm{s}/A_\mathrm{jet} \approx 16/3$, represented by the cross-sectional areas of the settling chamber and the nozzle exit, the term $(A_\mathrm{jet}/A_\mathrm{s})^2$ is negligible. Thus we get:

$$\Delta p_m \approx \frac{\rho}{2} U_\infty^2 \ . \tag{3.4}$$

Eq. (3.4) shows the proportionality between the measured pressure difference Δp_m and the dynamic pressure in the jet. To account for the losses and the applied simplifications, a calibration factor of the nozzle

$$f_N = \frac{p_{dyn,m}}{\Delta p_m} \tag{3.5}$$

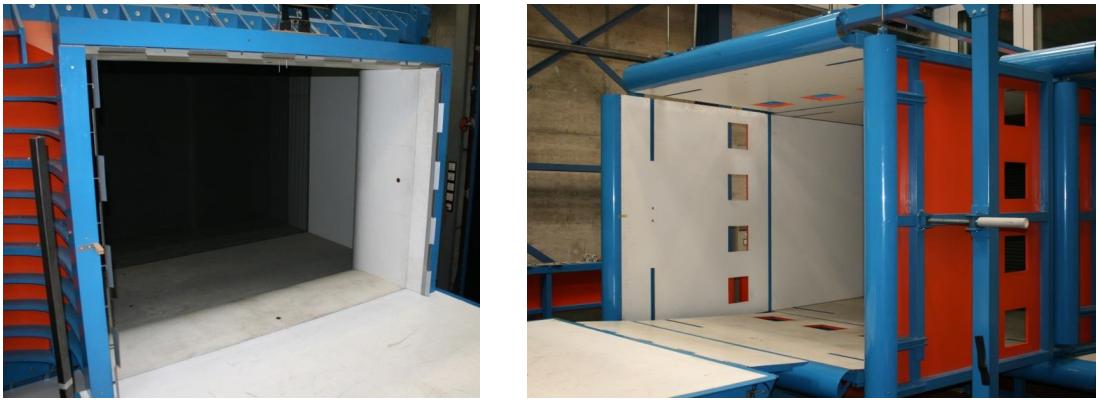
can be determined by measuring the mean dynamic pressure $p_{dyn,m}$ in the empty test section at various values of the pressure difference Δp_m. This leads to the velocity of the jet

$$U_\infty = \sqrt{\frac{2}{\rho} \left(f_N \cdot \Delta p_m \right)} \ , \tag{3.6}$$

where the density ρ is calculated from the equation of state

$$\rho = \frac{p_0}{\mathcal{R} T} \ . \tag{3.7}$$

$\mathcal{R}$ denotes the specific gas constant of air ($\mathcal{R} = 287$ Jkg^{-1}K^{-1}) and T is the jet temperature measured at the nozzle exit. By averaging the dynamic pressures



(a) **(b)**

Figure 3.10: The 2m–wind tunnel of the Institute of Fluid Mechanics and Heat Transfer at Graz University of Technology. (a) Nozzle exit, (b) collector.

measured at n points in the working section, the calibration factor of the nozzle is

$$f_N = \frac{\sum_{i=1}^{n} p_{dyn,m_i}}{n\Delta p_m} = 1.032\ . \tag{3.8}$$

Blockage of the wind tunnel

The blockage of the wind tunnel test section by the implemented building model causes a change of the stream line pattern. This may be either compression or expansion depending on the specific design (open / closed). This constriction of the streamlines causes a change of the pressure distribution around the model compared to the free flow around the object. To ensure the comparability of the real flow with the reproduced flow, the blockage ratio

$$\varphi_o = \frac{A_m}{A_n}\ , \tag{3.9}$$

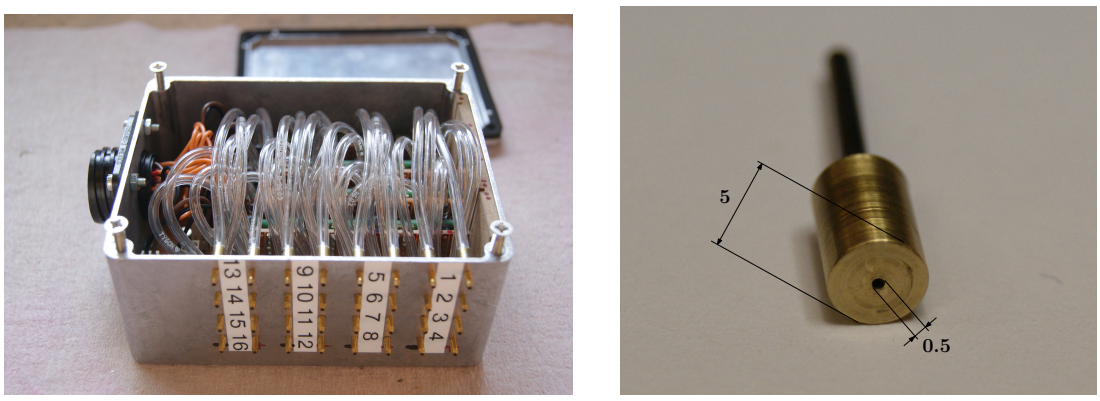
where A_m is the projection surface of the model and A_n the cross sectional area of the wind tunnel nozzle at its exit, should be small and not exceed 5% (Hunt, 1982). In investigations of road vehicles, blockage ratios of $\varphi_o = 20\%$ are common (Hucho, 2013). In the present work for the building models, blockage ratios with a maximum of 6.4% were achieved.

3.3 Pressure Measurements

The ambient pressure was measured with pressure sensors of type HCA0811ARH8 from SensorTechnics with a full range of $800 - 1100$ mbar. The pressure distribution on the building surface due to the atmospheric boundary layer flow was measured with low differential pressure sensors of type LBAS100B (SensorTechnics) with a full range of ± 100 Pa. 16 of these sensors were put into a pressure control box (cf. Fig. 3.11(a)). Data were processed with CompactDAQ components and recorded with the software package LabView, both from National Instruments. The pressure taps, flash-mounted with the surface of the building model, were manufactured by the institute's workshop (see Fig. 3.11 (b)).

The recording of the pressure differences relative to the ambient pressure acting on the building model in 1:75 scale was started after setting the desired boundary layer profile in the boundary layer wind tunnel. The wind tunnel was set to velocities of 4 and 7 m/s in a height of $z = 50$ cm (corresponding to $z = 37.5$ m in real scale) using a reference velocity probe.

The pressure differences were measured for 11 incidence angles α at 17 window positions $W_1 - W_{17}$ from the 2^{nd} to the 10^{th} storey, sketched in Fig. 3.12. An overview of the measurement configurations is given in Table 3.1. The exact position of the pressure taps can be seen in Fig. 3.13 (a). The temperature in the jet is measured using a Pt100 temperature probe. With the temperature and the ambient pressure,



(a) **(b)**

Figure 3.11: (a) Pressure control box, equipped with low differential pressure sensors of type LBAS100B from SensorTechnics. (b) Pressure tap. Dimensions in mm.

U_∞	Incidence angle α										
$[m/s]$	0°	10°	20°	30°	33.3°	45°	50°	60°	70°	80°	90°
4	✓	✓	✓	✓	✓	✓	✓	✓	✓	✓	✓
7	✓	✓	✓	✓	✓	✓	✓	✓	✓	✓	✓

Table 3.1: Configurations for measurements of the pressure differences on the building model on a scale of 1:75.

the air density in the jet was calculated from the equation of state 3.7), and thus the pressure coefficient c_p via Eq. (2.77).

The particular pressure coefficients measured at the positions shown in Fig. 3.13 (a) were fitted by a multidimensional polynomial function of the following form for each surface of the building:

$$\begin{aligned} c_{p,\text{fitted}}(x,z) = \quad & a_1 + a_2x + a_3z + a_4x^2 + a_5xz + a_6z^2 + a_7x^3 + a_8x^2z + \\ & + a_9xz^2 + a_{10}z^3 + a_{11}x^4 + a_{12}x^3z + a_{13}x^2z^2 + a_{14}xz^3 + a_{15}z^4 + \\ & + a_{16}x^5 + a_{17}x^4z + a_{18}x^3z^2 + a_{19}x^2z^3 + a_{20}xz^4 + a_{21}z^5 \ , \end{aligned} \tag{3.10}$$

where a_1 to a_{21} denote the coefficients of the polynomial function. This was done by the method of least squares using the software Package MatLab R2011a. Subsequently, the mean force coefficients were calculated by integrating the fitted function over

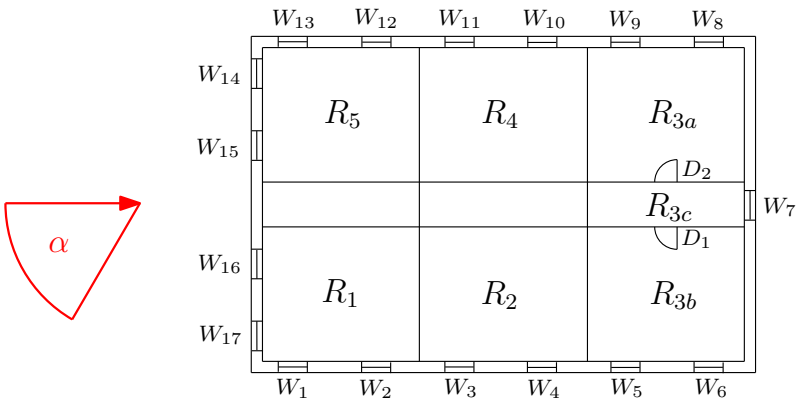


Figure 3.12: Incidence angles and room numbers for the configurations given in Table 3.1.

the building surfaces

$$F_D = \frac{\rho}{2} U_\infty^2 \int_A c_{p,\text{fitted}} \, \mathrm{d}A \tag{3.11}$$

and subtracting the results for the windward side from those of the leeward side for the $x-$ and $y-$direction (directions sketched in Fig. 3.13 (b)). The force tangential to the building surface, i.e. viscous forces, can be neglected in comparison to pressure acting perpendicular to the building surface (Sockel, 1994).

A very comprehensive study on mean force coefficients for buildings in turbulent boundary layers was published by Akins and Peterka (1977). The coordinate system and the definitions of the incidence angles in Fig. 3.13 (b) were chosen in accordance with that study. The aerodynamic force coefficients for the particular surfaces are

$$c_{D,x} = \frac{F_{D,x}}{\frac{\rho}{2} U_\infty^2 W H} \qquad \text{and} \qquad c_{D,y} = \frac{F_{D,y}}{\frac{\rho}{2} U_\infty^2 L H} \, . \tag{3.12}$$

In contrast to the usual normalization of the pressure coefficients with the dynamic pressure in building height, Akins and Peterka (1977) related the aerodynamic coefficients to the velocity $\overline{U}_a$ averaged over the building height. Starting from Eq. (2.67) and the known profile exponent α for the measurements, a conversion between the two types of normalization is possible. The velocity $\overline{U}_a$, averaged over

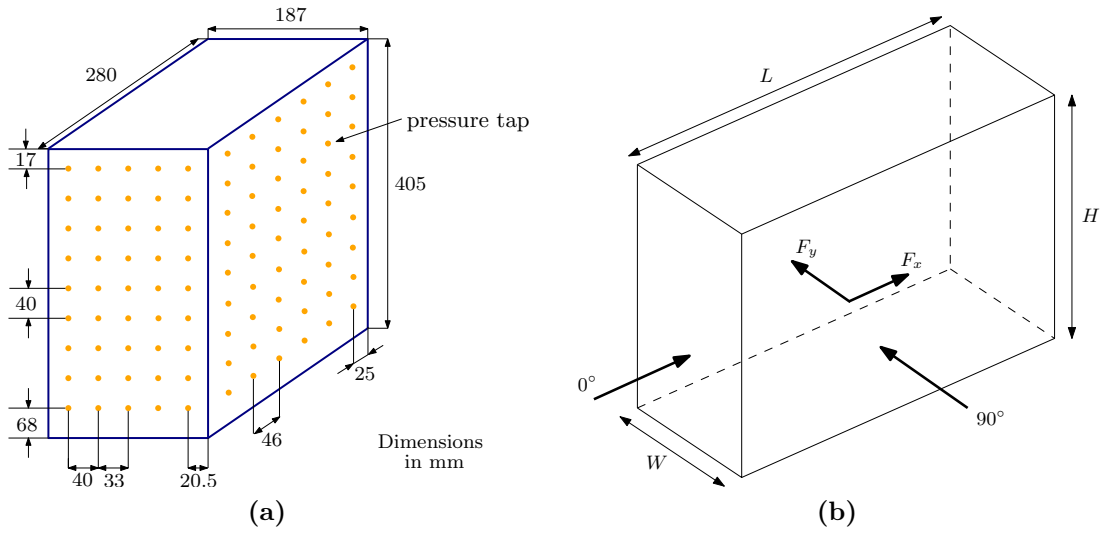


Figure 3.13: (a) Positions of the pressure taps for the model in 1:75 scale. (b) Definition of the incidence angles and forces.

the building height, follows by integration of the velocity profile

$$\overline{U}_a = \frac{1}{H} \int_0^H \overline{u}_{ref} \left(\frac{z}{z_{ref}} \right)^{\alpha} \mathrm{d}z = \frac{\overline{u}_{ref}}{\alpha + 1} \left(\frac{H}{z_{ref}} \right)^{\alpha} . \tag{3.13}$$

Setting $z_{ref} = H$ results in a conversion factor independent of the building height. This enables the comparison of buildings of different height, for which the pressure coefficients are related to the dynamic pressure in building height. Thus, the aerodynamic coefficients can be converted to the average velocity. With the profile exponent $\alpha = 0.22$ applied in the present study the following factor for the conversion of the aerodynamic coefficients from the reference velocity $\overline{U}_H$ to the height-averaged velocity $\overline{U}_a$ is achieved:

$$\frac{\overline{U}_H^2}{\overline{U}_a^2} = (\alpha + 1)^2 = 1.4884 . \tag{3.14}$$

According to Akins and Peterka (1977), this type of normalization yields smoother curves in the representation of the force coefficients as functions of the incidence angles depending only marginally on the boundary layer characteristics and the height.

3.4 Velocity Measurements

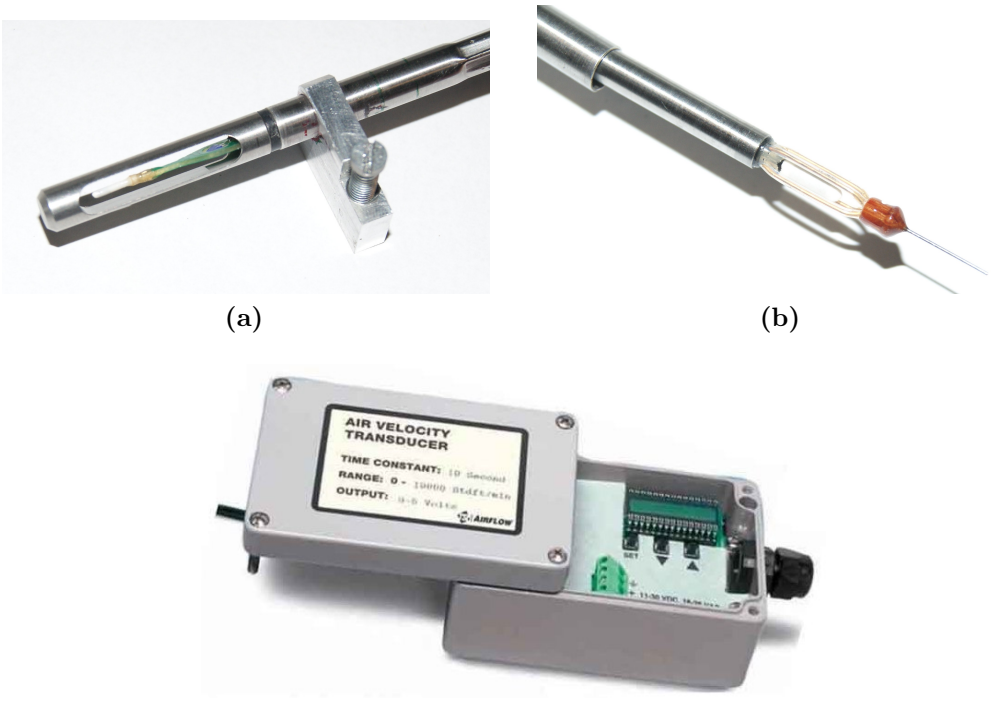
The velocity measurements in window and door cross sections of the models on scales of 1:25 and 1:10 were performed with air velocity transducers model 8455 and 8465 (TSI Inc.) with adjustable ranges, as shown in Fig. 3.14. In the present application, the range was set from 0.125 to 10.0 m/s. The output signals were processed with CompactDAQ components, and data were acquired using the software package LabView (both from National Instruments). The accuracy of the velocity transducers is specified with ±2.0% of the reading (within a temperature range from $18°C$ to $28°C$) and ±0.5% fso. Outside this range, 0.2% per °C has to be added within the temperature compensation range. The conversion of the transducer output

signal into a velocity follows the relation

$$V = \frac{E_{out} - E_0}{E_{FS} - E_0} V_{FS} \ , \tag{3.15}$$

where V denotes the measured velocity V_{FS} is the full scale velocity according to the specified range, E_{out} the measured output voltage, E_0 the zero flow output voltage and E_{FS} the full scale voltage.

According to the pressure differences obtained from the measurements in the boundary layer wind tunnel, the velocities exemplarily were measured for the 3^{rd} and 8^{th} building storey for two reference velocities 4 m/s and 7 m/s in a height of 37.5 m (this corresponds to 2.805 m/s and 4.709 m/s in a height of 10 m) and four incidence angles (given in Table 3.2) referring to the incidence angle α sketched in Fig. 3.1. For fully open windows, the air velocity transducers were positioned at the height of the diagonal intersection point of the rectangular window cross sectional area, but inside the room at a distance of 9 mm from the inner wall (Teppner et al., 2014a).



(a) **(b)**

(c)

Figure 3.14: (a) Velocity transducer model 8455. (b) Velocity transducer model 8465. (c) Velocity transducer control air unit.

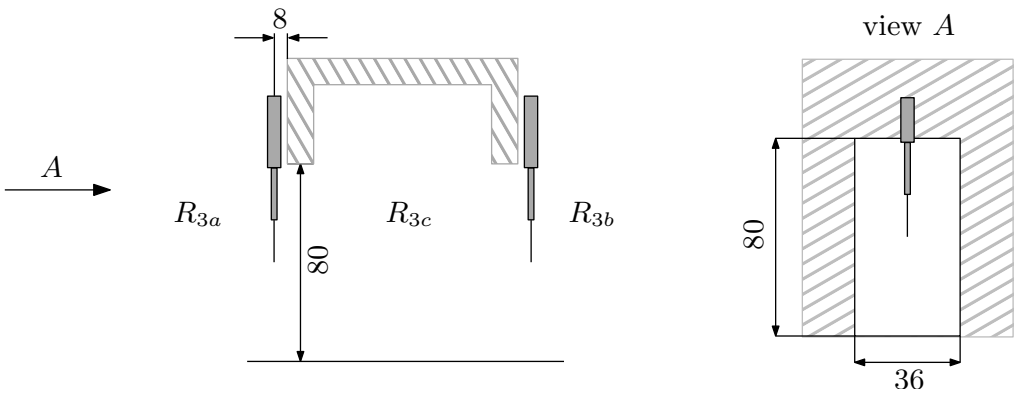


Figure 3.15: Positions of the velocity sensors in the door cross sectional area on scale 1:25. Dimensions in mm. Location of the rooms see Fig. 3.12. Reprinted from Teppner et al. (2014a), with permission from Elsevier.

U_∞ $[m/s]$	α [°]	Room R_1	Room R_2	Rooms R_{3a+3c}	Rooms R_{3b+3c}	Rooms $R_{3a+3b+3c}$	Room R_4	Room R_5
3.6	0	✓	✓	✓ $_{D_2}$	✓ $_{D_1}$		✓	✓
3.6	33.3							✓
3.6	90	✓				✓ $_b$		
3.6	180		✓	✓ $_{D_2}$	✓ $_{D_1}$		✓	
3.8	0	✓	✓	✓ $_{D_2}$	✓ $_{D_1}$		✓	✓
3.8	33.3							✓
3.8	90	✓				✓ $_b$		
3.8	180		✓	✓ $_{D_2}$	✓ $_{D_1}$		✓	
5.1	0	✓	✓	✓ $_{D_2}$	✓ $_{D_1}$		✓	✓
5.1	33.3							✓
5.1	90	✓				✓ $_b$		
5.1	180		✓	✓ $_{D_2}$	✓ $_{D_1}$		✓	
5.7	0	✓	✓	✓ $_{D_2}$	✓ $_{D_1}$		✓	✓
5.7	33.3							✓
5.7	90	✓				✓ $_b$		
5.7	180		✓	✓ $_{D_2}$	✓ $_{D_1}$		✓	

Table 3.2: Configurations for velocity measurements in the storey model in 1:25 scale for fully open windows.

U_∞ $[m/s]$	α $[^\circ]$	Rooms R_{3a+3c}	Rooms R_{3b+3c}	Rooms $R_{3a+3b+3c}$
3.6	0			$\checkmark_b$
3.6	33.3			
3.6	90		$\checkmark_{D_1}$	$\checkmark_b$
3.6	180			$\checkmark_b$
3.8	0			$\checkmark_b$
3.8	33.3			
3.8	90		$\checkmark_{D_1}$	$\checkmark_b$
3.8	180			$\checkmark_b$
5.1	0			$\checkmark_b$
5.1	33.3			
5.1	90		$\checkmark_{D_1}$	$\checkmark_b$
5.1	180			$\checkmark_b$
5.7	0			$\checkmark_b$
5.7	33.3			
5.7	90		$\checkmark_{D_1}$	$\checkmark_b$
5.7	180			$\checkmark_b$

Table 3.3: Configurations of velocity measurements for the sample storey model in 1:25 scale for tilted windows. According to Fig. 3.16, the subscript D_1 means ventilation through door D_1, while D_2 is closed and window W_7 is tilted. The subscript b denotes that both doors are open and window W_7 is closed, while windows W_5, W_6, W_8 and W_9 are tilted.

Since the velocity sensors are not directionally sensitive, the direction and orientation of the flow through the windows were determined visually using thread probes. By this method, the local angle of the velocity vectors for determining the volumetric flow rate was estimated (Teppner et al., 2014a). The effective cross sectional area resulting from these directions was accounted for in the calculation of the volumetric flow rates (cf. Eq. (2.88)). Due to the above mentioned positioning of the velocity sensors inside the rooms, the jet contraction defined in Section 2.3.4 is taken into account in calculating the air velocity only for windows with the flow direction pointing into the room (Teppner et al., 2014a).

Velocity measurements for tilted windows at the model scale 1:25 were impossible due to the small open cross sections. Only measurements in the open door cross sections D_1 and D_2 (see Fig. 3.12) were carried out for selected scenarios. For the measurements in the doors for the tilted windows cases, the velocity sensors were mounted in the diagonal intersection point of the rectangular door cross sectional

area at a distance of 8 mm from the inner wall of the room (see Fig 3.15).

The velocities in the single storey model in 1:25 scale were measured for four incidence angles α (cf. Table 3.2) at 17 window positions $W_1 - W_{17}$ and for cross ventilation in case of tilted windows in the doors D_1 and D_2. The measurements were realized in the aerodynamic wind tunnel for the 3^{rd} and the 8^{th} floor of the building. An overview of the measurement configurations for fully open windows is given in Table 3.2. Only those measurements are marked where precise velocity directions could be determined by the thread probes. In Table 3.2, the subscript D_1 means ventilation through door D_1, while D_2 is closed and window W_7 is open (according to Fig. 3.16). Subscript D_2 means ventilation through door D_2, while D_1 is closed and window W_7 is open. The subscript b denotes that both doors are open and window W_7 is closed, while windows W_5, W_6, W_8 and W_9 are open.

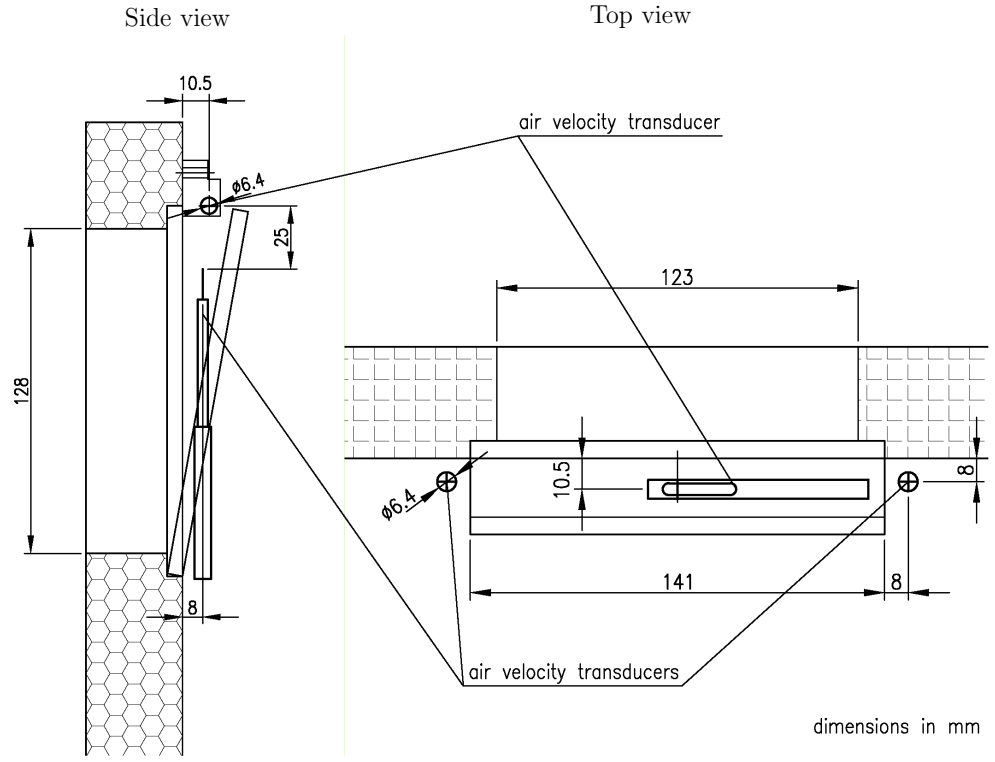
Velocity measurements in the open doors D_1 and D_2 (cf. Fig. 3.12) were possible for the cases of tilted windows as summarized in Table 3.3. Measurements in the open cross sections of tilted windows were realised in the 1:10 scale single room model, with three velocity transducers mounted in the gaps of the tilted windows as shown in Fig. 3.16(a) and (b). The velocity measurements were done for 8 different incidence angles α within a range from $-40°$ to $90°$ according to Fig. 3.16 (c), for two velocities U_∞ of 3.6 m/s and 5.1 m/s and three different window scenarios: (1) windows W_1 to W_4 tilted, (2) W_1 and W_2 tilted and (3) W_1 and W_4 tilted. Detailed measurement configurations are specified in Table 3.4.

The volumetric flow rates were calculated as products of the measured velocities with the appropriate either lateral triangular areas or rectangular area overhead

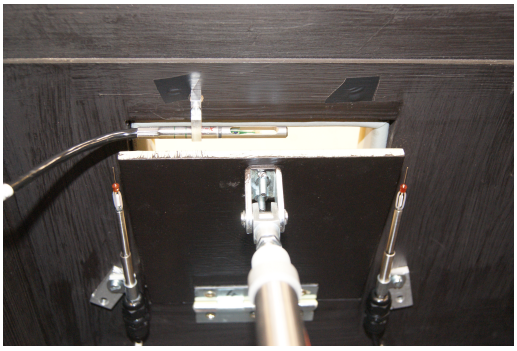
U_∞	Windows	Incidence angle α							
$[m/s]$	tilted	$-40°$	$-20°$	$0°$	$20°$	$40°$	$60°$	$80°$	$90°$
3.6	W_1 to W_4	✓	✓	✓	✓	✓	✓	✓	✓
3.6	W_1 and W_4	✓	✓	✓	✓	✓	✓	✓	✓
3.6	W_1 and W_2	✓	✓	✓	✓	✓	✓	✓	✓
5.1	W_1 to W_4	✓	✓	✓	✓	✓	✓	✓	✓
5.1	W_1 and W_4	✓	✓	✓	✓	✓	✓	✓	✓
5.1	W_1 and W_2	✓	✓	✓	✓	✓	✓	✓	✓

Table 3.4: Configurations of the velocity measurements for the single room model in 1:10 scale for tilted windows.

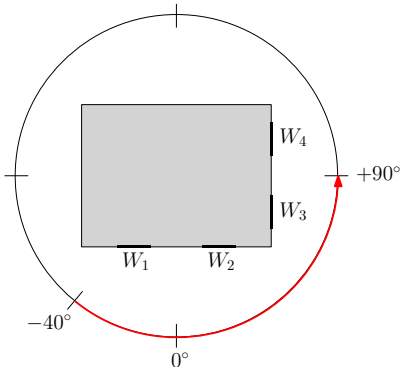
(Fig. 3.16(a) and (b)), taking into account the flow direction (inflow or outflow) as detected by the thread probes, and a 15.8% blockage of the area overhead and a 18.9% blockage of the lateral areas, respectively, caused by the velocity sensors. The jet contraction, as introduced by Eq. (2.87) for open windows, was not taken into account for tilted windows, because the inflow is not perpendicular to the frontal area (Sockel, 1984).



(a)



(b)



(c)

Figure 3.16: Velocity transducers in the single room model (Fig. 3.3 (b)). (a) Schematic, (b) photograph, (c) incidence angles and notation of the windows for the single room model; (a) and (b) reprinted from Teppner et al. (2014a), with permission from Elsevier.

3.5 Tracer gas measurements

In order to determine the air exchange rate by a method alternative to the velocity measurements, the air exchange rate was determined again by tracer gas measurements in the sample single room model in 1:10 scale.

For determining air change processes quantitatively, in particular the air exchange rate, the tracer gas method is well established (VDI, 2001). Most commonly used variants of this method are the constant-injection method, the constant-concentration method and the concentration-decay method. In the present experiments, the latter method was applied. A detailed description of all the methods and advice for the choice of an adequate tracer gas can be found in VDI (2001), Heidt (1987), Heidt and Rabenstein (1990) and Charlesworth (1988).

Using the concentration-decay method, carbon dioxide was injected into the single room model exposed to the defined external flow field in the wind tunnel with all the windows closed. The inner surface of the walls was coated with an appropriate enamel to suppress diffusion of the tracer gas through the wooden walls. After formation of a homogeneous mixture of the room air with the CO_2, the windows were tilted with pneumatically driven suspensions for a fixed time interval $\Delta t = t_2 - t_1$, so that the air outside interacted with the room air. The tracer gas concentration was measured at both instances t_1 and t_2. For these measurements, the CO_2/air mixture in the model room was passed to an infrared Multi Gas Monitor Innova 1316-2 (LumaSense Technologies) and analysed for its carbon dioxide content (the functional principle will be explained later in this section). This procedure was repeatedly carried out to obtain a time profile of the decaying CO_2 concentration in the room air due to the exposure to the external flow field. Following VDI (2001), Raatschen (1988a,b), Wegner (1983) and Roulet (2008), the air exchange rate was calculated from the decay of the carbon dioxide concentration versus time. The difference between the molar masses of the gaseous mixture at the beginning and at the end of the decay for every case was smaller than 13.4%, so that the molar mass was treated as constant in the following.

For homogeneous mixtures of the tracer gas with the room air, the rate of change of mass m of the tracer gas within a single zone in contact with the outdoor

environment is given by

$$\frac{\mathrm{d}m}{\mathrm{d}t} = I + Y_o\,\dot{m}_{oi} - Y_i\,\dot{m}_{io}\ . \tag{3.16}$$

Here I is the mass injection rate of tracer gas, Y is the tracer gas mass fraction and $\dot{m}$ is the gas mixture mass flow rate. The subscripts represent the internal or the external environment, e.g. $\dot{m}_{io}$ means the gas mixture mass flow rate from indoor to the outdoor environment (cf. Fig. 3.17). Assuming that the mass flow rates of the gas mixture into and out of the zone are equal, $\dot{m}_{io} = \dot{m}_{oi}$, and using the relation $m = Y_i M$ between the tracer mass m and the mass M of the gaseous mixture in the zone, Eq. (3.16) becomes

$$M\frac{\mathrm{d}Y_i}{\mathrm{d}t} = I + \dot{m}_{io}\,(Y_o - Y_i)\ . \tag{3.17}$$

Constant mass M in the room is assumed, which is the case for constant thermodynamic state of the gaseous mixture. After injection of tracer gas to reach a measureable initial concentration $Y_{i,0}$, the injection is stopped at time $t_0 = 0$, so that $I = 0$ during the measurement process thereafter. The solution of Eq. (3.17) describes the decay of the tracer mass fraction over time as per

$$Y_i(t) - Y_o = (Y_{i,0} - Y_o)\exp\left(\frac{-\dot{m}_{io}}{M}\,t\right)\ . \tag{3.18}$$

From Eq. (3.18) the ACH can be directly deduced as

$$\mathrm{ACH} = \frac{1}{\rho\,V_R}\,\frac{M}{\Delta t}\,\ln\left(\frac{\Delta Y(t)}{\Delta Y(t+\Delta t)}\right)\ , \tag{3.19}$$

where $\Delta Y(t) = Y_i(t) - Y_o$ (VDI, 2001; Roulet, 2008; Maas, 1995). For $\rho = const.$ Eq. (3.19) simplifies to

$$\mathrm{ACH} = \frac{1}{\Delta t}\,\ln\left(\frac{\Delta Y(t)}{\Delta Y(t+\Delta t)}\right)\ . \tag{3.20}$$

According to Roulet (2008) and Maas (1995), the success of air change measurements using a tracer gas depends on the adherence of the following conditions: the used tracer gas should

- be easily analysable, preferably at low concentrations, so that density changes

can be avoided,

- have a low background concentration,
- be chemically stable and inert, neither flammable nor explosive and non-toxic at the concentration used in the measurements,
- have a density close to the air density at a given state, i.e. a molecular weight close to 29 g/mole.

The mixture within the measurement zone is considered to be completely uniform, i.e. there are no concentration gradients inside the zone. Changes in the tracer gas concentration in the measuring zone should solely come about by the supply of tracer gas or by removal with the room air, i.e. there must be no chemical degradation of the tracer gas or reactions with other substances. The supply of a tracer gas into the measurement zone should not significantly alter the density of the internal air (Maas, 1995). As mentioned above, CO_2 was used as the tracer gas in this work. It is a natural component of the atmosphere and exists at a concentration of 300 ppm. Carbon dioxide is colorless, odourless, tasteless, and chemically stable under normal conditions.

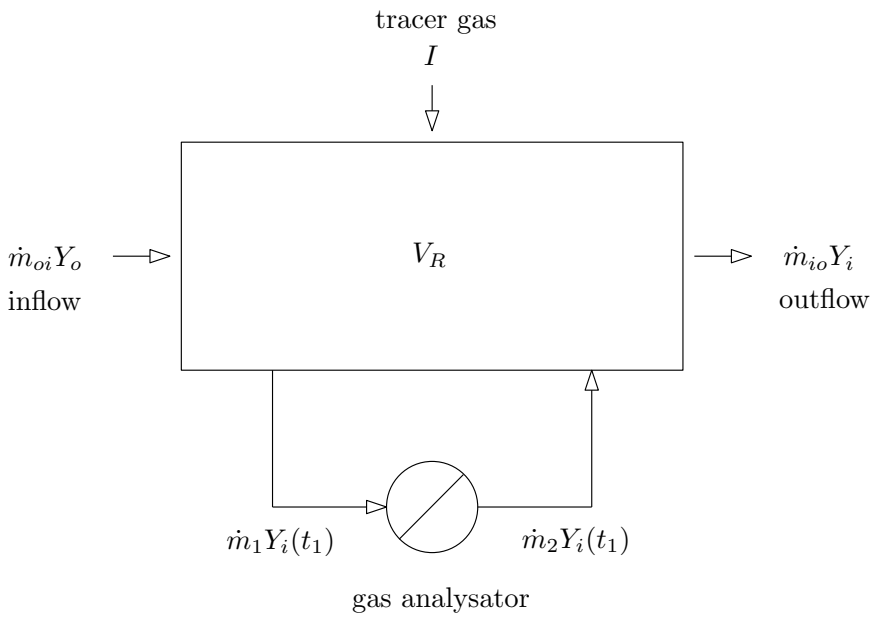


Figure 3.17: Model of a measurement zone using the tracer gas method. Referring to Maas (1995).

Precise knowledge of the nature or concentration of a gas is of vital importance for a number of applications, whether it is the exact knowledge of the anesthetic gas concentration in surgery or even the knowledge of the carbon dioxide concentration inside a room, to name only a few. There exist numerous sensor-based solutions for the measurement of gas concentrations, such as by spectroscopy, chemical reactions, thermal conductivity, or ultrasonic waves. Non-dispersive infrared (NDIR) sensors are simple spectroscopic devices used for the carbon dioxide analysis in this work.

The non-dispersive infrared spectroscopy is based on an optical measurement method, the light absorption. The absorption analysis utilizes the property of atoms to absorb radiation of visible and non-visible light at particular wavelengths. For this purpose, the infrared radiation is particularly suitable because frequencies assigned to the molecular oscillations in this wavelength range ($10^{-3}\,\mathrm{m} \leq \lambda \leq 7,8 \times 10^{-7}\,\mathrm{m}$) are sharply separated. Each gas, except for the mono-atomic inert gases and diatomic gases, has an absorption spectrum consisting of individual absorption bands and specific for the gas of interest (Etheridge and Sandberg, 1996; Laussmann and Helm, 2011).

Quantitatively, the absorption of light is described by the absorption law of Lambert and Beer (Demtröder, 2009). The intensity of the outgoing light I is a function of the incoming light intensity I_0, the path length d and the absorption coefficient η

$$I = I_0 \ \exp(-\eta\, d). \tag{3.21}$$

The absorption coefficient η is a function of the gas compound, the temperature and the wave length.

In non-dispersive infrared absorption spectrometers, the whole band of the infrared radiation is used, while dispersive gas analysers are tuned to a fine band of interesting frequencies of a specific gas (Etheridge and Sandberg, 1996).

Fig. 3.18 shows the functional principle of non-dispersive gas analyser and illustrates the splitting of the light from the infrared source along two paths. One path leads through a reference cell with clean air, the other one leads along a path with a sample of the gas mixture to be analysed. The gas in the mixture to be analysed is also located in the two completely sealed chambers of the detector. The detection of the radiation after passing the measuring volume can happen in various

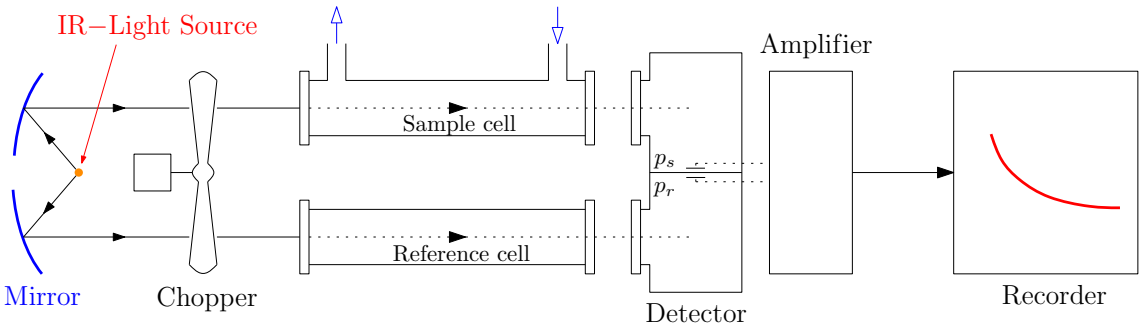


Figure 3.18: Non-dispersive infrared (NDIR) gas analyser. Referring to Etheridge and Sandberg (1996).

ways. The detector exemplarily may be filled with an absorbent gas such that the incident radiation causes a temperature and pressure increase, which can be measured. Using non-dispersive methods, the spectral range may be limited by various filters.

The detector is filled with the gas, whose concentration has to be determined in the measuring volume. Thus, only the spectral range, in which the sample component absorbs, is recorded by the detector. In presence of the gas component in the measuring volume, less radiation is absorbed in the detector, leading to a smaller pressure increase than in the absence of the gas component. Since the radiation of

U_∞ $[m/s]$	Windows tilted	Incidence angle α							
		$-40°$	$-20°$	$0°$	$20°$	$40°$	$60°$	$80°$	$90°$
3.6	W_1 to W_4	✓	✓	✓	✓	✓	✓	✓	✓
3.6	W_1 and W_4	✓	✓	✓	✓	✓	✓	✓	✓
3.6	W_1 and W_2	✓	✓	✓	✓	✓	✓	✓	✓
3.8	W_1 to W_4	✓	✓	✓	✓	✓	✓	✓	✓
3.8	W_1 and W_4	✓	✓	✓	✓	✓	✓	✓	✓
3.8	W_1 and W_2	✓	✓	✓	✓	✓	✓	✓	✓
5.1	W_1 to W_4	✓	✓	✓	✓	✓	✓	✓	✓
5.1	W_1 and W_4	✓	✓	✓	✓	✓	✓	✓	✓
5.1	W_1 and W_2	✓	✓	✓	✓	✓	✓	✓	✓
5.7	W_1 to W_4	✓	✓	✓	✓	✓	✓	✓	✓
5.7	W_1 and W_4	✓	✓	✓	✓	✓	✓	✓	✓
5.7	W_1 and W_2	✓	✓	✓	✓	✓	✓	✓	✓

Table 3.5: Configurations of tracer gas measurements for the single room model for tilted windows.

other gases cannot be detected, the radiation of the gas component to be measured is not influenced. The amplitude of the pressure difference, modulated by a chopper, can be measured either directly by a thin metal diaphragm or indirectly by recording the flow rate of the gas by the pressure difference (Etheridge and Sandberg, 1996).

The change in concentration of CO_2 was measured for four wind velocities U_∞, 8 different incidence angles α and the following tilting scenarios of the windows: (1) W_1 to W_4 tilted, (2) W_1 and W_4 tilted and (3) W_1 to W_2 tilted, as indicated in Fig. 3.16 (c). Detailed measurement configurations are given in Table 3.5.

3.6 Determination of the air exchange rate considering thermal influence

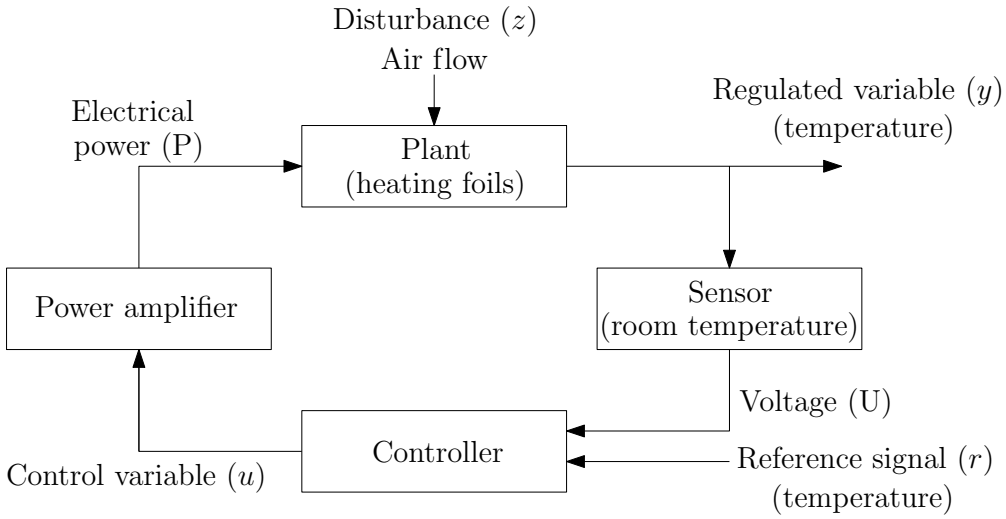
A difference in density between the external and internal air of a building due to a temperature difference between inside and outside causes natural ventilation driven by thermal buoyancy. Thus, a ventilation through the openings due to the difference of densities, develops. Additionally to Sections 3.4 and 3.5 solely considering wind-driven air exchange, we now identify both, thermal buoyancy and wind driven pressure differences, as the driving mechanisms of natural ventilation. A large number of factors influence natural ventilation, such as velocity, direction and turbulence of the wind, the size and position of openings in the building envelope, heat sources, conductance of the envelope and solar radiation (Li and Delsante, 2001). Obviously, the two mechanisms may occur separately, but in most cases they occur in combination and are interdependent.

As explained earlier in this chapter, the air exchange driven only by wind was investigated using velocity measurements and tracer gas measurements. To investigate thermally driven air change caused by temperature differences between indoor and outdoor, flexible heating foils (acting as a floor heating system) were installed in the single room model. Furthermore, the superposition of thermal and wind-driven air change was examined in this work.

Four heating foils (Fig. 3.20) of the type Thermo (Thermo technologies) operated at a nominal voltage of 230 V with an effective output of 65 W $\pm$ 10% and dimensions 300 mm $\times$ 120 mm $\times$ 0.4 mm, were used (see Fig. 3.19 (a)). To set a constant



(a)



(b)

Figure 3.19: (a) Heating foil, (b) control circuit

temperature inside the single room model, a thyristor TE10 A (Eurotherm) with a nominal current and voltage of 16 A and 230 V, respectively, was used as a power controller. The power is calculated as $P_{\mathrm{el}} = E_{\mathrm{eff}}\, I_{\mathrm{eff}}$ from current I_{eff} and voltage E_{eff} measured by appropriate transducers (Eurotherm, Series E1). Ohmic losses were neglected.

The temperature inside the room model was recorded using the Foxboro 2500 Controller (Eurotherm) and controlled by a PID controller of the software package LabView (National Instruments). The whole control circuit is depicted in Fig. 3.19(b). In order to keep heat losses as low as possible, all inside walls of the room model were insulated with a vapour resistant insulating mat X-trem-Isolator of 10 mm thickness with a thermal conductivity of 0.020 W/mK $\leq \lambda \leq$ 0.035 W/mK. The wooden panels of the single room model are of type Egger MDF-ST E1, and the thermal conductivity is given as 0.10 W/mK $\leq \lambda \leq$ 0.14 W/mK for thicknesses

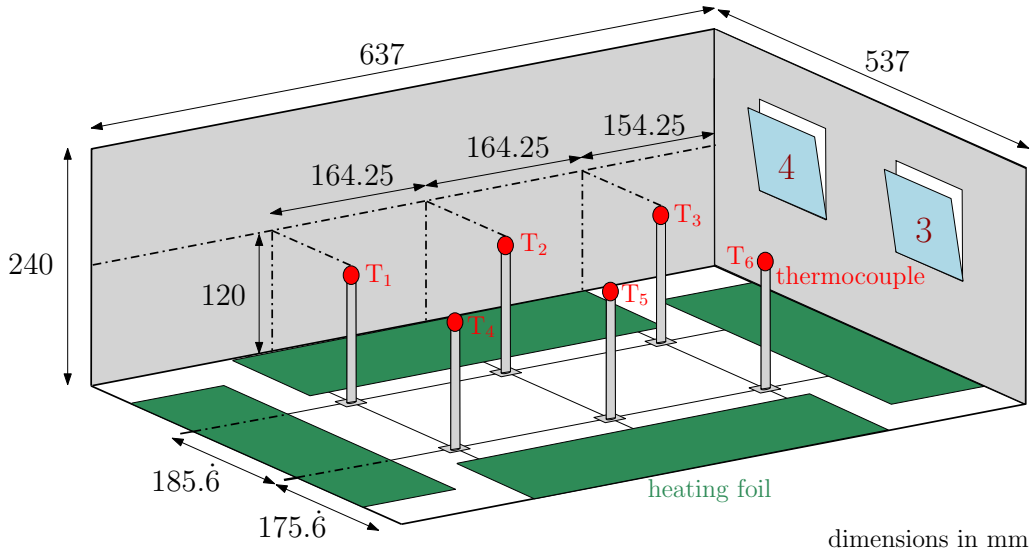


Figure 3.20: Positions of the thermocouples and the heating foils within the single room model. Internal dimensions with insulation, in mm.

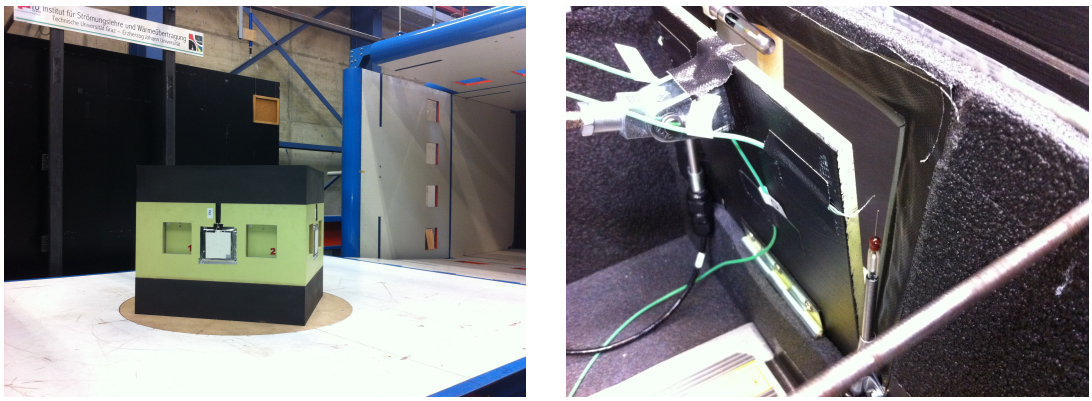
between 6 and 40 mm. To measure the temperatures within the single room, 6 thermocouples of type K (Eurotherm) were positioned as given in Fig. 3.20. The thermocouples T_1 to T_6 were mounted vertically centered since no relevant change in temperature with the height could be determined by preliminary test measurements.

The desired room temperature is calculated as the arithmetic mean of the temperatures T_1 to T_6 measured by the 6 thermocouples as follows:

$$T_{i,mean} = \frac{1}{6} \sum_{i=1}^{6} T_i \,. \tag{3.22}$$

To quantify the heat losses caused by the heat transfer through the walls of the room model, the mean heat flux q of each wall was measured using heat flux sensors of type FQA018CSI (Almemo). Here, only the side walls were considered. The heat flux across the floor and ceiling surfaces is negligible due to double insulation. The heat flux plates were mounted to the wall with double-sided PVC tape as homogeneously as possible, as shown in Fig. 3.21(a).

To determine the heat transfer coefficients α_i and α_o using Eq. (2.104) (according to Fig. 2.28), a surface and an air temperature sensor were mounted on the inner and outer wall surfaces. The results of the heat transfer coefficients for all the different cases can be found in Table B1 in Appendix B.



(a) **(b)**

Figure 3.21: (a) Positions of the heat flux sensors on the side walls of the single room model in 1:10 scale. (b) Positions of the velocity sensors and the thermocouples in the gaps of a tilted window.

The subscripts i and o denote inside and outside positions for the given situation. Applying Eq. (2.105) the heat transfer coefficient k can also be determined. Again, thermocouples were used for measuring the surface temperatures. These were also attached with a double sided tape directly next to the heat flux plate.

If P_{el} is the electrical input power to keep the internal temperature of the room constant under the influence of wind at tilted windows, it follows:

$$P_{el} = \rho c_V \sum_{ij} T_{ij} v_{ij} A_{ij} + Q_w \ , \tag{3.23}$$

where i and j denote the gaps at a window, and the number of the window, respectively. Q_w denotes the heat transfer across the walls. The air volume flow rate can be calculated as follows:

$$\sum_{ij} v_{ij}^{in} A_{ij} = -\sum_{ij} v_{ij}^{out} A_{ij} \ . \tag{3.24}$$

Applying

$$\sum_{ij} v_{ij}^{in} A_{ij} = \dot{V} \ , \tag{3.25}$$

Eq. (3.24) reads

$$\dot{V} = -\sum_{ij} v_{ij}^{out} A_{ij} \ . \tag{3.26}$$

Considering the heat transfer through the walls of the single room model and setting

$T_{ij}^{in} = T_0 = T_{air} = const.$ for the inflowing air yields

$$P_{el} = \rho c_V \left(-\dot{V} T_{air} + \sum_{ij} T_{ij}^{out} v_{ij}^{out} A_{ij} \right) - k A_w \left(T_{air} - T_{i,mean} \right) \ , \tag{3.27}$$

where A_w is the total area of the side walls. The air exchange rate ACH results in

$$ACH = \frac{\dot{V}}{V_R} = -\frac{360}{\rho c_V T_{air} V_R} \left[P_{el} + k A_w \left(T_{air} - T_{i,mean} \right) - \rho c_V \sum_{ij} T_{ij}^{out} v_{ij}^{out} A_{ij} \right] \ . \tag{3.28}$$

The heat flux was measured with closed windows in order to determine the wall heat flux, considering two wind velocities U_∞ of 3.6 m/s and 5.1 m/s, 4 temperature differences ΔT, and 8 incidence angles α (sketched in Fig. 3.16(c)).

With this experimental setup, purely thermally induced air exchange rates (i.e. flow velocity $U_\infty = 0$) were investigated, and on the other hand the superposition of thermally induced and wind-driven air exchange was examined. Table 3.6 shows the measurement configurations for determining the air exchange rate and, neglecting the temperature differences, even for the measurement of the heat flux by the heat flux plates.

U_∞	Windows	ΔT	Incidence angle α							
$[m/s]$	tilted	$[K]$	$-40°$	$-20°$	$0°$	$20°$	$40°$	$60°$	$80°$	$90°$
3.6	W_1 to W_4	2	✓	✓	✓	✓	✓	✓	✓	✓
3.6	W_1 to W_4	8	✓	✓	✓	✓	✓	✓	✓	✓
3.6	W_1 and W_4	2	✓	✓	✓	✓	✓	✓	✓	✓
3.6	W_1 and W_4	8	✓	✓	✓	✓	✓	✓	✓	✓
3.6	W_1 and W_2	2	✓	✓	✓	✓	✓	✓	✓	✓
3.6	W_1 and W_2	8	✓	✓	✓	✓	✓	✓	✓	✓
5.1	W_1 to W_4	2	✓	✓	✓	✓	✓	✓	✓	✓
5.1	W_1 to W_4	8	✓	✓	✓	✓	✓	✓	✓	✓
5.1	W_1 and W_4	2	✓	✓	✓	✓	✓	✓	✓	✓
5.1	W_1 and W_4	8	✓	✓	✓	✓	✓	✓	✓	✓
5.1	W_1 and W_2	2	✓	✓	✓	✓	✓	✓	✓	✓
5.1	W_1 and W_2	8	✓	✓	✓	✓	✓	✓	✓	✓

Table 3.6: Configurations for velocity measurements for the single room model for tilted windows.

3.7 Scaling factor of the air exchange rate

The conversion between the air exchange rates in real dimensions and in a scaled model is determined by a scaling factor. If the subscripts m and r denote *model* and *real*, respectively, the air exchange rate in the model scale is given as

$$ACH_m = \frac{\dot{V}_m}{V_{R,m}} = \frac{U\,A_m}{V_{R,m}} \tag{3.29}$$

and, for flows with the same velocity U, in real scale as

$$ACH_r = \frac{U\,A_r}{V_{R,r}}\ . \tag{3.30}$$

Using a scale of $1:m$ yields

$$\frac{ACH_m}{ACH_r} = m \quad \Longrightarrow \quad ACH_r = \frac{1}{m}\,ACH_m = \frac{1}{m}\frac{\dot{V}_m}{V_{R,m}}\ . \tag{3.31}$$

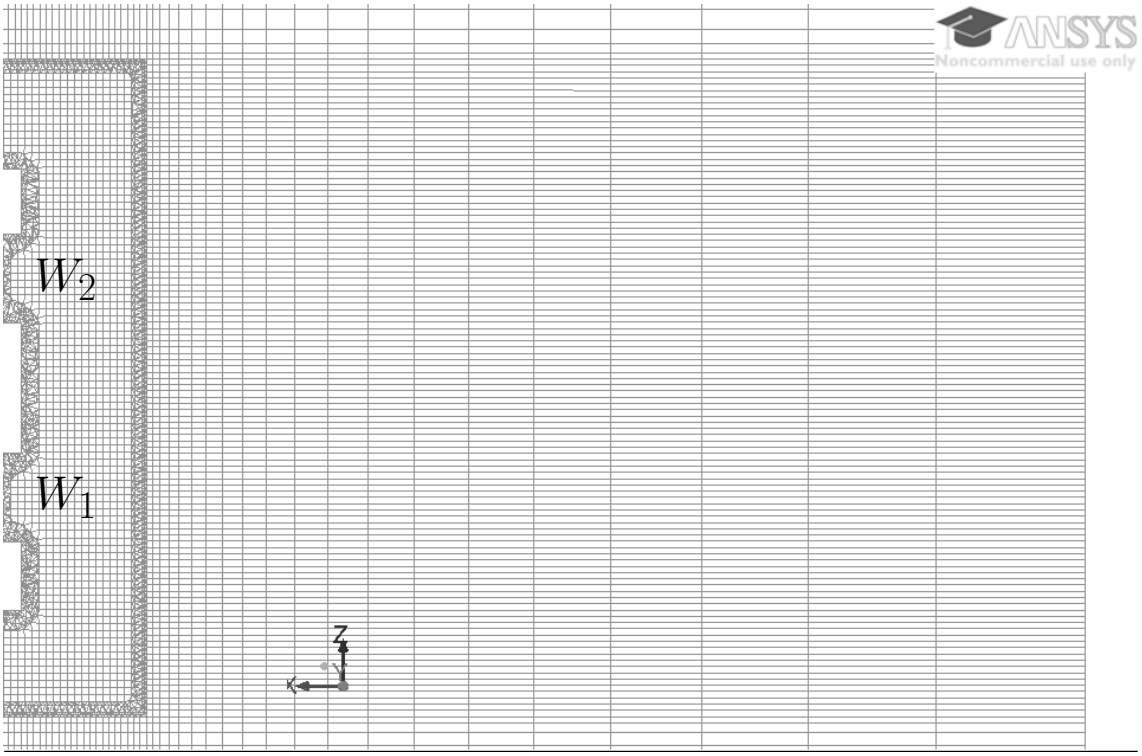
The length scales enter to the second power into the window area and the corresponding volumetric flow rate, but to the third power into the volume. For flows in real dimensions with the same inflow velocity as in the model case, the ACH in real dimensions can therefore be calculated by multiplying the ACH in the model with the scaling factor $1/m$. E.g., for the situation in real dimensions the ACH is expected to be 1/25 times the value of the ACH determined in a 1:25 model, which is also confirmed by the experimental results.

3.8 Numerical simulations

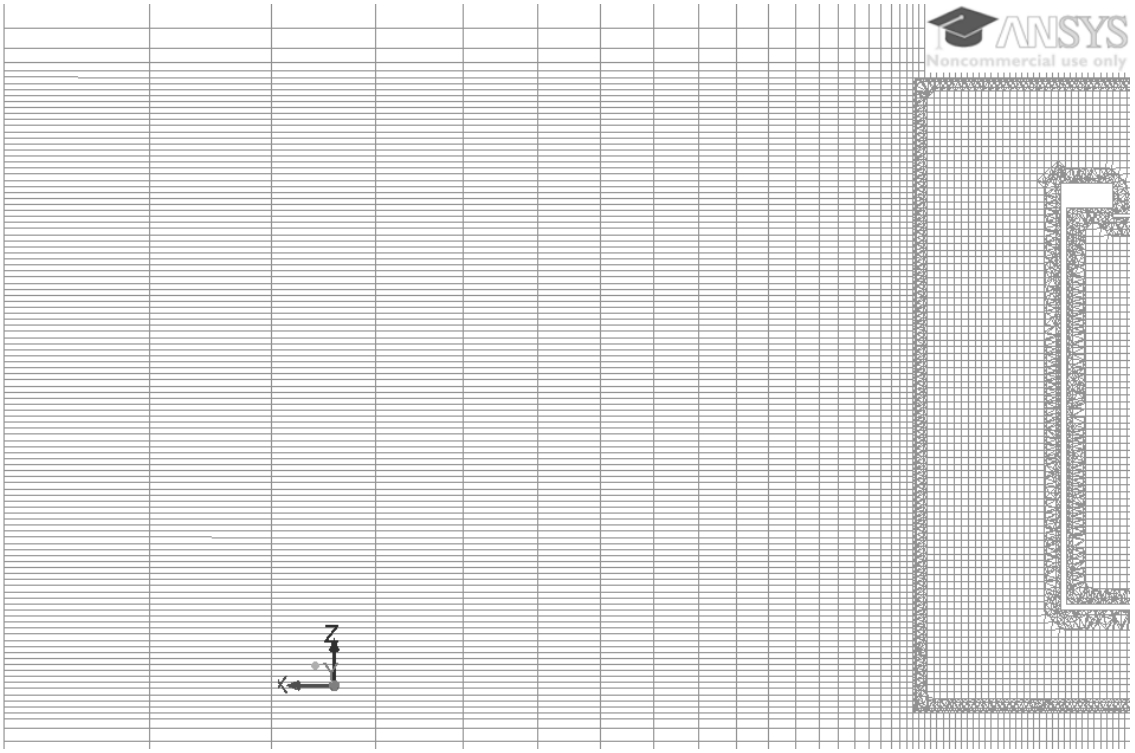
In the performed numerical simulations, the aim was to solve the equations of conservation in accordance with initial and boundary conditions and to examine that they qualitatively and quantitatively represent the results obtained from the experiments. Furthermore, these simulations provide a contribution for a better understanding of the complex flow structure within the model room, which cannot be represented from our experiments.

Numerical simulations for the sample storey model in 1:25 scale were done by the Austrian Institute of Technology. Detailed information may be found in Teppner et al. (2014a).

A full three-dimensional numerical simulation was carried out by the author on the building model in 1:10 scale. The computation domain extends 4 m in the streamwise, 3 m in the spanwise, and 1.76 m in the vertical direction. Preprocessing was done using ANSYS Gambit 2.4, where the mesh of overall 3 million volumes, consisting of hexahedral and tetrahedral elements, was generated. The smallest mesh



(a)



(b)

Figure 3.22: Top view of the computational grids for (a) inlet and (b) outlet used in the simulations of the single room model.

size starts with 10 mm in the zone surrounding the single room model and gradually increases towards the boundaries of the domain. Figure 3.8 show the mesh for the (a) inlet and (b) outlet.

High mesh resolution around the building geometry comes from the requirement of solving the flow in the near wall region (at the walls of the single room model), as well as from the tendency to solve the flow structures appearing around and inside the model room. The mesh surrounding the complex part of the geometry in the region of the tilted windows and in close proximity to the walls contains tetrahedral elements, which can be seen in Fig. 3.23. In the inlet and the outlet part of the domain, a grid using hexahedral elements was generated, to provide sufficient accuracy at larger mesh size and reduce the computational time. Tetrahedral mesh was chosen due to the complexity of the geometry around window openings.

The hexahedral grid enabled reduction in number of cells while maintaining reasonable accuracy in describing inflow and outflow region of the domain. The

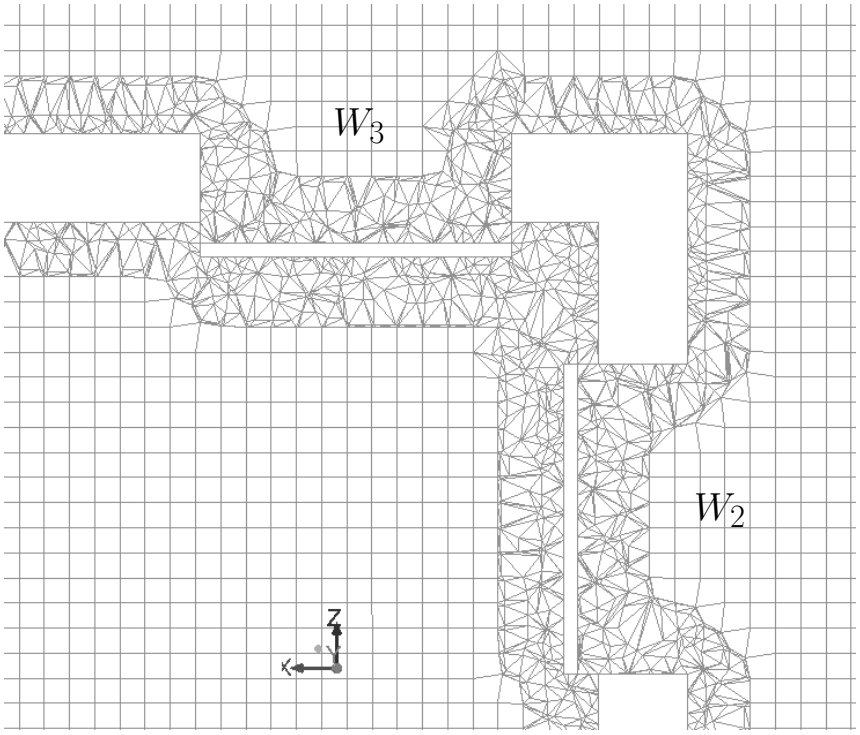
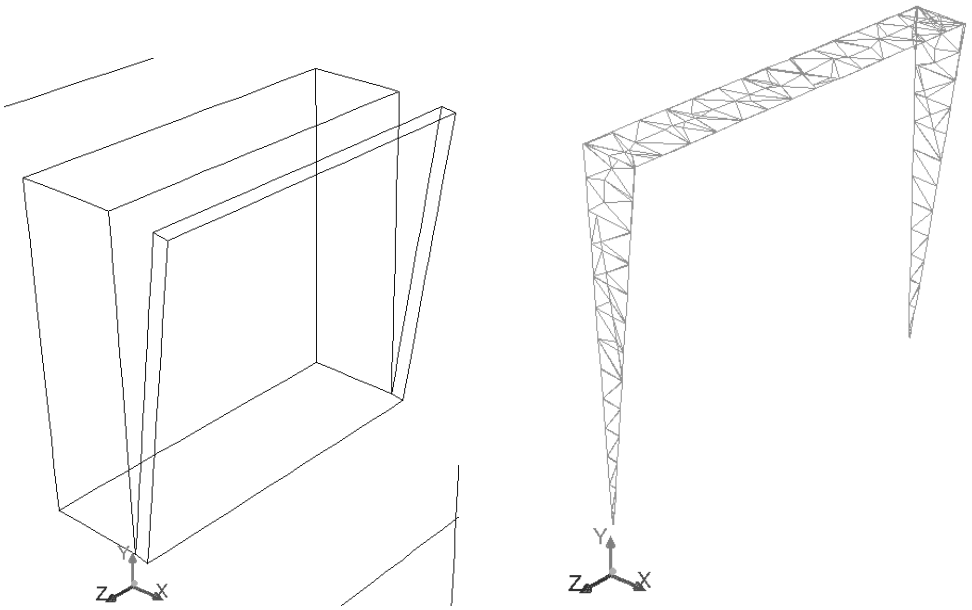


Figure 3.23: Top view of the near wall region for the windows W_2 and W_3, exemplarily.

minimum mesh size and resolution were limited by and adjusted to available computational resources. Geometrical variations included different incident wind angles as well as different scenarios regarding the opening of the windows. The maximum value of wall y^+ is calculated to be around 130 (cf. Fig. 3.25).

At the domain inlet, a velocity inlet boundary condition was set. The inlet geometry was modelled equal to the geometry of the nozzle exit of the wind tunnel. Boundaries representing the nozzle, ground and model walls were set as walls with no slip. The rest of the boundaries were defined by pressure outlet with the overpressure set to zero. At the inlet, the velocity inlet boundary condition was prescribed enabling the variation of the velocity for 3.6 m/s and 5.1 m/s in order to match the wind tunnel measurements. For turbulence modelling, the realizable $k - \varepsilon$ model was applied and with the values of turbulent viscosity ratio and turbulence intensity set to 10 and 0.13%, respectively. With ANSYS Fluent (Ansys, 2011), release 12.0, the steady RANS equations were solved. The comparison against measurements was done comparing the air exchange rates for different scenarios.

The convergence criterion for the solution was judged following the residuals of



(a) **(b)**

Figure 3.24: (a) Tilted window. (b) Grid points for the top and side areas of the window gaps.

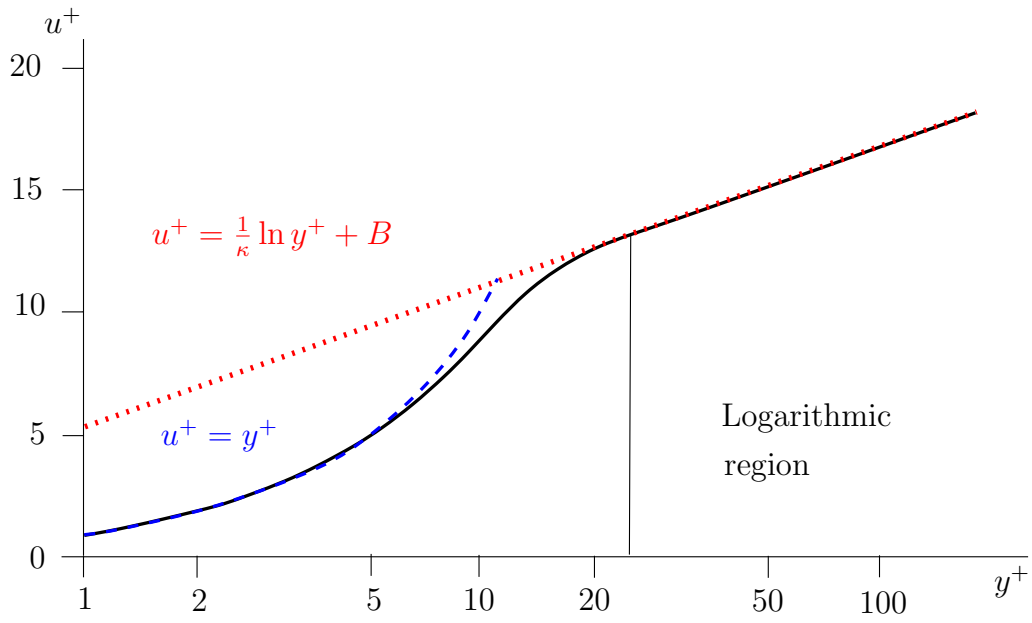


Figure 3.25: Law of the wall

continuity and momentum equations in all directions, respectively. For all of the computations residuals dropped below 10^{-3} for the continuity and below 10^{-4} for the momentum, which presented a converged solution.

Chapter 4

Results

As described above, extensive velocity and tracer gas measurements on building models in different scales were performed for the investigation of the air exchange of buildings by natural ventilation. The results obtained are presented and discussed in this chapter. Furthermore, the results obtained from experiments are compared with those from numerical simulations, which were performed at the AIT-Austrian Institute of Technology for the storey model in 1:25 scale and at the Institute of Fluid Mechanics and Heat Transfer at Graz University of Technology for the single room model in 1:10 scale. Some descriptions in this chapter were already published in Teppner et al. (2013) and in Teppner et al. (2014a).

4.1 Simulation of the atmospheric boundary layer

As mentioned in Section 3.2.1, in the present study we focus on areas with uniform vegetation and suburban development. The present experiments cover the two wind velocities $u_{10} = 2.8$ m/s and $u_{10} = 4.7$ m/s.

The wind velocity profiles realised in the boundary layer wind tunnel, scaled to real dimensions, are shown in Fig. 4.1. The required agreement with the power-law profile (represented by Eq. (2.68)) in the range between 3 m and 40 m height is well achieved.

The Reynolds number of the flow around the model formed with the smallest

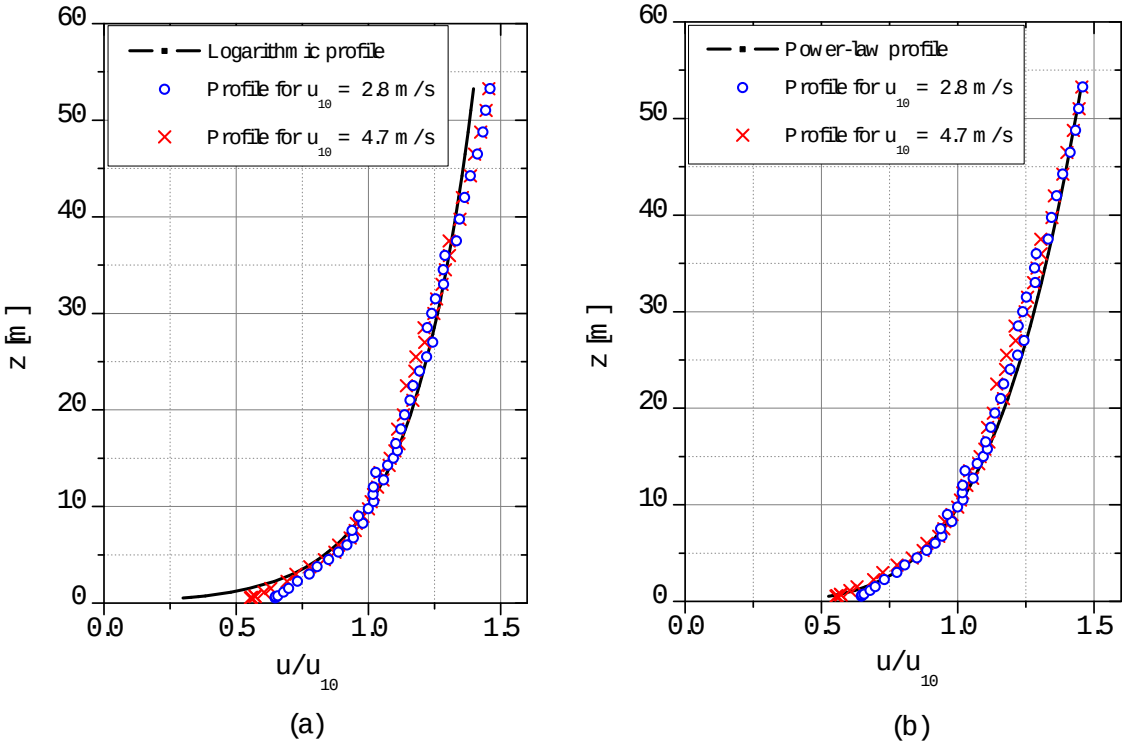


Figure 4.1: Experimental profiles $u(z)/u_{10}$ compared to the (a) logarithmic and (b) power-law profile.

building dimension is

$$Re = \frac{u_H W}{\nu} = 3.7 \cdot 10^6 \,, \tag{4.1}$$

where u_H is the velocity at the building height, the width W is the smallest building dimension ($W = 0.187$ m in the 1:75 model) and ν the kinematic viscosity of the air. The similarity requirement $Re > 5 \cdot 10^4$ is satisfied (Plate, 1982b). In the experiments, a practically constant turbulence level with the height above ground could be adjusted, as can be seen in Fig. 4.2. This is a further indication for the high quality of the boundary layer velocity profile in the wind tunnel. Figures 4.2(a) and (b) show the behaviour of the turbulence intensities for the $x-$ and $z-$directions. Figures 4.2(c) and (d) show the constancy of the turbulent shear stresses within the simulated height of the Prandtl layer. Applying Eq. (2.65) and Fig. 2.12, a plot in a semi-logarithmic scale allows the reading of the parameters u_τ from the inclination of the regression line and z_0 from the intersection point of the regression line with the ordinate in the case of the logarithmic wall law (cf. Fig. 4.3(a)). From Fig. 4.3(b),

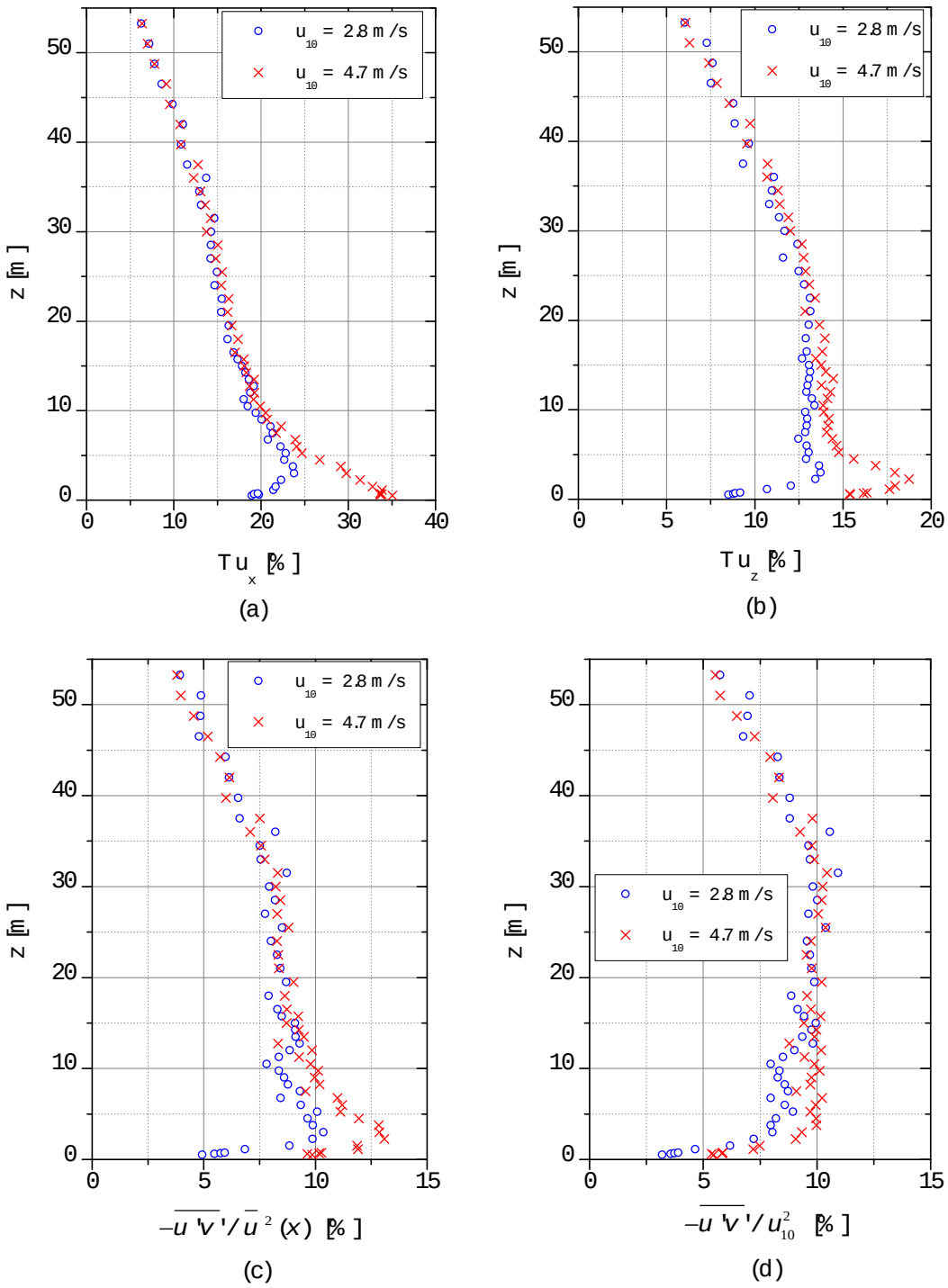


Figure 4.2: Turbulence intensities in (a) $x-$direction and (b) $z-$direction. Normalized turbulent shear stresses in (c) and (d).

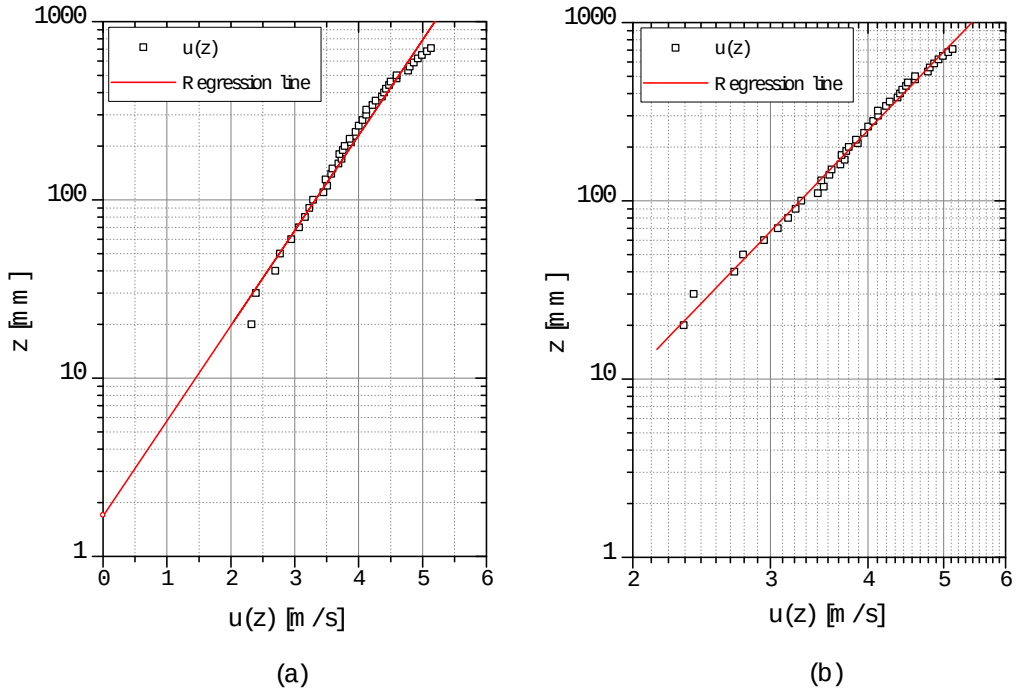


Figure 4.3: Measured wind profile by means of regression analysis by (a) a logarithmic and (b) a power-law profile, both exemplarily for $u_{10} = 4.7$ m/s.

in case of the power law, the profile parameter α can be read from the gradient of the regression line in a double logarithmic scale (Gromke und Ruck, 2005).

The adaptation of the logarithmic wall law by regression analysis, using $u(z)$ as the dependent and z as the independent variables, leads to a roughness length $z_0 = 0.137$ m and a friction velocity $u_\tau = 0.45$ m/s in the case of $u_{10} = 4.7$ m/s and to $z_0 = 0.126$ m and a friction velocity $u_\tau = 0.33$ m/s in the case of $u_{10} = 2.8$ m/s. An appropriate analysis for the adaptation of the power law yields $\alpha \approx 0.22$ for both cases, which perfectly matches the desired value of 0.22.

4.1.1 Pressure distributions and force coefficients

According to the configurations specified in Table 3.1, the pressure differences over the whole facade were measured for the building model in 1:75 scale, and the pressure coefficients c_p were calculated using Eq. (2.77).

Applying Eq. (3.10), the coefficients were determined by a multidimensional

polynomial function to get the mean drag force coefficients by integrating over the particular building surfaces, as described in Section 3.3. The results of this calculation are demonstrated examplarily for the case of an inflow velocity of $u_{10} = 4.7$ m/s at an incidence angle of $\alpha = 0°$ (cf. Fig. 4.4).

The pressure distribution for the windward wall can be fitted by

$$\begin{aligned} c_{p,\text{fitted, windward}}(x,z) &= 0.212 - 0.09066x + 4.553z - 0.9438x^2 + 0.2232xz \\ &\quad -12.95z^2 - 4.928x^2z - 0.006761xz^2 + 18.1z^3 + 4.898x^2z^2 \\ &\quad -0.1351xz^3 - 9.137z^4 \,, \end{aligned} \tag{4.2}$$

and for the leeward wall by

$$\begin{aligned} c_{p,\text{fitted, leeward}}(x,z) &= -0.09888 - 0.02576x - 0.5678z - 0.0984x^2 + 0.2111xz \\ &\quad +1.892z^2 - 0.2319x^2z - 0.4622xz^2 - 3.005z^3 + 0.3192x^2z^2 \\ &\quad +0.2809xz^3 + 1.58z^4 \,. \end{aligned} \tag{4.3}$$

Figure 4.4 exemplarily shows the fitted pressure distribution for the windward wall for an inlet velocity of $u_{10} = 4.7$ m/s and an incidence angle of $\alpha = 0°$, represented by the multidimensional polynomial function in Eq. (4.2) in comparison to the data obtained by measurement. In the following the wall surfaces are denoted as sketched in Fig. 4.5.

The pressure distribution on the building surface is shown exemplarily in Fig. 4.6 for the flow velocity of $u_{10} = 4.7$ m/s and an incidence angle of $\alpha = 0°$. The pressure distributions are presented as contour plots. As already mentioned, this was done by means of a least squares approach using the software packages MatLab R2011a and OriginPro 8G. The coefficient R^2 is 0.985 and the sum of squared errors $SSE = 0.020$ (cf. Fig. 4.6(a)). The coefficient of determination R^2 and the sum of squared errors SSE are given for each contour plot in the figure caption.

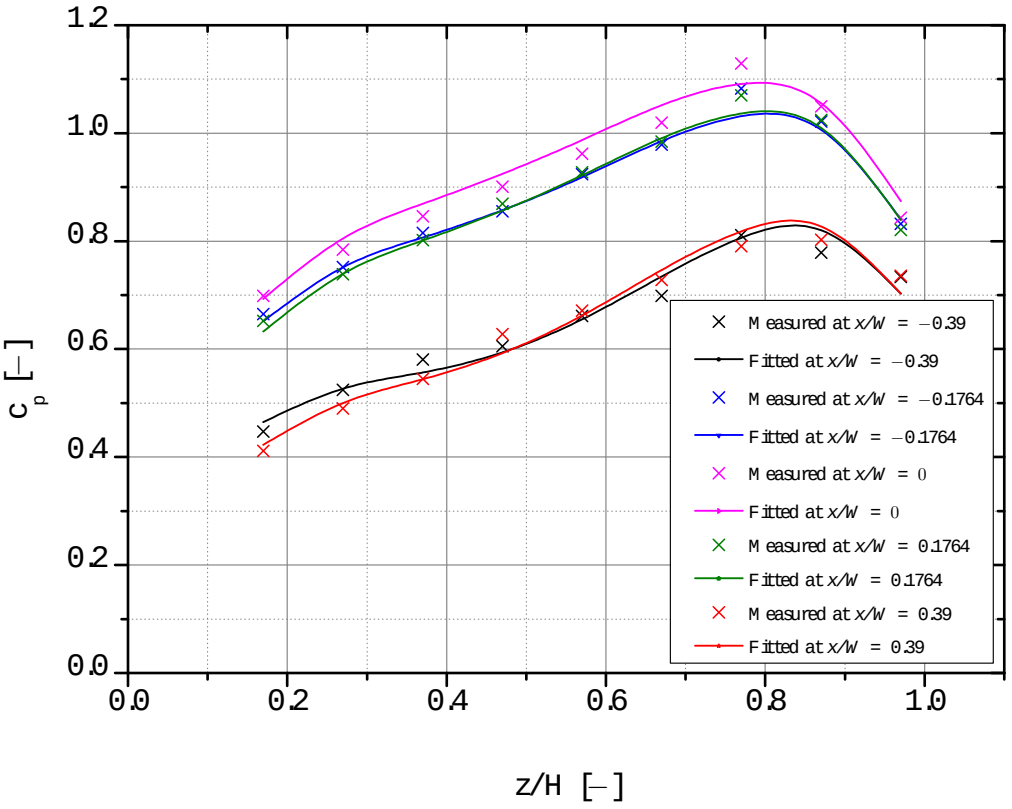


Figure 4.4: Comparison of measured and fitted pressure distributions represented by c_p for $u_{10} = 4.7$ m/s and $\alpha = 0°$ at the windward wall.

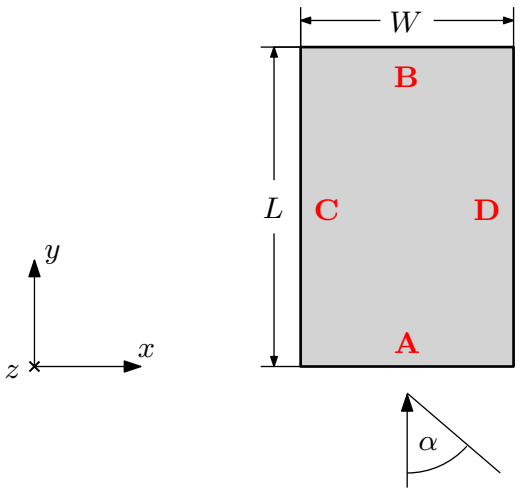
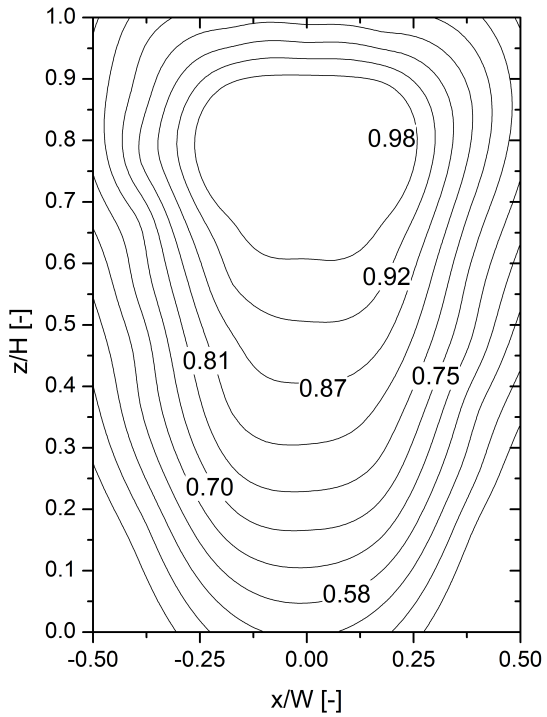
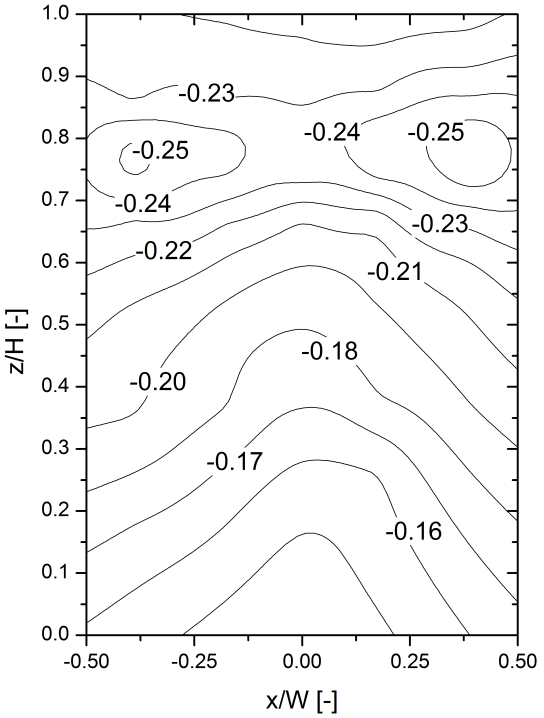


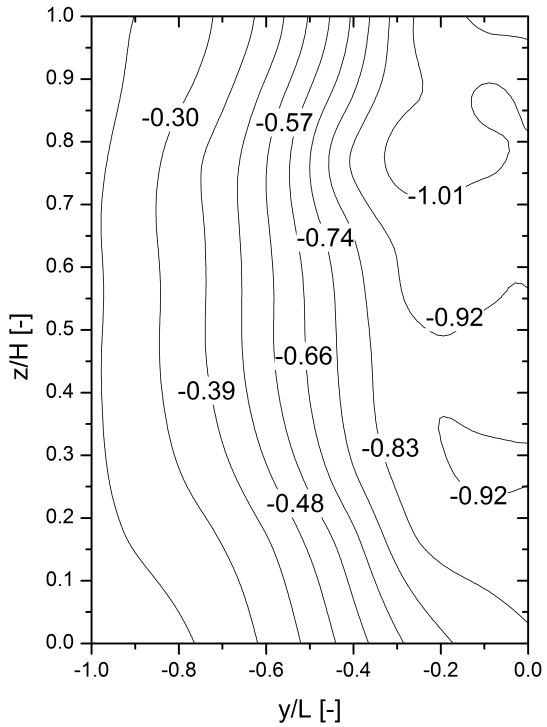
Figure 4.5: Notation of the wall surfaces.



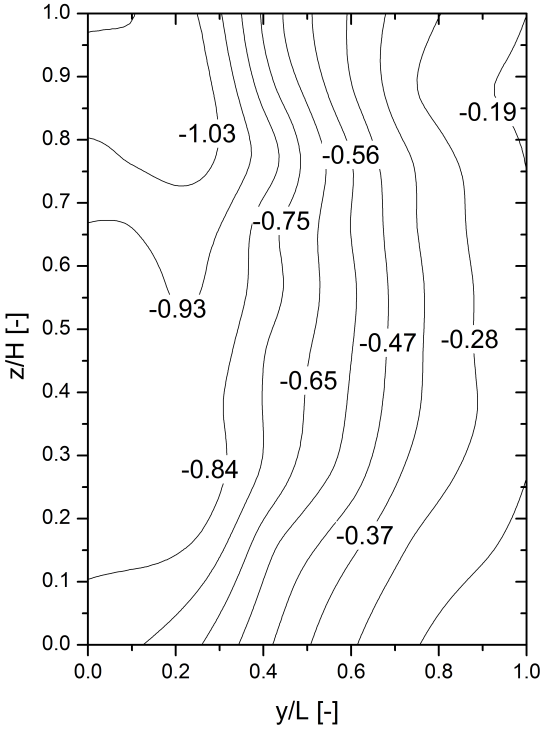
(a) View A. $R^2 = 0.985, SSE = 0.020$.



(b) View B. $R^2 = 0.950, SSE = 0.002$.



(c) View C. $R^2 = 0.994, SSE = 0.029$.



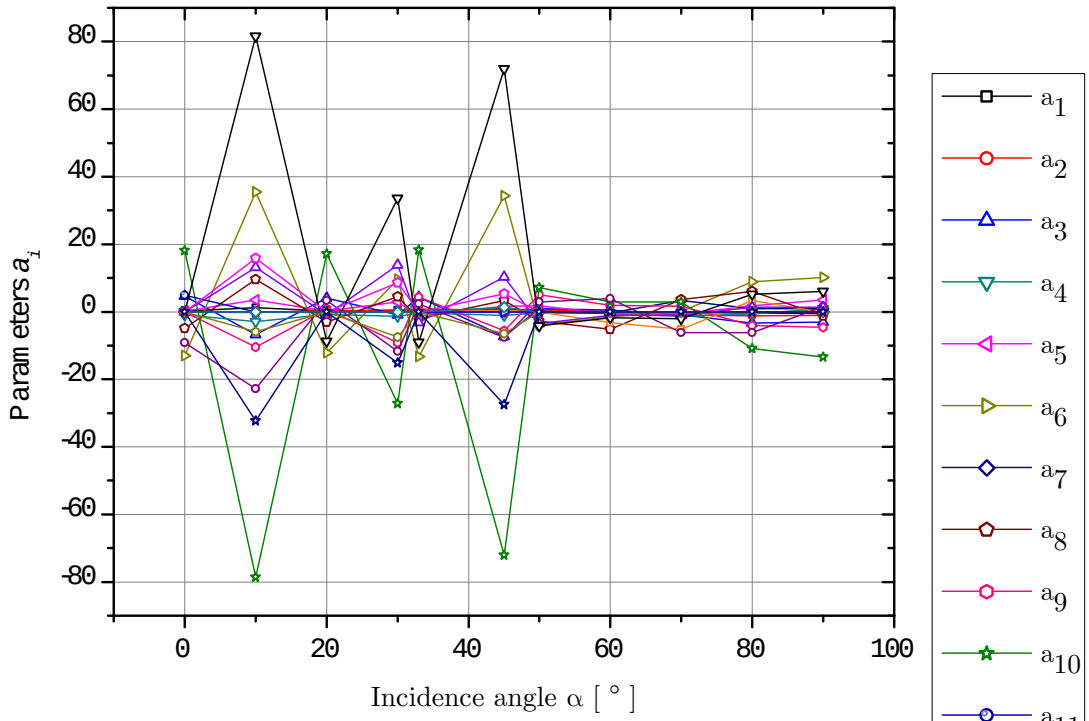
(d) View D. $R^2 = 0.955, SSE = 0.198$.

Figure 4.6: Distribution of pressure coefficient c_p for an inflow velocity of $u_{10} = 4.7$ m/s and an incidence angle of $\alpha = 0°$.

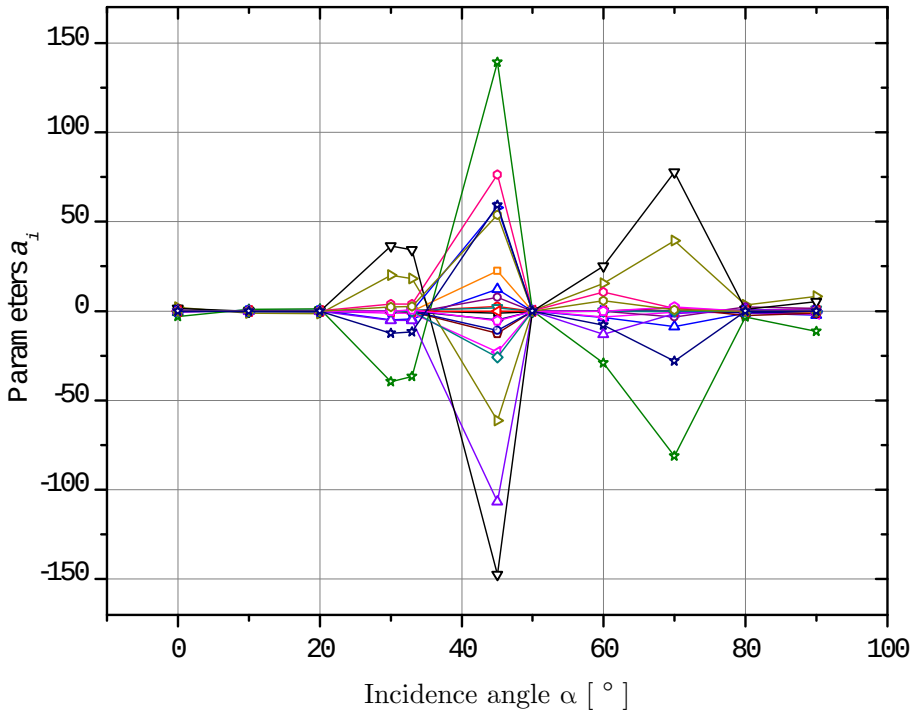
For a boundary layer wind profile impinging on the windward wall, the pressure increases with the height above ground due to the velocity increase. As can be seen in Fig. 4.6(a) at heights between $0.7H$ and $0.8H$ of the building, a stagnation point is formed (cf. Section 2.3.1). Above the stagnation point the flow is directed upward and flows over the top of the building, while below the flow goes down towards the ground. In this height a typical corner vortex is formed, resulting in a motion against the wind, which comes to rest at a stagnation point on the ground in front of the building. Thus, the flow rolls up into a horse shoe vortex (cf. Section 2.3.1) by forming a horizontal roll in front of the windward wall, which affects the pressure distribution on the windward surface of the building (Martinuzzi, 1992). In other words, the boundary layer flow separates due to an increasing pressure in the flow direction, and a typical corner vortex is formed, which continues laterally around the building so that the horseshoe vortex is formed. The pressure coefficient c_p at the top of the building takes a value within a range between 0.7 and 0.9, which corresponds to observations of Cook (1985).

Along the side walls of the building (cf. Figs. 4.6(c) and (d)), the flow in a height where the horse shoe vortex acts on, is significantly faster than the incident wind at this level. The vertical distribution of the pressure coefficient on the side walls is more homogeneous due to the vertical mixing, caused by the horse shoe vortex (Cook, 1985). The relatively high negative values of the pressure coefficient at the windward edge of the side wall indicate suction which decreases downstream. The vertical differences between the pressure coefficients are commonly very small, which conforms to the statements of Cook (1985). With increasing incidence angle α, a horizontal shift of the pressure coefficent maximuma occurs, as can be seen in Figs. A.1 – A.10 in Appendix A.

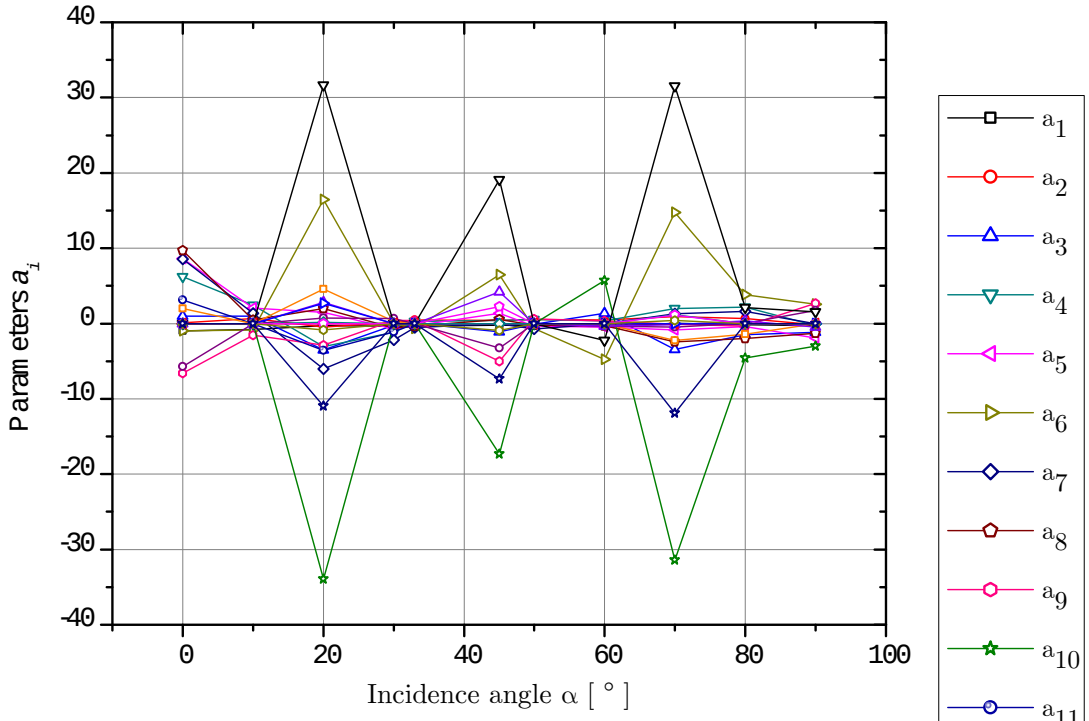
The distribution of the parameters a_i of the multi-dimensional polynomial function Eq. (3.10) shows a clearly symmetric behaviour regarding a specific incidence angle α. This is exemplified in Fig. 4.7 for a flow velocity of $u_{10} = 4.7$ m/s depending on the incidence angle α. The approximate mirror symmetry with respect to the parameters a_{10} and a_{15} or a_6 and a_{11}, which is clearly recognizable in Fig. 4.7(a), can be explained by the symmetric distribution of the pressure coefficient c_p with regard to a vertical line through $x/W = 0$ (cf. Fig. 4.6). The distribution of the parameters a_i for $u_{10} = 2.8$ m/s can be found in the Appendix in Fig. A.11.


Parameters a_i
80
60
40
20
0
-20
-40
-60
-80
0
20
40
60
80
100
Incidence angle α [°]
a_1
a_2
a_3
a_4
a_5
a_6
a_7
a_8
a_9
a_{10}
a_{11}
a_{12}
a_{13}
a_{14}
a_{15}
a_{16}
a_{17}
a_{18}
a_{19}
a_{20}
a_{21}

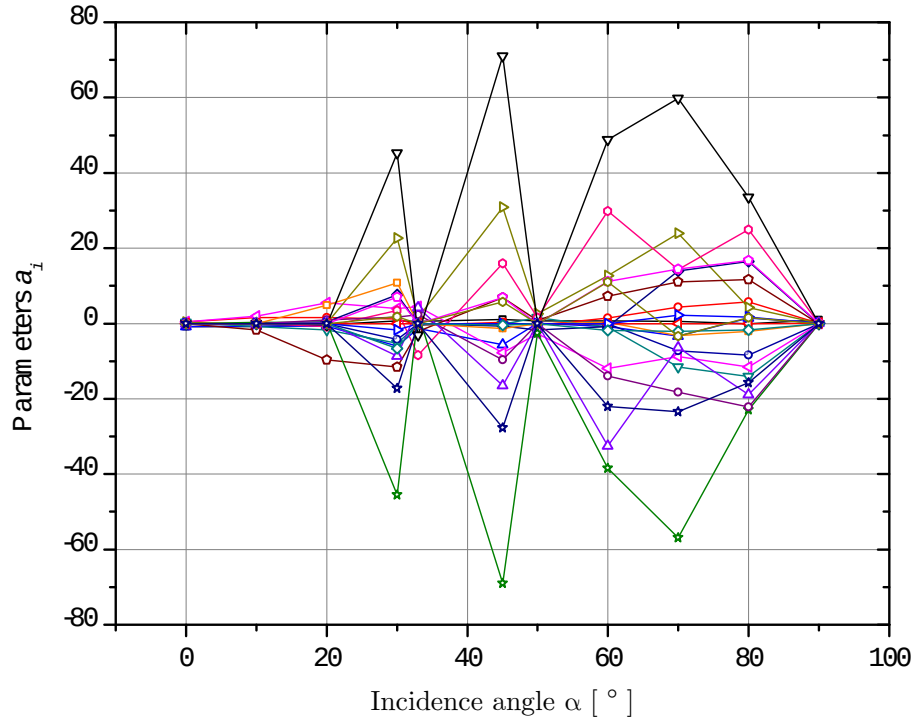
(a)


Parameters a_i
150
100
50
0
-50
-100
-150
0
20
40
60
80
100
Incidence angle α [°]

(b)



(c)



(d)

Figure 4.7: Distribution of the parameters a_1 to a_{21} for the multidimensional polynomial function in Eq. (3.10) for (a) the windward wall (view A), (b) the leeward wall (view B), (c) the left wall (view C), and (d) the right wall (view D) for $u_{10} = 4.7$ m/s.

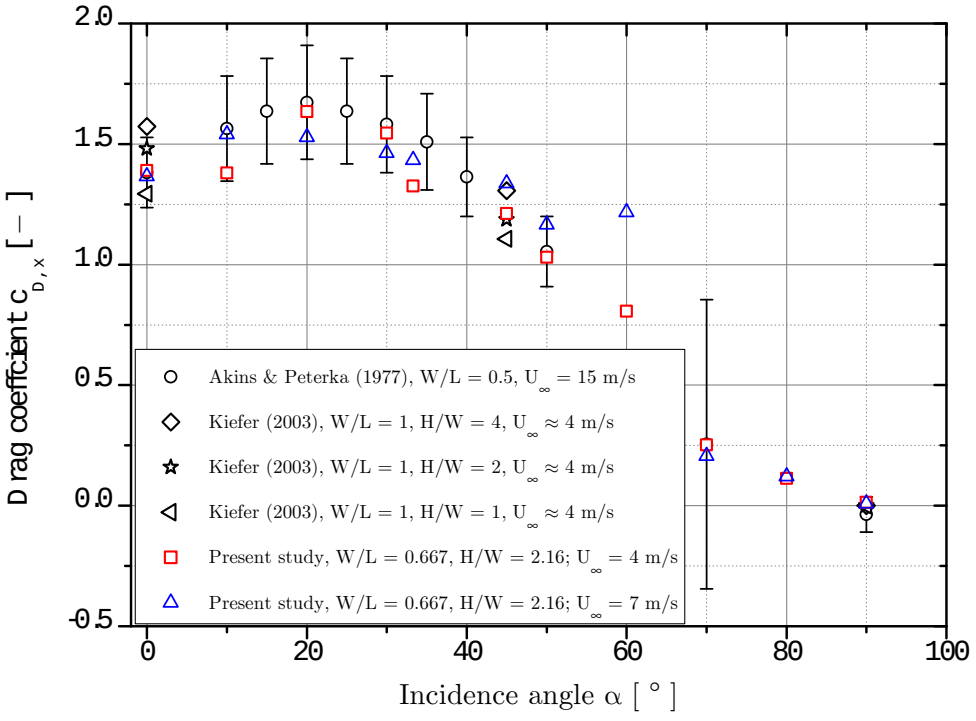
4.1.2 Validation of the pressure distribution – force coefficients

To validate the pressure distributions found by measurements, the force coefficients were calculated by integration according to Eq. (3.11)

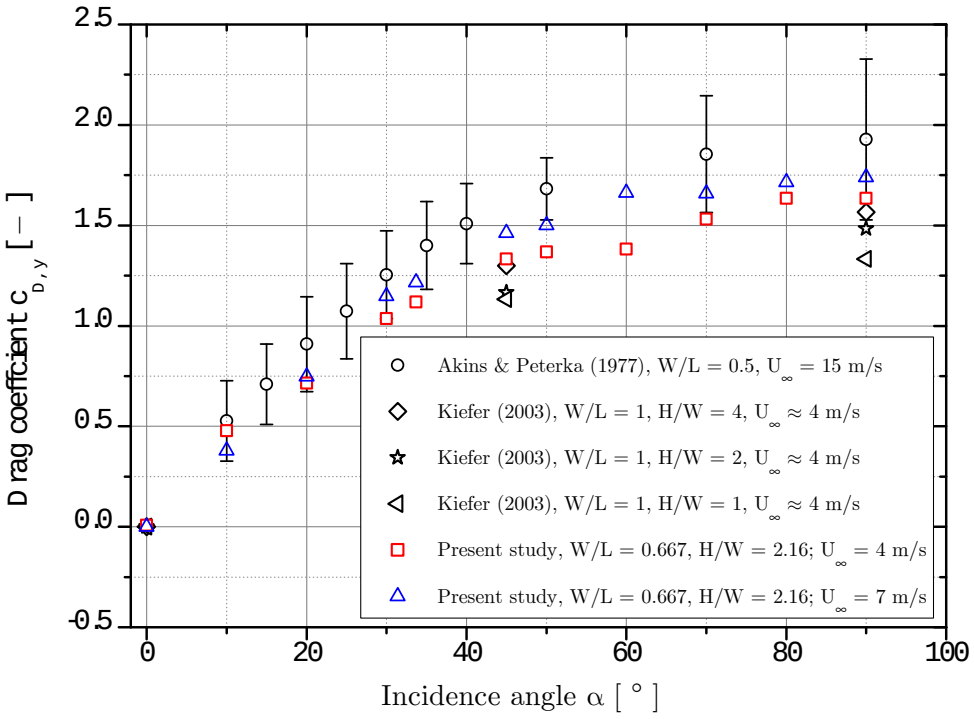
$$\int_{-0.5}^{0.5}\int_{0}^{1} c_{p,\text{fitted}}\,\mathrm{d}z^{\star}\,\mathrm{d}x^{\star}\ ,$$

where $z^{\star} = z/H$ and $x^{\star} = x/W$, and compared with data in the literature.

Subtracting the results for the windward wall from that for the leeward wall, both obtained by Eq. (3.11), and multiplying by the factor of conversion according to Akins and Peterka (1977), given by Eq. (3.14), yields a force coefficient in the $x-$direction of $c_{D,x} = 1.36615$ for $u_{10} = 4.7$ m/s and $\alpha = 0°$. An analogous procedure, using the appropriate integral boundaries, leads to the force coefficient $c_{D,y} = -0.000248067$ in the $y-$direction.



(a)



(b)

Figure 4.8: Force coefficients in the direction of the body axes (related to U_∞), compared with the results of Akins and Peterka (1977) and Kiefer (2003): (a) for $x-$direction, (b) for $y-$direction.

In Fig. 4.8 the results of the investigations of Akins and Peterka (1977), and of Kiefer (2003), are compared with the force coefficients determined in the present work. The results of Akins and Peterka (1977) are given with deviation bars to represent the broad scattering of data resulting from different boundary layer profiles and ratios H/W. Overall, Figs. 4.8(a) and (b) show good agreement of the present data with the data of Akins and Peterka (1977) in the given scattering range, which indicates that our pressure measurements provide realistic results.

4.2 Determination of the air exchange rate by velocity measurements

4.2.1 ACH obtained by velocity measurements for fully open windows

The velocity measurements in the window cross sections of the fully open windows were carried out for the two velocities $U_\infty = 4$ m/s and $U_\infty = 7$ m/s, each for the heights of approximately 8 m and 23 m above the ground (corresponding to the 3^{rd} and 8^{th} floor of the building).

U_∞ $[m/s]$	α [°]	Room R_1	Room R_2	Rooms R_{3a+3c}	Rooms R_{3b+3c}	Rooms $R_{3a+3b+3c}$	Room R_4	Room R_5
3.6	0	246.36	26.50	39.23	39.98	–	29.43	249.25
3.6	33.3	–	–	–	–	–	–	138.21
3.6	90	222.15	–	–	–	46.41	–	–
3.6	180	–	20.05	96.25	94.97	–	19.06	–
3.8	0	257.8	30.55	40.49	42.00	–	60.78	261.56
3.8	33.3	–	–	–	–	–	–	144.86
3.8	90	233.95	–	–	–	49.06	–	–
3.8	180	–	19.95	101.97	99.74	–	19.50	–
5.1	0	356.50	47.00	55.16	54.70	–	43.96	365.45
5.1	33.3	–	–	–	–	–	–	201.57
5.1	90	314.34	–	–	–	66.87	–	–
5.1	180	–	30.57	140.59	138.9	–	29.2	–
5.7	0	401.47	41.35	57.16	55.00	–	42.6	394.11
5.7	33.3	–	–	–	–	–	–	211.23
5.7	90	341.38	–	–	–	76.38	–	–
5.7	180	–	32.20	143.60	145.60	–	35.35	–

Table 4.1: Up-scaled ACH-values [1/h] from velocity measurements in the storey model for fully open windows.

Table 4.1 shows the results of the up-scaled air exchange rate (cf. Section 3.7) for those measurements in 1:25 scale, where precise velocity directions could be determined by thread probes, as already mentioned. An overview over the different scenarios concerning the opening of the doors D_1 and D_2 is given in Table 3.2 in Section 3.4.

Looking at the air exchange rates for the room R_1 at a flow direction of 0°, it can be seen that these tend to increase with the wind velocity. The same trend can also be recognized in room R_5 under the same conditions. Comparison of the air exchange rates for rooms R_1 and R_5 show that the values are approximately equal for the same flow velocity and incidence angle. The same observation can be made for the rooms R_2 and R_4. This is also due to the arrangement of rooms in the storey model.

4.2.2 ACH obtained by velocity measurements for tilted windows

The sample single room model in 1:10 scale (Fig. 3.3(b)) served for velocity measurements in the open cross sections of tilted windows (Fig. 3.16(a) and (b)). The corresponding results are given in Table 4.2. The velocity measurements at no more than 3 locations of the opening of a tilted window may provide a plausible estimate of the ACH, but may not yield exact data. The accuracy of the representation of the ACH, as an integral property of the flow, by local velocities depends strongly on the place of the measurements. In comparison to that, the tracer gas method may

U_∞	Windows	Incidence angle α							
$[m/s]$	tilted	$-40°$	$-20°$	$0°$	$20°$	$40°$	$60°$	$80°$	$90°$
3.6	W_1 to W_4	60.58	70.48	69.68	61.70	24.13	37.09	68.06	67.66
3.6	W_1 and W_4	31.71	33.34	33.73	24.50	9.54	21.46	36.52	37.75
3.6	W_1 and W_2	16.65	12.67	1.59	14.21	20.59	9.30	15.66	3.64
5.1	W_1 to W_4	90.29	103.17	103.98	92.46	35.78	53.30	98.60	98.25
5.1	W_1 and W_4	43.14	45.67	45.7	33.63	13.23	28.75	49.91	50.84
5.1	W_1 and W_2	28.87	17.04	2.75	16.08	21.72	13.88	18.06	6.92

Table 4.2: Up-scaled air exchange rate in [1/h] obtained by velocity measurements for the single room model for tilted windows.

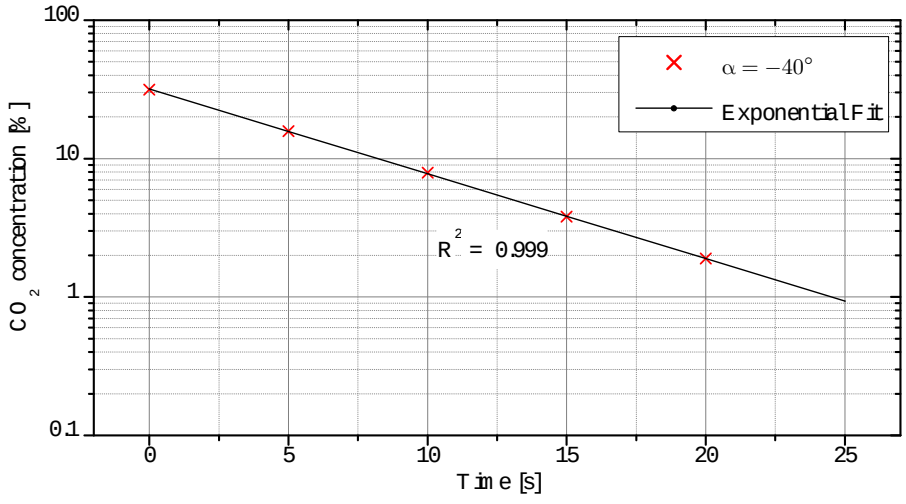
be more accurate.

The experiments with the single room model (1:10) can only represent one room of the sample storey model (1:25). This single room is separated from the configuration of the storey. The flow field around the single room therefore differs from the corresponding field around the whole storey, so that comparisons of the ACH are reasonable only for the incidence angles of 0° and 90°.

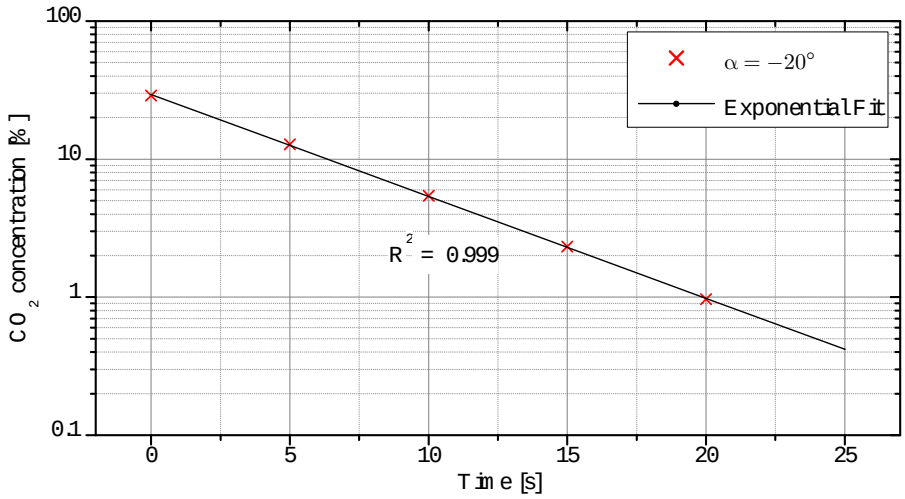
Table 4.2 shows the results for the air exchange rate calculated from the velocity measurements in the window gaps for the listed cases. In case of the incidence angle of $\alpha = 0°$, the air exchange rate increases with the wind velocity for all tilting scenarios of the windows. A comparison with the incidence angle $\alpha = 90°$ shows the same behaviour. The air exchange rates for the different tilting scenarios are approximately equal. The deviation arises from geometrical reasons, since the floor area of the room is not square-shaped, but rectangular.

4.3 Determination of the air exchange rate by tracer gas measurements for tilted windows

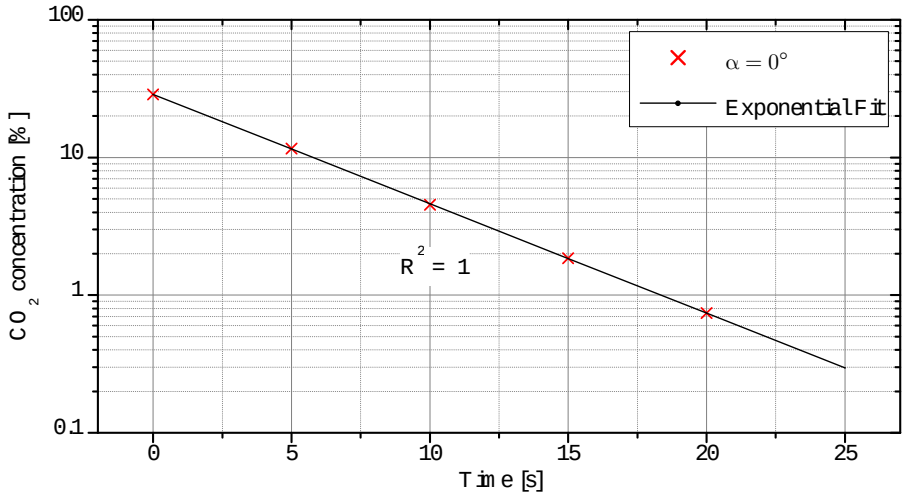
The tracer gas measurements based on the concentration decay method, using the evaluation method described in Section 3.5, allow the direct determination of the air exchange rates.



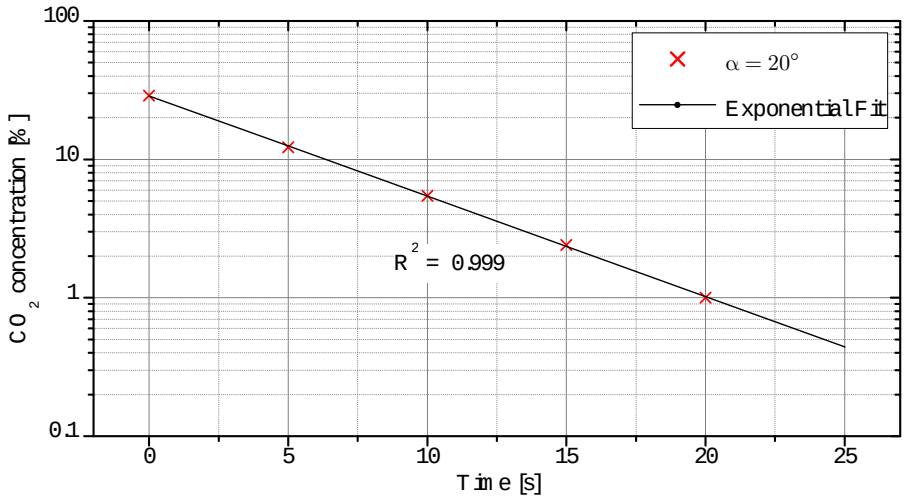
(a)


100
10
1
0.1
CO2 concentration [%]
0
5
10
15
20
25
Time [s]
α = −20°
ExponentialFit
R2 = 0.999

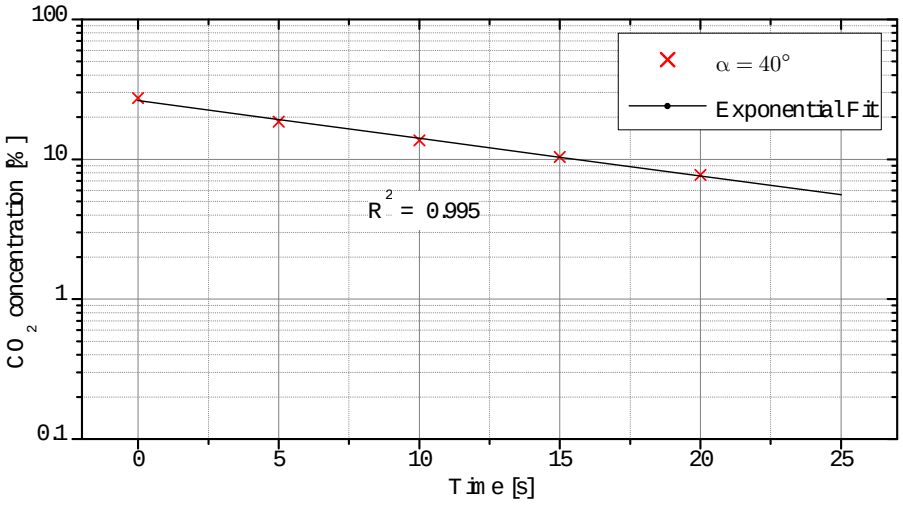
(b)


100
10
1
0.1
CO2 concentration [%]
0
5
10
15
20
25
Time [s]
α = 0°
ExponentialFit
R2 = 1

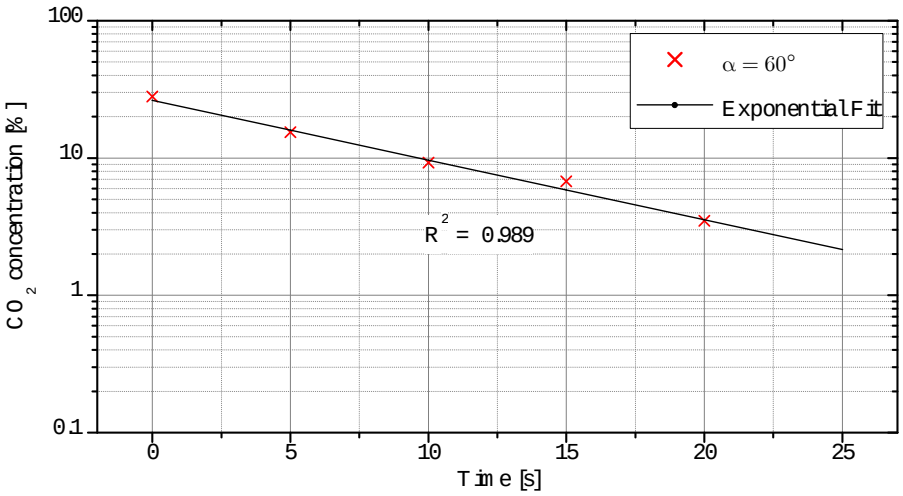
(c)


100
10
1
0.1
CO2 concentration [%]
0
5
10
15
20
25
Time [s]
α = 20°
ExponentialFit
R2 = 0.999

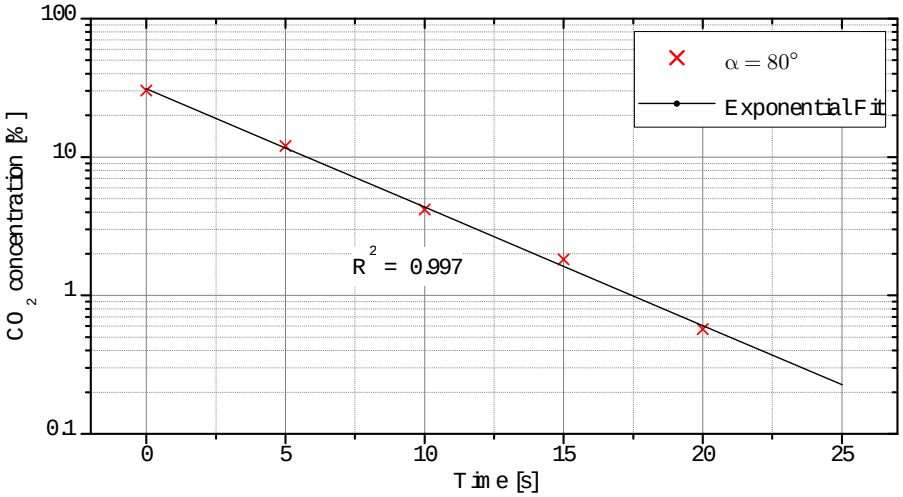
(d)


100
10
1
0.1
0
5
10
15
20
25
CO2 concentration [%]
Time [s]
α = 40°
ExponentialFit
R2 = 0.995

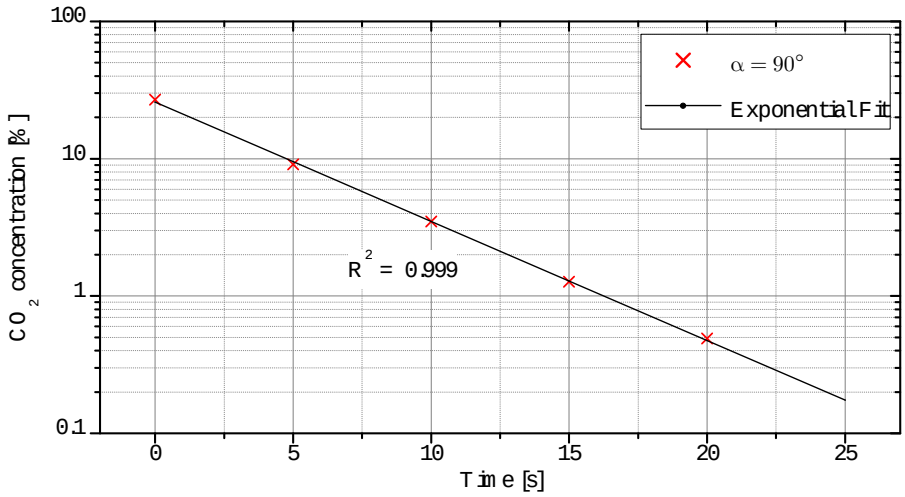
(e)


100
10
1
0.1
0
5
10
15
20
25
CO2 concentration [%]
Time [s]
α = 60°
ExponentialFit
R2 = 0.989

(f)


100
10
1
0.1
0
5
10
15
20
25
CO2 concentration [%]
Time [s]
α = 80°
ExponentialFit
R2 = 0.997

(g)



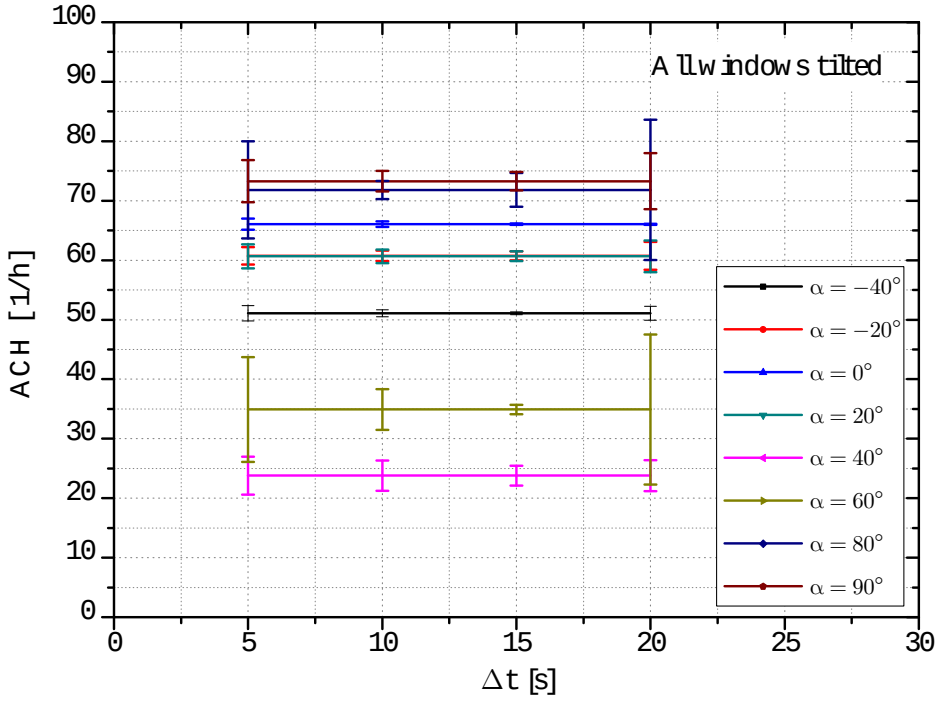
(h)

Figure 4.9: (a)-(h): CO_2 concentration as a function of time and exponential fits, exemplarily given for an inlet velocity of 3.6 m/s and different incidence angles α, all windows tilted.

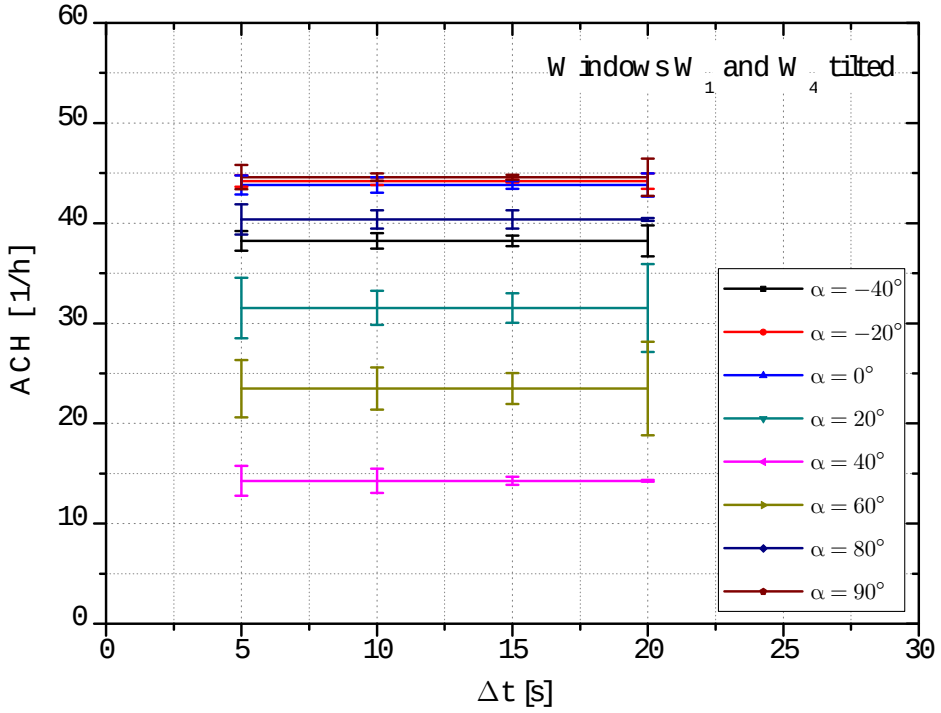
Fig. 4.9 exemplarily shows the temporal decrease in the concentration of carbon dioxide for an inlet velocity of 3.6 m/s and different incidence angles α for the case that all windows are tilted. A logarithmic plot of the ordinate shows very good agreement with exponential fits of the measured concentration values, which can be seen from the relevant coefficients of determination R^2 not less than 0.989.

Using the tracer gas method, the air exchange rate can be determined by the change of concentration of the used tracer gas between two points in time. For our measurements, these changes in concentration were measured for different lengths of time intervals, and then an average value for the air exchange rate was calculated. Time intervals were set to 5, 10, 15, and 20 seconds. The individual points in the diagram represent the ACH measured at time steps of different length. The average was calculated from all the individual values.

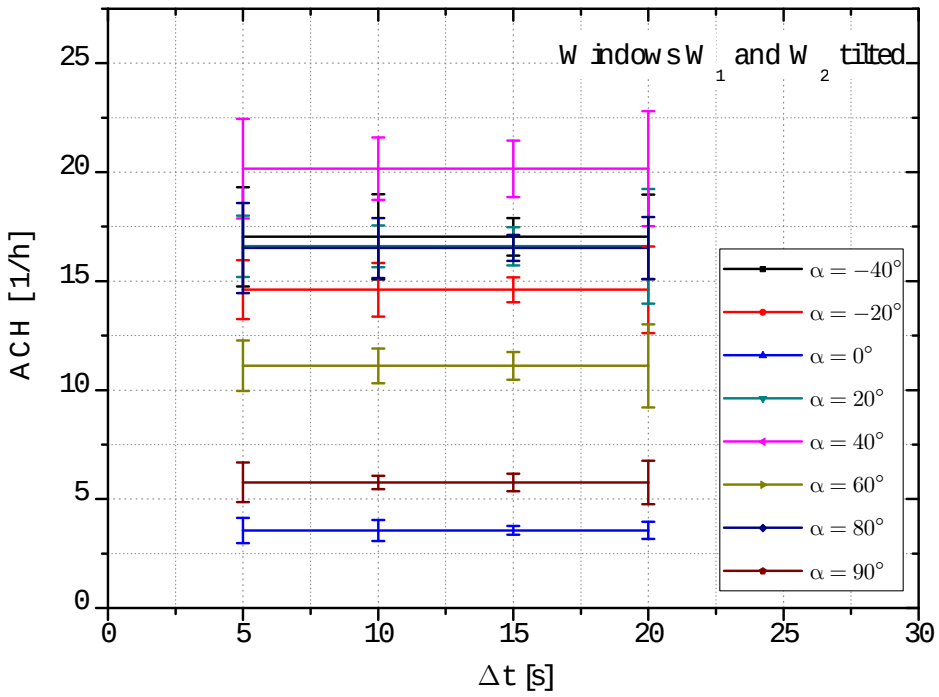
The dependence of the air exchange rate on the time interval can be seen in Fig. 4.10 for different tilting scenarios, exemplarily for the wind velocity of $U_\infty = 3.6$ m/s. The average concentration changes are represented by the horizontal lines. The data show that the ACH obtained are widely independent from the length of the measurement interval, but that the scatter of the individual data decreases with increasing length Δt. Overall the fluctuation level of the ACH is about 6.78 %.


All windows tilted
ACH [1/h]
Δt [s]
α = −40°
α = −20°
α = 0°
α = 20°
α = 40°
α = 60°
α = 80°
α = 90°

(a)


Windows W1 and W4 tilted
ACH [1/h]
Δt [s]
α = −40°
α = −20°
α = 0°
α = 20°
α = 40°
α = 60°
α = 80°
α = 90°

(b)



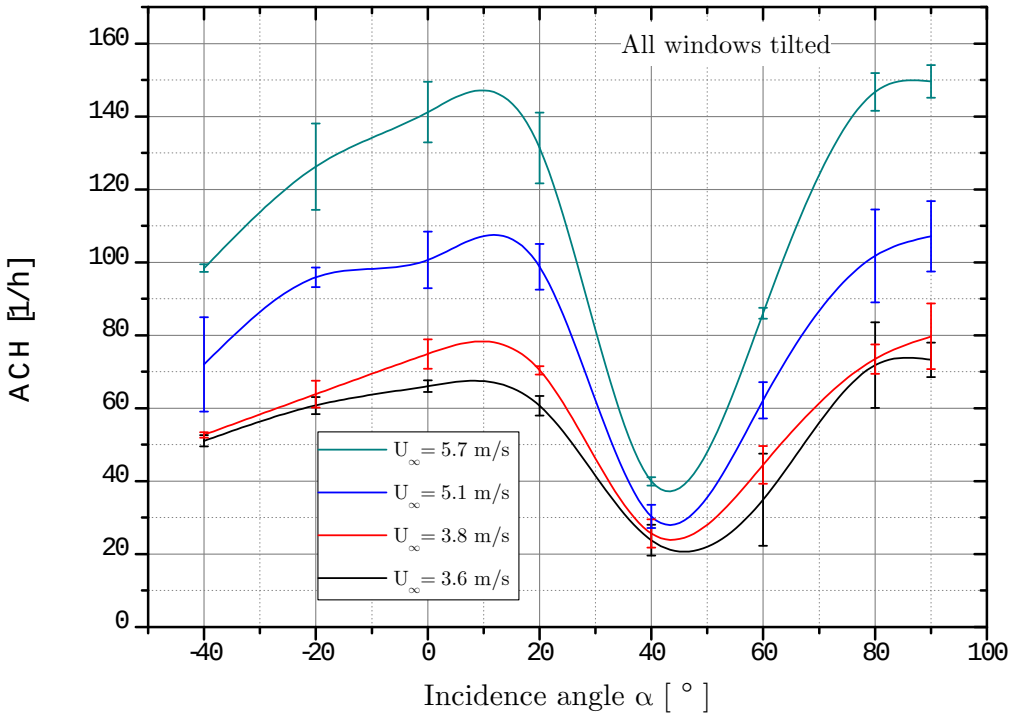
(c)

Figure 4.10: Up-scaled air exchange rate over time interval for (a) all windows, (b) windows W_1 and W_4, and (c) windows W_1 and W_2 tilted. $U_\infty = 3.6$ m/s.

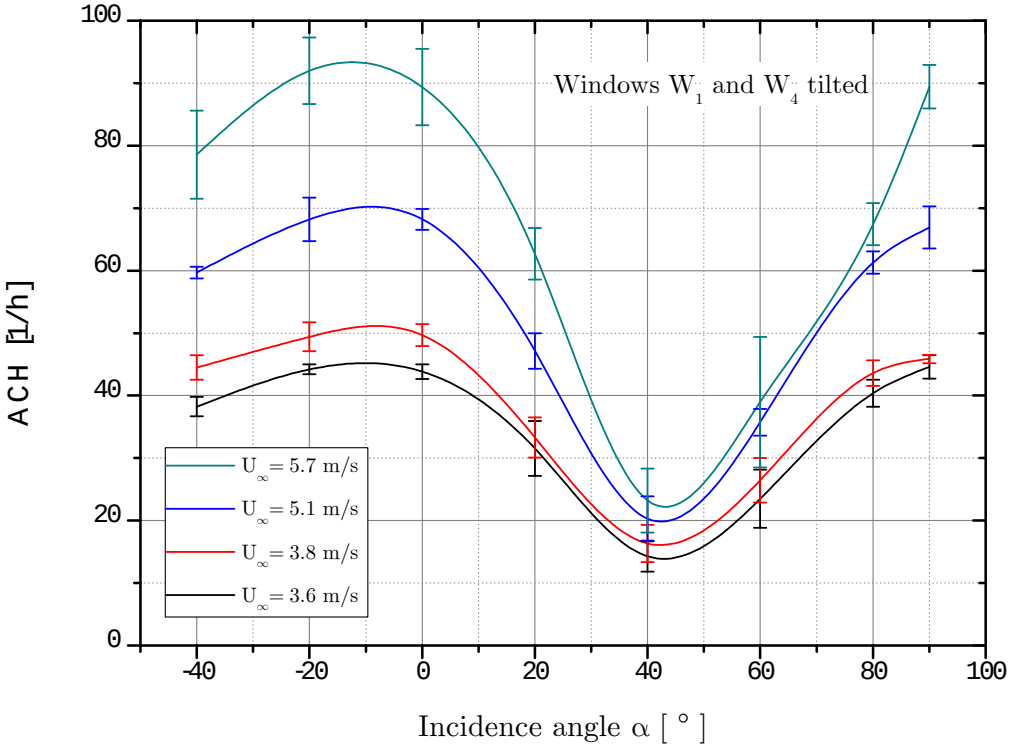
U_∞ $[m/s]$	Windows tilted	Incidence angle α							
		$-40°$	$-20°$	$0°$	$20°$	$40°$	$60°$	$80°$	$90°$
3.6	W_1 to W_4	51.07	60.74	66.05	60.66	23.79	34.90	71.81	73.28
3.6	W_1 and W_4	38.23	44.20	43.81	31.53	14.26	23.48	40.37	44.59
3.6	W_1 and W_2	17.03	14.60	3.56	16.59	20.16	11.11	16.52	5.76
3.8	W_1 to W_4	52.67	63.87	74.86	70.38	25.64	44.45	73.48	79.72
3.8	W_1 and W_4	44.49	49.38	49.68	33.29	16.35	26.44	43.57	45.85
3.8	W_1 and W_2	17.36	17.60	4.01	16.64	19.24	12.88	17.13	5.93
5.1	W_1 to W_4	72.02	95.91	100.65	98.80	30.33	62.19	101.76	107.16
5.1	W_1 and W_4	59.67	68.19	68.20	47.15	20.33	35.73	61.28	66.90
5.1	W_1 and W_2	24.57	23.93	5.48	22.64	27.17	13.74	21.11	7.89
5.7	W_1 to W_4	98.39	126.22	141.19	131.37	39.94	86.07	146.70	149.62
5.7	W_1 and W_4	78.57	91.97	89.37	62.68	23.21	38.95	67.41	89.43
5.7	W_1 and W_2	34.86	30.35	6.47	32.75	38.80	20.96	32.39	13.21

Table 4.3: Up-scaled air exchange rates from the tracer gas measurements for the single room model for tilted windows. ACH given in [1/h].

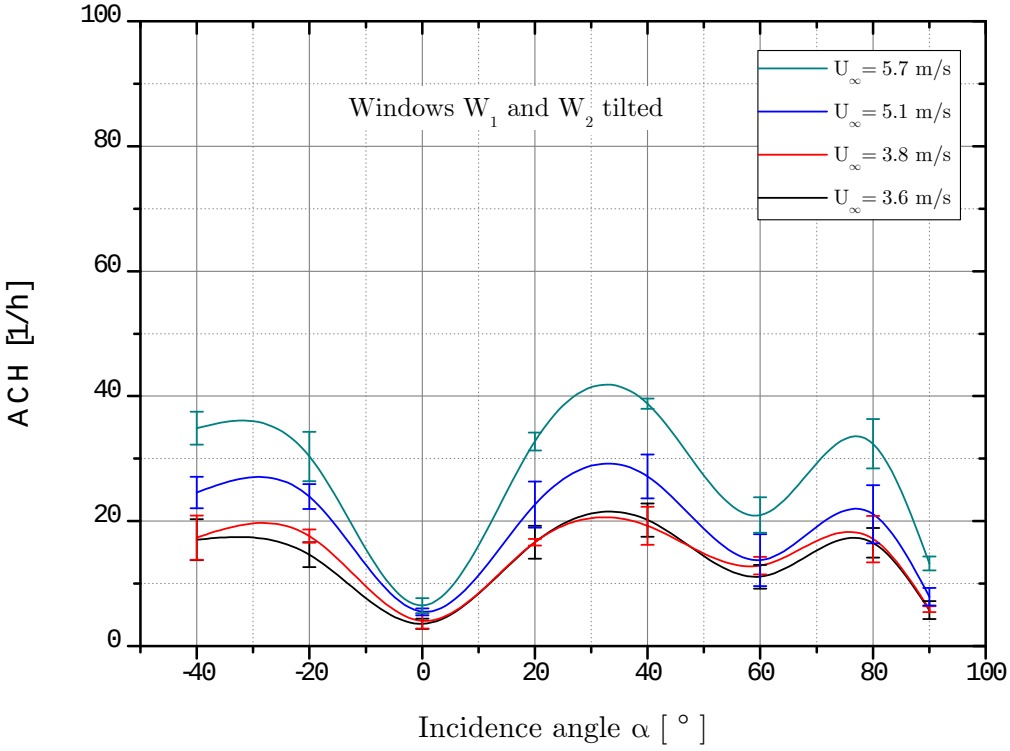
The results for the air exchange rates in the case of tilted windows derived from the tracer gas measurements on the single room model in 1:10 scale are presented in Table 4.3 and Fig. 4.11. For every incidence angle α and all tilting scenarios the numerical values of the air exchange rate increase with the wind velocity, as can be seen in Table 4.3 and Fig. 4.11. Comparing, for example, the results for the incidence angles of $\alpha = 0°$ and $\alpha = 90°$ against each other – these are geometrically almost identical cases – quite good agreement in the magnitude of the obtained ACH values can be seen. For those cases where all windows or the windows W_1 and W_4 are tilted, generally speaking, for the cases with cross ventilation, maximum air exchange rates result at incidence angles $\alpha = 0°$, $\alpha = 90°$ and $\alpha = -20°$, depending on the tilting scenario. The latter can be explained by the geometric position of the windows W_1 and W_4 (cf. Fig. 3.16(c)). Clearly lower numerical values of the air exchange rate result in case of single sided ventilation. Here, the highest values are found for an incidence angle of about $\alpha = 40°$.



(a)



(b)



(c)

Figure 4.11: Up-scaled air exchange rates according to Table 4.3: (a) for all windows, for windows (b) W_1 and W_4 and (c) W_1 and W_2 tilted.

4.4 Thermal influence on the air exchange rate

In everyday life natural ventilation, either by fully opening or tilting a window, is not influenced solely by the effect of wind, but also by a thermally induced potential of air exchange. To investigate the air exchange solely driven by temperature differences between indoor and environment, and additionally the superposition of thermal and wind influences, flexible heating foils (acting as a floor heating system) were installed in the single room model. As mentioned in Section 3.6, heat flux plates were mounted to the wall of the single room model to determine the heat transfer coefficients α_i, α_o and the over all heat transfer coefficient k using Eqs. (2.104) and (2.105). Results for the heat transfer coefficients are summarized in Table B1 in the Appendix B.

Table 4.4 gives the numerical values of the air exchange rate for solely thermally driven air exchange and an overview of the Gr, Pr, and Ra numbers, while Table 4.5 gives the numerical values of the air exchange rate for the different wind velocities and temperature differences. Gr was related to the inner height $H_{M,i} = 0.24$ m (in 1:10 scale) of the model room according to Eq. (2.24). Unsurprisingly, it can be seen in Table 4.4 that with increasing temperature difference an increase in the air exchange rate is accompanied. The value of $Ra = 10^9$ (cf. Eq. (2.114)) distinguishes between laminar and turbulent flow. The Rayleigh numbers in Table

Windows tilted	ΔT [K]	ACH [1/h]	Gr [–]	Pr [–]	Ra [–]
W_1 to W_4	2	2.53	3.84×10^6	0.7149	2.74×10^6
W_1 to W_4	4	6.44	7.68×10^6	0.7142	5.48×10^6
W_1 to W_4	6	8.29	1.15×10^7	0.7139	8.22×10^6
W_1 to W_4	8	9.96	1.54×10^7	0.7137	1.10×10^7
W_1 and W_4	2	2.13	3.84×10^6	0.7149	2.74×10^6
W_1 and W_4	4	5.45	7.68×10^6	0.7142	5.48×10^6
W_1 and W_4	6	7.34	1.15×10^7	0.7139	8.22×10^6
W_1 and W_4	8	8.65	1.54×10^7	0.7137	1.10×10^7
W_1 and W_2	2	2.35	3.84×10^6	0.7149	2.74×10^6
W_1 and W_2	4	5.53	7.68×10^6	0.7142	5.48×10^6
W_1 and W_2	6	5.99	1.15×10^7	0.7139	8.22×10^6
W_1 and W_2	8	7.96	1.54×10^7	0.7137	1.10×10^7

Table 4.4: Up-scaled ACH [1/h] from velocity measurements in the window gaps of the single room model for tilted windows and Gr, Pr, and Ra numbers, $U_\infty = 0$ m/s.

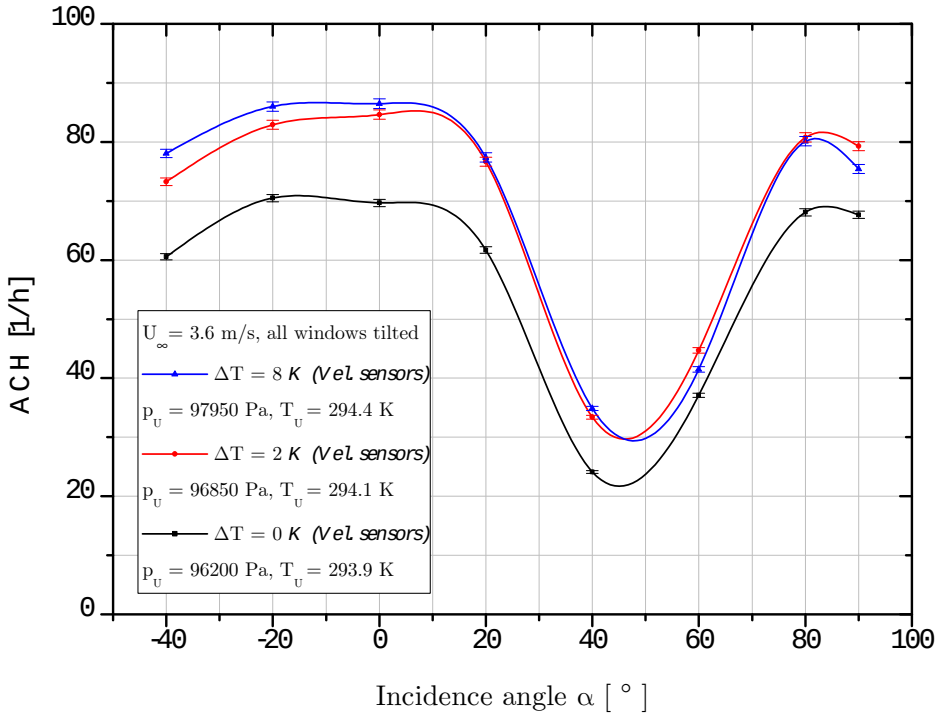
4.4 for the investigated cases of the present study leads to the conclusion that the flow is laminar.

The dependence of the solely thermally driven air exchange rate on the temperature difference is given by a square root function, which is analysed in Section 4.6.3.

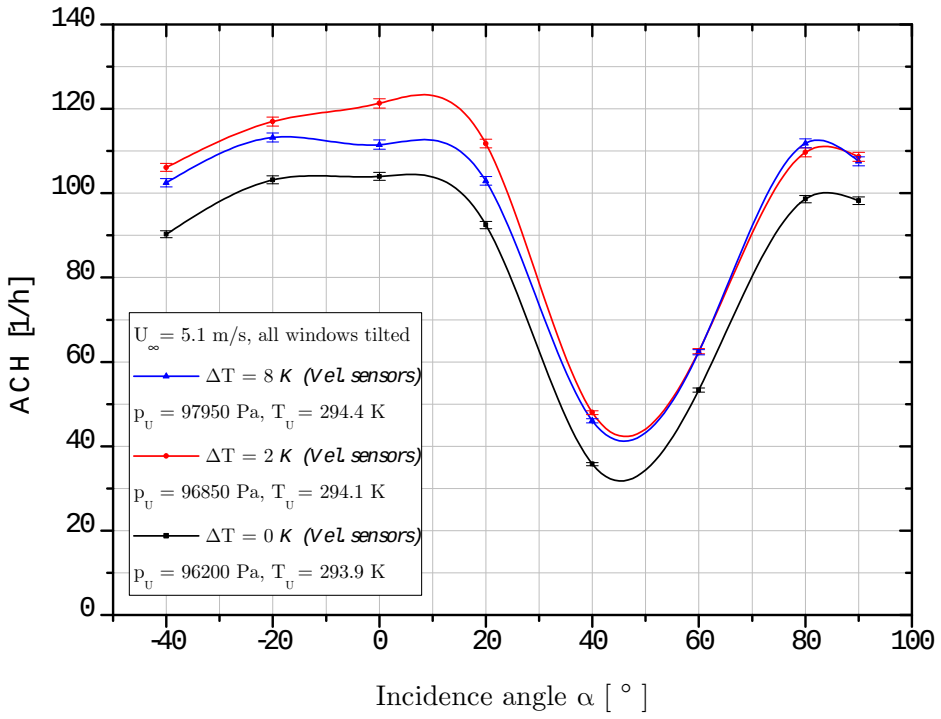
Analogous to the results in Section 4.2 obtained by purely wind-driven air exchange, the behaviour of increasing ACH values for increasing wind velocities also became apparent in case of the superposition of both wind and thermal effects. In case of cross ventilation under simultaneous action of wind and a temperature difference $\Delta T \neq 0$, higher ACH values are recognizable than for only wind driven air exchange, as can be seen in Figs. 4.12 and 4.13. There the ACH values for $\Delta T = 2$ K and $\Delta T = 8$ K do not make much of a difference. In case of single sided ventilation (cf. Fig. 4.14) there is virtually no difference between the ACH values, whether the temperature difference ΔT is zero or not. As will be shown by means of numerical simulations in Section 4.6, vortices in the window gaps occur, which obviously affect the measurement of the velocity sensors considerably. This effect predominates in cross ventilation. In single sided ventilation, i.e. for windows W_1 and W_2 tilted, it is virtually absent.

U_∞	Windows	ΔT	Incidence angle α							
$[m/s]$	tilted	$[K]$	$-40°$	$-20°$	$0°$	$20°$	$40°$	$60°$	$80°$	$90°$
3.6	W_1 to W_4	2	73.26	82.89	84.61	76.66	33.40	44.71	80.78	79.30
3.6	W_1 to W_4	8	78.10	85.99	86.49	77.38	34.87	41.49	80.12	75.45
3.6	W_1 and W_4	2	35.54	33.14	38.84	28.28	11.20	21.79	35.65	37.01
3.6	W_1 and W_4	8	33.91	35.07	37.52	27.75	10.39	20.30	34.22	35.44
3.6	W_1 and W_2	2	16.68	11.82	2.90	12.79	17.41	10.92	12.99	4.76
3.6	W_1 and W_2	8	14.54	11.06	2.27	10.27	15.74	10.10	14.04	3.03
5.1	W_1 to W_4	2	106.11	116.98	121.30	111.78	47.98	62.54	109.69	108.59
5.1	W_1 to W_4	8	102.50	113.22	111.53	102.92	46.05	62.33	111.83	107.56
5.1	W_1 and W_4	2	49.86	53.17	52.17	41.25	17.01	30.26	49.98	51.26
5.1	W_1 and W_4	8	48.31	52.68	52.99	38.22	11.84	28.58	49.69	50.67
5.1	W_1 and W_2	2	25.85	18.75	3.13	18.88	24.80	14.69	21.98	6.30
5.1	W_1 and W_2	8	21.17	15.05	1.69	13.31	19.66	13.68	19.33	4.53

Table 4.5: Up-scaled ACH [1/h] from velocity measurements for the single room model for tilted windows.

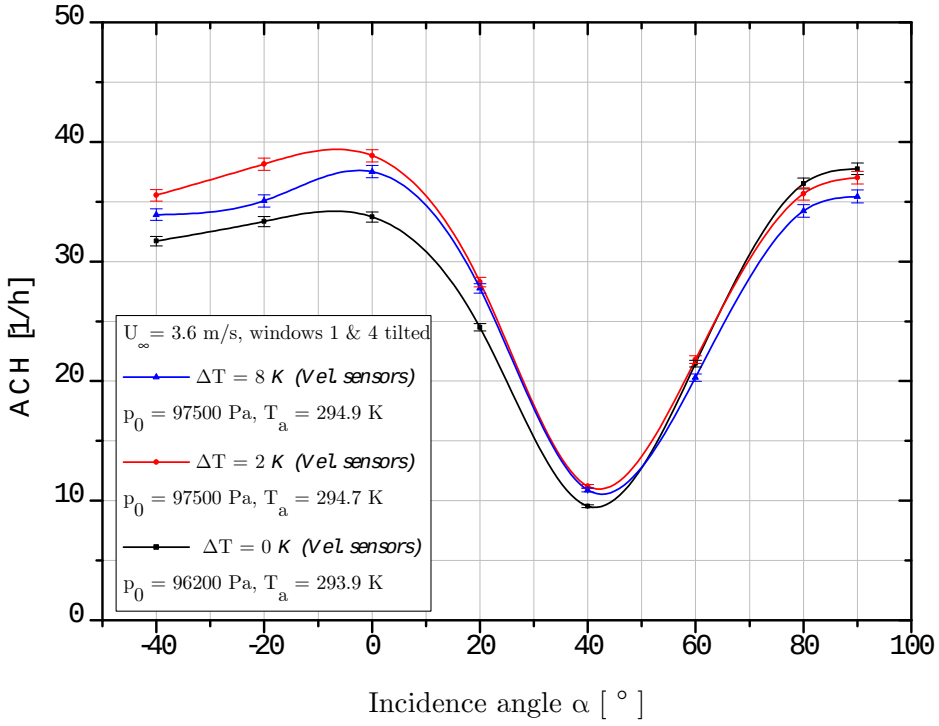


(a)

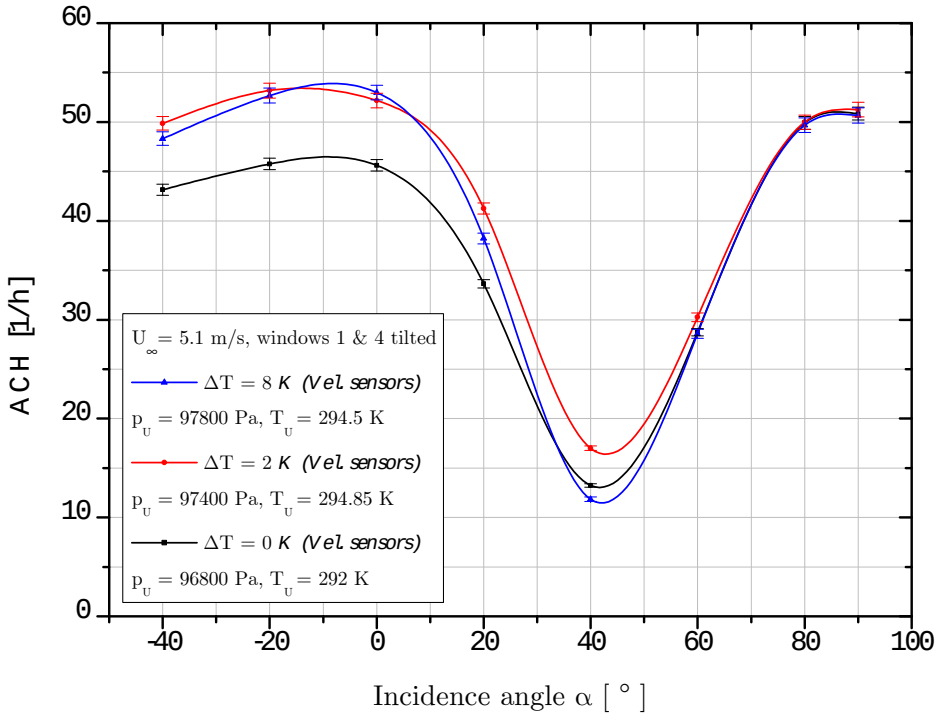


(b)

Figure 4.12: Up-scaled ACH in 1/h for the inlet velocities of (a) 3.6 m/s and (b) 5.1 m/s with different thermal influences, all windows tilted.

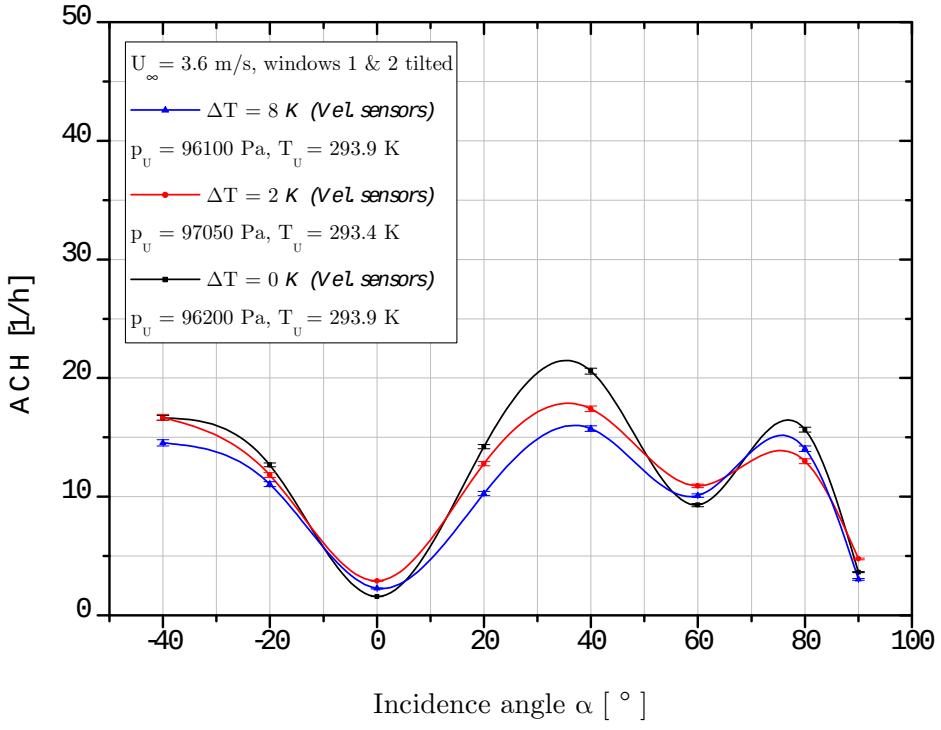


(a)

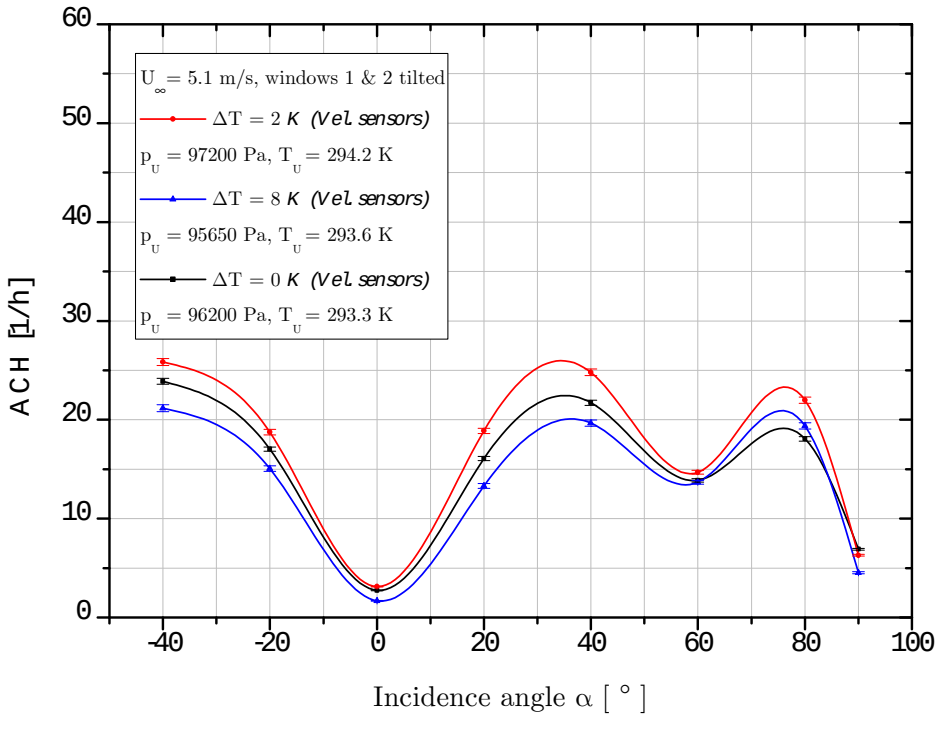


(b)

Figure 4.13: Up-scaled ACH in 1/h for the inlet velocities of (a) 3.6 m/s and (b) 5.1 m/s with different thermal influences, windows W_1 and W_4 tilted.



(a)



(b)

Figure 4.14: Up-scaled ACH in 1/h for the inlet velocities of (a) 3.6 m/s and (b) 5.1 m/s with different thermal influences, windows W_1 and W_2 tilted.

Comparing the thermally driven with the wind-driven air exchange rates, and both of them with the air exchange rates resulting from the superposition of both effects, it is found that these effects are not superimposed additively. These results find confirmation in the experimental investigations of Maas (1995). For cases where all windows (cf. Fig. 4.12) or the windows W_1 and W_4 (cf. Fig. 4.13) are tilted, a maximum value of the air exchange rate is found between $-20°$ and $0°$, which is due to the suction effect arising from the pressure difference between the windward and the side wall of the model room. A minimum air exchange rate arises for both cases at an incidence angle of $40°$, which is self-explanatory viewing the geometry and the arrangement of the windows in Fig. 3.16(c) and the velocity vectors from the numerical simulation in Fig. 4.24(e) for this case (cf. Section 4.5).

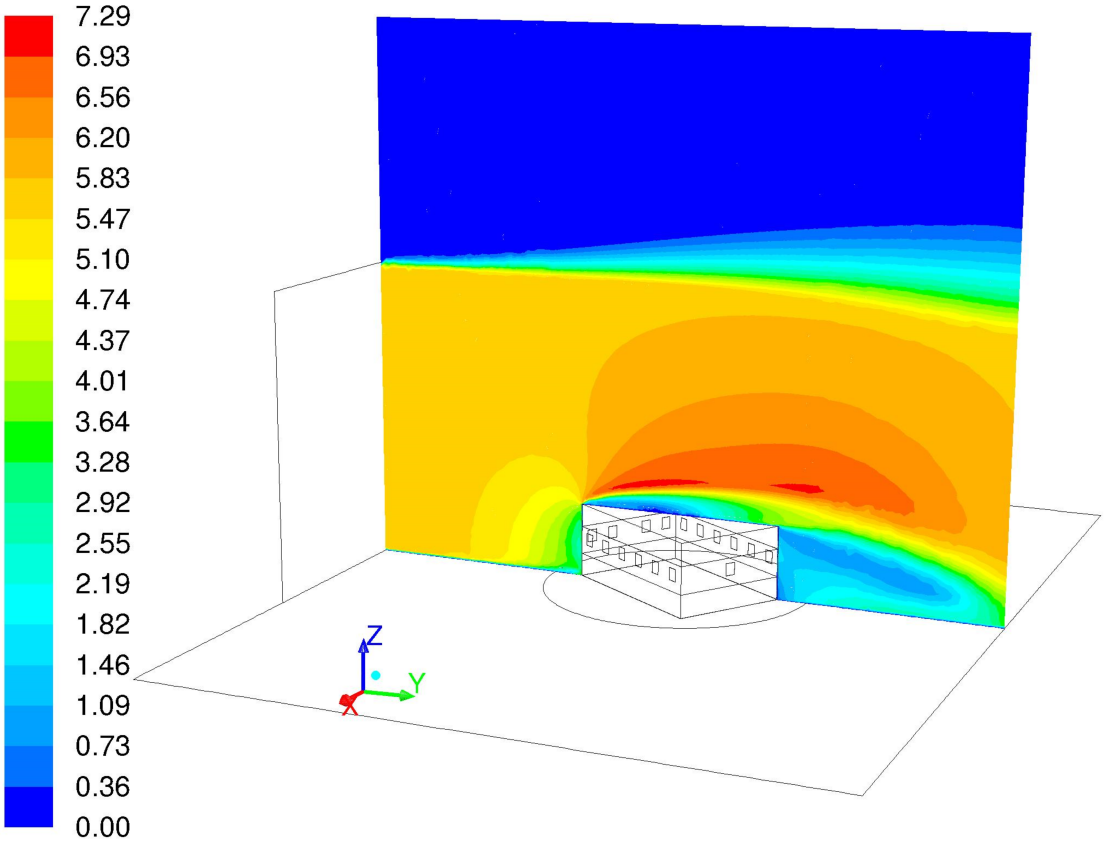


Figure 4.15: Velocity magnitude in m/s in the mid cut plane for the inlet velocity 5.7 m/s and the incidence angle 33.3°. Reprinted from Teppner et al. (2014a), with permission from Elsevier.

4.5 Air exchange rates from numerical simulations

4.5.1 Simulations on the storey model

As mentioned in Section 3.8, numerical simulations were done by the Austrian Institute of Technology. In the following, results of these simulations, used for comparison with measured data, are presented. More detailed information on the numerical model can be found in Teppner et al. (2014a), since that was not part of this work. As shown in Fig. 3.3(a), the storey model included dummy storeys above and below, which were also parts of the numerical representation by the Austrian Institute of Technology.

Figures 4.15, 4.16 and 4.17 give an overview of the flow situation, exemplarily for 5.7 m/s inlet velocity and the incidence angle of 33.3°. Figures 4.15 and 4.16 clearly show the shear layer of the free stream from the inlet cross section, the stagnation of the velocity in front of the storey model, the acceleration of the flow over and around the model, and the large wake region.

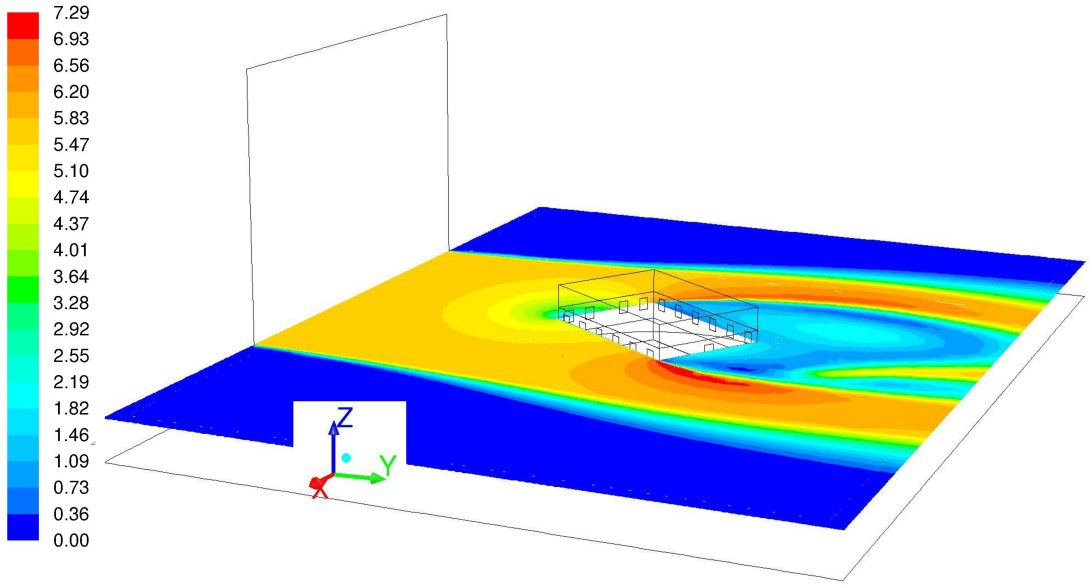


Figure 4.16: Velocity magnitude in m/s in a $z-$cut plane at the height 4.875 m (in real dimensions) of the window centres for the inlet velocity 5.7 m/s and the incidence angle 33.3°. Reprinted from Teppner et al. (2014a), with permission from Elsevier.

Additionally, the horse shoe vortex in front of and around the storey model and the overall flow situation are indicated in Fig. 4.17 by a streamline plot. A sketch of the typical vortex structures around a wall mounted cuboid for 0° incidence angle can be found in Fig. 2.17 for comparison. Because of the sharp edge at the front of the configuration for the incidence angle of 33.3°, the horse shoe vortex is not that strongly developed at the front side.

The foregoing numerical results (Figs. 4.15 – 4.17) provide a good overview of the overall flow behaviour which is not possible to derive from the experimental data. Detailed comparisons are given later in Section 4.6.

For an incidence angle of 0°, Fig. 4.18 clearly depicts the horse shoe vortex in front of and around the room model, as introduced in Fig. 2.17. Figure 4.19 depicts the ACH values derived from the simulations, for rooms with tilted windows in the leeward region, for different incidence angles, and for the situation with doors D_1, D_2 open, W_7 closed. This configuration leads to equal ACH values in the rooms R_{3a} and R_{3b} when cross flow through both rooms occurs (Fig. 4.19(b), (c)). In case of

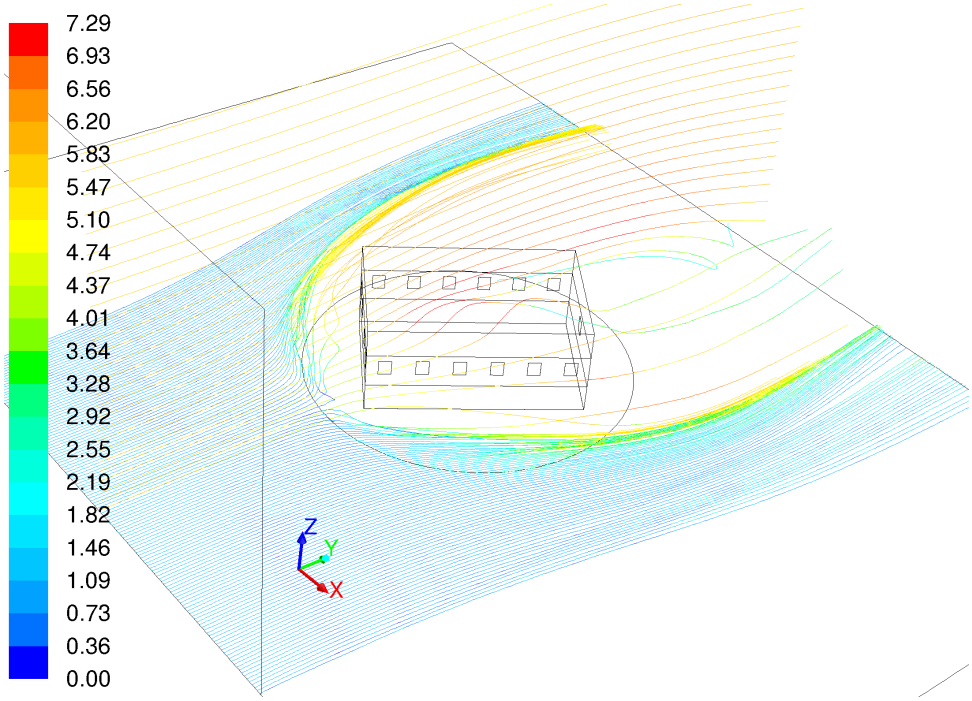


Figure 4.17: Streamlines for the configuration of Fig. 4.15 showing the horse shoe vortex in front of and around the model. The colour scale shows the velocity magnitude in m/s. Reprinted from Teppner et al. (2014a), with permission from Elsevier.

incidence angles 0° and 180° , the air in R_{3a} and R_{3b} is mainly exchanged via the tilted windows in the sidewalls of each room. Hardly any air exchange via the two open doors was detected in these cases. This evidently results from the symmetric flow situations for these incidence angles.

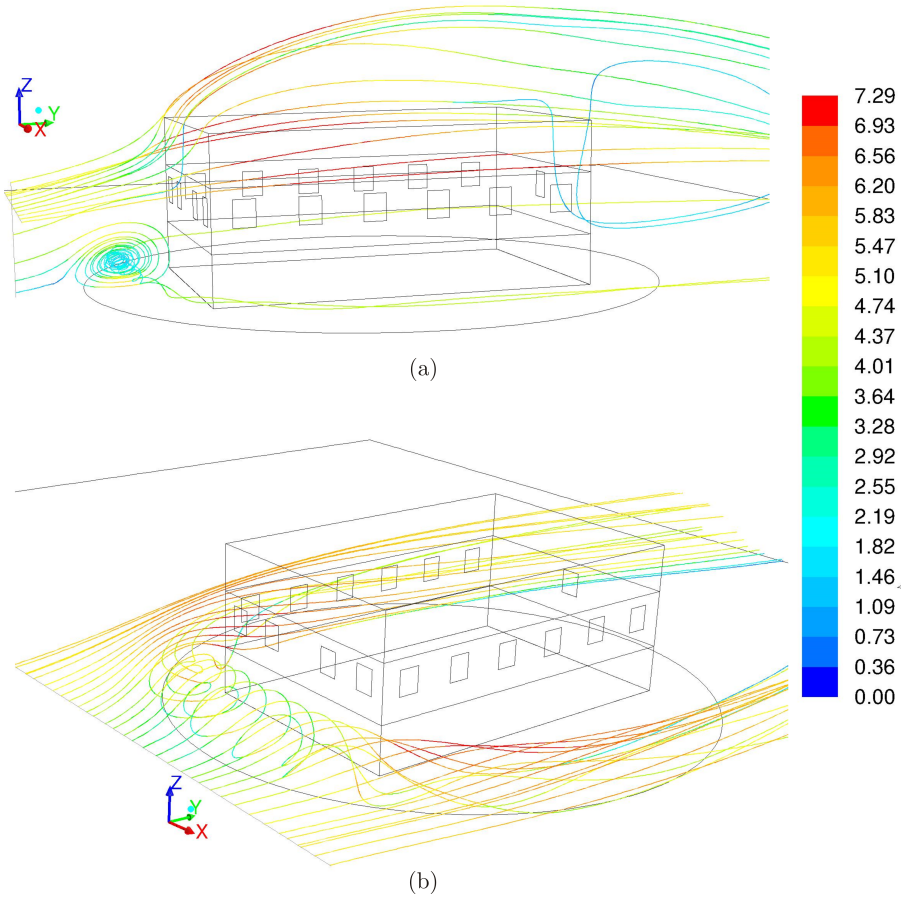


Figure 4.18: (a) and (b) Streamlines for an inlet velocity of 5.7 m/s and an incidence angle of 0° showing the horse shoe vortex in front of and around the model. The colour scale shows the velocity magnitude in m/s. According to Teppner et al. (2014b).

As introduced in Section 2.3.4, the volume flow rate through an opening is given by the orifice equation (2.90) containing the discharge coefficient C_D. Using values from the pressure distributions in Fig. 4.19 we now compare ACH results for tilted windows with values from Eq. (2.92), using the loss coefficient ζ obtained by Eq. (2.91). The loss coefficient was determined to $\zeta = 28.9$ after Idelchik (1994) for an opening blocked by a movable flap (cf. Fig. 4.20).

For our case of $l_{fl}/b_{fl} = 0.831$ and $\alpha = 4.8°$ the loss coefficient ζ was calculated

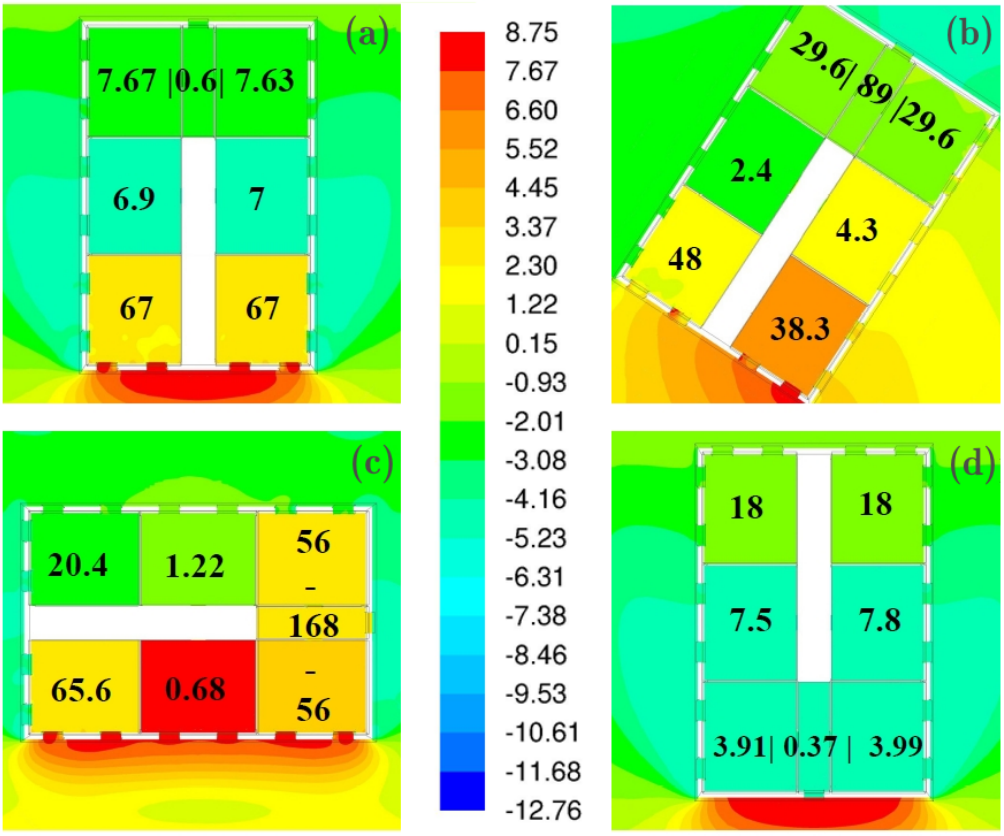


Figure 4.19: Pressure distributions in Pa in the cut plane through the window centres, and up-scaled roomwise ACH for the incidence angles (a) 0°, (b) 33.3°, (c) 90°, (d) 180°. Inlet velocity 3.6 m/s, doors D_1, D_2 open, windows tilted but W_7 closed. Reprinted from Teppner et al. (2014a), with permission from Elsevier.

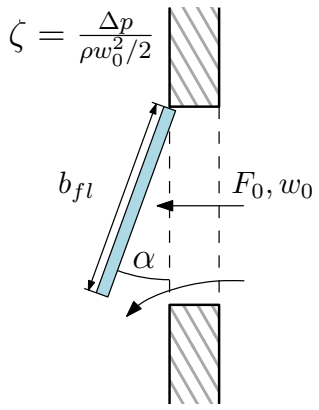


Figure 4.20: Sketch of a single top-hinged flap. l_{fl} is the flap length perpendicular to the drawing plane. Referring to Idelchik (1994).

by extrapolation along the values of α and the values of l_{fl}/b_{fl} given in Table 4.6, respectively.

Hence, with $A = 1.82$ m^2 and $A_G = 0.377$ m^2 for the actual configuration, the discharge coefficient was calculated by Eq. (2.91). The result $C_D = 0.67$ is in accordance to Heiselberg et al. (2001), who showed that $C_D > 0.6$ for small opening areas, and to Iqbal et al. (2012), who found an increase of the discharge coefficient from 0.6 up to 0.71 for a decreasing tilt angle of the window in an angular range between 15° and 40°.

Eq. (2.91) is exemplarily applied to room R_1 for 0° incidence angle, 3.6 m/s inlet velocity and tilted windows. The minimal inlet cross section of the two tilted windows is 0.754 m^2. From the pressure differences across the openings depicted in Fig. 4.19(a) with $\Delta p = 6.6$ Pa and $C_D = 0.67$, Eq. (2.90) yields an air flow rate of 1.671 m^3/s. With the room volume of 93.75 m^3, Eq. (2.92) yields the value ACH = 64.2 h^{-1}, which differs by around 4.2% from the ACH given in Fig. 4.19 (deviation given relative to the data from the numerical simulations).

Evaluating Eq. (2.93) with $C_v = 0.5$ in our case for room R_1, incidence angle of 0° , fully open windows and 3.6 m/s wind velocity, we obtain an air flow rate of 6.55 m^3/s for 2 windows with cross sections of 1.48 m × 1.23 m each. With a room volume of 93.75 m^3 this leads to ACH = 251 h^{-1} which agrees with the measured result ACH = 246.36 for room R_1 within a deviation of 1.9% relative to the value from the experiment. These comparisons show that the numerical simulations represent the ACH well and provide usefule data for building layout purposes.

l_{fl}/b_{fl} [−]	Incidence angle α						
	15°	20°	25°	30°	45°	60°	90°
1.0	11	6.3	4.5	4.0	3.0	2.5	2.0
2.0	17	12	8.5	6.9	4.0	3.1	2.5
∞	30	16	11	8.6	4.7	3.3	2.5

Table 4.6: Values of the loss coefficient ζ for a top-hinged flap. b_{fl} and α given as in Fig. 4.20 and l_{fl} is the flap length. Referring to Idelchik (1994).

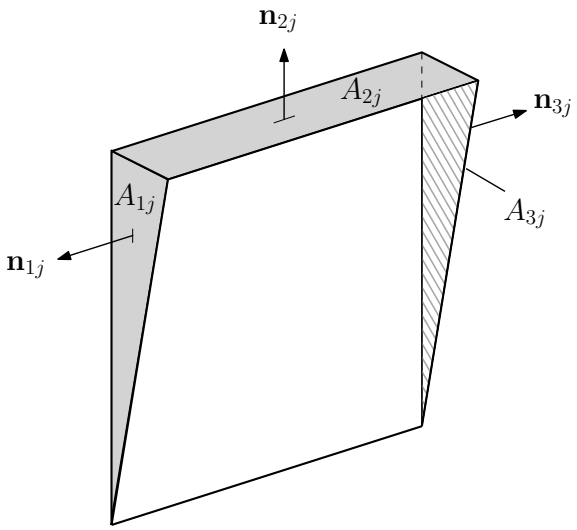


Figure 4.21: Sketch of the window gaps with normal vectors $\mathbf{n}_{ij}$ on the cross sectional areas A_{ij}.

4.5.2 Simulations on the single room model

For the cases for which the air exchange rates were determined using velocity measurements in the window gaps (cf. Table 4.2), numerical simulations (cf. Section 3.8) were performed by the author. The results are listed in Table 4.7, which shows the same trends as already observed in the tracer gas measurements and the velocity measurements: the numerical values of the air exchange rate increase with the wind velocity no matter what incidence angle or tilting scenario. The comparison of the ACH values for the geometrically almost identical cases $\alpha = 0°$ and $\alpha = 90°$ show a good agreement in the magnitude of the values. For the cases governed by cross ventilation, i.e. for all windows tilted or windows W_1 and W_4 tilted, a maximum air exchange rate results at incidence angles of $\alpha = 0°$ or $\alpha = 90°$ depending on the tilting scenario. In case of single sided ventilation, i.e. for windows W_1 and W_2 tilted, maximum ACH values are found for incidence angles $\alpha = -40°$ and $\alpha = 80°$.

The volumetric flow rate $\dot{V}$ was automatically calculated in ANSYS Fluent as the sum of the inner products of the averaged flow velocities and the cross sectional areas A_{ij} of the different window gaps, where i denotes the number of the window and j the number of the gap (cf. Fig. 4.21).

U_∞	Windows	Incidence angle α							
$[m/s]$	tilted	$-40°$	$-20°$	$0°$	$20°$	$40°$	$60°$	$80°$	$90°$
3.6	W_1 to W_4	59.30	64.92	61.21	49.26	25.27	37.02	69.36	71.10
3.6	W_1 and W_4	32.18	36.05	35.20	28.47	13.66	20.91	31.60	32.15
3.6	W_1 and W_2	20.23	17.03	2.85	18.12	22.78	15.29	20.95	7.19
5.1	W_1 to W_4	81.85	92.7	88.02	68.29	34.05	52.64	81.13	101.72
5.1	W_1 and W_4	45.02	50.31	51.11	40.41	19.70	28.35	47.67	49.5
5.1	W_1 and W_2	31.14	24.56	4.63	29.67	19.37	19.24	31.51	5.38

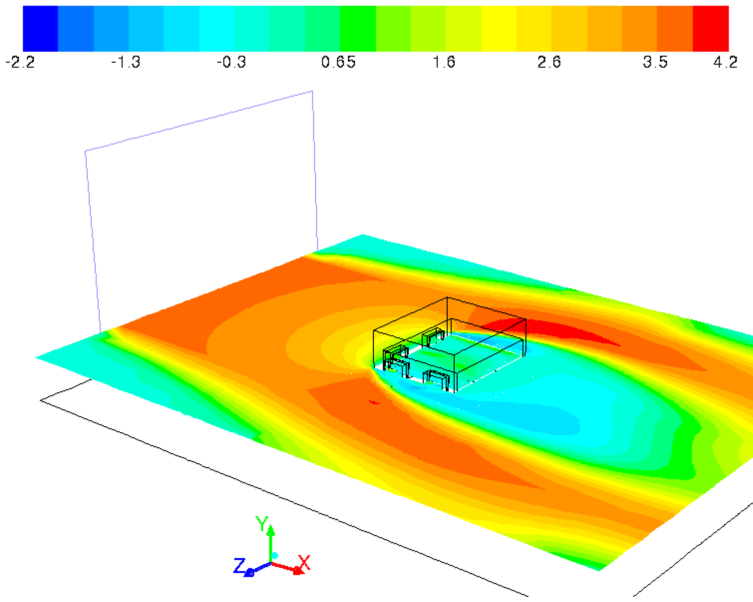
Table 4.7: Up-scaled air exchange rates in [1/h] for the single room model obtained by numerical simulations.

α	All windows tilted			W_1 and W_4 tilted			W_1 and W_2 tilted		
$[\,^\circ\,]$	$\dot{V}_{in}$	$\dot{V}_{out}$	$\Delta[\%]$	$\dot{V}_{in}$	$\dot{V}_{out}$	$\Delta[\%]$	$\dot{V}_{in}$	$\dot{V}_{out}$	$\Delta[\%]$
-40	17.54	19.28	$+9.92$	9.94	9.75	-1.91	5.56	4.7	-15.46
-20	19.01	19.73	$+3.78$	10.65	11.07	$+3.94$	3.89	3.85	-1.02
0	20.65	24.09	$+16.65$	10.38	10.39	$+0.09$	0.62	0.71	$+12.90$
20	15.51	19.02	$+22.6$	8.25	9.38	$+13.68$	3.61	4.1	13.57
40	8.34	10.17	$+21.0$	3.00	3.65	$+21.6$	4.79	5.72	$+19.41$
60	11.7	11.9	$+1.7$	6.73	6	-10.84	2.93	2.95	$+0.68$
80	21.05	20.74	-1.47	9.35	9.67	$+3.42$	4.85	4.97	2.47
90	22.14	20.68	-6.59	10.01	9.65	-3.59	2.42	2.03	-16.11

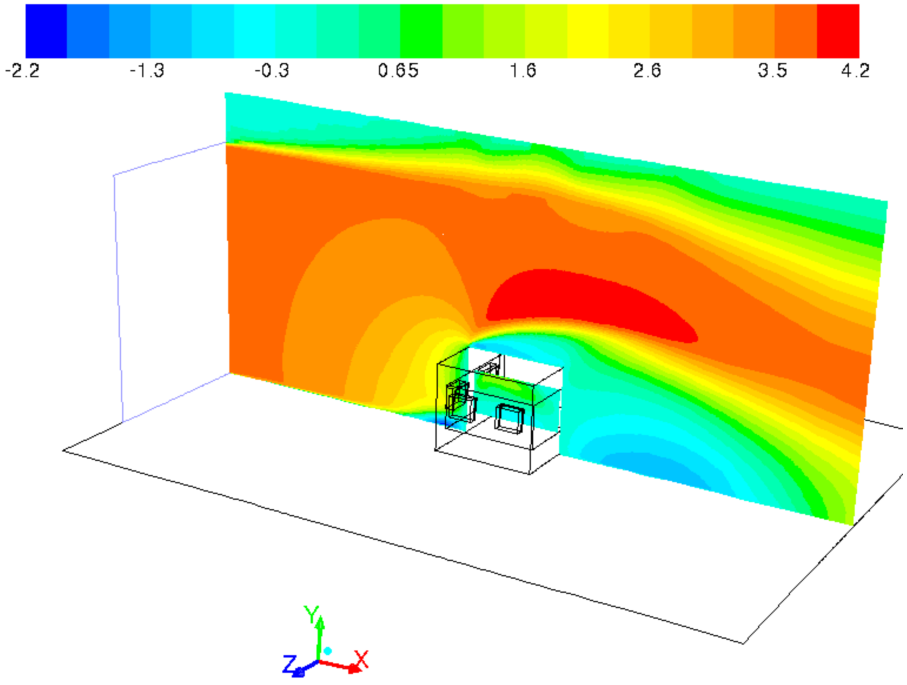
Table 4.8: Volumetric flow rates (in and out) in 10^{-3} m^3/s for $U_\infty = 3.6$ m/s from the numerical simulations of the single room model. Deviations are given relative to the volumetric inflow rate.

Table 4.8 exemplarily shows the inflow and outflow volumetric flow rates for the different tilting scenarios and incidence angles. For continuity reasons, the flow rates for the inflow and outflow should be the same for the appropriate cases, which is reflected satisfactorily by Table 4.8.

A comparison between Tables 4.2 and 4.7 shows that the air exchange rates obtained by the numerical simulations show the behaviour to increase with the wind velocity (exemplarily for an incidence angle of $\alpha = 0°$ or $\alpha = 90°$) for all tilting scenarios found in the experiment.



(a)



(b)

Figure 4.22: Velocity magnitude in m/s in the (a) mid cut plane, (b) $y-$cut plane through the window centres. Both for an incidence angle of 0°, all windows tilted and 3.6 m/s inlet velocity.

Exemplarily, the velocity magnitude for the inlet velocity of 3.6 m/s and an incidence angle of 0° is shown in the mid cut plane in Fig. 4.22(a), and in a $y-$cut plane at the height of the window centres in Fig. 4.22(b). In front of the vertically oriented upstream wall of the single room model, the flow is slowed down and kinetic energy is converted into static pressure, i.e. the velocity magnitude gets zero, as can be seen in Fig. 4.22(a). In other words, the flow approaching the single model room is decelerated by the pressure field generated by the model until it separates near the wall (cf. also Fig. 4.18 for the storey model).

The region of the side walls and roof of the model room is influenced by the flow separation at the leading edge and the effect of the horseshoe vortex along the sides, which is redirected downstream immediately behind the room model.

The processes in the backflow region and in the near-wake region of the single room model are influenced by the separation at the leading edge and the interaction between the horseshoe vortex and the rear edges of the room model (cf. Section 2.3.1 and Cook (1985)).

Both Figs. 4.22(a) and (b) clearly show the acceleration of the flow over and around the single room model.

The influence of the horseshoe vortex, introduced in Section 2.3.2, in front of and around the single room model on the pressure distribution on the building surface can be seen in Fig. 4.23 for an inlet velocity of 3.6 m/s and an incidence angle of 0°. As already explained in Section 2.3.1 according to Cook (1985) and depicted in Fig. 2.20(b), particularly at the height of the drawn black line in front of the windward wall in Fig. 4.23 the impact of the corner vortex, leading to a reduction of pressure especially from the middle of the windward wall along the black line in both directions, can be observed. Without the development of this corner vortex, which then forms itself to the horseshoe vortex around the room model, a homogeneous pressure distribution would prevail on the front wall. As mentioned previously in this work, the pressure maximum is between $0.7H$ and $0.8H$ of the single model room, which can clearly be seen in Fig. 4.23, too.

Figures 4.24(a)-(h) exemplarily show plots of the velocity vectors in a horizontal cross section of the room at a height of 0.284 m (in 1:10 scale) halfway up the windows. The flow fields were obtained by steady-state simulations for an inlet velocity of

3.6 m/s and different incidence angles for all windows tilted. The incidence angle is from right to left. Incidence angle and notation of the windows are as given in Fig. 3.16(c).

For the incidence angles from $\alpha = -20°$ to $\alpha = 20°$ and for $\alpha = 80°$ and $\alpha = 90°$ (cf. Fig. 4.24) a dominant jet flow is seen, much more developed for the incidence angles 0° and 90°, which, due to the geometry of the building and this special configuration, is not a surprise. Beside this jet region, slower moving zones exhibiting jet-driven circulation are located. For the incidence angles of $-40°$, 40°, and 60°, the flow no longer follows such a dominant jet as in the cases mentioned above, but the flow structure is clearly separated into several vortices, as can be seen in Figs. 4.24(a), (e), and (f).

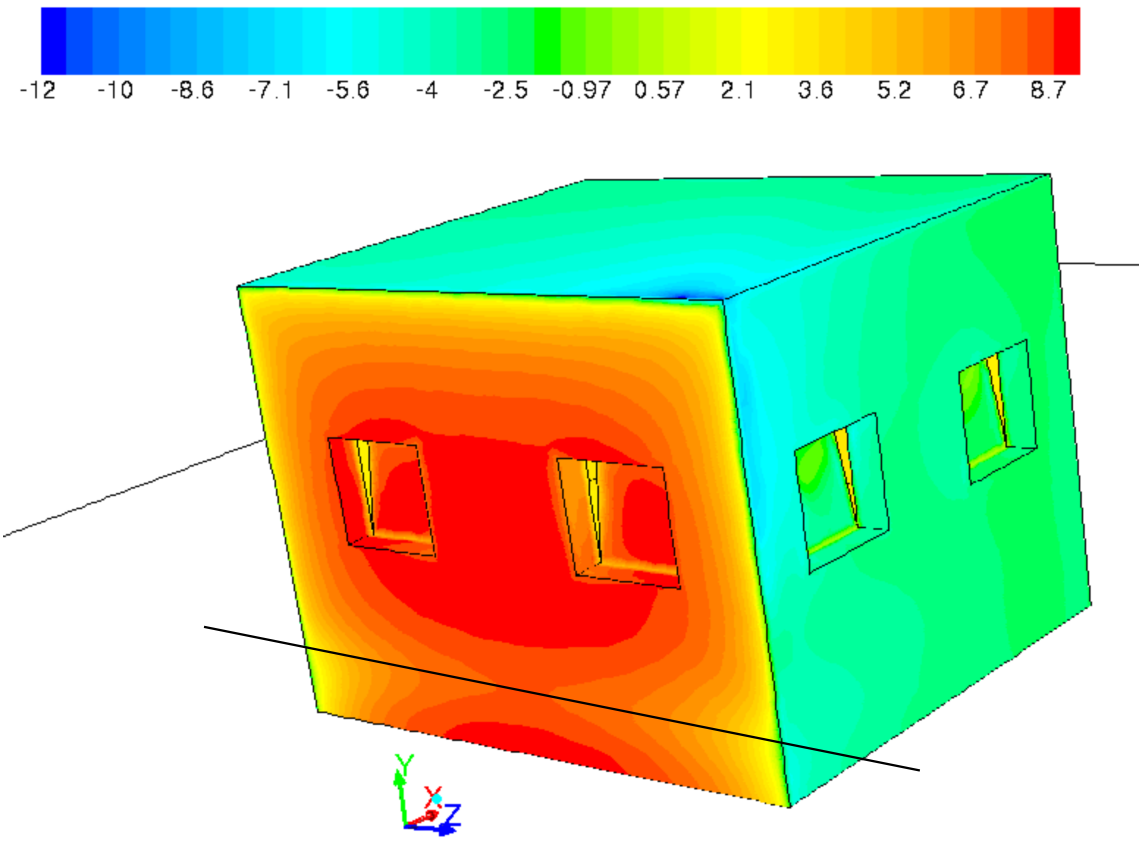
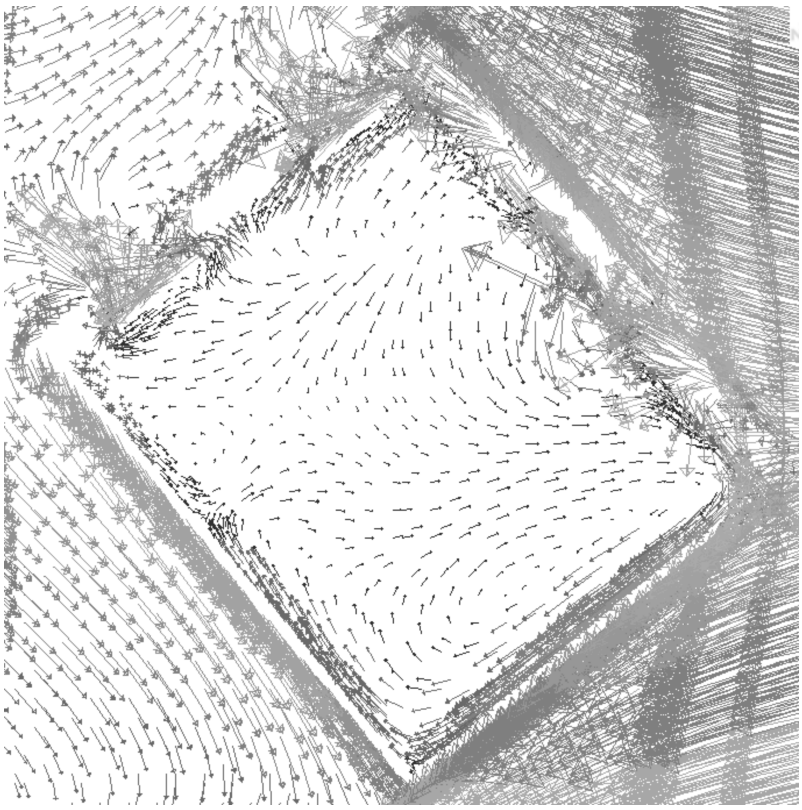
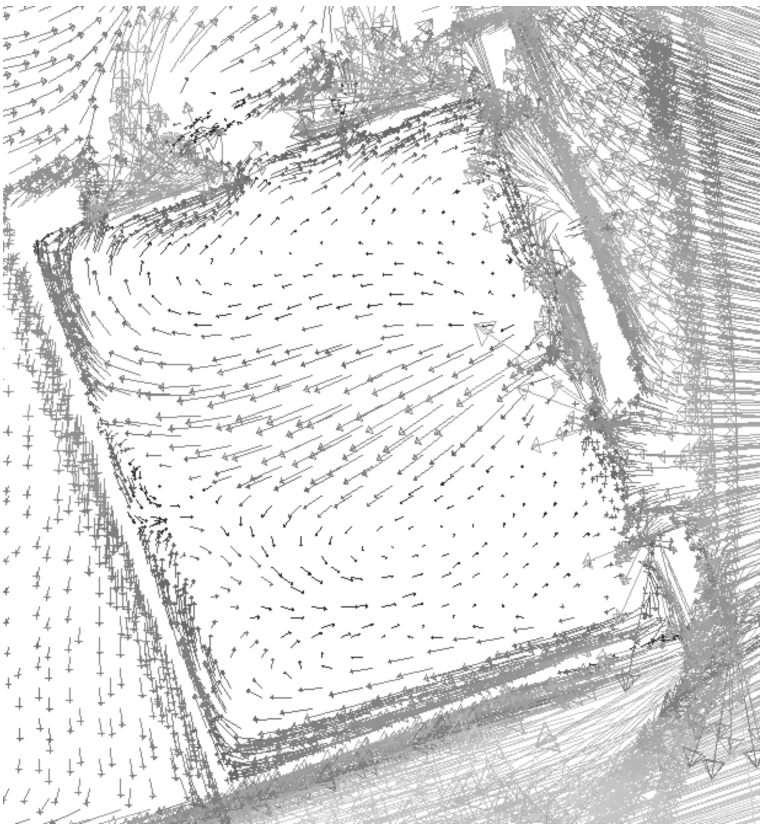


Figure 4.23: Pressure distribution in Pa for 3.6 m/s inlet velocity, incidence angle of 0°, all windows tilted.

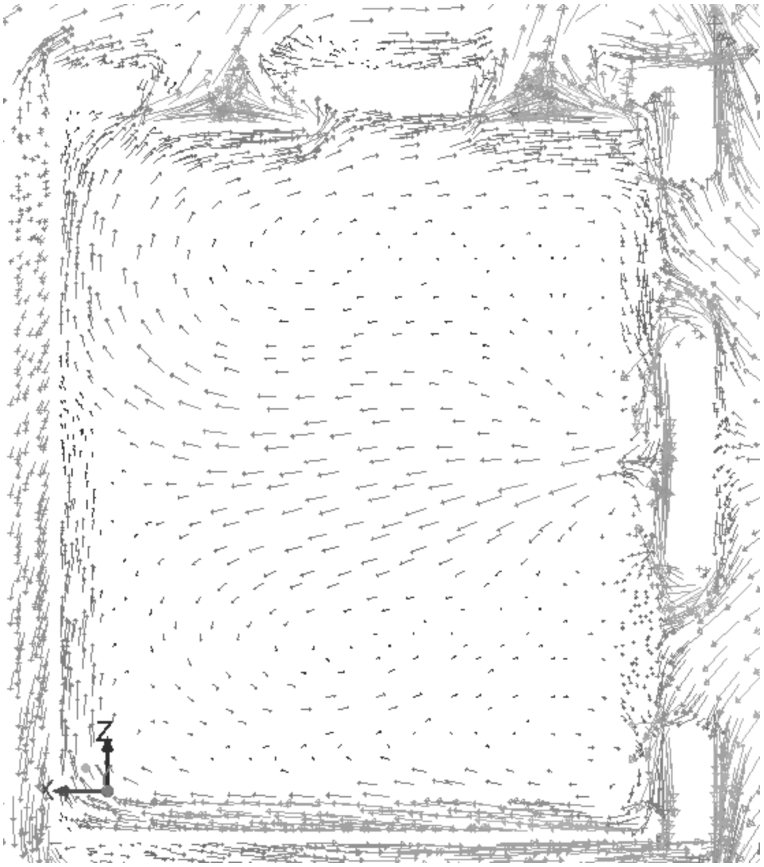
Particularly for the incidence angle of 60° (cf. Fig. 4.24(f)), the flow entering window W_4 is skewed, and a fast moving jet is directed along the inner walls in a large recirculation region. The recirculation region formed beside the jet occurs when the jet impinges on an opening (in this case a gap of a tilted window), which is narrower than the jet itself. One part of the jet constricts and exits through the gap of the tilted window. The other part splits on both sides and is directed along the side walls, where it moves against the jet direction until it is decelerated by the action of the main flow. Thus, recirculation regions, usually obstructing the air exchange, develop within the single room model. The prevailing vortices are also detected by the sensors for the velocity measurements mounted in the gaps of the tilted windows, so that these may not yield data indicating air exchange, as already mentioned above.



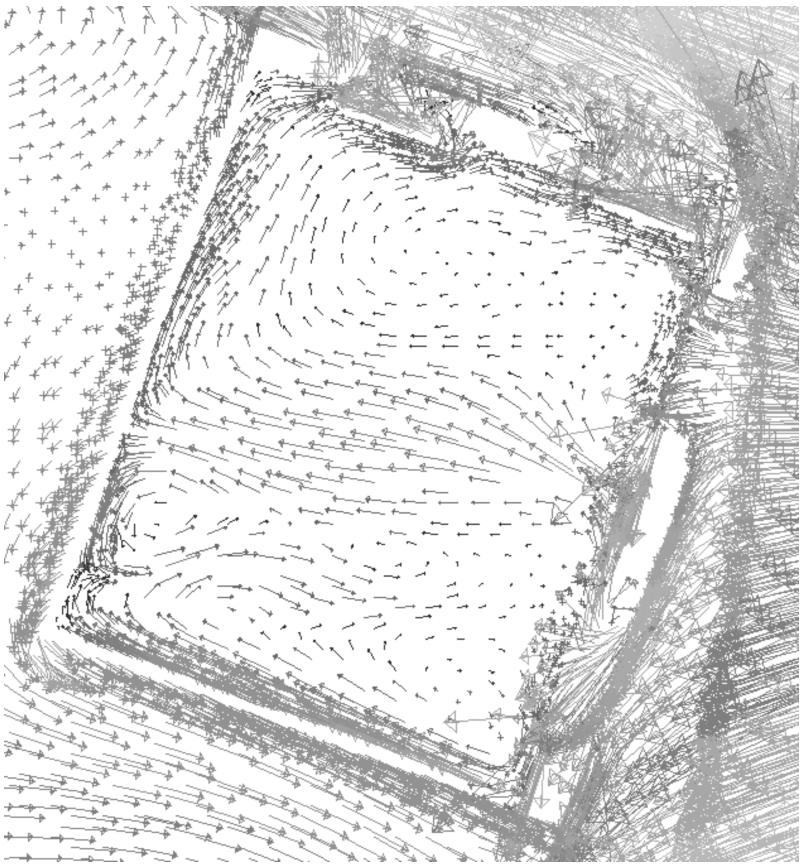
(a) $\alpha = -40°$.



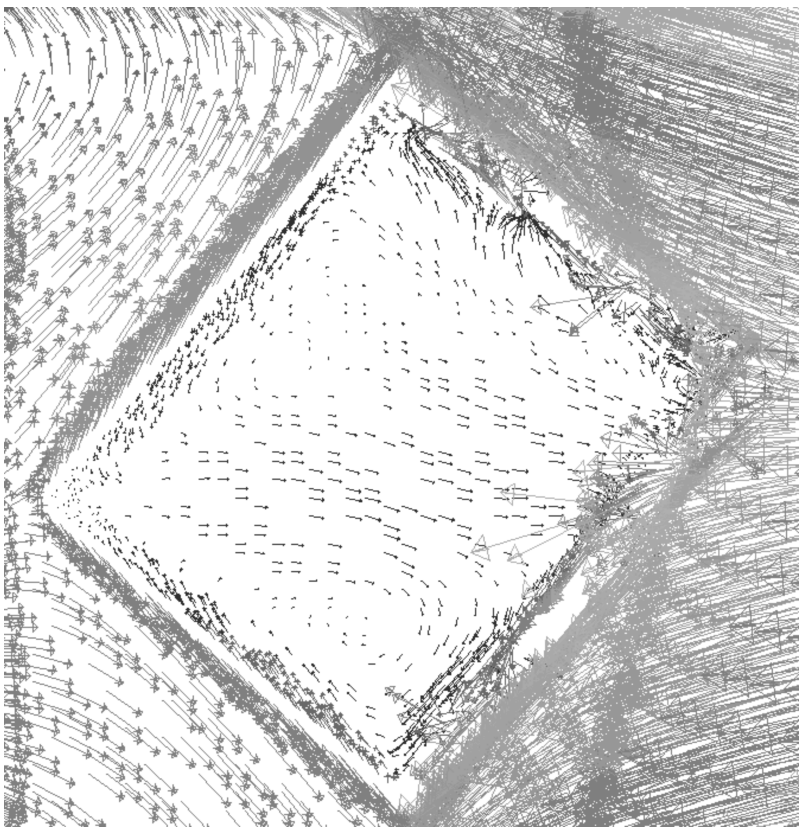
(b) $\alpha = -20°$.



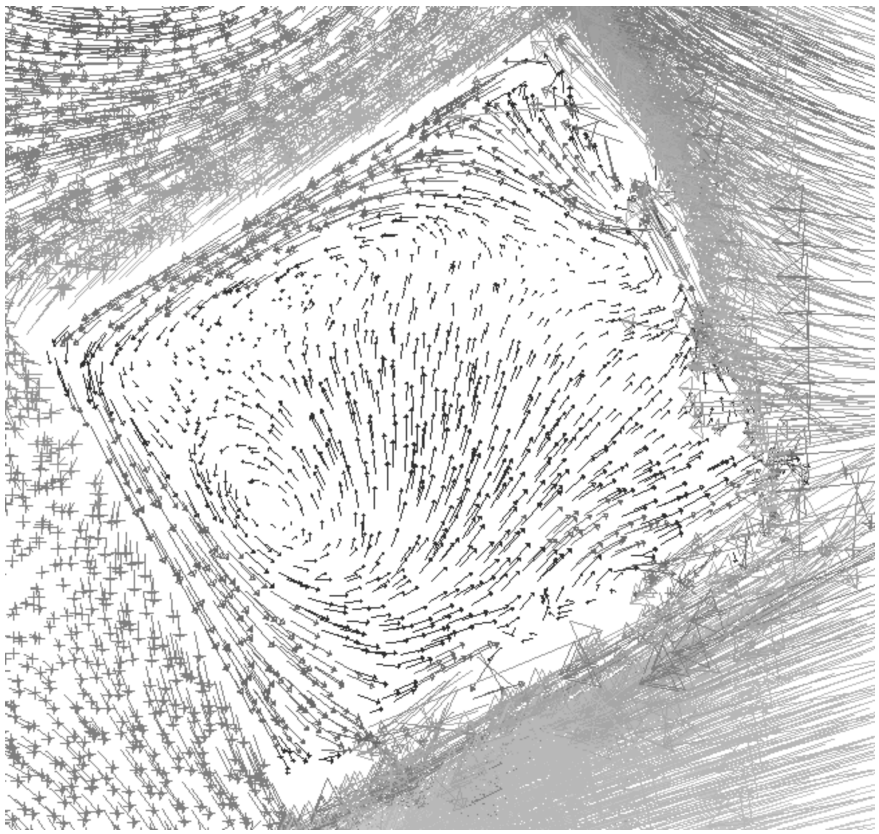
(c) $\alpha = 0°$.



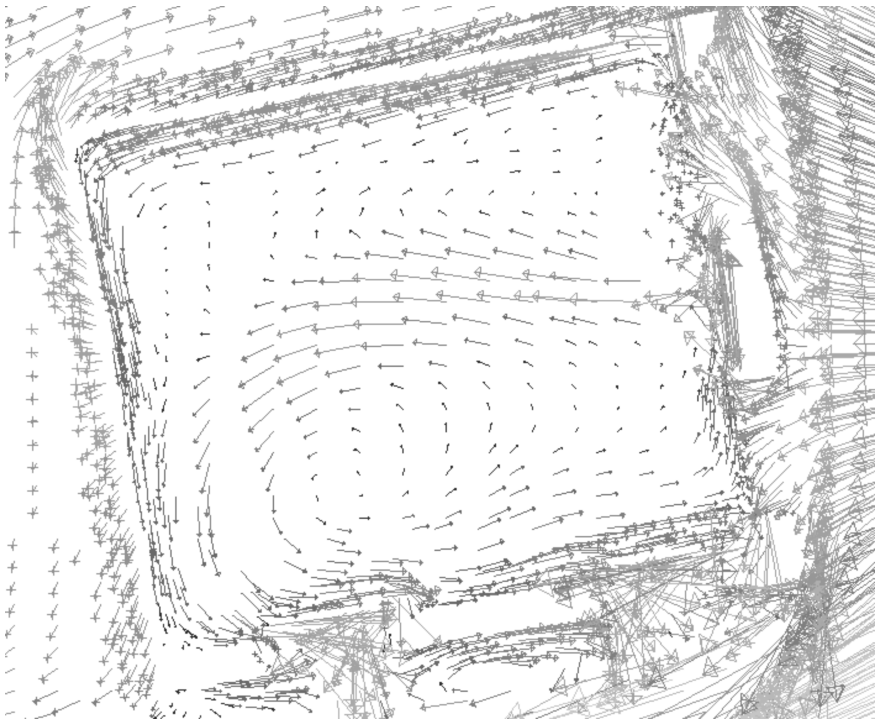
(d) $\alpha = 20°$.



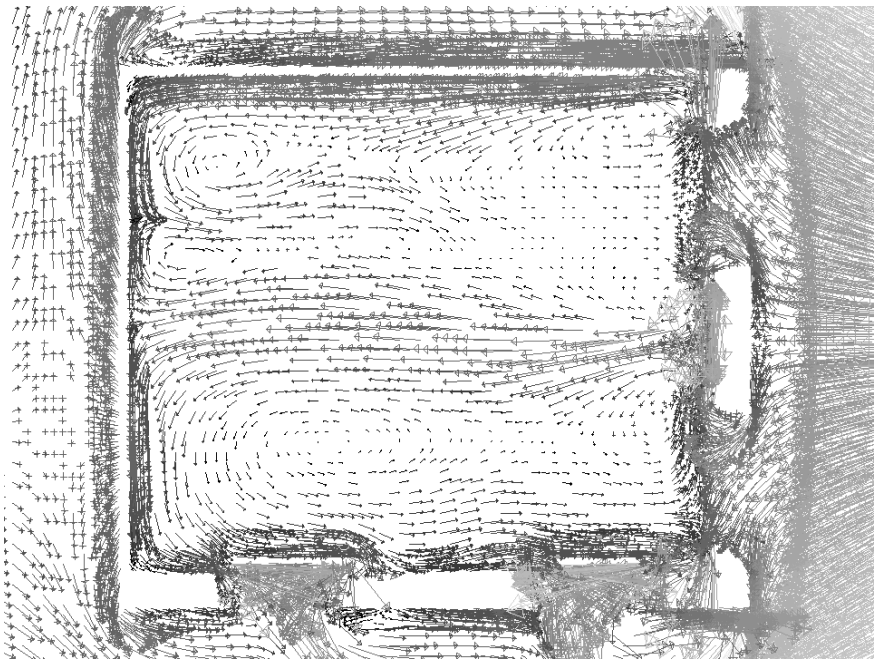
(e) $\alpha = 40°$.



(f) $\alpha = 60°$.



(g) $\alpha = 80°$.



(h) $\alpha = 90°$.

Figure 4.24: Velocity vectors for an inlet velocity of 3.6 m/s. Incidence angles from (a) $\alpha = -40°$ to (h) $\alpha = 90°$, all windows tilted. Incidence angle from right to left for all cases.

4.6 ACH dependencies

4.6.1 Comparison of air exchange rates obtained by different methods

As described in detail in this work, air exchange rates were determined using various methods: on the one hand by means of velocity measurements and tracer gas measurements, and on the other hand by numerical flow simulation.

Tables 4.9 – 4.11 represent the ACH values and Fig. 4.25 shows them exemplarily for a wind velocity of 3.6 m/s without any influence of temperature, obtained by use of the different methods. The deviations in Tables 4.9 – 4.11 are given relative to the data obtained by the tracer gas measurements, since the tracer gas method appeared to be more reliable than the velocity measurements. The ACH values were calculated taking into account the blockage caused by the velocity sensors, as mentioned in Section 3.4.

Angle α [°]	ACH [1/h] from tracer gas measurements	velocity measurements	numerical simulation
−40	51.07	60.58 (+18.62%)	59.01 (+15.54%)
−20	60.74	70.48 (+16.03%)	64.1 (+5.53%)
0	66.06	69.67(+5.46%)	61.1 (−7.51%)
20	60.66	61.7 (+1.71%)	49.2 (−18.89%)
40	23.79	24.13 (+1.43%)	25.1 (+5.49%)
60	34.91	37.09 (+6.24%)	37.3 (+6.85%)
80	71.81	68.08 (−5.19%)	69.09 (−3.79%)
90	73.27	67.66 (−7.66%)	71.1 (−2.97%)

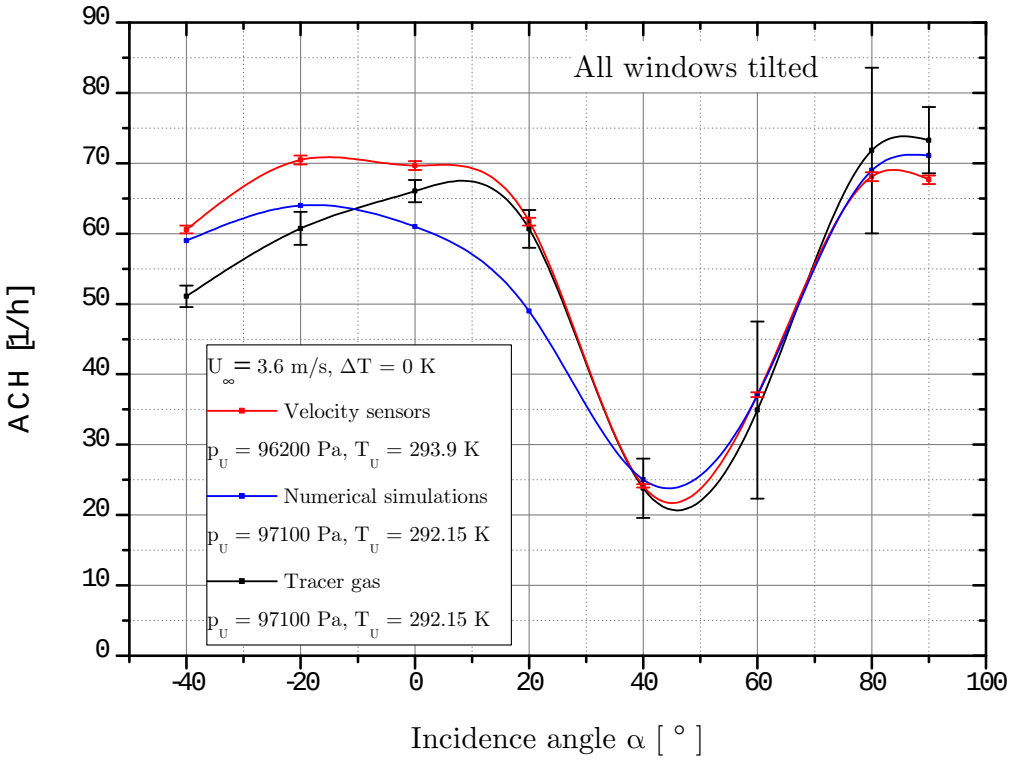
Table 4.9: Up-scaled ACH values. Inlet velocity 3.6 m/s, incidence angle of 0°, all windows tilted. Deviations enclosed in parantheses are given relative to the data from the tracer gas measurements.

Angle α [°]	ACH [1/h] from tracer gas measurements	velocity measurements	numerical simulation
−40	38.23	31.71 (−17.05%)	32.18 (−15.83%)
−20	44.20	33.34 (−24.57%)	36.05 (−18.45%)
0	43.81	33.73 (−23%)	35.2 (−19.66%)
20	31.53	24.50 (−22.30%)	28.47 (−9.71%)
40	14.26	9.54 (−33.10%)	13.66 (−4.27%)
60	23.48	21.46 (−8.60%)	20.91 (−10.97%)
80	40.37	36.52 (−9.54%)	31.6 (−21.72%)
90	44.59	37.75 (−15.34%)	32.15 (−27.89%)

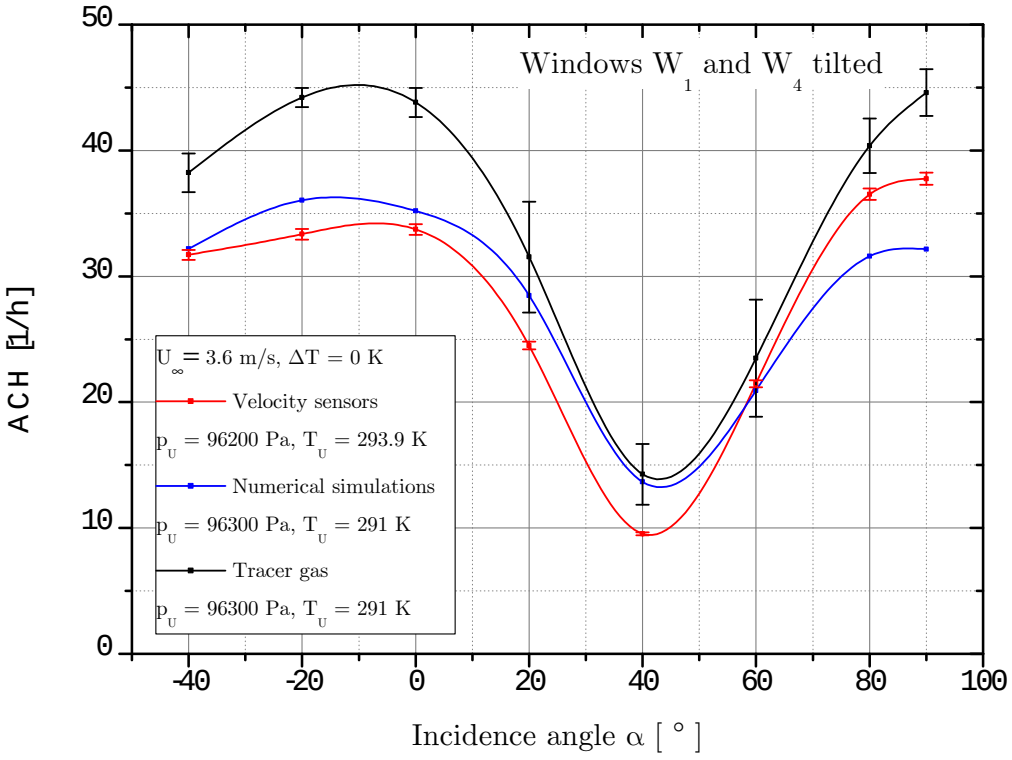
Table 4.10: Up-scaled ACH values. Inlet velocity 3.6 m/s, incidence angle of 0°, windows W_1 and W_4 tilted. Deviations enclosed in parantheses are given relative to the data from the tracer gas measurements.

Angle α [°]	ACH [1/h] from tracer gas measurements	velocity measurements	numerical simulation
−40	17.03	16.65 (−2.33%)	20.23 (+18.76%)
−20	14.6	12.67 (−13.22%)	17.03 (+16.61%)
0	3.56	2.58 (−27.53%)	2.85 (−19.92%)
20	16.59	14.21 (−14.35%)	18.12 (+9.16%)
40	20.16	20.59 (+2.13%)	22.78 (+12.99%)
60	11.11	9.30 (−16.29%)	15.29 (+37.59%)
80	16.52	15.66 (−5.21%)	20.95 (+26.81%)
90	5.76	3.64 (−36.81%)	7.19 (+24.78%)

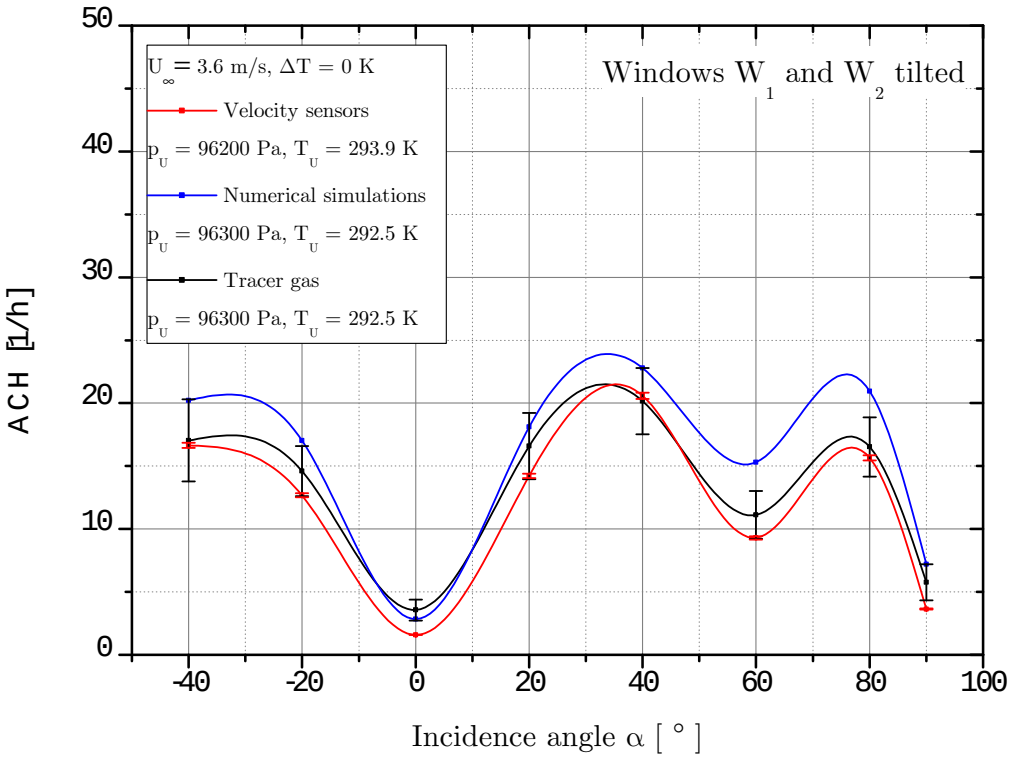
Table 4.11: Up-scaled ACH values. Inlet velocity 3.6 m/s, incidence angle of 0°, windows W_1 and W_2 tilted. Deviations enclosed in parantheses are given relative to the data from the tracer gas measurements.



(a)



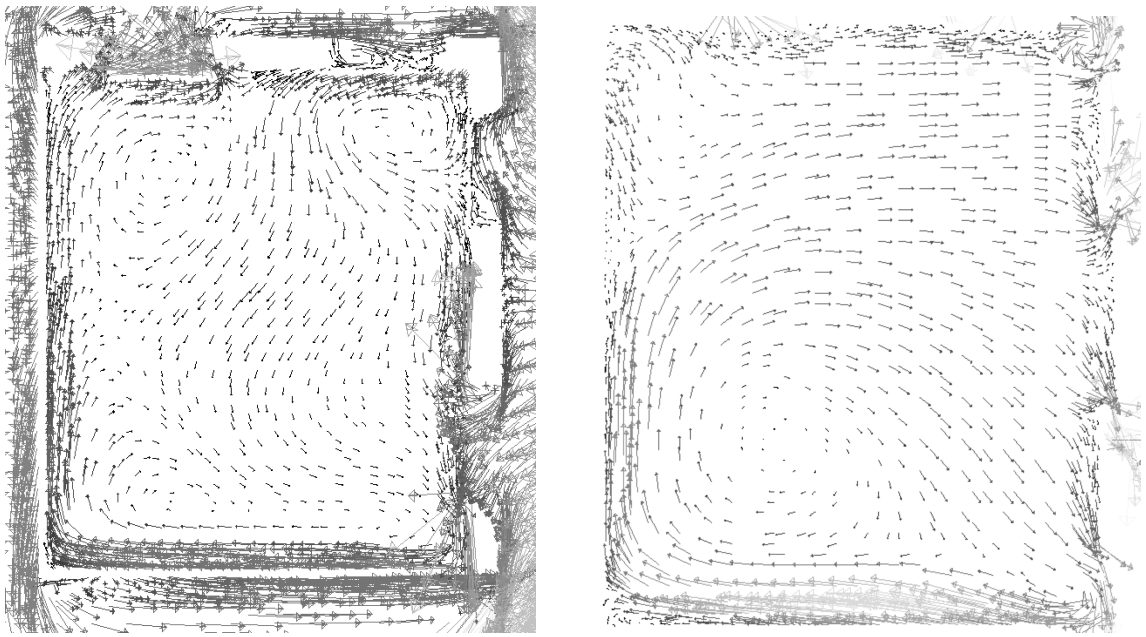
(b)



(c)

Figure 4.25: Up-scaled air exchange rates for different methods: (a) for all windows, for windows (b) W_1 and W_4 and (c) W_1 and W_2 tilted.

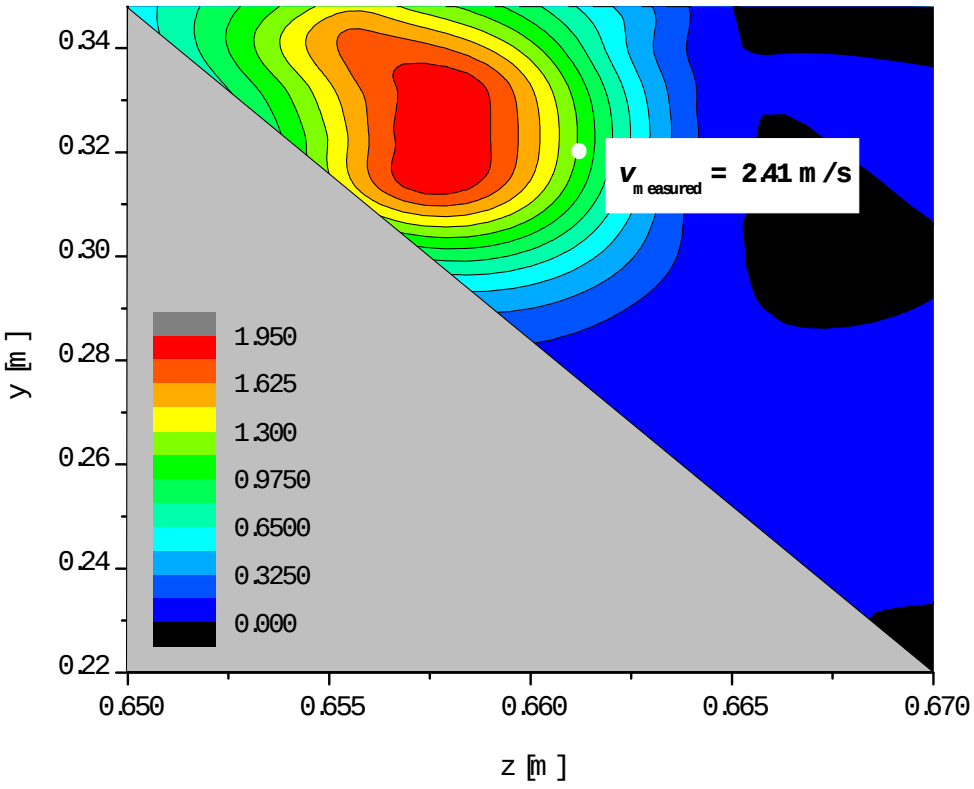
In Fig. 4.25, particularly in the case of cross ventilation discrepancies between the different measurement methods and the numerical simulations become evident. For all windows tilted (cf. Fig. 4.25(a)), the velocity sensors tended to display larger values for the measured velocity, resulting in larger air exchange rates. For windows W_1 and W_4 tilted (cf. Fig. 4.25(b)), the velocity sensors display smaller values for the measured velocity, resulting in smaller air exchange rates. This effect was taken into account in the calculation of the volumetric flow rates through the consideration of the 15.8% blockage of the area overhead and the 18.9% blockage of the lateral areas, respectively, caused by the velocity sensors (cf. Section 3.4). A comparison of the vector plots (Figs. 4.24(a) and 4.26(a) and (b)), exemplarily given for an inlet velocity of 3.6 m/s and an incidence angle of 0°, for the three different tilting scenarios of the windows leads to the conclusion that the formation of the vortices inside the room may be an additional reason for the discrepancies. It seems that the vortices may strongly affect the flow near the sensor locations. For single sided ventilation, i.e. for windows W_1 and W_2 tilted, no major discrepancies can be determind, as can be seen in Fig. 4.25(c).



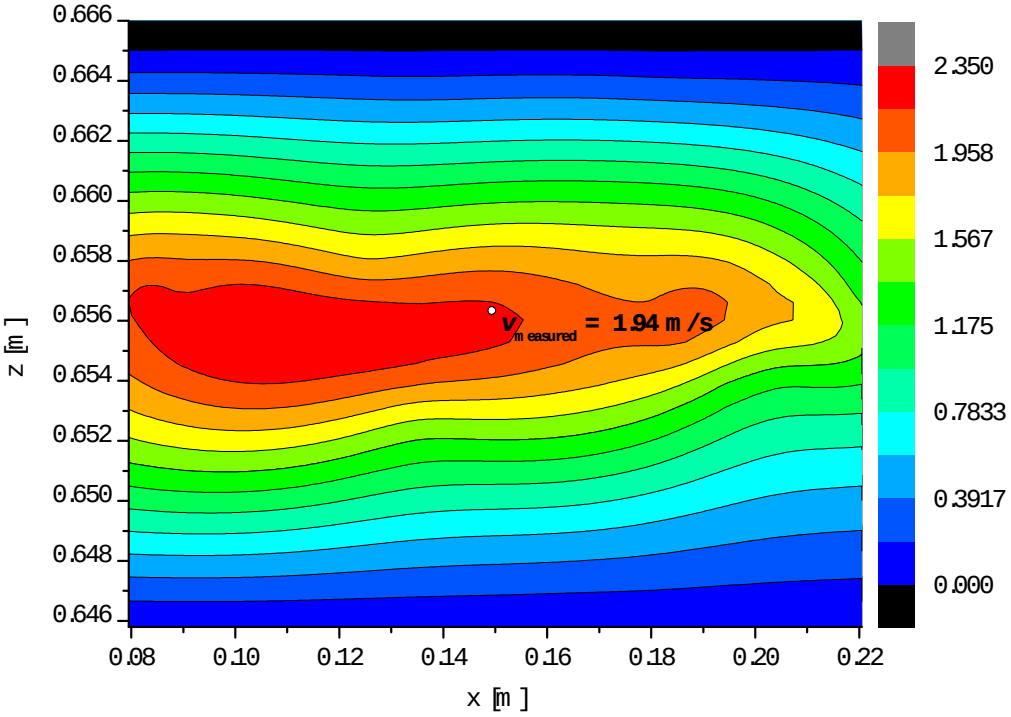
(a) **(b)**

Figure 4.26: Velocity vectors for an inlet velocity of 3.6 m/s and an incidence angle of 0°.(a) windows W_1 and W_4, (b) windows W_1 and W_2 tilted.

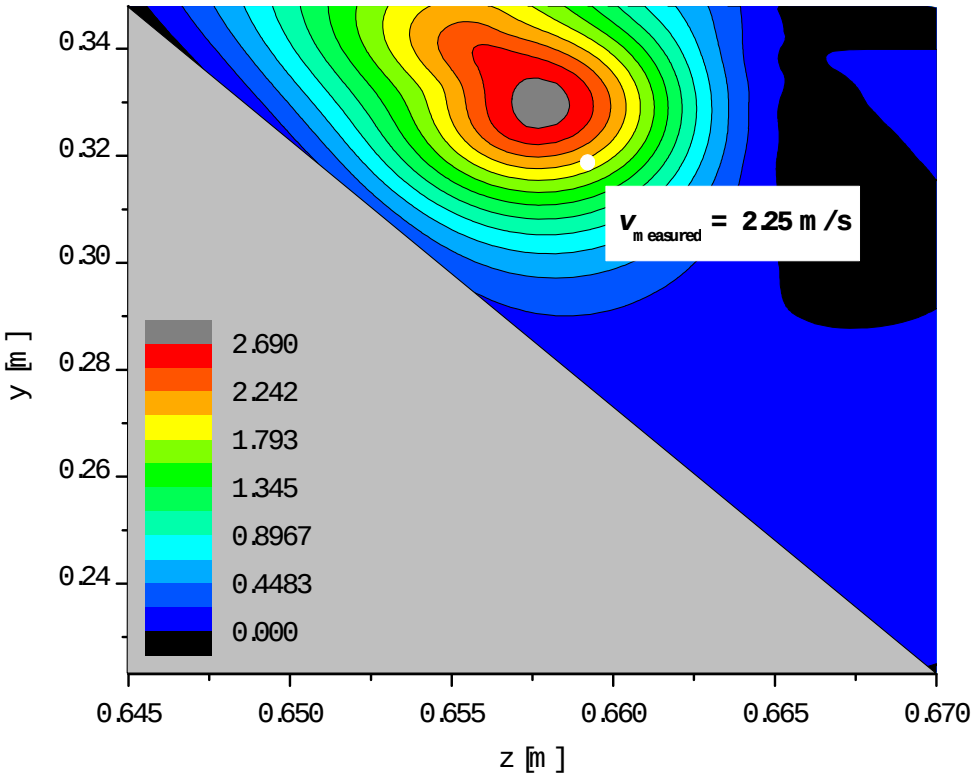
The tendency of the velocity sensors (mounted in the gaps of the tilted windows) to show too large values for the measured velocity, is immediately clarified in Fig. 4.27: here each of the position of the velocity sensors in the experiment and the distribution of velocity magnitude in the window gaps can be seen, exemplarily for $U_\infty = 3.6$ m/s, an incidence angle $\alpha = 0°$, and all windows tilted. The windows W_3 and W_4 are depicted because there the vortices play a major role, as can be seen in the plot of the velocity vectors in Fig. 4.24(c). Particularly for the left gaps (Fig. 4.27(a) and (d)) a discrepancy between the measured velocity and the one obtained by numerical simulations can be recognized, while for the other cases the consistency is very good.



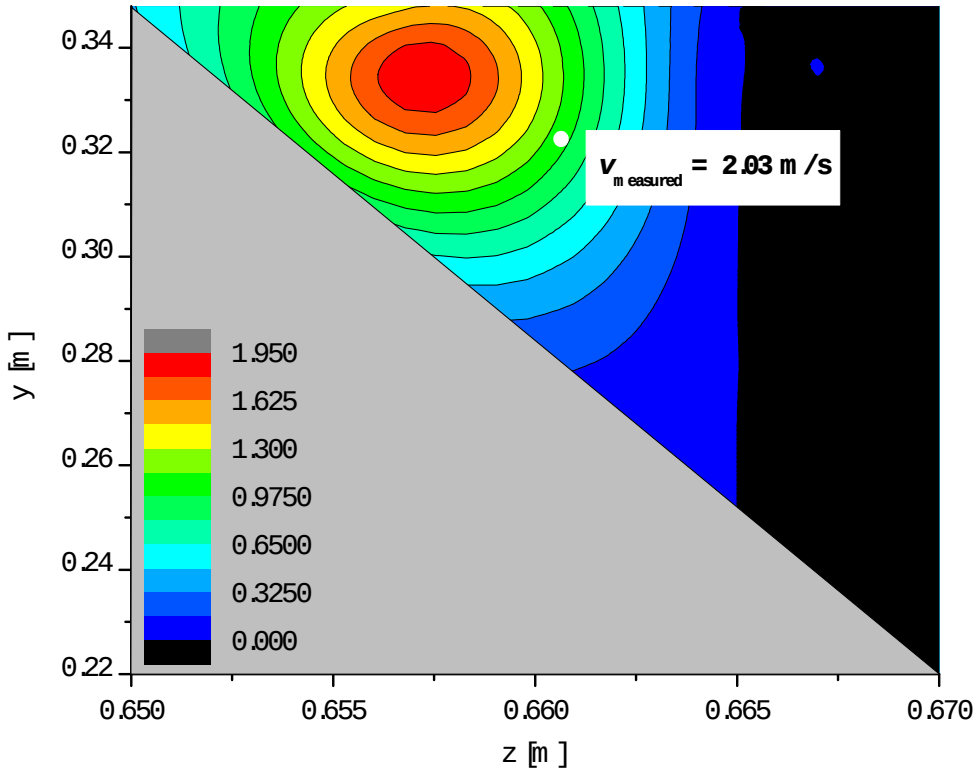
(a) Window W_3, left gap.



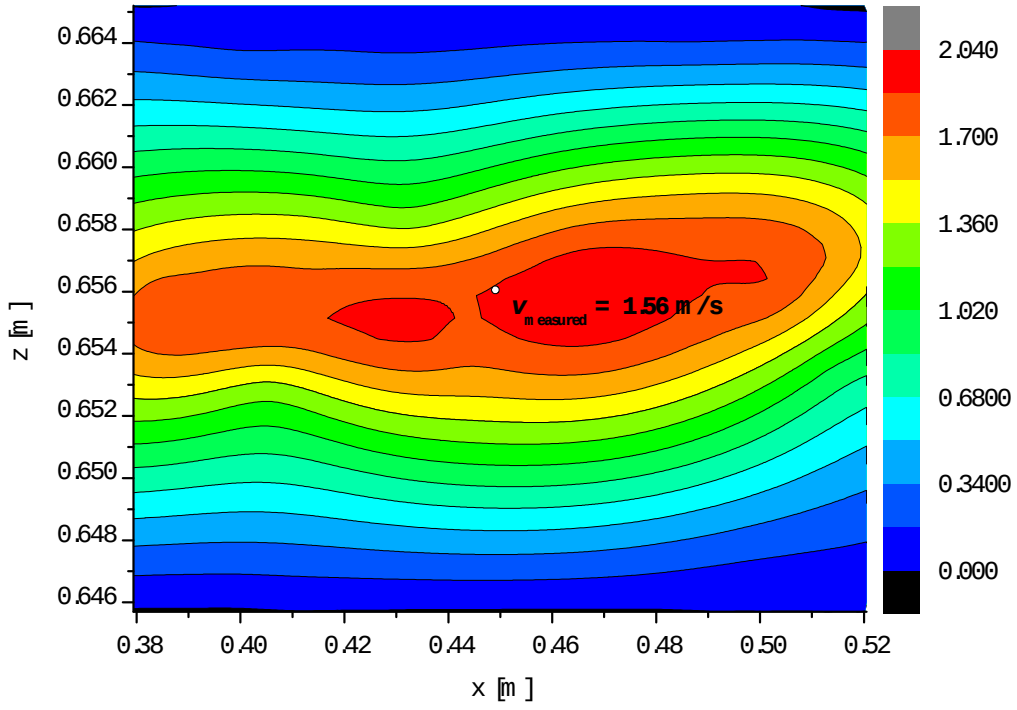
(b) Window W_3, upper gap.



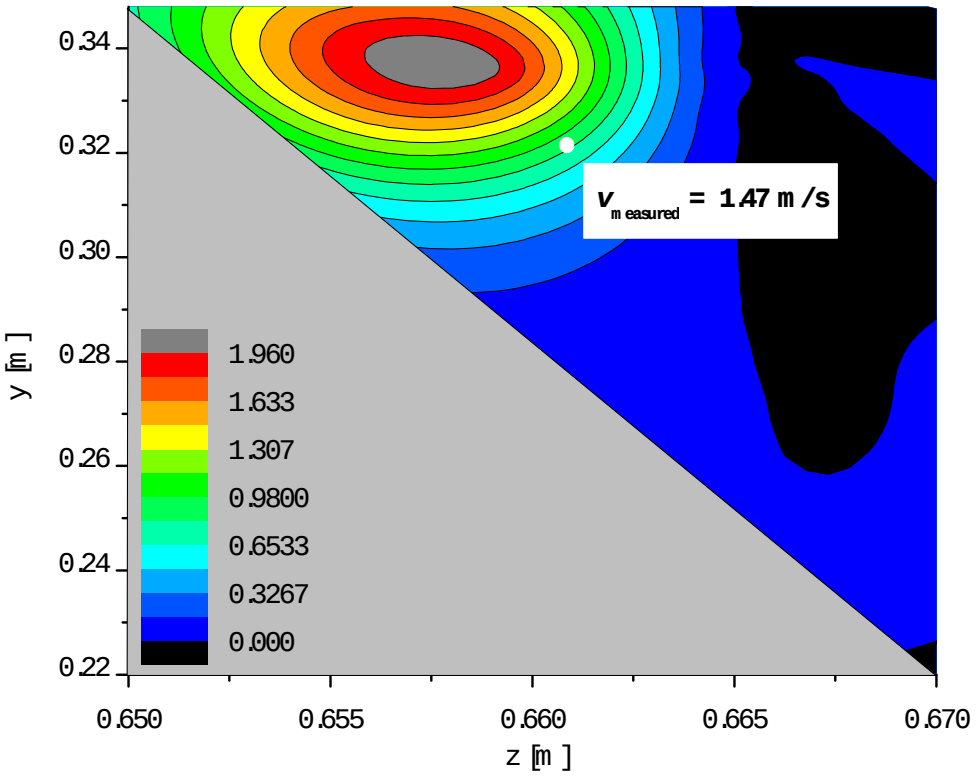
(c) Window W_3, right gap.



(d) Window W_4, left gap.



(e) Window W_4, upper gap.



(f) Window W_4, right gap.

Figure 4.27: Distribution of the velocity magnitude in m/s in the window gaps, all windows tilted, $U_\infty = 3.6$ m/s, and incidence angle $\alpha = 0°$.

In summary it can therefore be said that the noticed discrepancies for the velocity values may result from: (i) the formation of the vortices inside the room (exemplarily shown in Fig. 4.26(a)) affecting the flow near the sensor locations and (ii) the limitation of computational resources enforcing coarse computational grids in the simulations. The consequence is a limited accuracy of the local velocity distribution, which can be seen from the discrepancies in Fig. 4.27. Full agreement of the velocity values determined experimentally with those obtained from the numerical simulations was anyway not to be expected since in the simulations the velocity sensors were not considered.

Another reason for the discrepancies of the velocity values is that the velocity is only measured locally at a single location within the window gap and the volumetric flow rate is calculated applying this value over the entire cross-sectional area of the gap. The velocity measurements within the gaps, however, lead to an increase of the

velocity values in consequence of the blockage by the velocity sensors themselves, which can clearly be seen in Fig. 4.27. Therefore, this blocked area was accounted for when calculating the volumetric flow rates as already mentioned above.

4.6.2 Comparison of air exchange rates for different wind velocities obtained by tracer gas measurements

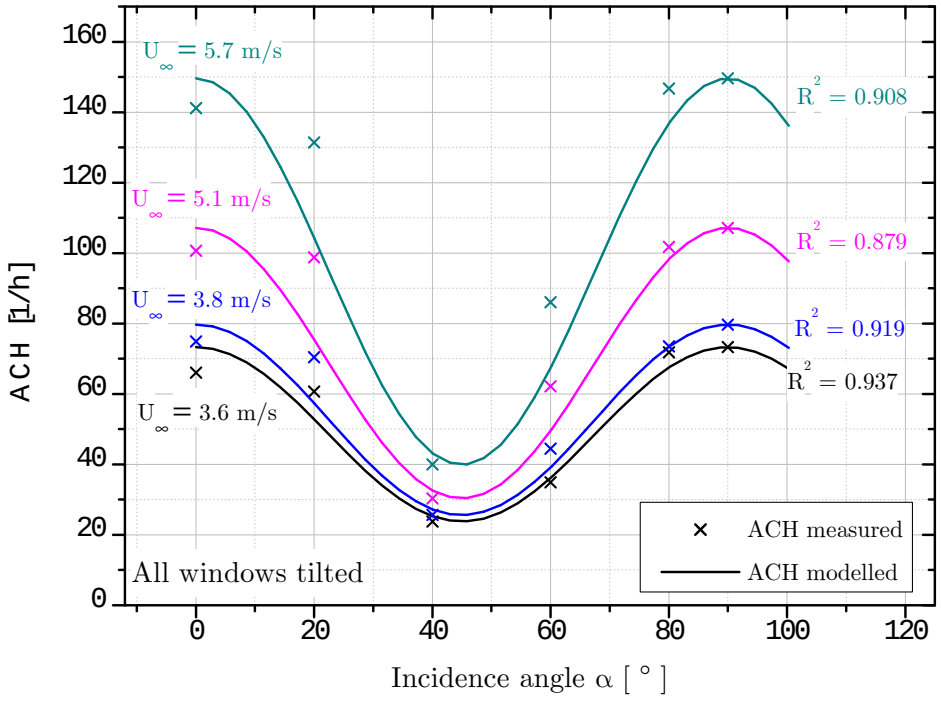
Knowing the specific airflow characteristics and the air exchange rates for a room or better the global air exchange rates in buildings is essential for both designers and engineers interested in the velocity distributions in a zone, the size of ventilation inlets and outlets, or the ventilation efficiency depending on the boundary conditions of the specific problem. To find a dependence of the air exchange rate on the inflow velocity U_∞ and the incidence angle α, the air exchange rate $ACH(\alpha, U_\infty)$ was modelled according to

$$ACH(\alpha, U_\infty) = \underbrace{a_1 + a_2 U_\infty}_{=:A} + \underbrace{(b_1 + b_2 U_\infty)}_{=:B} \cos^2(2\alpha) \; . \tag{4.4}$$

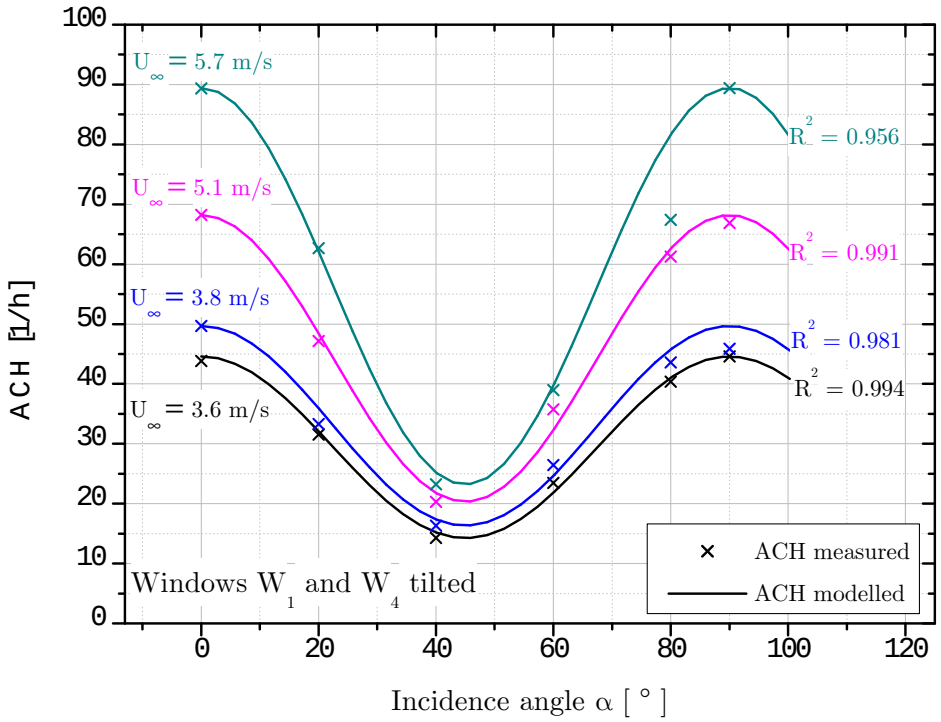
In this equation, A and B are the fitting parameters. For the present study, measured ACH data together with the model curves are exemplarily shown in Fig. 4.28 for cross ventilation.

The mathematical relation Eq. (4.4) reflects the behaviour of the air exchange rate depending for varying incidence angle and wind velocity well, in particular in case of cross ventilation through the two windows W_1 and W_4 as can be seen in Fig. 4.28(b).

To depict the influence of the wind velocity on the air exchange, the results from the tracer gas measurements, without consideration of temperature differences, are exemplarily plotted for all the different window opening scenarios in Fig. 4.29. It can be recognized that the air exchange rate and, hence, the volumetric air flow rate for angles between 0° and 90° are proportional to the wind velocity. These results are consistent with those of Maas (1995), Hall (2004), Larsen (2006), and Horan and Finn (2008).



(a)



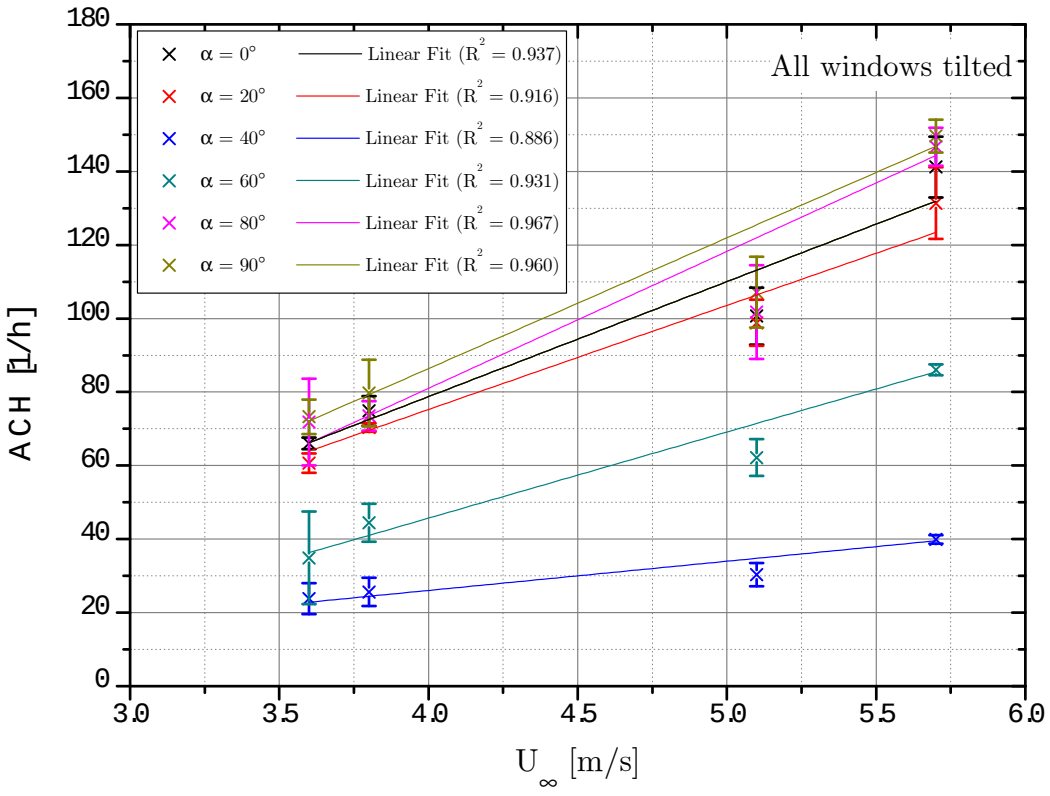
(b)

Figure 4.28: Comparison between measured and modelled air exchange rates (up-scaled) for (a) all windows and (b) windows W_1 and W_4 tilted.

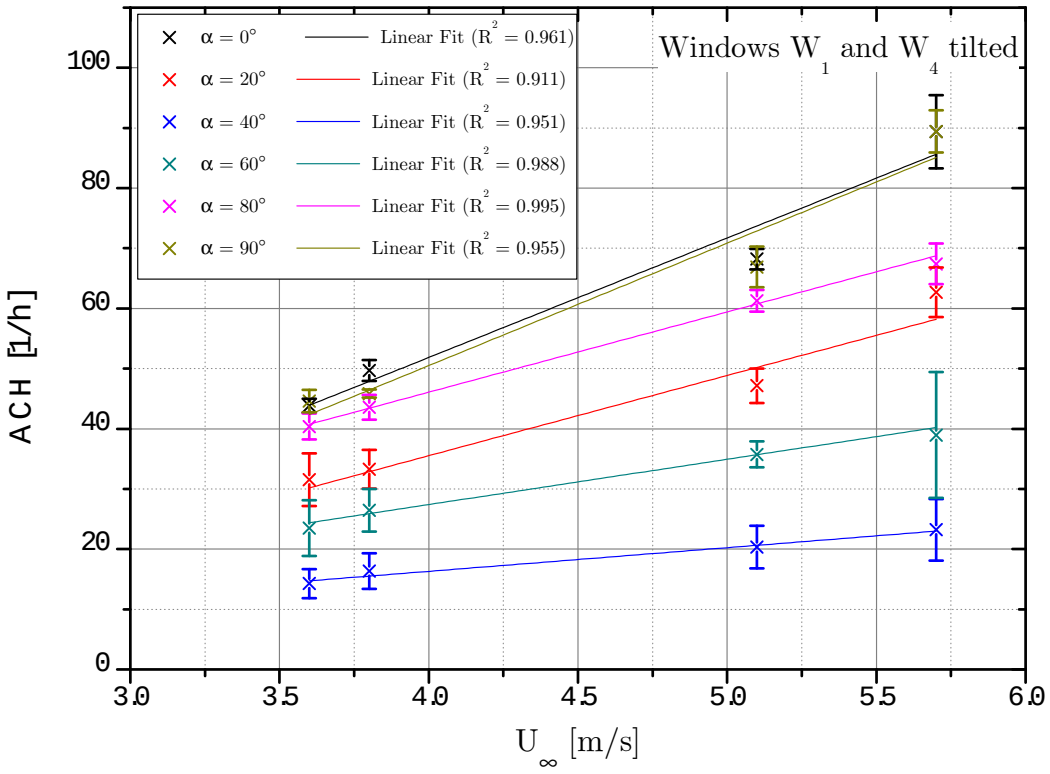
For all windows tilted, the proportionalities are resulting in parallel curves for incidence angles of 0° and 90°, as well as for incidence angles of 20° and 80°, which can be seen in Fig. 4.29(a). For the incidence angles 40° and 60°, the measured values exhibit a wider scattering and lower air exchange rates than for the other incidence angles because the flow proceeds parallel to the walls containing the openings so that no stagnation regions near the openings exist. An analogous behaviour is seen in Fig. 4.29(b) for the case that windows W_1 and W_4 are tilted. For the case that two windows on the same wall are tilted, i.e. W_1 and W_2 in Fig. 4.29(c), a different behaviour is apparent due to the single sided ventilation.
The parameters A and B in Eq. (4.4) for modeling the air exchange rate exhibit a linear proportionality to the wind velocity U_∞ (cf. Fig. 4.30). For all windows tilted the parameters A and B are

$$A = -46.495 + 26.157\,U_\infty \tag{4.5}$$

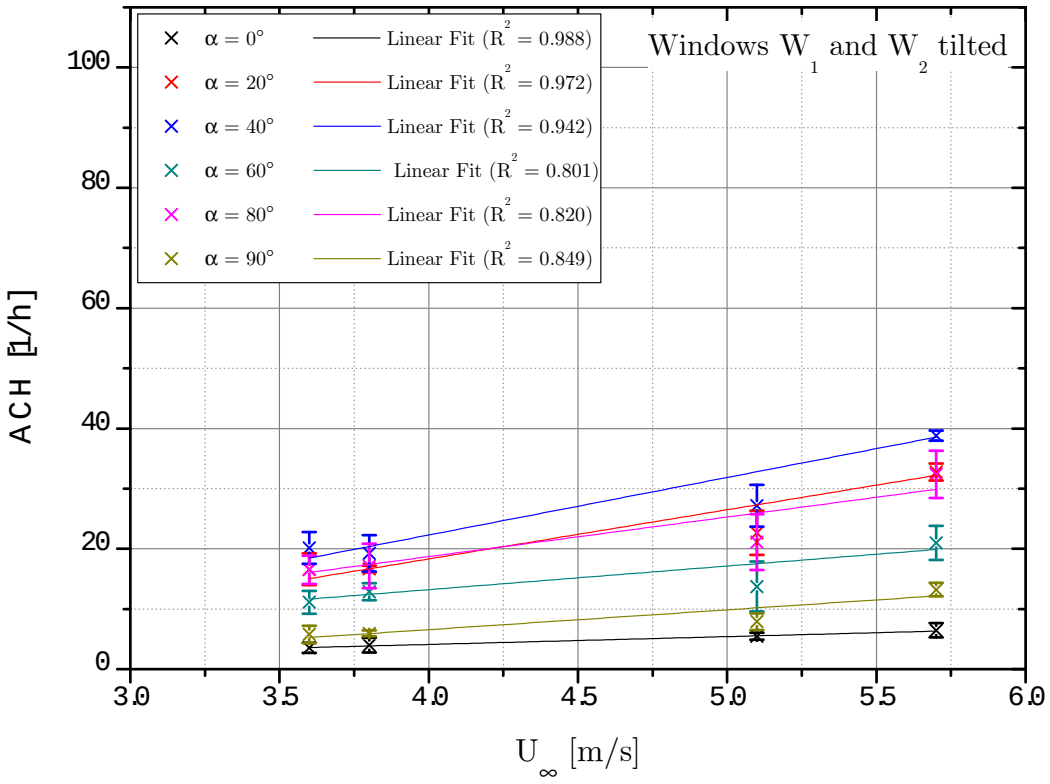
$$B = -0.674 + 6.725\,U_\infty\ , \tag{4.6}$$



(a)

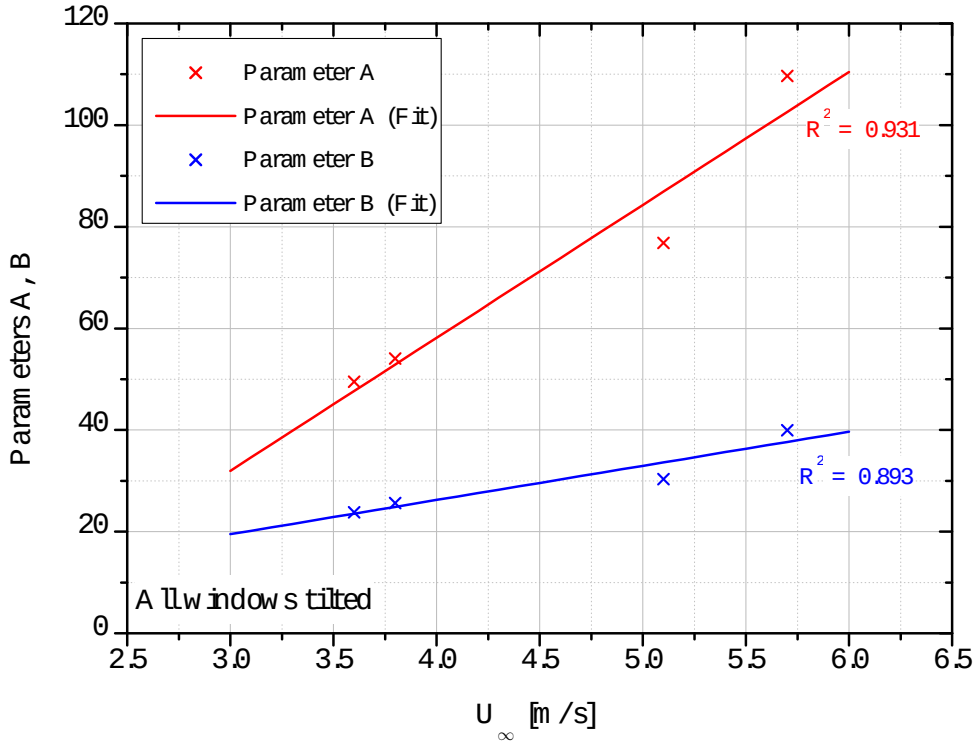


(b)

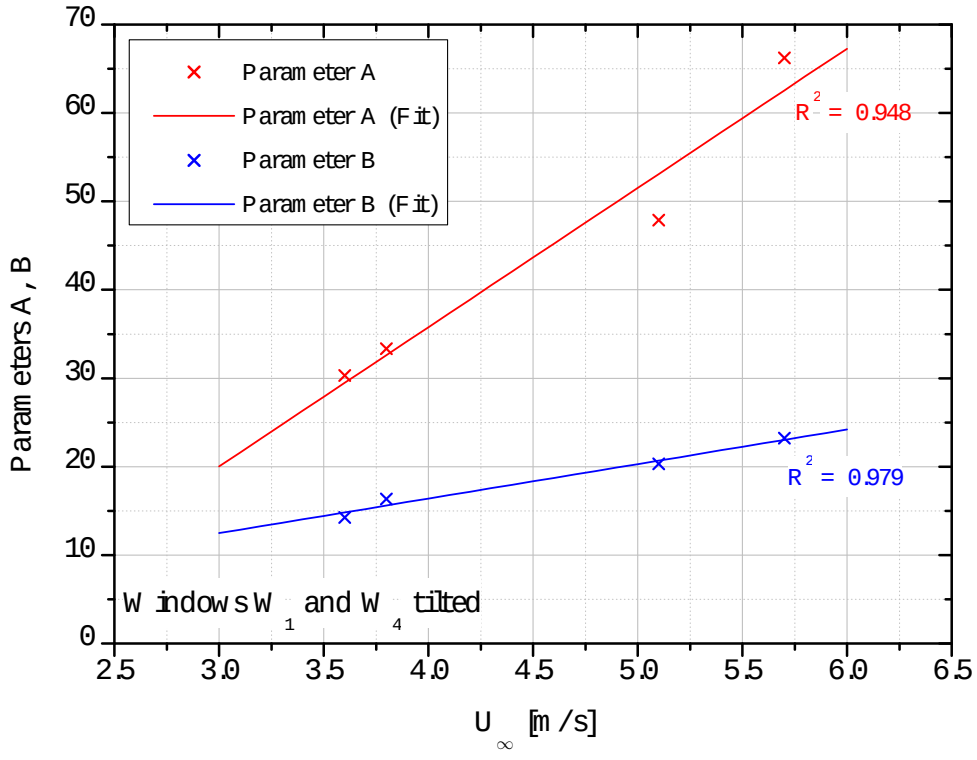


(c)

Figure 4.29: Up-sclaed air exchange rates according to Table 4.3 for (a) all windows, (b) windows W_1 and W_4, and (c) W_1 and W_2 tilted.



(a)



(b)

Figure 4.30: Parameters A and B according to Eq. (4.4) for (a) all windows and (b) windows W_1 and W_4 tilted.

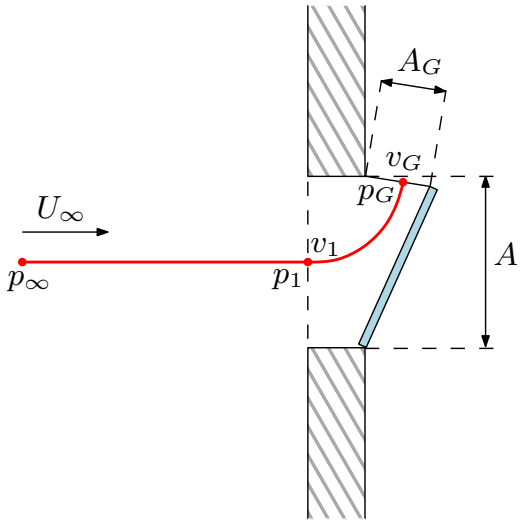


Figure 4.31: Schematic sketch of a tilted window.

and for windows W_1 and W_4 tilted

$$A = -27.236 + 15.752\,U_\infty \tag{4.7}$$

$$B = -0.764 + 3.906\,U_\infty\ . \tag{4.8}$$

In Eqs. (4.5) – (4.8) the parameters A and B are obtained in h^{-1} with the velocity U_∞ entered in m/s. To explain this linear dependence, in the following we show, on the one hand, that the total pressure is constant along a streamline from the undisturbed flow to a point on the wall of the room model, and, on the other hand, that therefrom actually this linear proportionality between the ACH and the flow velocity follows by applying Bernoulli's equation.

Using Bernoulli's equation along a streamline from one point in the undisturbed flow to another point within the window cross sectional area A according to Fig. 4.31, yields

$$p_\infty + \frac{\rho}{2}U_\infty^2 = p_1 + \frac{\rho}{2}v_1^2\ . \tag{4.9}$$

Applying Bernoulli's equation again from the window cross sectional area A to the cross sectional area A_G of the gap of the tilted window (here A_G corresponds to the sum of the lateral and the upper surfaces of the window gap), we get

$$p_1 + \frac{\rho}{2}v_1^2 = p_G + \frac{\rho}{2}v_G^2\ . \tag{4.10}$$

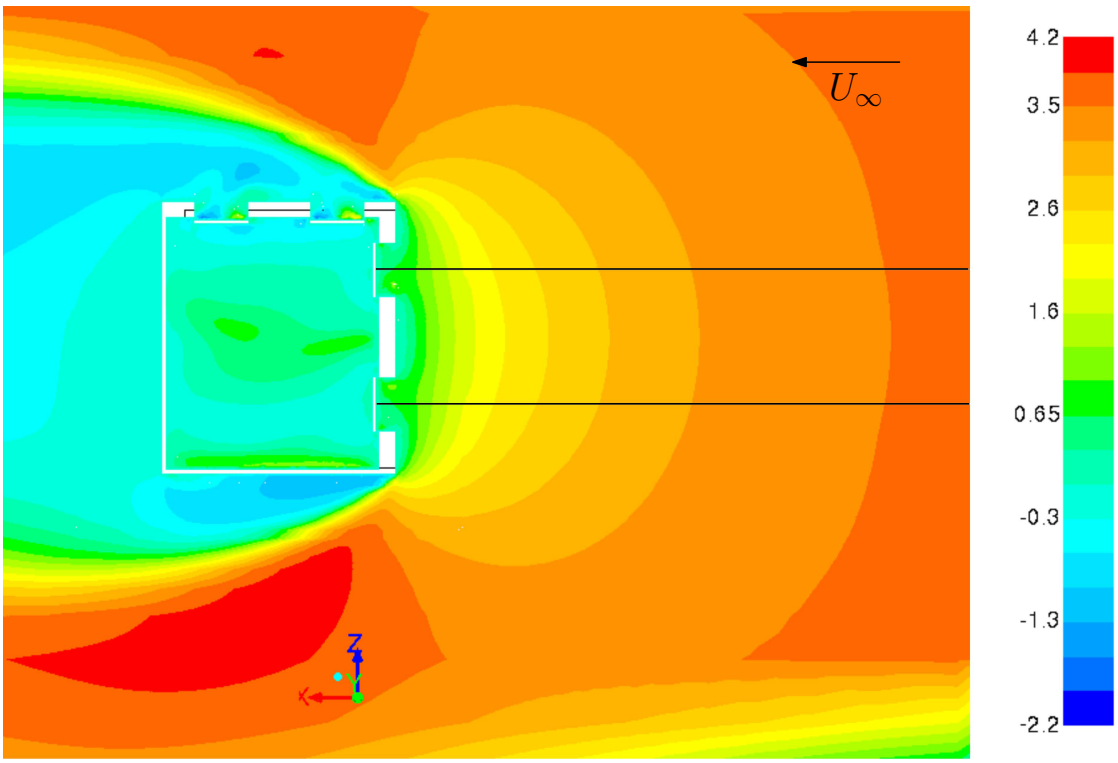


Figure 4.32: Contours of the $x-$velocity in m/s for an inflow velocity of 3.6 m/s and an incidence angle $\alpha = 0°$ (in the mid cut plane through the window centres).

Assuming that the total pressure is the same in the undisturbed flow and in point 1, and applying the incompressible continuity equation $Av_1 = A_G v_G$, results in

$$p_1 - p_G = \frac{\rho}{2} U_\infty^2 \left[\left(\frac{A}{A_G} \right)^2 - 1 \right] . \tag{4.11}$$

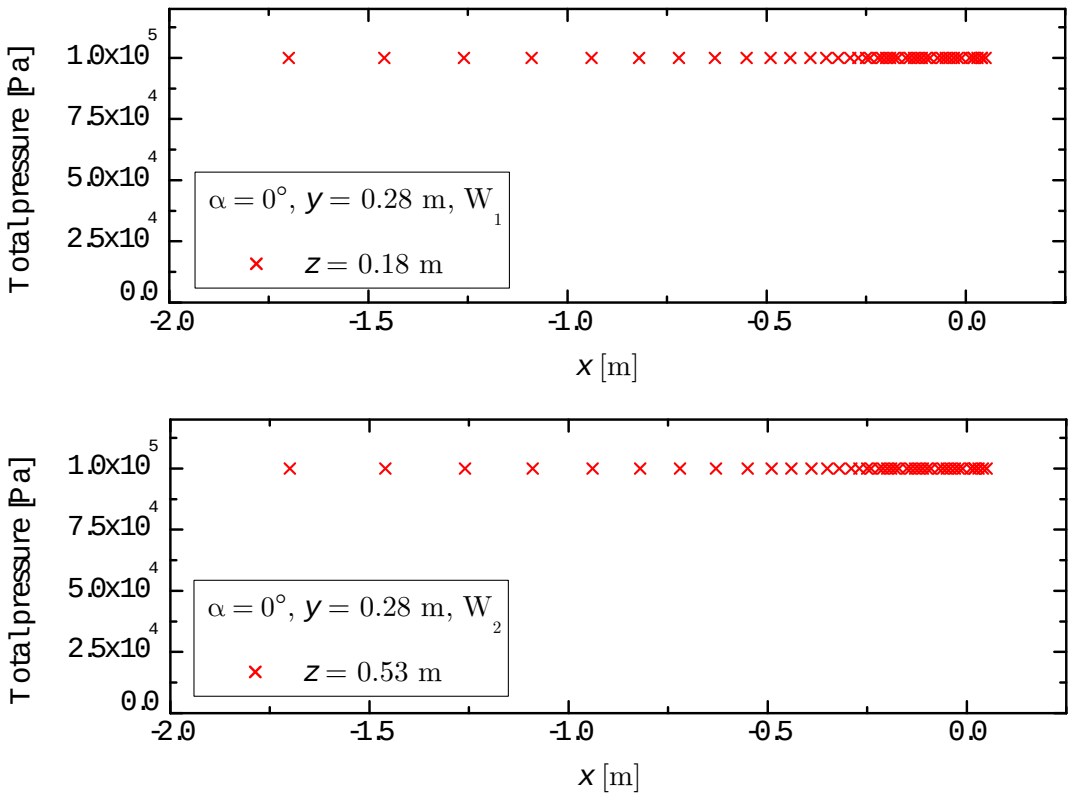
If we consider the losses using the orifice equation (2.90), the air exchange rate is given by

$$ACH = \frac{C_D \, A_G}{V_R} \sqrt{\frac{2 \, \Delta p}{\rho}} , \tag{4.12}$$

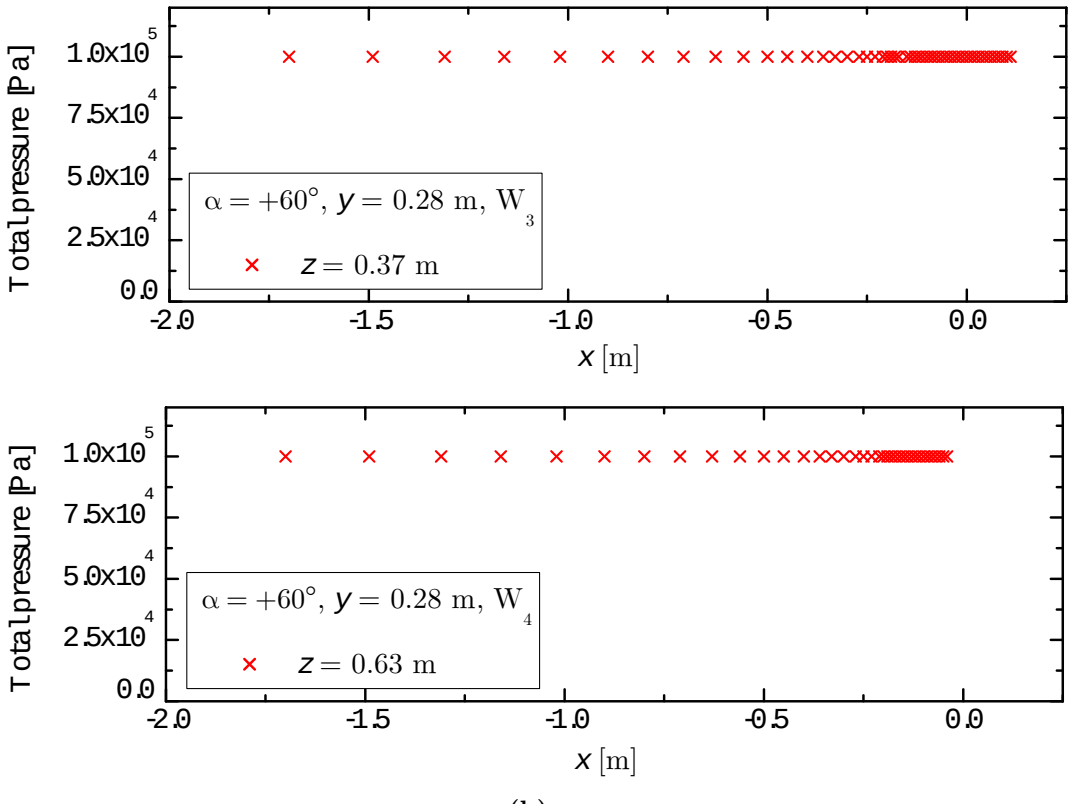
where $\Delta p = p_1 - p_G$. Substituting Eq. (4.11) into Eq. (4.12) we obtain

$$ACH = \frac{C_D \, A_G}{V_R} \, u_\infty \sqrt{\left(\frac{A}{A_G} \right)^2 - 1} , \tag{4.13}$$

Since all the occurring quantities in Eq. (4.13) are constant (also C_D for a constant



(a)



(b)

Figure 4.33: Distribution of the total pressure along the $x-$direction for wind velocity $U_\infty = 3.6$ m/s: (a) $\alpha = 0°$, and (b) $\alpha = 60°$.

angle α is a constant), the air exchange rate is linearly proportional to the flow velocity U_∞, which corresponds to the behaviour described earlier in this section.

The assumption that the total pressure of the undisturbed flow is equal to that in point 1 of Fig. 4.31, was verified by numerical simulations of the single room model following the lines in Fig. 4.32. Exemplarily, the distribution of the total pressure for a wind velocity of $U_\infty = 3.6$ m/s and an incidence angle of (a) $\alpha = 0°$ for the windows W_1 and W_2 and (b) $\alpha = 0°$ for the windows W_3 and W_4 is shown in Fig. 4.33.

Since the flow along the lines sketched in Fig. 4.32 is isentropic (no losses), the total pressure must be constant. Due to the approach to the rigid wall, the kinetic energy is reduced towards the stagnation point and the static pressure is increased. The sum is constant, as can exemplarily be seen in Fig. 4.33 for two different incidence angles (a) $\alpha = 0°$ and (b) $\alpha = 60°$.

4.6.3 Comparison of air exchange rates for different temperatures

Theoretical considerations by Daler et al. (1984) and Maas (1995) for steady flow processes show that the air flow rate, i.e. the air exchange rate, through a large single opening (Daler et al., 1984) and through tilted windows (Maas, 1995) in the building envelope driven by a temperature difference is proportional to the square root of the difference between inside and outside temperature, if the process is only thermally driven

$$\dot{V} = C\,\sqrt{\Delta T}\,, \tag{4.14}$$

where C is a constant and $\Delta T := T_i - T_o$. This relation is obtained by the following derivation. The decrease of the hydrostatic pressure of the atmosphere between two considered levels (of different height) can be assumed to be approximately linear over the height of conventional buildings. For $\rho = const.$ applies

$$p_2 = p_1 - \rho g z \tag{4.15}$$

and using the equation of state for the ideal gas $\rho = p_{atm}/\mathcal{R}T$, where $\mathcal{R}$ is the specific gas constant, yields

$$p_2 = p_1 - \frac{p_{atm}}{\mathcal{R}T}\, gz \ . \tag{4.16}$$

Applying Eq. (4.16) twice yields the pressure drop p_o outside and the weaker decrease of p_i at the warmer interior of the building. The resulting thermal pressure difference Δp_t between internal and external air reads

$$\Delta p_t := p_{2i} - p_{2o} = \frac{p_{atm}}{\mathcal{R}} \left(\frac{1}{T_o} - \frac{1}{T_i} \right) gz \ . \tag{4.17}$$

Relating Δp_t to the difference of height Δz between to levels of the building, yields

$$\frac{\Delta p_t}{\Delta z} = \frac{p_{atm} g}{\mathcal{R} T_o T_i} (T_i - T_o) \tag{4.18}$$

or for

$$K_t := \frac{p_{atm} g}{\mathcal{R} T_o T_i} \quad \text{and} \quad \Delta T = T_i - T_o$$

to the linear relation

$$\frac{\Delta p_t}{\Delta z} = K_t \, \Delta T \ , \tag{4.19}$$

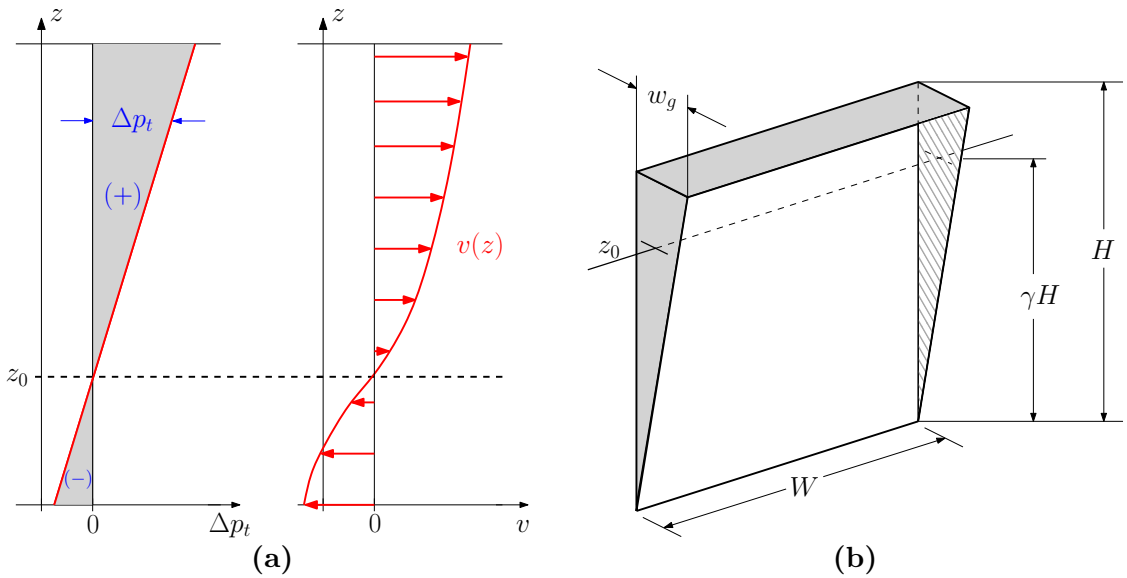


Figure 4.34: (a) Pressure and flow conditions in a room with several individual openings, (b) relevant quantities for the thermal air exchange in a tilted window. According to Daler et al. (1984)

where the value of K_t turns out very accurately constant even for changing pressure p_{atm}. Its value is 0.04 Pa/mK.

In each room there exists a pressure neutral level z_0 at which there is neither over nor under pressure relative to the outside air (cf. Fig. 4.34(a)). The location of the neutral level z_0 is independent of changes in the temperature difference, it depends only on the particular complexity of the openings and thus resulting air flows. Applying Eq. (4.19) to the orifice equation (2.90) gives

$$\dot{V} = \underbrace{C_D A \sqrt{\frac{2K_t}{\rho}}}_{=const.} \sqrt{\Delta T\,|z|}\ . \tag{4.20}$$

For a tilted window, the neutral axis z_0 due to the vertical asymmetrical area conditions is located above the center of the tilted window with the gap width w_g, as can bee seen in Fig. 4.34(b). For the determination of the supply air flow, the location of the neutral axis z_0 in accordance with the continuity condition $\dot{V}_{in} = \dot{V}_{out}$ has to be found. Requiring $T_i > T_o$, the inflow takes place at the two triangular surfaces below z_0, the outflow above z_0.

According to Fig. 4.35(a), it follows for the gap width $w(z)$ (varying with the $z-$coordinate)

$$w(z) = \left(\gamma + \frac{z}{H}\right) w_g f_\triangle\ , \tag{4.21}$$

where $f_\triangle$ is a factor indicating how strong the form and the magnitude of the wedge-shaped surfaces differ from an ideal triangle for different opening widths w_g due to the present gate fold. According to Daler et al. (1984) $f_\triangle = 0.7$ for opening widths 1 cm $\leq w_g \leq$ 12 cm. With Eq. (4.20) we get for the local flow velocity

$$v(z) = \frac{\dot{V}}{A} = C_D \sqrt{\frac{2K_t}{\rho}}\ \sqrt{\Delta T\,|z|} \tag{4.22}$$

and, thus, for the overall supply airflow

$$\dot{V}_{in} = 2 \int_{-\gamma H}^{0} v(z) \cdot w(z)\,\mathrm{d}z\ . \tag{4.23}$$

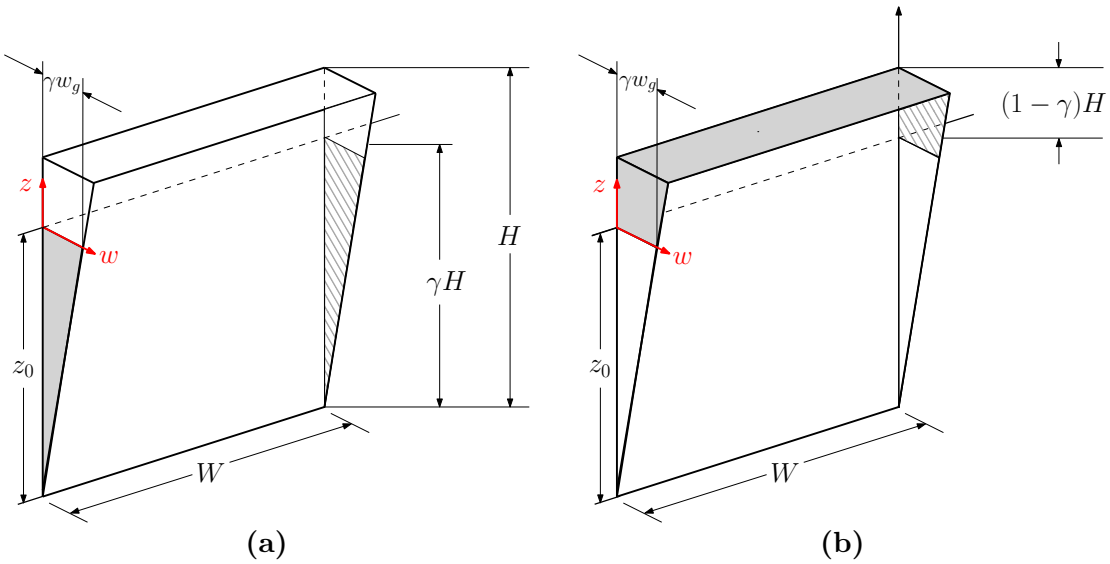


Figure 4.35: (a) Supply air cross sectional area, and (b) exhaust air cross sectional area. According to Daler et al. (1984).

The lateral exhaust airflow through the vertical trapezoidal area can be calculated as

$$\dot{V}_{out,1} = 2 \int_0^{(1-\gamma)H} v(z) \cdot w(z)\, \mathrm{d}z \; . \tag{4.24}$$

With $z = (1-\gamma)H$ and Eq. (4.20) the exhaust airflow on the horizontal rectangular gap is given by

$$\dot{V}_{out,2} = C_D W w_g \sqrt{\frac{2K_t}{\rho}} \sqrt{\Delta T (1-\gamma) H} \; . \tag{4.25}$$

After the integrations, from the continuity equation $\dot{V}_{in} = \dot{V}_{out,1} + \dot{V}_{out,2}$ the relative height γ of the neutral axis z_0 in implicit form reads

From Fig. 4.36 a ventilation factor $\sqrt{\gamma^5} f_\triangle$ dependent on the dimensionless ratio W/H can be read off (Daler et al., 1984). Hence, a solution for the volumetric flow rate depending on the gap width w_g is possible by

$$\dot{V}_{w_g} = C \sqrt{\gamma^5} f_\triangle C_D w_g \sqrt{H^3} \sqrt{\Delta T} \; , \tag{4.26}$$

where C is a constant, summarizing all other occurring constants. In summary, it can be stated that the calculations after Daler et al. (1984) for solely thermally driven air exchange yield a direct proportionality of the air exchange rate to the square root of

the temperature difference between the interior of the building and the environment.

$$\frac{W}{H f_{\triangle}} = \frac{4}{15}\left[2\sqrt{\frac{\gamma^5}{1-\gamma}} + 2\gamma^2 + \gamma - 3\right] . \tag{4.27}$$

As far as our investigations are concerned, considering the air exchange rates depending on temperature differences for three different window tilting scenarios, Fig. 4.37 shows that the representation of the measured data by a square root function reflects also our cases of tilted windows without the influence of wind quite well. The trends, however, nonetheless seem to be different in our cases inasmuch as an onset value for ΔT seems to exist which must be exceeded to set the ventilating airflow into motion. Therefore, we perform a model adaptation for the mathematical description of purely thermally induced air exchange for the case of tilted windows using

$$ACH = A_{th}\ \sqrt{\Delta T - \Delta T_{crit}}\ , \tag{4.28}$$

where A_{th} and ΔT_{crit} are constants and $\Delta T := T_i - T_o$.

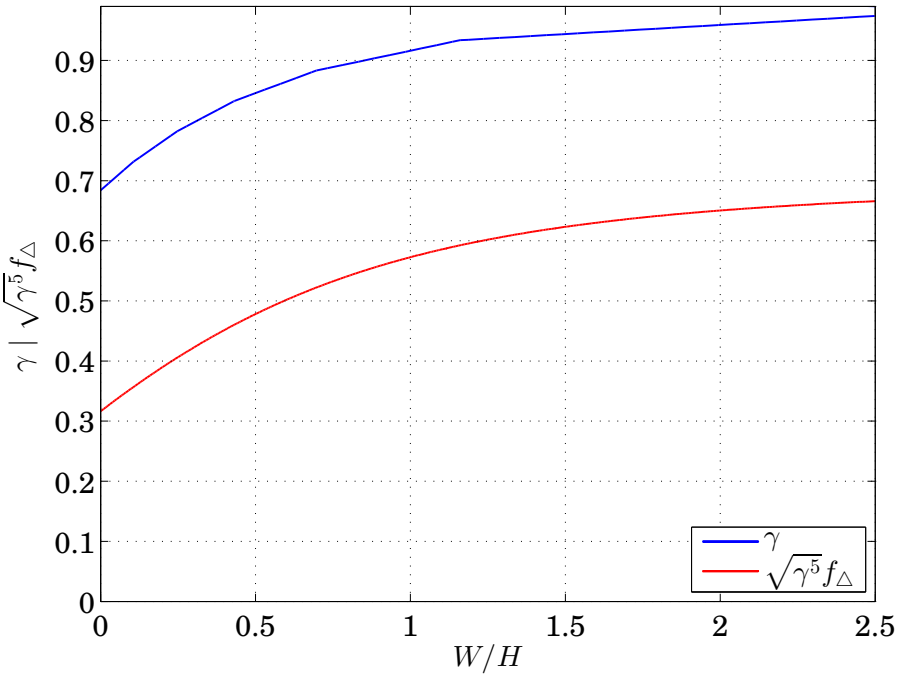


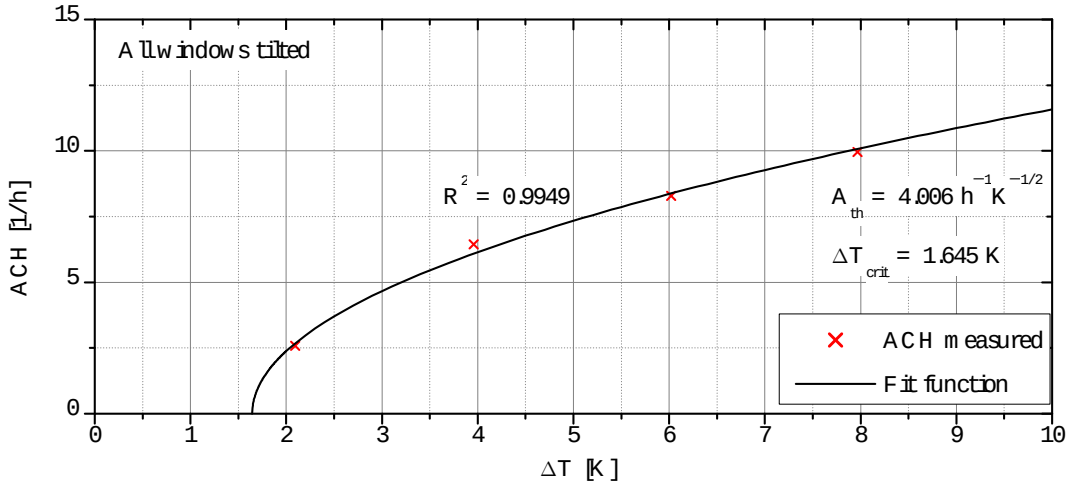
Figure 4.36: Plot of γ and $\sqrt{\gamma^5} f_{\triangle}$ depending on the ratio W/H. According to Daler et al. (1984).

For all three different tilting scenarios, Fig. 4.37 shows that a temperature change in the lower region (left) generates a far greater change in the air exchange rate than in the upper region (right). Further, the parameter ΔT_{crit} seems to describe the minimum temperature difference, which has to be exceeded in general to make an air exchange possible at all. The phenomenology that flows driven by thermally induced buoyancy need a certain minimum driving temperature difference before they can become effective was also found in Ruck (1993).

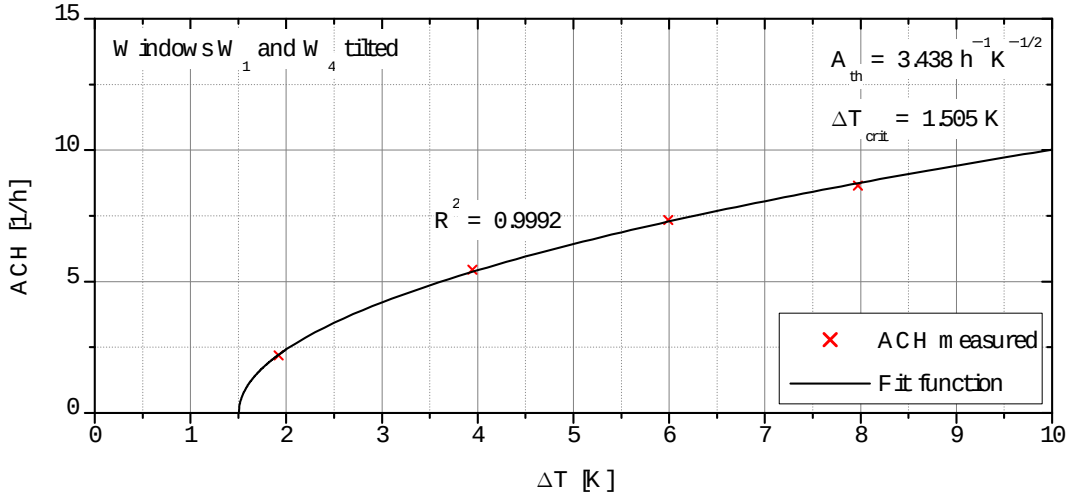
Fig. 4.38 shows a fluid in between two large, horizontal plates with different temperatures T_1 and T_2. Considering the case (a) $T_2 > T_1$, the density decreases in the direction of the gravitational force. According to Incropera and De Witt (2002), the conditions in this particular case are unstable, if the temperature difference exceeds a critical value. Buoyancy forces have the ability to overcome the decreasing influence of viscous forces. Because the gravitational force on the denser fluid in the upper layers is larger than that affecting the lighter fluid in the lower layers, the heavier fluid descends, being warmed up in the meantime, while the lighter one arises, cooling down thereby. For the case (b) $T_1 > T_2$, the density does not decrease in direction of the gravitational force, which leads to stable conditions without bulk fluid motion. In the former case the heat transfer from the lower plate to the higher one occurs by free convection, while in the latter case it occurs from the higher plate to the lower one by conduction.

The concept of a critical Rayleigh number Ra_{crit} dependent on a critical temperature difference ΔT_{crit}, which must be exceeded for the existence of thermal convection, is also reflected in Bergmann and Schäfer (2001). This critical Rayleigh number Ra_{crit} depends on both the geometry and the boundary conditions of the relevant configuration. According to Oertel (2013) the critical Rayleigh number increases in a convection container heated from the bottom, since the vertical boundary conditions of the horizontal temperature layer have a stabilizing effect due to the additional friction and delay the onset of convection. If the temperature difference, and thus the Rayleigh number as the characteristic variable, increases, at sufficiently large temperature differences disturbances develop, the temperature stratification becomes unstable, and heat is transferred by convection through the fluid.

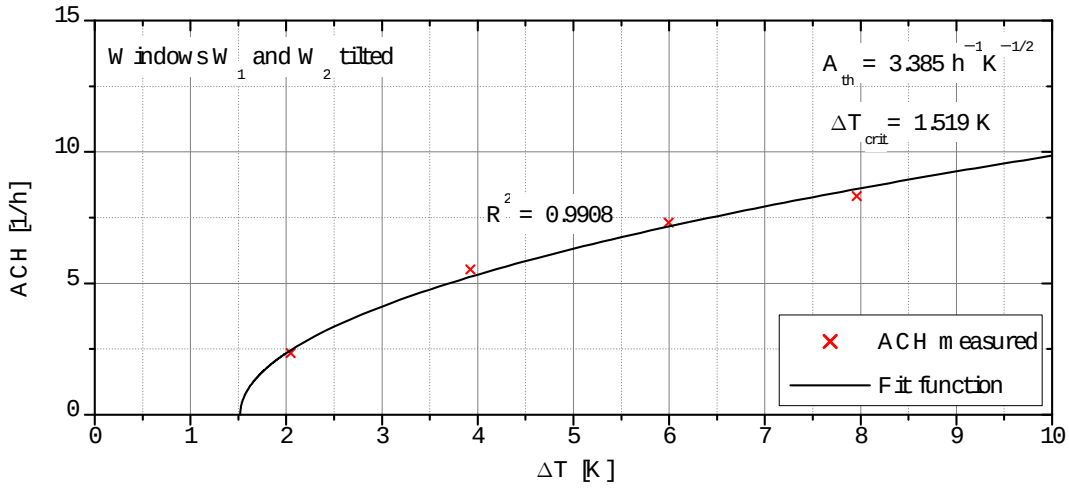
Kaczorowski (2009) examined turbulent thermal convection for $Ra \leq 2.31 \times 10^8$ in both rectangular containers and cubes. After Kaczorowski (2009) the influence of



(a)



(b)



(c)

Figure 4.37: Up-scaled purely thermally driven air exchange rates compared to the fit function $ACH = A_{th}\sqrt{\Delta T - \Delta T_{crit}}$, for (a) all windows, (b) windows W_1 and W_4, and (c) W_1 and W_2 tilted.

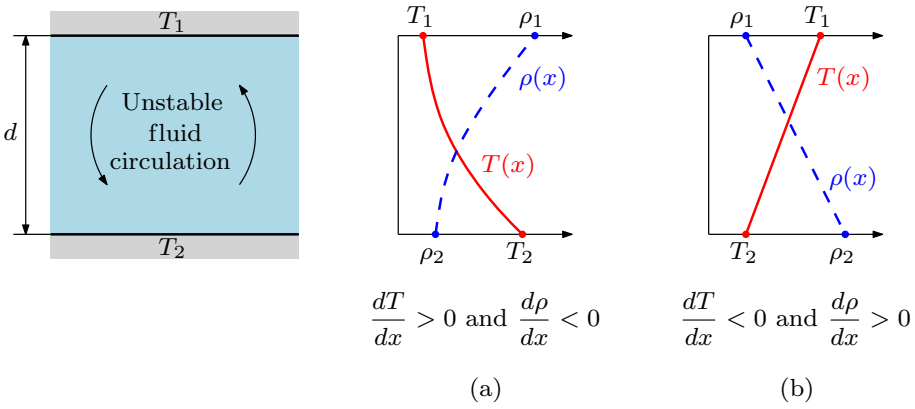


Figure 4.38: Fluid conditions in between large horizontal plates of different temperatures. (a) Unstable, and (b) stable temperature gradient. According to Incropera and De Witt (2002).

the side walls of the room model may be neglected for large ratios of the length to the height of the model (exemplarily expressed in this work is a ratio of $L/H \approx 247$). For an aspect ratio of $L/H \approx 2.7$, as present in our case, the effect of the walls cannot be neglected, because their influences determine the flow significantly.

As already mentioned above, the vertical side walls stabilize the basic solution, since the instabilities of the velocity field are damped due to the no slip condition. The convection, therefore, begins considerably later. Adiabatic boundary conditions, however, lead to an earlier onset of convection, since temperature instabilities are not damped by the wall in this case.

According to Kaczorowski (2009), a comparison of the different geometries investigated (rectangular, cubic, etc.) indicates that the properties of the heat transport align to each other with increasing Rayleigh number. The differences in the flow field at low Rayleigh numbers are attributable to the influence of the geometry. From the comparison of the heat transfer rates Kaczorowski (2009) concludes the existence of a Rayleigh number $Ra = 2 \times 10^7$, for which the characteristic turbulent structures are a lot smaller than the characteristic length scale of the geometry and, thus, the heat transfer is independent of the geometry.

In our study, we obtain critical Rayleigh numbers

$$Ra_{crit} = Gr \cdot Pr = \frac{g\beta}{\nu a} \Delta T_{crit} H_{M,i}^3 \leq 2.26 \times 10^6 \ , \tag{4.29}$$

where ΔT_{crit} is the critical minimum driving temperature difference (depicted in Fig. 4.37) and $H_{M,i}$ the inner height of the model room (cf. Table 4.4 and Eq. (2.114)). Thus, there exists an influence of the geometry in our case. The magnitude of this critical Rayleigh number is consistent with the investigations of square cavities with heated vertical walls and conducting horizontal walls by Jones and Briggs (1989) (as cited in Xin and Quéré (2006)), in which a first time-periodic flow was observed at $Ra_{crit} = 3 \times 10^6$.

Lord Rayleigh attributed the onset of convection to the instability of the fluid layer against disturbances with a characteristic wavelength. The shape and type of the resulting structures, also referred to as Bénard cells, are characterized by the boundary conditions and the wavelength of the instability (Kaczorowski, 2009). Plotting the state of the system as a function of the Rayleigh number Ra, we obtain various critical Rayleigh numbers that define the transitions between different states. This transitions take the form of bifurcations (cf. Fig. 4.39). Different states, which differ from the ground states with small Ra numbers, are caused by the instability of the system. There exist many values for the Ra number marking the onset of instabilities. At high Rayleigh numbers, the system behaves turbulent (Willers, 2011).

Using the Boussinesq approximation, the Rayleigh-Bénard system can analytically be solved up to a certain extent. With a linear stability analysis for small Ra numbers the width of the convection rolls and in particular the critical Ra number can actually be calculated. Exact calculations are beyond the scope of this work and can be found in Chandrasekhar (1981) and Lülff (2011). The critical Rayleigh number Ra_{crit}, as

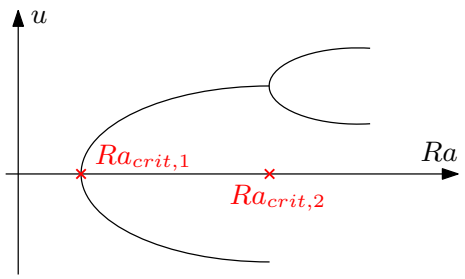


Figure 4.39: Schematic representation of the bifurcations occurring by a change of Ra. Referring to Willers (2011).

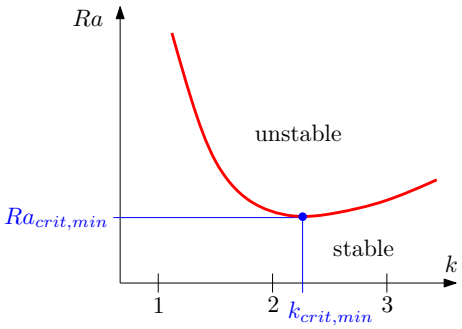


Figure 4.40: Schematic representation of the Rayleigh number depending on the dimensionless wave number k. Referring to Lülff (2011).

already discovered in 1916 by Rayleigh, is characterized by

$$Ra_{crit} = \frac{(k_{crit}^2 + \pi^2)^3}{k_{crit}^2} \,, \tag{4.30}$$

wherein the dimensionless critical wave number k_{crit} or the dimensionless critical wave length $\lambda_{crit} = 2\pi d/k$ specify the horizontal expansion of the convection rolls (d is the distance between the horizontal plates in Fig. 4.38) . The first instability corresponds to the first critical Ra number (cf. Fig. 4.39). The critical Rayleigh number thus depends on the aspect ratio width to height of the convection rolls and has a minimum at $k_{crit,min} = \pi/\sqrt{2}$, or in other words at $\lambda_{crit,min} = 2\sqrt{2}$, which corresponds to an aspect ratio of width/height $= \sqrt{2} : 1$ and yields

$$Ra_{crit,min} = \frac{27}{4}\pi^4 \approx 657.5 \tag{4.31}$$

as the first instability for two free horizontal boundaries (cf. Fig. 4.40 and Lülff (2011)). For two rigid horizontal boundaries the first critical Rayleigh number, regardless of the used medium, is $Ra_{crit} = 1708$. The convection rolls develop immediately at the critical Rayleigh number in the entire horizontal layer confirming that the resulting convection starts absolutely unstable (Oertel, 2013). Vertical walls, as they are present in our case of the room model, have a stabilizing effect influencing the flow significantly, as already mentioned above (Oertel, 2013).

The values for solely thermally induced air exchange rates, obtained in the present work, are much higher than those prescribed in the Austrian standard ÖNORM B 8110-3 (1999), where very small fixed temperature-independent ACH values between 1 h^{-1} and 3 h^{-1} are given, depending only on the window locations on (different)

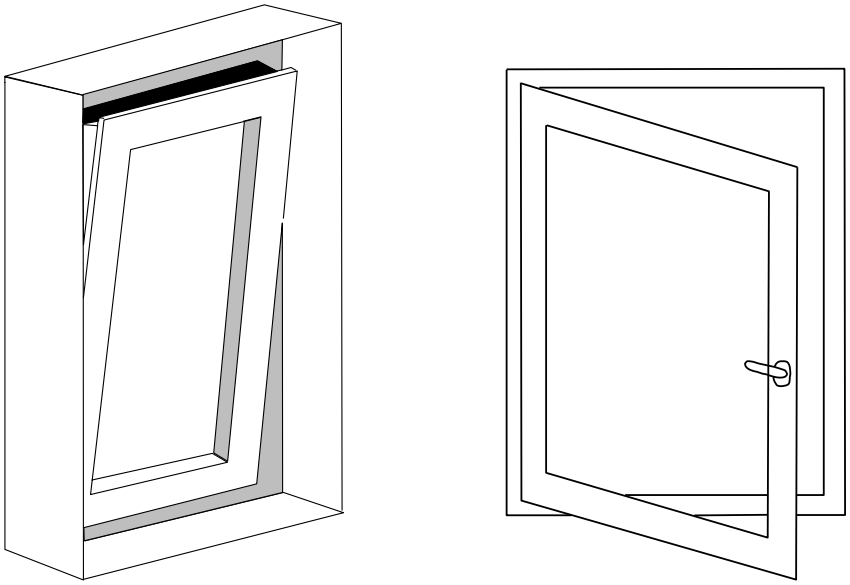


Figure 4.41: Sketch of (a) a tilted window with an embrasure and (b) a pivoted sash window (not fully opened), according to Hall (2004).

facade surfaces.

Maas (1995) and Hall (2004) have studied the air exchange through windows with different tilting angles for temperature differences 0 K $\leq \Delta T \leq$ 20 K and compared their results with those of Daler et al. (1984). According to Maas (1995) and Hall (2004), the case of a pivoted sash window (cf. Fig. 4.41(b)) results in a much larger air exchange rate than a tilted window (cf. Fig. 4.41(a)). At approximately the same opening area of tilted and pivoted sash windows, the air exchange rate of a tilted window reaches only about 60% of the value for a pivoted sash window, which is confirmed by Daler et al. (1984).

4.6.4 Impact of wind driven air exchange in thermal building simulations of the sample storey

Since ACH values are input parameters in thermal building simulations, they have an impact on the planning process of a building. Either infiltrations, which can only be estimated, or the ventilation power of a mechanical HVAC system, or the air volume exchange of a natural ventilation concept using defined openings like windows, are

expressed by the ACH values. From a practical and energy saving point of view, natural ventilation concepts for residential buildings in Austria using windows as the ventilation openings are only reasonable for the summer period. For comparison of the impact of the different ACH values, an artificial scenario was defined, for which thermal building simulations of the representative sample storey with the cross section shown in Fig. 3.1 were carried out by the industrial partner of the underlying research project, the Dr. Pfeiler GmbH in Graz, using the software package Design Builder Version 3.0.0.105, utilizing Energy Plus Version 7.0.0.036 for computations.

The summer season (beginning of April to end of September, i.e. 6 months) was chosen as the simulation period. Both fully open and tilted windows were represented by the corresponding ACH, which were either taken from the standards ÖNORM B 8110-3 (1999, 2012) or from the results of Section 4.5.1. In the defined artificial simulation scenario, a constant wind with velocity $u_{10} = 2.8$ m/s according to the numerical simulations done by the Austrian Institute of Technology was assumed as an external weather condition for the whole period of 6 months. This is the meteorologically most probable wind velocity in Vienna in a ten-years average over all wind directions. The wind-driven ACH values of Section 4.5.1 are due to an inlet velocity of 3.6 m/s which corresponds to a sample storey on the 3^{rd} floor exposed to $u_{10} = 2.8$ m/s. Furthermore the air temperatures and the solar radiation of the very hot summer of 2003 (test reference year 2003) from April until September were used. The following additional assumptions on the storey used in the simulations are listed:

- No heat flux through floor or ceiling (i.e. adiabatic boundary condition for these surfaces)
- No flow obstructions (i.e. insect screens) in the window cross sections
- Optimal sun protection system (i.e. no direct irradiation through the windows into the room)
- Ventilation profile: windows of a room are open or tilted as long as the outside air temperature is below the inside room temperature
- Profile of internal loads for residential buildings as prescribed in ÖNORM B 8110-3 (1999, 2012)

- Values for the overall heat transfer coefficient k derived for default material data, wall thicknesses and the fixed convective heat transfer coefficients:
  - outside walls of the storey: 0.35 W/m^{2}K
  - interior walls between rooms: 0.9 W/m^{2}K
  - window with its frame: 1.4 W/m^{2}K
  - window total energy transmittance $g = \tau_e + q_i$, defined as the fraction of incoming solar energy transmitted to the room (τ_e is the direct solar transmittance, q_i is an internal heat transfer factor including thermal radiation and convective heat transfer; cf. Manz (2004)): 0.56
- Fixed convective heat transfer coefficients, prescribed according to Karava et al. (2004) and Seifert et al. (2006):
  - outside walls of the storey: exterior 25 W/m^{2}K, interior 7.7 W/m^{2}K
  - interior walls between rooms: at every side 7.7 W/m^{2}K
  - window with its frame: exterior 25 W/m^{2}K, interior 7.7 W/m^{2}K

According to ÖNORM B 8110-3 (1999, 2012), the maximum room temperatures during the day between 6 am and 10 pm of 27°C and during the night between 10 pm and 6 am of 25°C should not be exceeded.

Simulations were carried out for

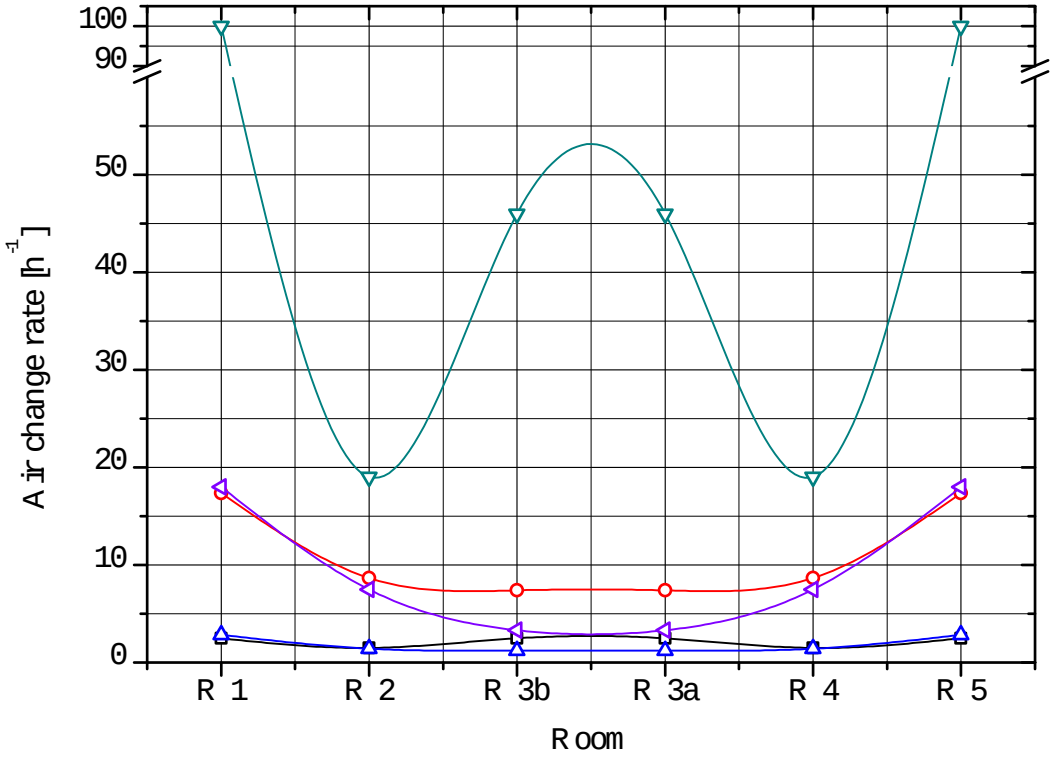
(1) ACH values taken for open windows without temperature differences according to ÖNORM B 8110-3 (1999),

(2a) ACH values calculated with temperature differences for fully open windows according to ÖNORM B 8110-3 (2012),

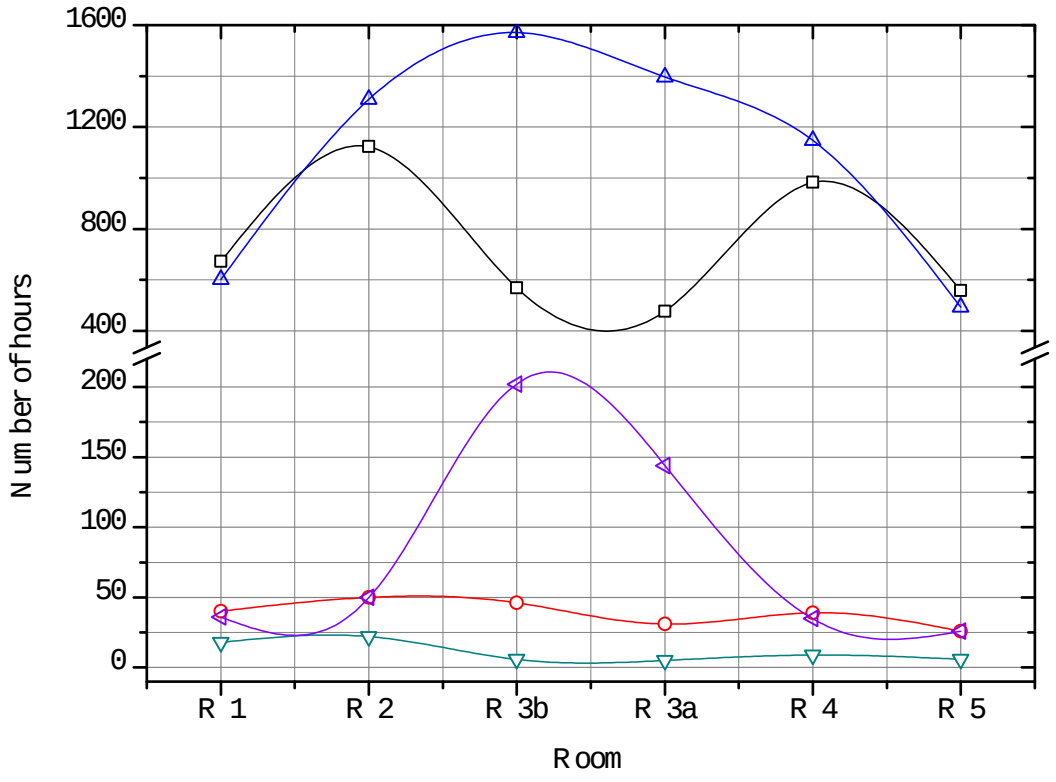
(2b) ACH values calculated with temperature differences for tilted windows according to ÖNORM B 8110-3 (2012),

(3a) ACH values for fully open windows with results from CFD and wind tunnel measurements,

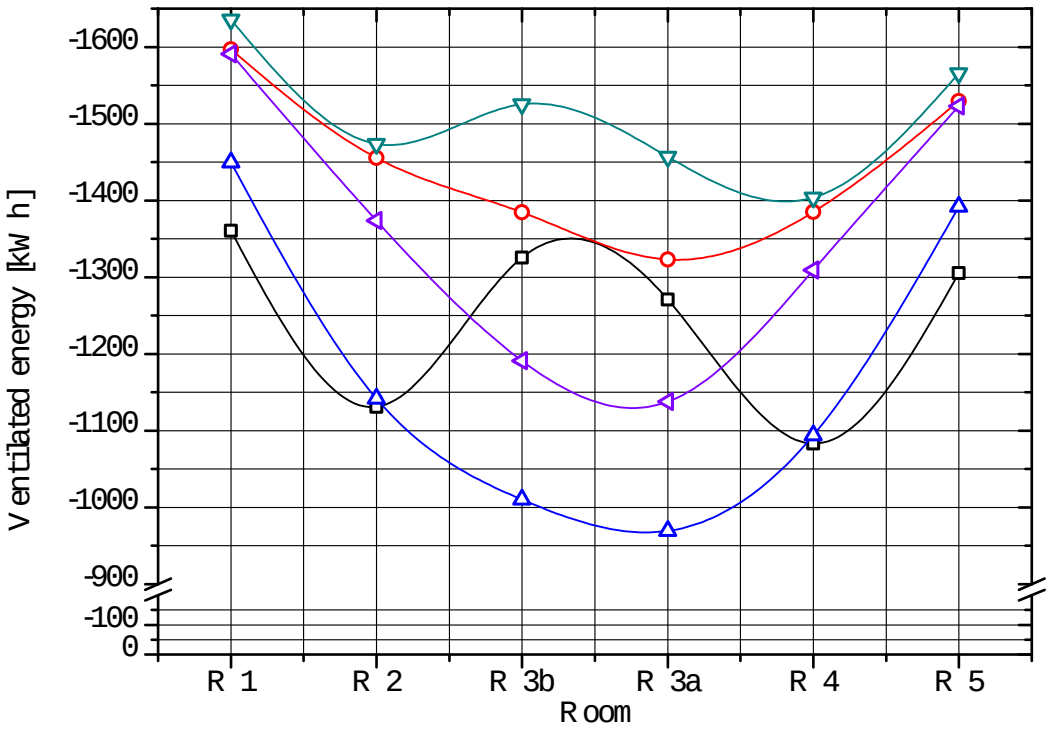
(3b) ACH values for tilted windows with results from CFD and wind tunnel measurements.


100
90
50
40
30
20
10
0
Air change rate [h-1]
R 1
R 2
R 3b
R 3a
R 4
R 5
Room

(a)


1600
1200
800
400
200
150
100
50
0
Number of hours
R 1
R 2
R 3b
R 3a
R 4
R 5
Room

(b)



(c)

(1) ÖNORM B 8110-3, windows fully open (ÖNORM B 8110-3, 1999).

(2a) ÖNORM B 8110-3, windows fully open, considering temperature differences, doors D_1, D_2 open, window W_7 closed (ÖNORM B 8110-3, 2012).

(2b) ÖNORM B 8110-3, windows tilted, considering temperature differences, doors D_1, D_2 open, window W_7 closed (ÖNORM B 8110-3, 2012).

(3a) Simulation, with results from CFD & wind tunnel experiments, windows fully open, inflow velocity 3.6 m/s, doors D_1, D_2 open, window W_7 closed.

(3b) Simulation, with results from CFD & wind tunnel experiments, windows tilted, inflow velocity 3.6 m/s, doors D_1, D_2 open, window W_7 closed, incidence angle: 180°.

Figure 4.42: (a) Input ACH for each room in the thermal simulations of the sample storey, (b) resulting number of hours per room in which the temperature limits were exceeded, (c) the resulting amount of ventilated energy. According to Teppner et al. (2014a).

In Fig. 4.42(a) the ACH values used in the simulations of the artificial scenario are graphically shown. There, (3a) maps a situation with open windows and the smallest ACH for each room over all examined incidence angles. In contrast, for the situation with tilted windows in (3b), as an arbitrary example it was chosen to use the ACH values of an incidence angle of 180° (Fig. 4.19(d)) in each room of the storey. For (3a) it has to be noted that the software package Design Builder restricts the ACH value to a maximum of 100 h^{-1}. For higher ACH, as obtained from the experiments and CFD, therefore, this maximum value was used in the simulations.

The simulation results in Fig. 4.42(b) show the number of hours during the summer period, in which for the chosen artificial scenario the given maximum room temperatures were exceeded. In Fig. 4.42(c) the amount of ventilated energy according to $Q \cdot \Delta t = \rho c_p \cdot ACH \cdot V_R(T_i - T_o) \cdot \Delta t$ for the simulation period Δt of 6 months is depicted.

In the framework of the assumed artificial scenario, the results quantify the impact of assuming different (wind-driven, temperature-driven) ACH values in thermal building simulations. In Fig. 4.42 the red symbols stand for results with the ACH values depicted in Fig. 4.19(d). Since rooms R_{3a} and R_{3b} show the lowest ACH values, they have the highest number of hours with exceeded temperature limits. For the configuration with open windows (green symbols) this effect is not seen, since for each room the lowest ACH value out of all incidence angles was chosen in the simulations. The difference between using ACH values according to the applicable standards and using wind driven values is clearly depicted. This implies that an enhanced estimation of ACH values, taking the local external wind situation of a residential building into account, could enhance the prediction quality concerning the overheating during the summer period.

In the design of natural ventilation concepts for the prevention of high room temperatures during summer, the proper estimation of ACH values depending on the environmental conditions (wind driven, temperature driven) is of crucial importance. According to ÖNORM B 8110-3 (1999, 2012), the maximum room temperatures of 27°C during the day between 6 am and 10 pm and of 25°C during the night between 10 pm and 6 am should not be exceeded. The impact of the ACH on the predicted overheating (cf. Fig. 2.26) during a summer period was clearly shown by these thermal building simulations.

Chapter 5

Summary and Conclusions

Experimental investigations and numerical simulations to determine the air exchange rate in natural ventilation of a 10-storey residential building model in 1:75 scale in a suburban area, as well as detailed investigations on a sample storey model in 1:25 scale and a single room model in 1:10 scale, are the subject of the present work. The velocity profile of the natural wind, typical for a suburban area, was simulated in the boundary layer wind tunnel of the Institute of Fluid Mechanics and Heat Transfer at Graz University of Technology for different wind velocities and angles of incidence.

The pressure profile on the building envelope was measured using pressure sensors. Distributions of the pressure coefficient and non-dimensional force coefficients were calculated. Both show very good agreement with results from the literature, validating the quality of the present wind tunnel study.

According to the pressure differences obtained from these measurements in the boundary layer wind tunnel, the airflow velocities were exemplarily measured at the height of the diagonal intersection point of the rectangular window cross sectional area for the 3^{rd} and 8^{th} building storey for two reference velocities and four incidence angles. This was done on a sample storey model in 1:25 scale in the aerodynamic wind tunnel of the institute.

Numerical simulations were performed in parallel, on the one hand to obtain values comparable to the measured data, and on the other hand in order to gain insight into the large-scale flow structure around and inside the model, which was impossible by means of the measurements.

Measurements in the open cross sections of tilted windows were then realised in the single room model in 1:10 scale with three velocity sensors mounted in the gaps of each of the tilted windows. Several different wind velocities, incidence angles and tilting scenarios of the windows were investigated. The air exchange rate was obtained by calculating the volumetric flow rate as products of the measured velocities with the appropriate either lateral triangular areas or the rectangular area overhead, taking the determined flow direction into account. Furthermore, heating foils acting as a floor heating system were installed in the single room model in order to investigate thermally driven air exchange caused by temperature differences between indoor and environment.

The tracer gas measurement technique, using carbon dioxide as the tracer gas, was used as an alternative measurement method for wind driven air exchange. On the basis of physical modelling, the used concentration-decay method is explained in detail. Different wind velocities, wind directions, and tilting scenarios of the windows were considered as the relevant parameters using the single room model in 1:10 scale.

In summary, the following findings can be stated:

- For flows in real dimensions with the same upstream velocity as in the model, a scaling law determines the air exchange rate in real dimensions as follows: the air exchange rate in real dimensions is found as the air exchange rate in the model scale multiplied by the geometrical scaling factor. This scaling law proved for experiments of different scale and, independently, for numerical flow simulations of different scale.

- In addition to the wind velocity magnitude, the air exchange rate depends on the specific location of the openings of a room in relation to the local external flow and pressure situations, which is determined by the incidence angle.

- The solely wind-driven air exchange rate and, hence, the volumetric air flow rate, for incidence angles between 0° and 90° is proportional to the wind velocity acting on the model, agreeing well with results from the according literature.

- A model $ACH(\alpha, U_\infty) = a_1 + a_2 U_\infty + (b_1 + b_2 U_\infty)\cos^2(2\alpha)$ for the air exchange rate depending on the incidence angle α and the inflow velocity U_∞ was developed.

- Considering solely temperature differences as the driving mechanism, in literature a proportionality of the air exchange rate to the square root of the temperature difference between inside and outside temperature is specified. In the present study we found that a critical Rayleigh number Ra_{crit} and, thus, a critical temperature difference ΔT_{crit}, must be exceeded so that thermal convection is set in motion at all, which is not reflected in some literature. The proportionality of the ACH to $\sqrt{\Delta T}$ is unable to reflect this phenomenon. Our finding may be seen as an advancement of the knowledge in this respect. Critical Rayleigh numbers of $\mathcal{O}(10^6)$, found in our experiments, match well with results from literature obtained by numerical simulations for similar geometries.

- Air exchange rates influenced by thermal and wind effects simultaneously do not superimpose in an additive way. For low wind velocities, in case of simultaneous impact of thermal buoyancy and wind, the temperature effect predominates for $Gr/Re^2 \gg 1$. In contrast, for $Gr/Re^2 \ll 1$ the velocity of the wind is the driving quantity. For $Gr/Re^2 \approx 1$, the combined effects of free and forced convection have to be considered.

- In the design of natural ventilation concepts with respect to the prevention of high room temperatures during summer, the proper estimation of air exchange rate values depending on the environmental conditions (wind-driven, temperature-driven) is of crucial importance. For cross ventilation through tilted windows, the temperature-driven air exchange rate was found to be 3 times those prescribed in the Austrian standard Ö-NORM B 8110-3 version 2012. The impact on the predicted overheating during a summer period was clearly shown by thermal building simulations.

As for subsequent research in this field, using an optical method like particle image velocimetry could yield a detailed insight in the complex flow structure within the building, in particular the change of the flow behaviour close to the openings could therefore be better explained. Furthermore, investigations of the air exchange rate (wind driven and / or thermally induced) between two or more storeys of a building could provide interesting new results. Concerning the critical Rayleigh number, which has to be exceeded to activate thermal convection, studies of different geometries at different boundary conditions to quantify the influence of vertical side walls would be of great value.

Bibliography

R.E. Akins and J.A. Peterka. Mean force and moment coefficients for buildings in turbulent boundary layers. *Journal of Wind Engineering and Industrial Aerodynamics*, 2:195–209, 1977.

F. Allard. *Natural ventilation in buildings. A design handbook*. James and James (Science Publishers) Ltd, London, 2002.

C. Allocca, Q. Chen, and L.R. Glicksman. Design analysis of single-sided natural ventilation. *Energy and Buildings*, 35:785–795, 2003.

Ansys. Ansys fluent user's guide, release 14.0, 2011. URL `http://www.ansys.com`.

O.S. Asfour and M.B. Gadi. A comparison between cfd and network models for predicting wind-driven ventilation in buildings. *Building and Environment*, 42: 4079–4085, 2007.

ASHRAE. *Handbook of Fundamentals, System International Edition*. American Society of Heating, Refrigerating and Air-Conditioning Engineers, Atlanta, 2009.

M.N. Assimakopoulos, A. Tsangrassoulis, G. Mihalakakou, M. Santamouris, and Serge Jauré. Development of a control algorithm to optimize airflow rates through variable size windows. *Energy and Buildings*, 34:363–368, 2002.

L. Bergmann and C. Schäfer. *Lehrbuch der Experimentalphysik, Bd. 7, Erde und Planeten*. de Gruyter, Berlin, 2001.

R.B. Bird, W.E. Stewart, and E.N. Lightfoot. *Transport Phenomena*. John Wiley & Sons, 2007.

M. Cadloni and M. Ferrazzini. Natürlicher Luftaustausch durch Kippfenster. Master's thesis, ETH Zurich, 1997.

J.E. Cermak, editor. *Physical modelling of the atmospheric boundary layer (ABL) in long boundary layer wind tunnels (BLWT)*, Gaithesburg, Maryland, USA, 1982. In Proc. of the Int. Workshop of Wind Tunnel Modelling for Wind Engineering Applications.

S. Chandrasekhar. *Hydrodynamic and hydromganetic stability*. Dover Publications, New York, 1981.

P.S. Charlesworth. *Air Exchange Rate and Airtightness Measurement Techniques – An Applications Guide*. Air Infiltration and Ventilation Centre, Coventry, 1988.

C.R. Chu and B.F. Chiang. Wind-driven cross ventilation with internal obstacles. *Energy and Buildings*, 67:201–209, 2013.

N.J. Cook. *The desinger's guide to wind loading of building structurs, Part 1*. Butterworths, BRE London, 1985.

N.J. Cook. Letter to the editor: Jensen number; a proposal. *Journal of Wind Engineering and Industrial Aerodynamics*, 22:95–96, 1986.

J. Counihan. An improved method of simulating an atmospheric boundary layer in a wind tunnel. *Atmospheric Environment*, 3:197–214, 1969.

J. Counihan. Wind tunnel determination of the roughness length as a function of the fetch and the roughness density of three-dimensional roughness elements. *Atmospheric Environment*, 5:637–642, 1971.

H. Daler, E. Hirsch, F. Haberda, U. Knöbel, and W. Krüger. Bestandsaufnahme von Einrichtungen zur freien Lüftung im Wohnungsbau, Forschungsbericht T84-028. *Federal Ministry of Research and Technology, Germany*, pages ISSN–0340–7608, 1984.

E. Dascalaki, M. Santamouris, A. Argiriou, C. Helmis, D.N. Asimakopoulos, K. Papadopoulos, and A. Soilemes. Predicting single sided natural ventilation rates in buildings. *Solar Energy*, 55:327–341, 1995.

A.G. Davenport. The relationship of wind structure to wind loading. In *1st Conference on Wind Effects on Building and Structures*, number 16, 1963.

W. Demtröder. *Experimentalphysik 2. Elektrizität und Optik*. Springer-Verlag Berlin Heidelberg, 2009.

D. Etheridge and M. Sandberg. *Building Ventilation. Theory and Measurement*. John Wiley Sons Ltd, England, 1996.

D. Etling. *Theoretische Meteorologie. Eine Einführung*. Springer, Berlin Heidelberg, 2002.

K. Fitzner. *Raumklimatechnik. Band 4: Physik des Gebäudes*. Springer-Verlag, Berlin Heidelberg, 2013.

R.W. Fox, P.J. Pritchard, and A.T. McDonald. *Introduction to Fluid Mechanics, 7th ed.* John Wiley Sons, 2010.

G. Fracastoro, G. Mutani, and M. Perino. Experimental and theoretical analysis of natural ventilation by windows opening. *Energy and Building*, 34:817–827, 2002.

W. Gretler and W. Meile. Der 2m-Windkanal am Institut für Strömungslehre und Gasdynamik der Technischen Universität Graz. *Österreichische Ingenieur- und Architektenzeitschrift*, 3:90–96, 1993.

C. Gromke. *Einfluss von Bäumen auf die Durchlüftung von innerstädtischen Straßenschluchten*. PhD thesis, University of Karlsruhe, 2008.

C. Gromke and B. Ruck. Die Simulation atmosphärischer Grenzschichten in Windkanälen. Technical report, University of Karlsruhe, Germany, 2005. Fachtagung "Lasermethoden in der Strömungsmesstechnik".

M. Hall. *Untersuchungen zum thermisch induzierten Luftwechselpotential von Kippfenstern*. PhD thesis, University of Kassel, 2004.

F.D. Heidt. Zur Messung des Luftwechsels mit Spurengasmethoden. *Bauphysik 9*, 6: 272–278, 1987.

F.D. Heidt and R. Rabenstein. Die Messung des externen und interzonalen Luftaustausches. In *Proceedings of the 7th International Solar Forum*, volume 1, pages 450–455, 1990.

P. Heiselberg, K. Svidt, and P.V. Nielsen. Characteristics of airflow from open windows. *Energy and Buildings*, 36:859–869, 2001.

J.M. Horan and D.P. Finn. Sensitivity of air change rates in a naturally ventilated atrium space subject to variations in external wind speed and direction. *Energy and Buildings*, 40:1577–1585, 2008.

W.-H. Hucho. *Aerodynamik stumpfer Körper. Physikalische Grundlagen und Anwendungen in der Praxis*. Vieweg Braunschweig/Wiesbaden, 2013.

A. Hunt. Wind tunnel measurements of surface pressure on cubical building models at several scales. *Journal of Wind Engineering and Industrial Aerodynamics*, 10: 137–163, 1982.

I.E. Idelchik. *Handbook of Hydraulic Resistance*. CRC Press, Boca Raton, 1994.

F.P. Incropera and D.P. De Witt. *Fundamentalsof heat and mass transfer*. John Wiley Sons Ltd, England, 2002.

A. Iqbal, P.V. Nielsen, A. Afshari, and P. Heiselberg. Numerical predictions of the discharge coefficient of a window with moveable flap. *10th International Conference on Healthy Buildings 3*, pages 2485–2490, 2012.

Y. Jiang, D. Alexander, H. Jenkins, R. Arthur, and Q. Chen. Natural ventilation in buildings: measurement in a wind tunnel and numerical simulation with large eddy simulation. *Journal of Wind Engineering and Industrial Aerodynamics*, 9: 331–353, 2003.

D.N. Jones and D.G. Briggs. Periodic two-dimensional cavity flow: effect of linear horizontal thermal boundary condition. *Journal of Heat Transfer*, 111:86–91, 1989.

M. Kaczorowski. *Untersuchung turbulenter thermischer Konvektion in kartesischen Geometrien mittels DNS und LES*. PhD thesis, Technical University of Illmenau, 2009.

P. Karava, T. Stathopoulos, and A.K. Athienitis. Wind driven flow through openings – a review of discharge coefficients. *International Journal of Ventilation*, 3:255–266, 2004.

P. Karava, T. Stathopoulos, and A.K. Athienitis. Wind-induced natural ventilation analysis. *Solar Engery*, 81:20–30, 2007.

F. Kemper. Einfluss der korrelationsbedingten Flächenabhängigkeit von quasistatischen Windersatzlasten auf die Tragwerksreaktionen nicht-schwingungs-anfälliger Konstruktionen. Master's thesis, RWTH Aachen, 2004.

W. Kühnel. *Differentialgeometrie. Kurven - Flächen - Mannigfaltigkeiten*. Vieweg+Teubner, Wiesbaden, 2010.

H. Kiefer. *Windlasten an quaderförmigen Gebäuden in bebauten Gebieten*. PhD thesis, Universität Fridericiana zu Karlsruhe, 2003.

T.S Larsen. *Natural ventilation driven by wind and temperature difference*. PhD thesis, Aalborg University, Denmark, 2006.

T.S. Larsen and P. Heiselberg. Single-sided natural ventilation driven by wind pressure and temperature difference. *Energy and Buildings*, 40:1031–1040, 2003.

T.S. Larsen, N. Nikolopoulos, A. Nikolopoulos, G. Strotos, and K.-S. Nikas. Characterization and prediction of the volume flow rate aerating a cross ventilated building by means of experimental techniques and numerical approaches. *Energy and Buildings*, 43:1371–1381, 2011.

D. Laussmann and D. Helm. *Chemistry, Emission Control, Radioactive Pollution and Indoor Air Quality*, chapter Air Change Measurements Using Tracer Gases: Methods and Results. Significance of air change for indoor air quality, pages 365–406. INTECH open science, 2011.

T. Lawson. *Building Aerodynamics*. Imperial College Press London, 2001.

Y. Li and A. Delsante. Natural ventilation induced by combined wind and thermal forces. *Building and Environment*, 36(1):59 – 71, 2001.

P.E. Linden. The fluid mechanics of natural ventilation. *Annual Review of Fluid Mechanics*, 31:201–238, 1999.

J. Lülff. Statistische Eigenschaften turbulenter Rayleigh-Bénard-Konvektion. Master's thesis, University of Muenster, 2011.

L.J. Lo and A. Novoselac. Cross ventilation with small openings: Measurements in a multi-zone test building. *Building and Environment*, 57:377–386, 2012.

G.C.O. Lohmeyer and M. Post. *Praktische Bauphysik. Eine Einführung mit Berechnungsbeispielen*. Springer Vieweg, Heidelber Berlin, 2013.

A. Maas. *Experimentelle Quantifizierung des Luftwechsels bei Fensterlüftung*. PhD thesis, University of Kassel, 1995.

H. Manz. Total solar energy transmittance of glass double façades with free convection. *Energy and Buildings*, 36:127–136, 2004.

R. Martinuzzi. *Experimentelle Untersuchung der Umströmung wandgebundener, rechteckiger, prismatischer Hindernisse*. PhD thesis, Technische Fakultät der Universität Erlangen, 1992.

K.-S. Nikas, N. Nikolopoulos, and A. Nikolopoulos. Numerical study of a naturally cross-ventilated building. *Energy and Buildings*, 42:422–434, 2010.

N. Nikolopoulos, A. Nikolopoulos, T.S. Larsen, and K.-S.P. Nikas. Experimental and numerical investigation of the tracer gas methodology in the case of a naturally cross-ventilated building. *Building and Environment*, 56:379–388, 2012.

ÖNORM B 8110-3 (1999). Wärmeschutz im Hochbau - Teil 3: Wärmespeicherung und Sonneneinflüsse. Austrian Standards Institute, Vienna, 12 1999.

ÖNORM B 8110-3 (2012). Wärmeschutz im Hochbau - Teil 3: Vermeidung sommerlicher Überwärmung. Austrian Standards Institute, Vienna, 03 2012.

H. Oertel. Mein weg zum strömungsmechanischen modell. KIT Scientific Report 7649, University of Karlsruhe, 2013.

H. jr. Oertel. *Prandtl Führer durch die Strömungslehre*. Springer Vieweg, Wiesbaden, 2012.

M. Ohba, K. Irie, and T. Karabuchi. Study on airflow characteristics inside and outside a cross-ventilation model, and ventilation flow rates using wind tunnel experiments. *Journal of Wind Engineering and Industrial Aerodynamics*, 89: 1513–1524, 2001.

H.A. Panofsky. The athmospheric boundary layer below 150 meters. *Annual Review of Fluid Mechanics*, 6:147–177, 1974.

E.J. Plate. *Engineering meteorology: fundamentals of meteorology and their application to problems in environmental and civil engineering*, chapter Wind tunnel modeling of wind effects on structures in engineering, pages 573–639. Elsevier Scientific Publishing Company, 1982a.

E.J. Plate. *Abgasbelastungen durch den Kraftfahrzeugverkehr im Nahbereich verkehrsreicher Straßen.*, chapter Windkanalmodellierung von Ausbreitungsvorgängen in Stadtgebieten, pages 61–83. Verlag TÜV Rheinland, 1982b.

W. Raatschen. Was ist Lüftungseffektivität? *Ki Klima – Kälte – Heizung*, 5:226–231, 1988a.

W. Raatschen. Was ist Lüftungseffektivität? *Ki Klima – Kälte – Heizung*, 6:291–296, 1988b.

F. Reiher. Raumklima und thermische Behaglichkeit. *Berichte aus der Bauforschung Heft 104*, 1975.

C.-A. Roulet. *Ventilation and airflow in buildings: methods for diagnosis and evaluation*. Earthscan Publications Ltd., London, 2008.

B. Ruck. Wind-tunnel measurements of flow field characteristics around a heated model building. *Journal of Wind Engineering and Industrial Aerodynamics*, 50: 139–152, 1993.

H. Ruscheweyh. *Dynamische Windwirkung an Bauwerken, Band 1: Grundlagen*. Bauverlag, Wiesbaden, 1982.

H. Schlichting. *Boundary-Layer Theory*. McGraw-Hill Book Company, USA, 1979.

T. Schulze and U. Eicker. Controlled natural ventilation for energy efficient buildings. *Energy and Buildings*, 56:221–232, 2013.

J. Seifert, Y. Li, J. Axley, and M. Rösler. Calculation of wind-driven cross ventilation in buildings with large openings. *Journal of Wind Engineering and Industrial Aerodynamics*, 94:925–947, 2006.

H. Sockel. *Aerodynamik der Bauwerke*. Vieweg, Braunschweig, 1984.

H. Sockel. *Wind-excited vibrations of structures*. Springer, Udine, 1994.

J.H. Spurk. *Strömungslehre. Einführung in die Theorie der Strömungen*. Springer-Verlag, Berlin Heidelberg, 2010.

G.M. Stavrakakis, M.K. Koukou, M.Gr. Vrachopoulos, and N.C. Markatos. Natural cross-ventilation in buildings: Building-scale experiments, numerical simulation and thermal comfort evaluation. *Energy and Buildings*, 40:1666–1681, 2008.

A. Tecle, G.T. Bitsuamlak, and T.E. Jiru. Wind-driven natural ventilation in a low-rise building: A boundary layer wind tunnel study. *Building and Environment*, 59:275–289, 2013.

R. Teppner, B. Langensteiner, W. Meile, G Brenn, and S. Kerschbaumer. Air change rates driven by the flow around and through a building storey with fully open or tilted windows. In *Proceedings of the ANSYS Conference 9. CADFEM Austria Users' Meeting, online*, Vienna, 2014b.

R. Teppner, B. Langensteiner, W. Meile, G. Brenn, and S. Kerschbaumer. Flow around and through a building storey with fully opened or tilted windows. *2nd Central European Symposium on Building Physics, Vienna, Austria*, pages 717–724, 2013.

R. Teppner, B. Langensteiner, W. Meile, G. Brenn, and S. Kerschbaumer. Air change rates driven by the flow around and through a building storey with fully open or tilted windows: an experimental and numerical study. *Energy and Buildings*, 76: 640–653, 2014a.

VDI. Indoor air pollution measurement. measurement of the indoor air change rate. *VDI 4300 Part 7*, 2001.

J. Wegner. Untersuchungen des natürlichen Luftwechsels in ausgeführten Wohnungen, die mit sehr fugendichten Fenstern ausgestattet sind. *Gesundheits-Ingenieur*, 1: 1–5, 1983.

M. Wetter. Multizone airflow model in modelica. In C. Kral and A. Haumer, editors, *Proceedings of the 5th International Modelica Conference*, pages 431–440, Vienna, 2006.

C. Willers. Lagrange'sche Beschreibung der Rayleigh-Bénard-Instabilität, Bachelor thesis, University of Muenster, 2011.

S. Xin and P. Le Quéré. Natural-convection flows in air-filled, differentially heated cavities with adiabatic horizontal walls. *Numerical Heat Transfer, Part A*, 50: 437–466, 2006.

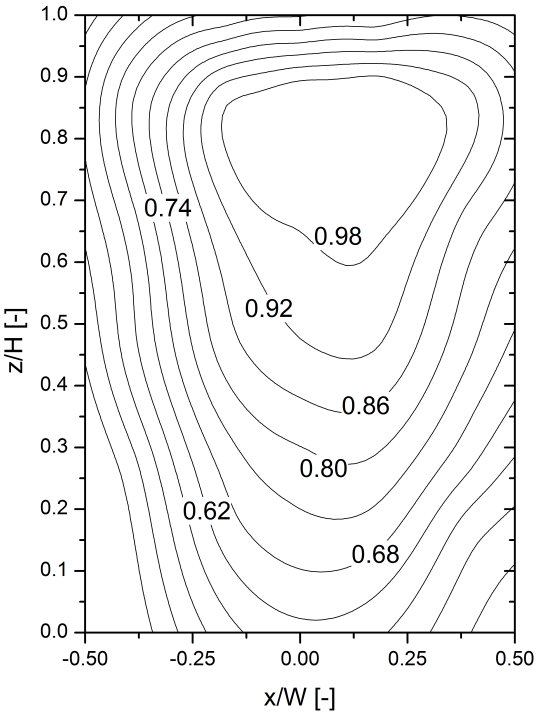
J. Zierep and K. Bühler. *Grundzüge der Strömungslehre. Grundlagen, Statik und Dynamik der Fluide*. Springer Vieweg, Wiesbaden, 2013.

Appendices

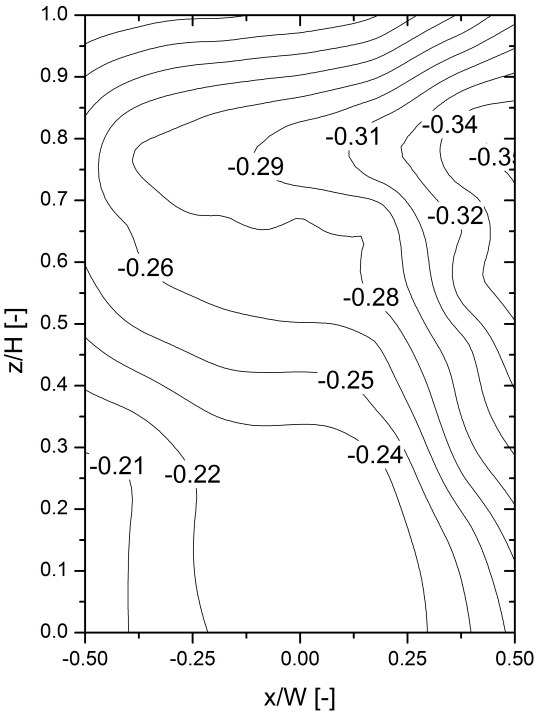
Appendix A

Pressure distribution

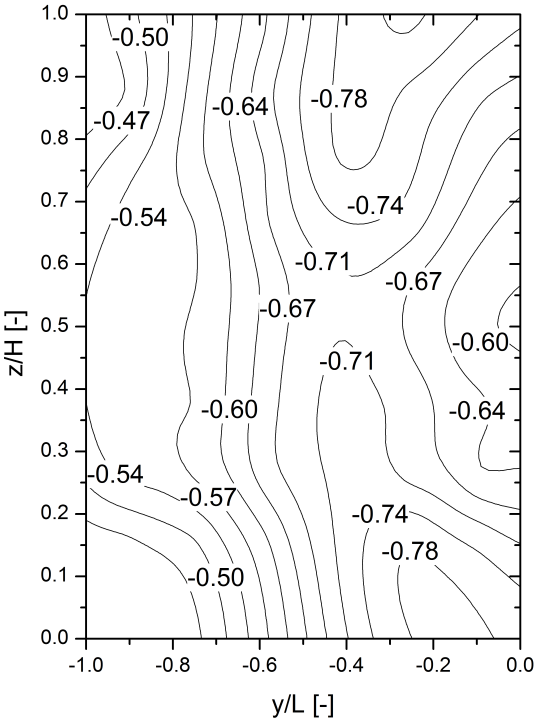
A.1 Distributions of the pressure coefficient



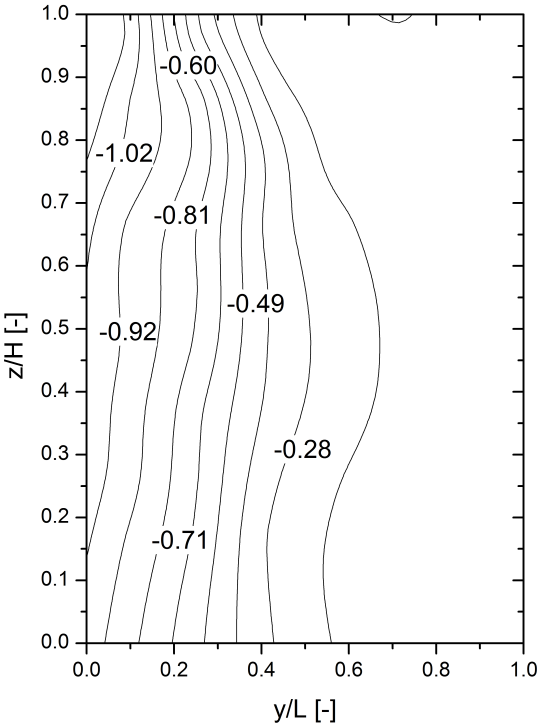
(a) View A. $R^2 = 0.996, SSE = 0.005$.



(b) View B. $R^2 = 0.962, SSE = 0.002$.

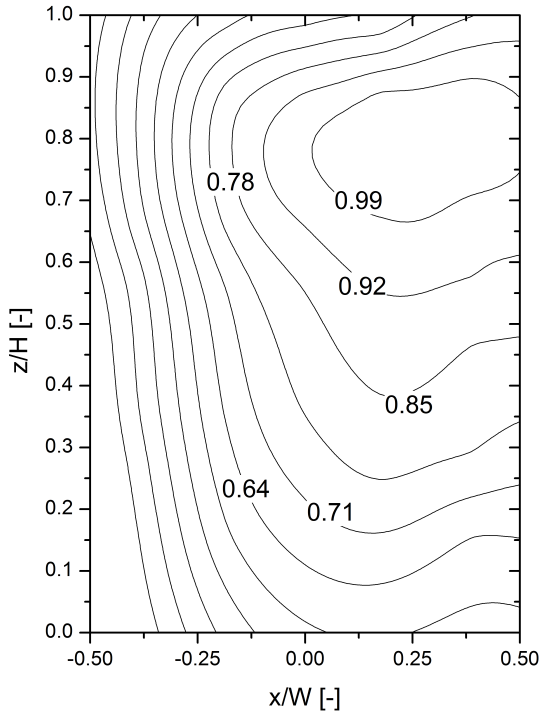


(c) View C. $R^2 = 0.960, SSE = 0.016$.

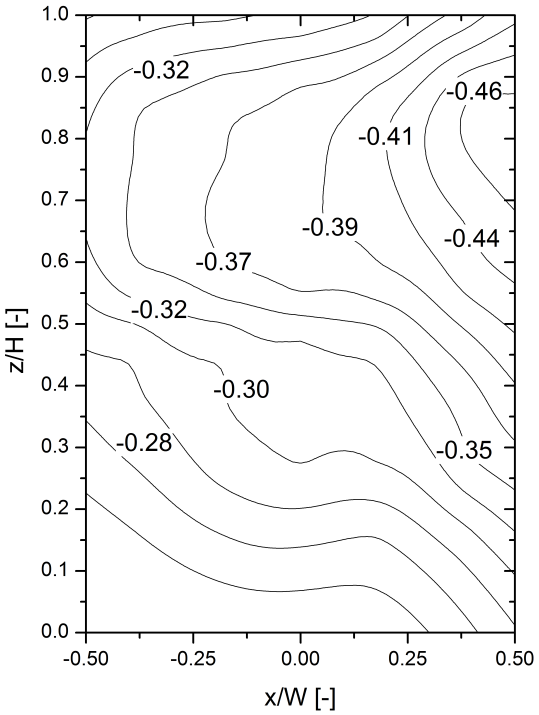


(d) View D. $R^2 = 0.977, SSE = 0.122$.

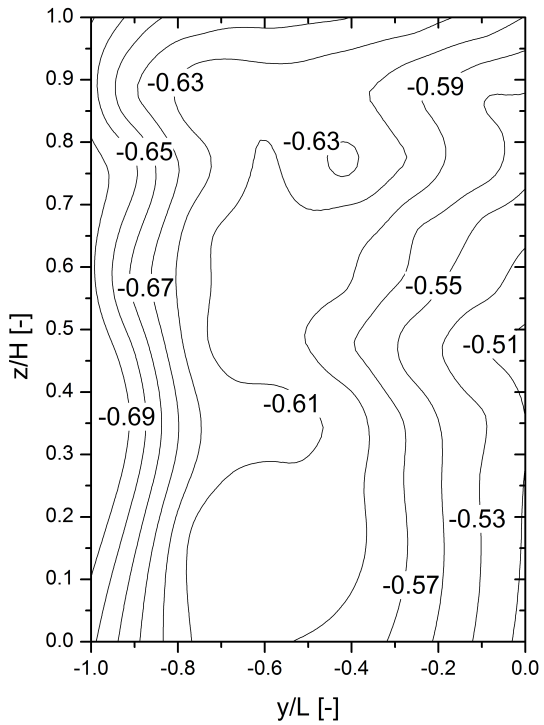
Figure A.1: Distribution of pressure coefficient c_p for an inflow velocity of $u_{10} = 4.7$ m/s and an incidence angle of $\alpha = 10°$.



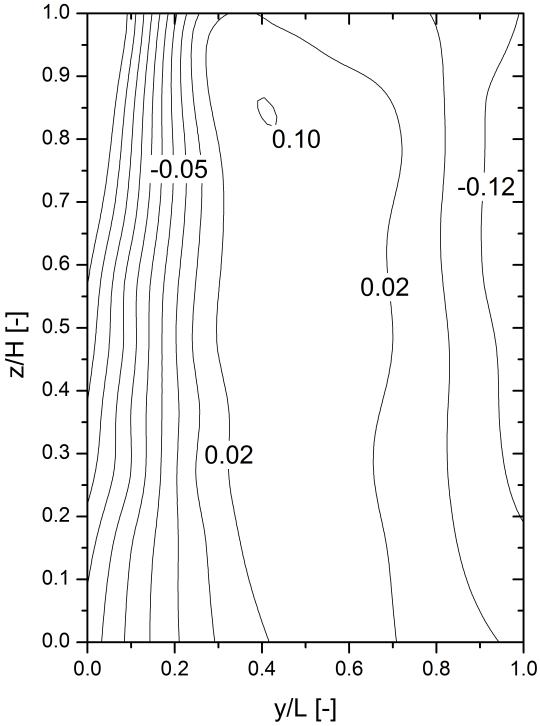
(a) View A. $R^2 = 0.992, SSE = 0.015$.



(b) View B. $R^2 = 0.976, SSE = 0.003$.

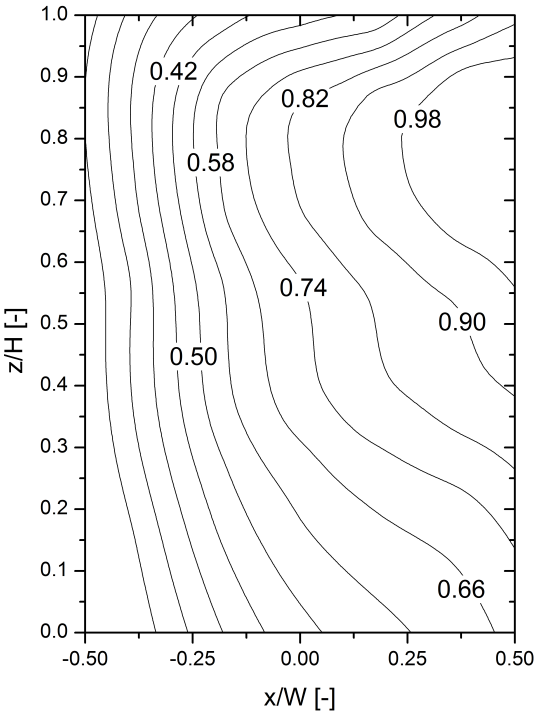


(c) View C. $R^2 = 0.966, SSE = 0.004$.

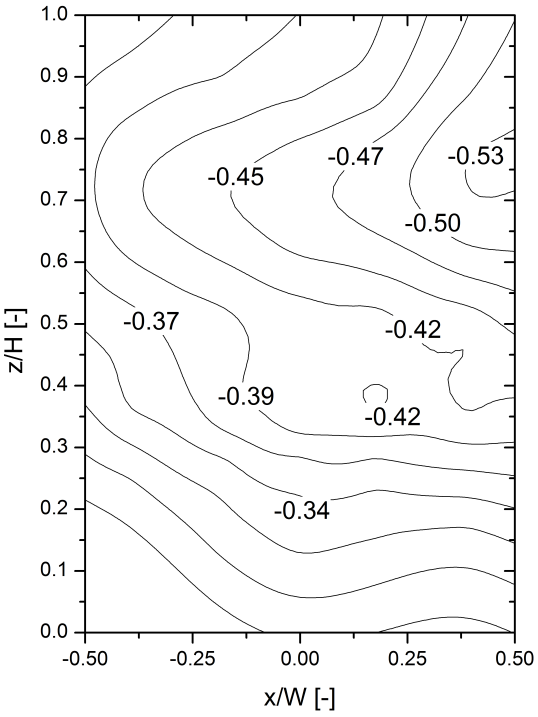


(d) View D. $R^2 = 0.985, SSE = 0.027$.

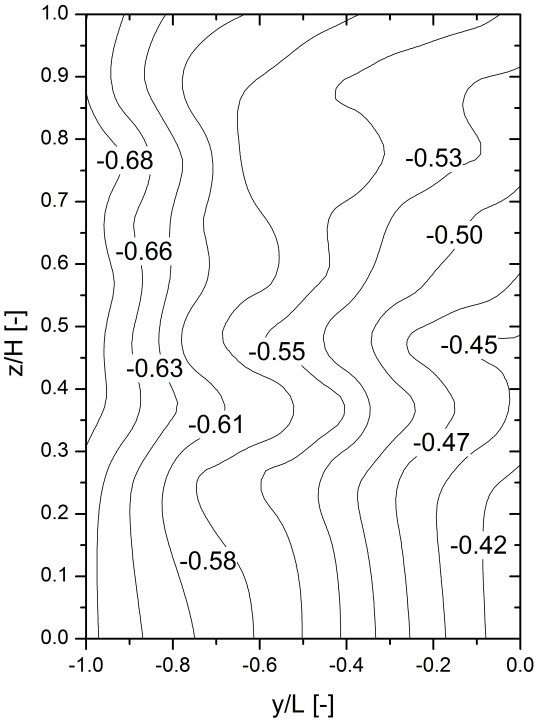
Figure A.2: Distribution of pressure coefficient c_p for an inflow velocity of $u_{10} = 4.7$ m/s and an incidence angle of $\alpha = 20°$.



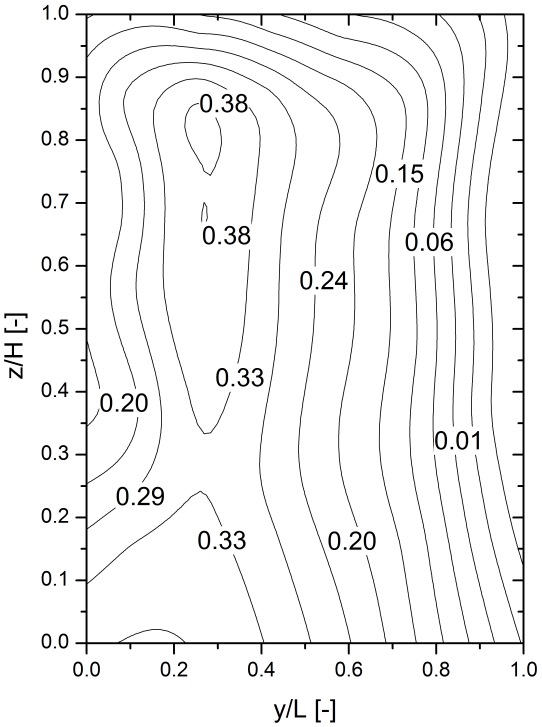
(a) View A. $R^2 = 0.994, SSE = 0.016$.



(b) View B. $R^2 = 0.944, SSE = 0.009$.

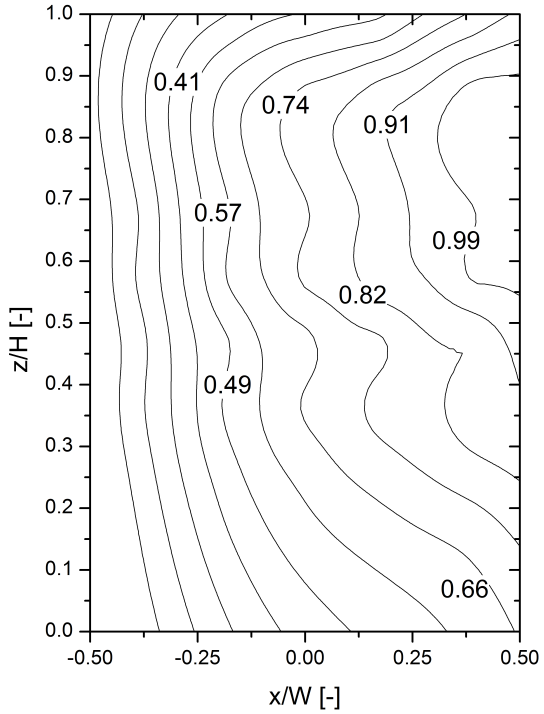


(c) View C. $R^2 = 0.959, SSE = 0.009$.

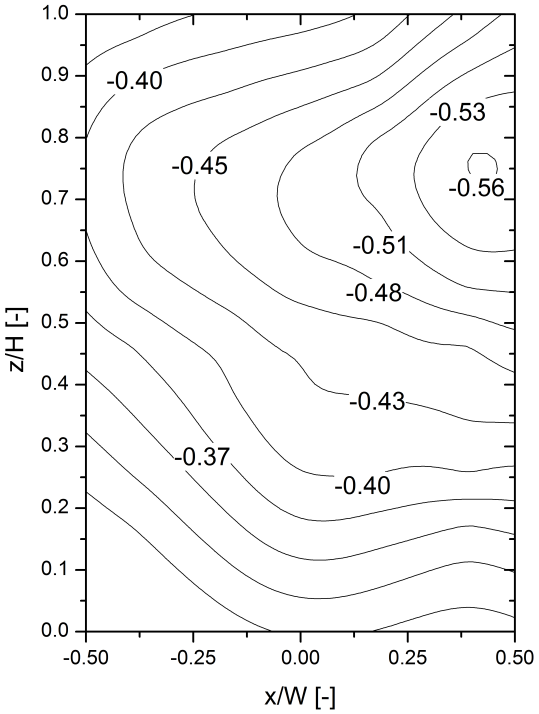


(d) View D. $R^2 = 0.995, SSE = 0.005$.

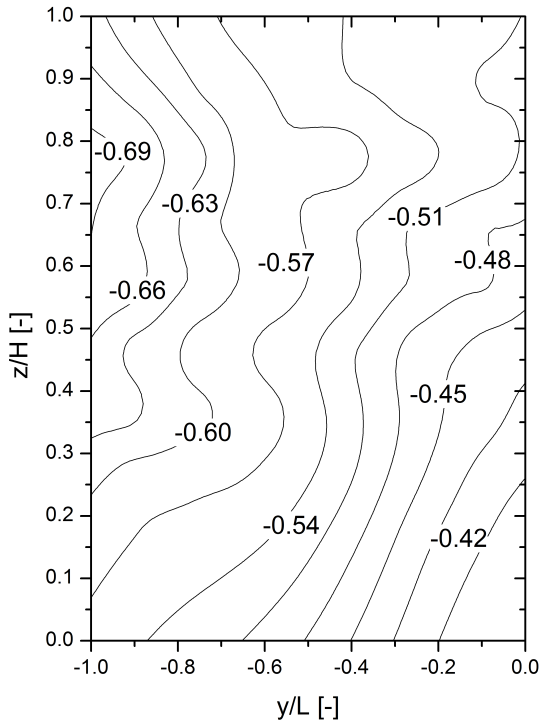
Figure A.3: Distribution of pressure coefficient c_p for an inflow velocity of $u_{10} = 4.7$ m/s and an incidence angle of $\alpha = 30°$.



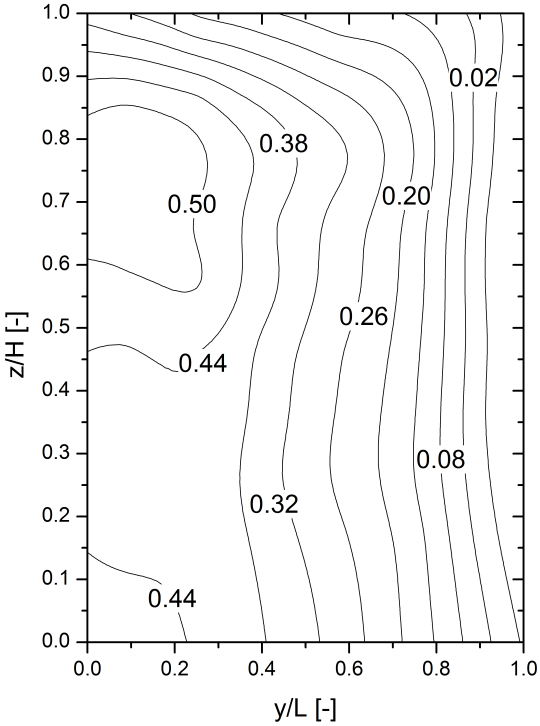
(a) View A. $R^2 = 0.985, SSE = 0.039$.



(b) View B. $R^2 = 0.994, SSE = 0.001$.

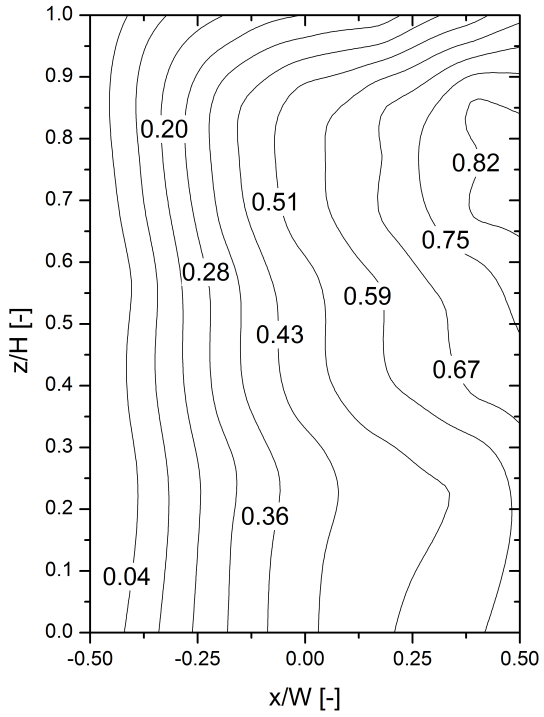


(c) View C. $R^2 = 0.965, SSE = 0.008$.

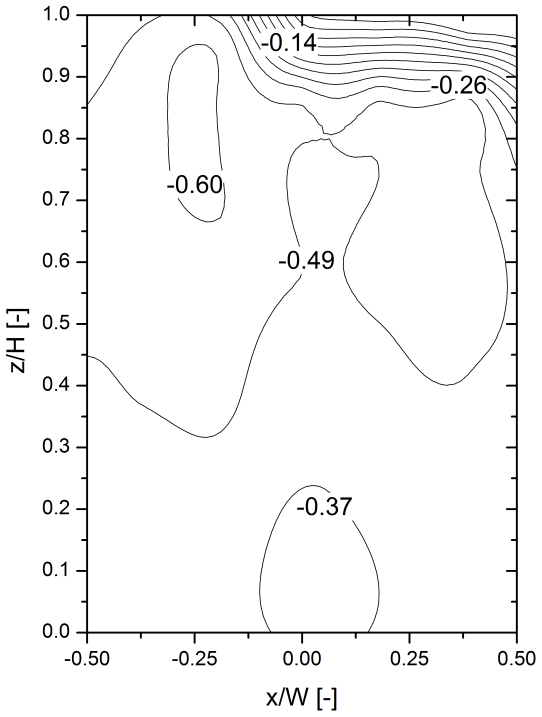


(d) View D. $R^2 = 0.992, SSE = 0.013$.

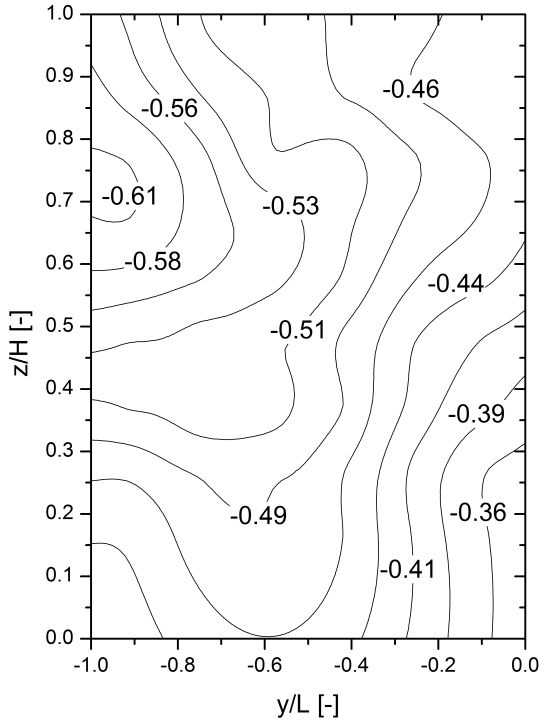
Figure A.4: Distribution of pressure coefficient c_p for an inflow velocity of $u_{10} = 4.7$ m/s and an incidence angle of $\alpha = 33.3°$.



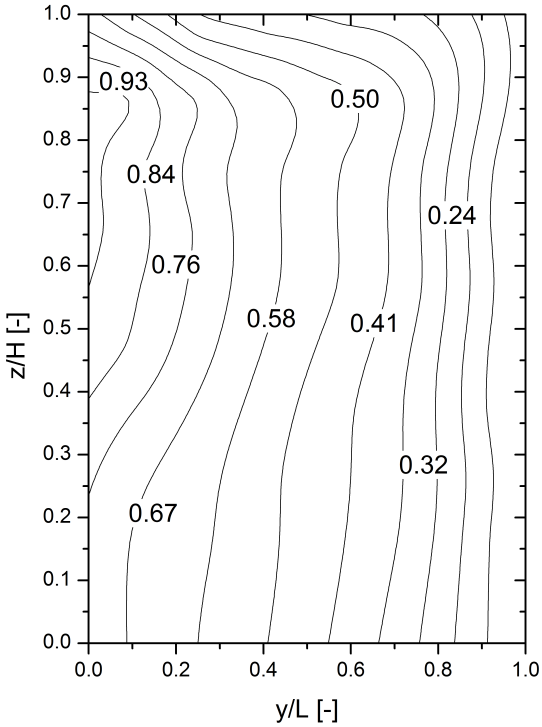
(a) View A. $R^2 = 0.996, SSE = 0.010$.



(b) View B. $R^2 = 0.956, SSE = 0.111$.

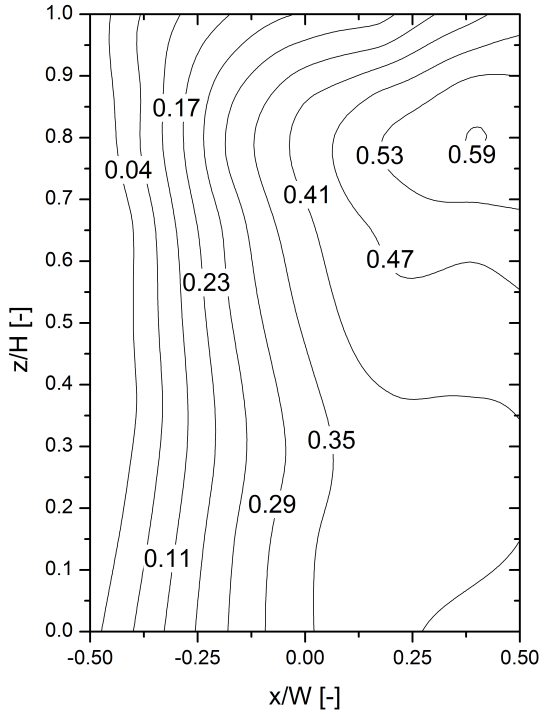


(c) View C. $R^2 = 0.978, SSE = 0.004$.

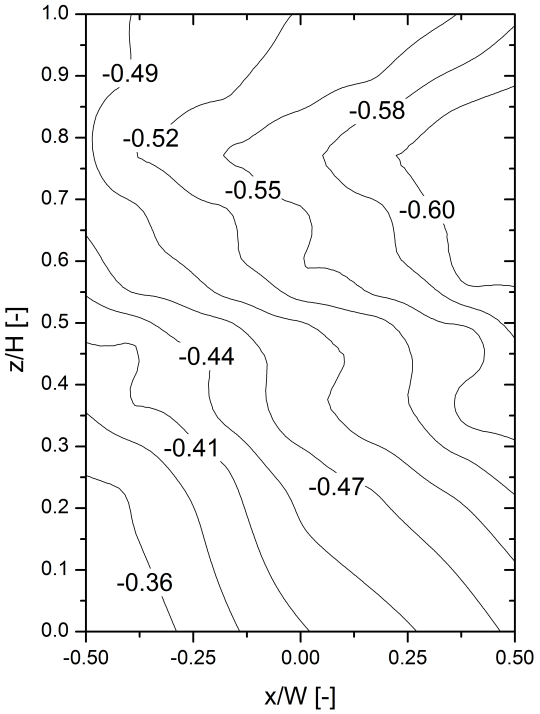


(d) View D. $R^2 = 0.996, SSE = 0.014$.

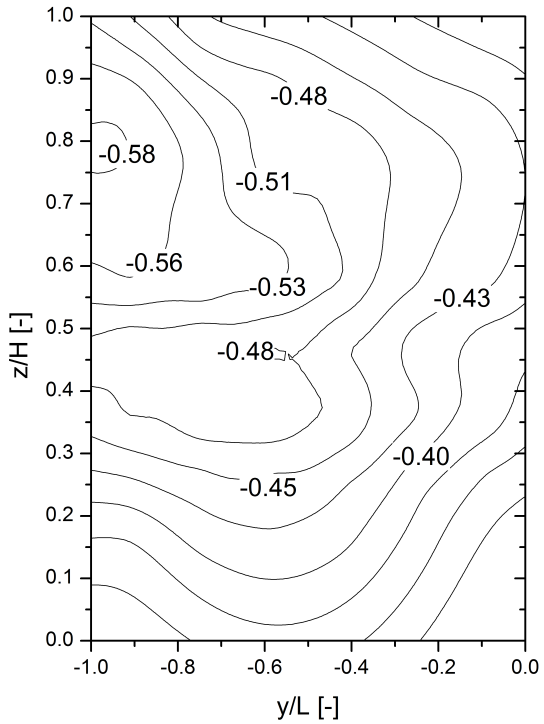
Figure A.5: Distribution of pressure coefficient c_p for an inflow velocity of $u_{10} = 4.7$ m/s and an incidence angle of $\alpha = 45°$.



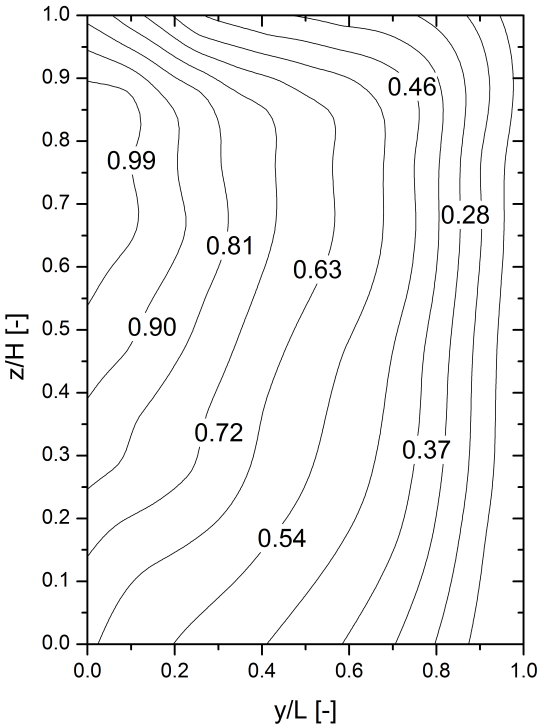
(a) View A. $R^2 = 0.994, SSE = 0.009$.



(b) View B. $R^2 = 0.950, SSE = 0.009$.

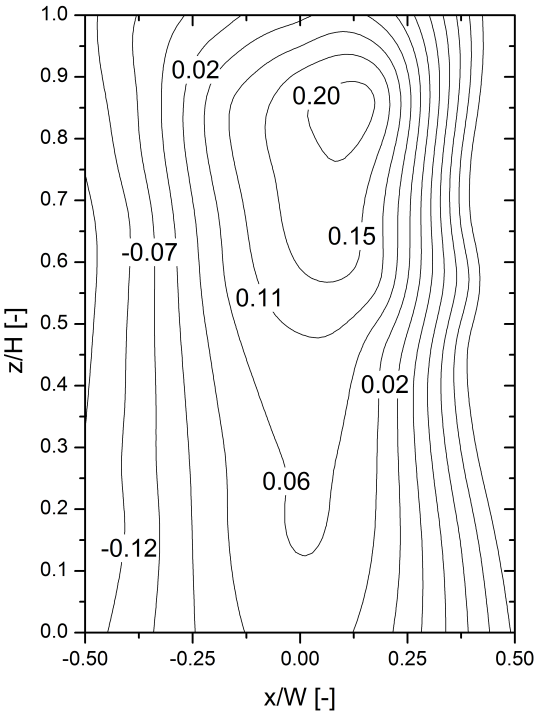


(c) View C. $R^2 = 0.959, SSE = 0.007$.

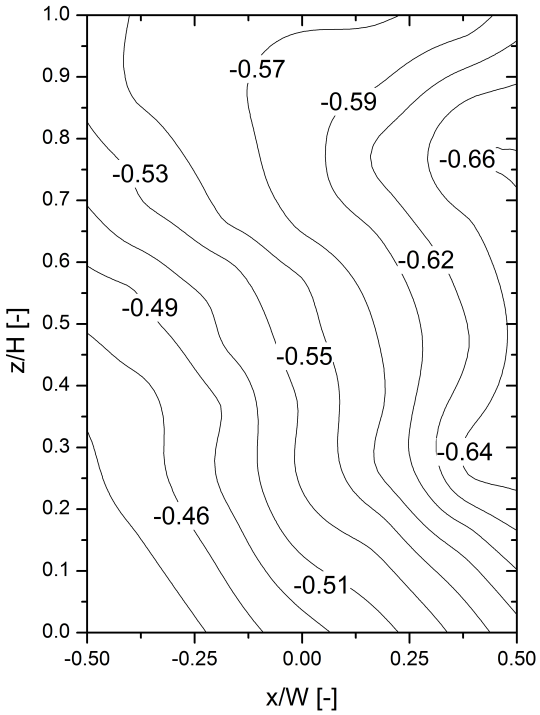


(d) View D. $R^2 = 0.985, SSE = 0.052$.

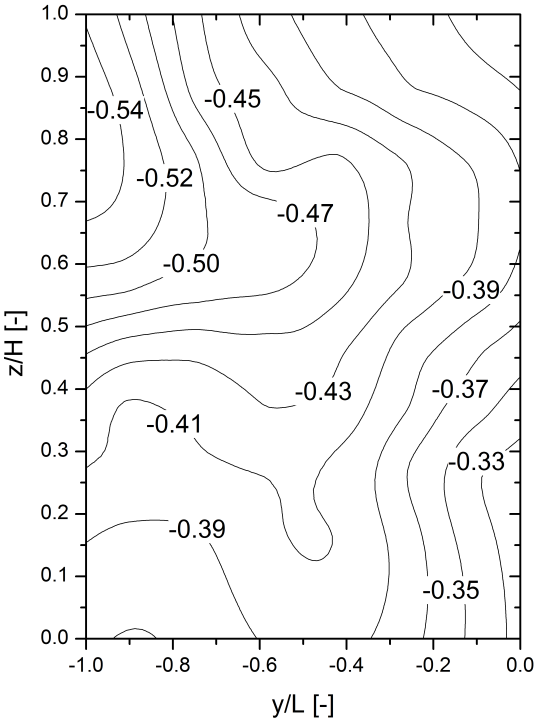
Figure A.6: Distribution of pressure coefficient c_p for an inflow velocity of $u_{10} = 4.7$ m/s and an incidence angle of $\alpha = 50°$.



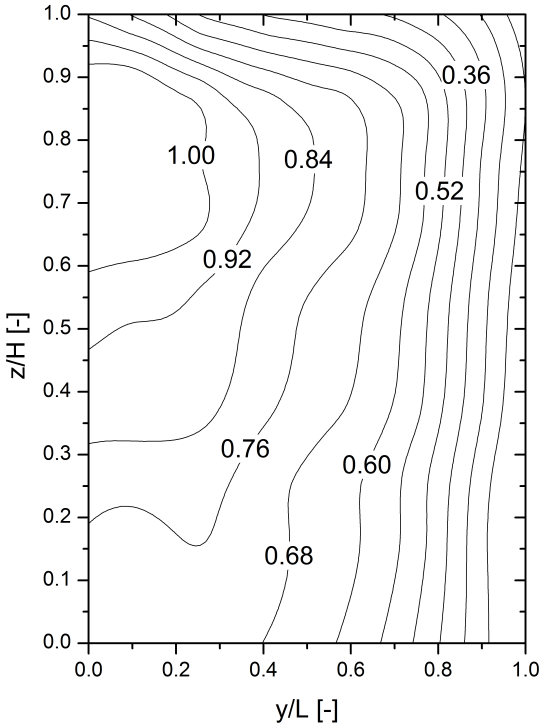
(a) View A. $R^2 = 0.984, SSE = 0.013$.



(b) View B. $R^2 = 0.989, SSE = 0.002$.

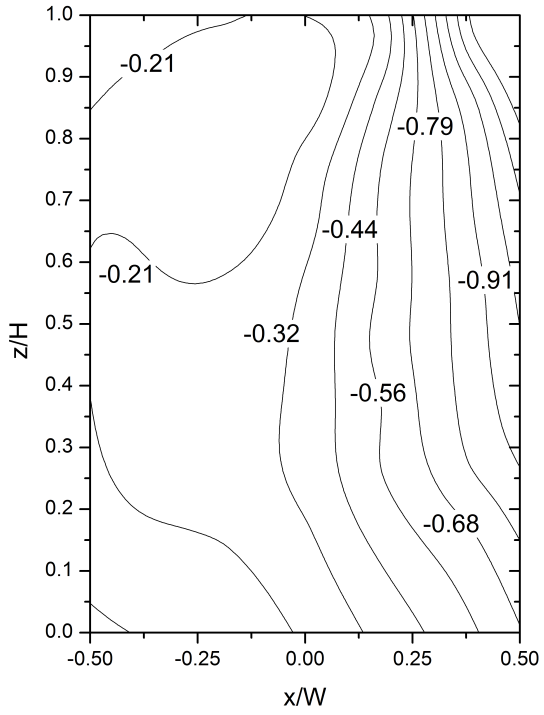


(c) View C. $R^2 = 0.968, SSE = 0.004$.

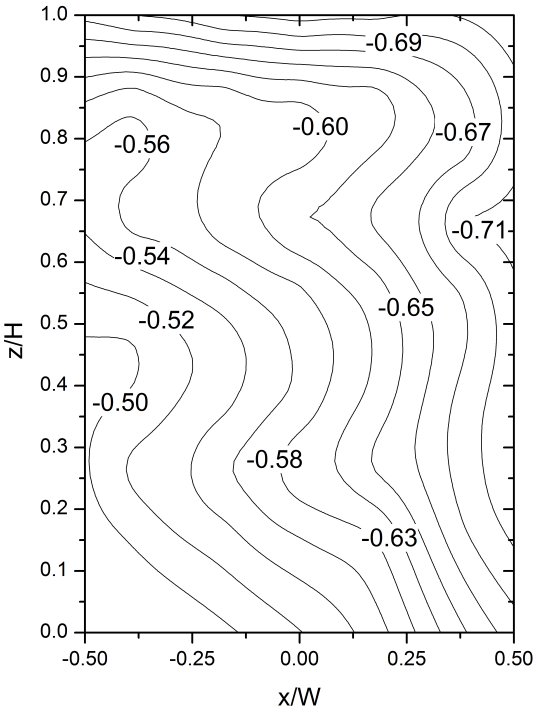


(d) View D. $R^2 = 0.995, SSE = 0.016$.

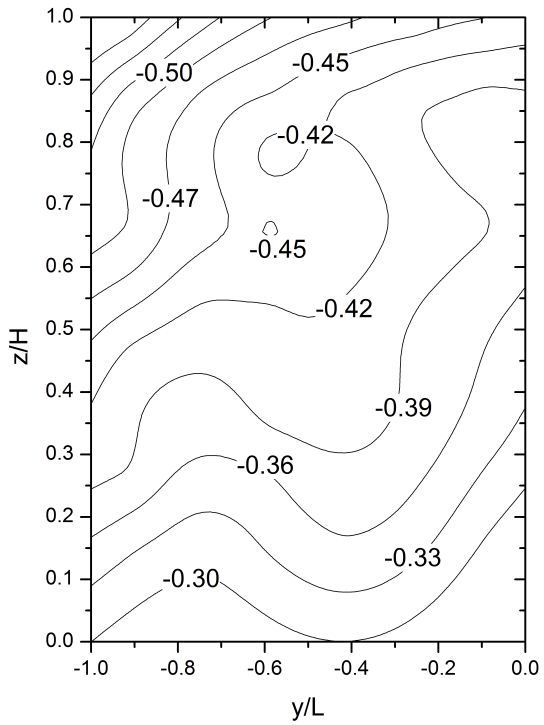
Figure A.7: Distribution of pressure coefficient c_p for an inflow velocity of $u_{10} = 4.7$ m/s and an incidence angle of $\alpha = 60°$.



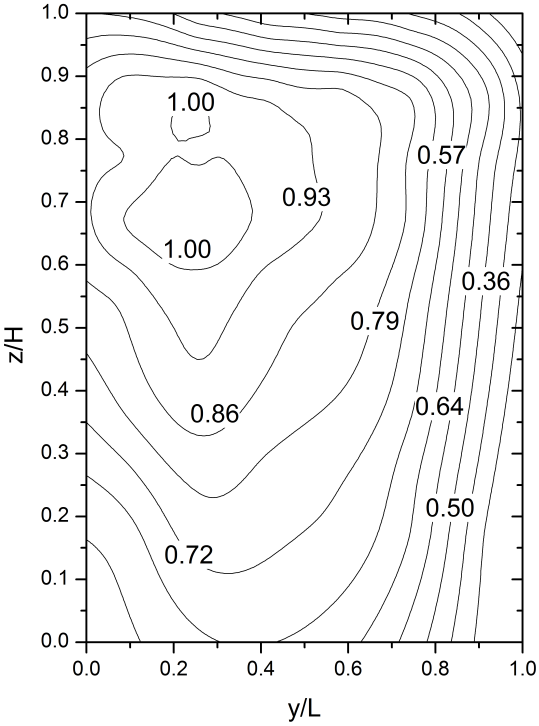
(a) View A. $R^2 = 0.987, SSE = 0.048$.



(b) View B. $R^2 = 0.986, SSE = 0.002$.

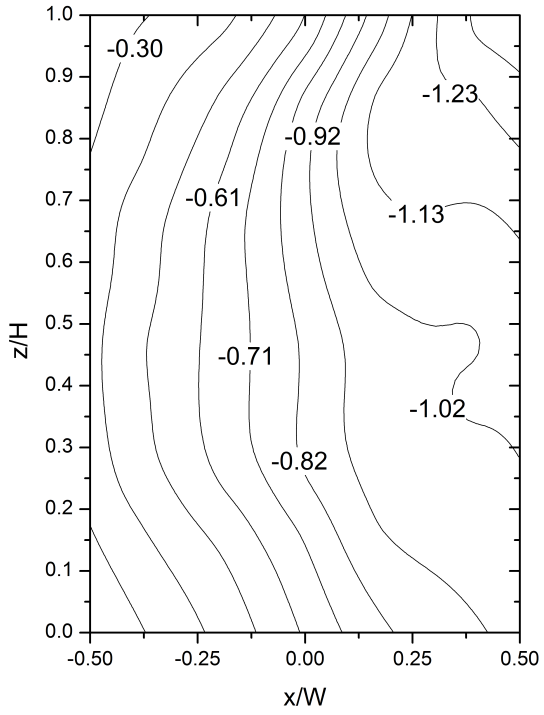


(c) View C. $R^2 = 0.984, SSE = 0.003$.

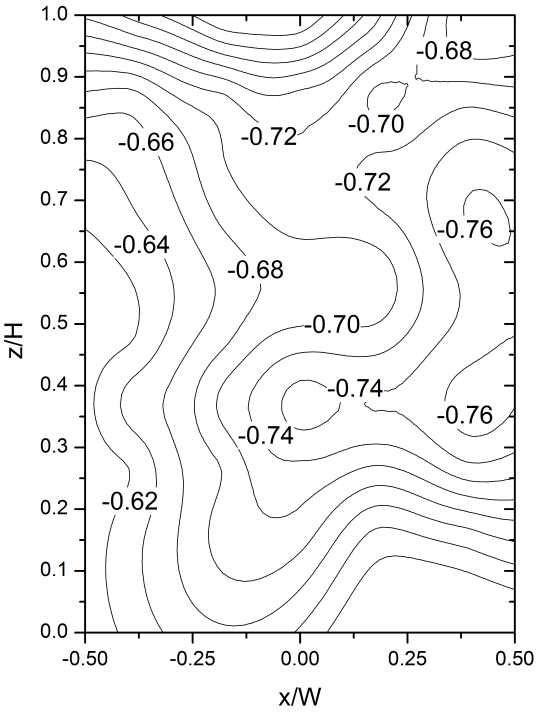


(d) View D. $R^2 = 0.991, SSE = 0.020$.

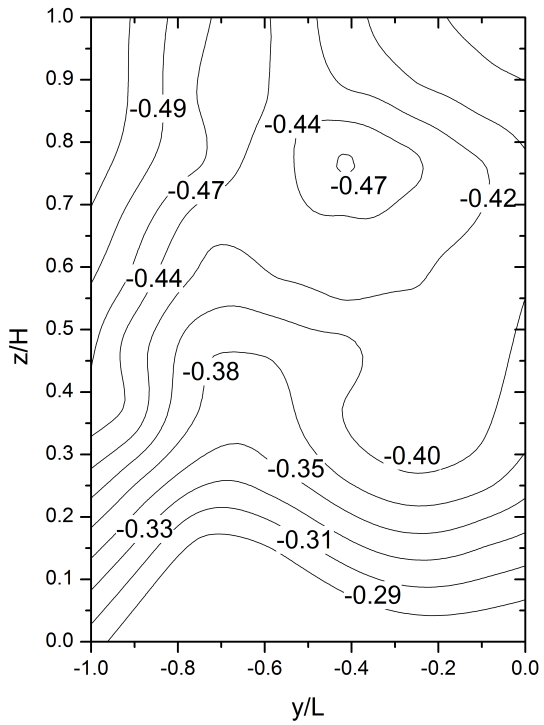
Figure A.8: Distribution of pressure coefficient c_p for an inflow velocity of $u_{10} = 4.7$ m/s and an incidence angle of $\alpha = 70°$.



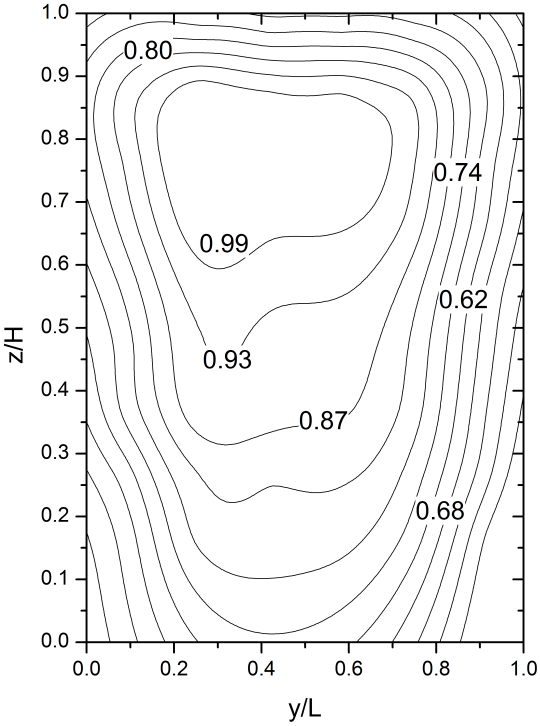
(a) View A. $R^2 = 0.993, SSE = 0.025$.



(b) View B. $R^2 = 0.897, SSE = 0.009$.

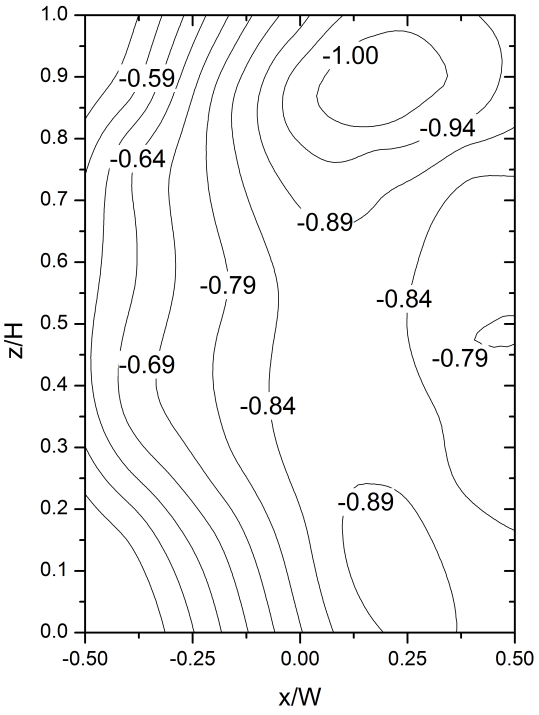


(c) View C. $R^2 = 0.968, SSE = 0.004$.

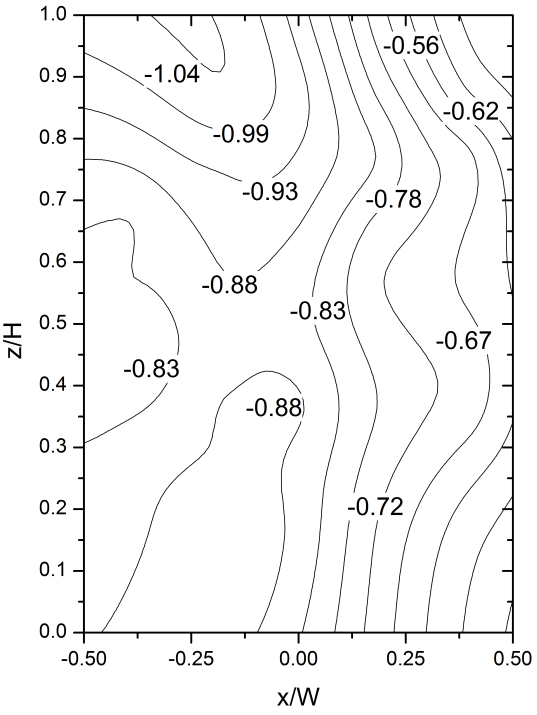


(d) View D. $R^2 = 0.991, SSE = 0.009$.

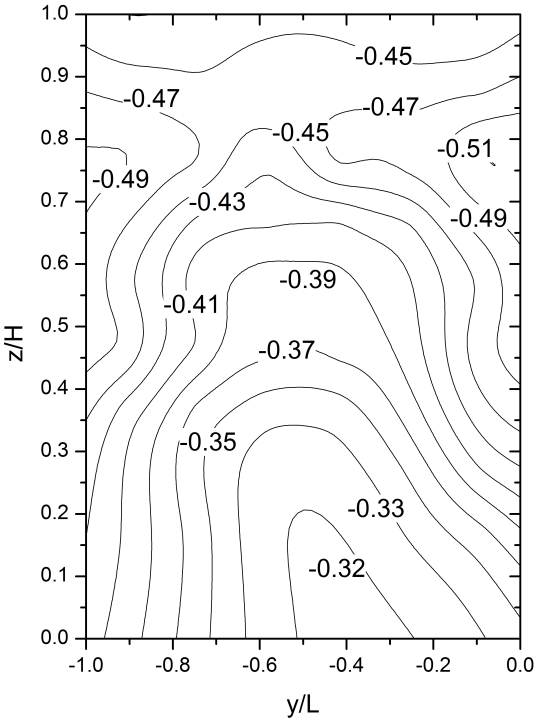
Figure A.9: Distribution of pressure coefficient c_p for an inflow velocity of $u_{10} = 4.7$ m/s and an incidence angle of $\alpha = 80°$.



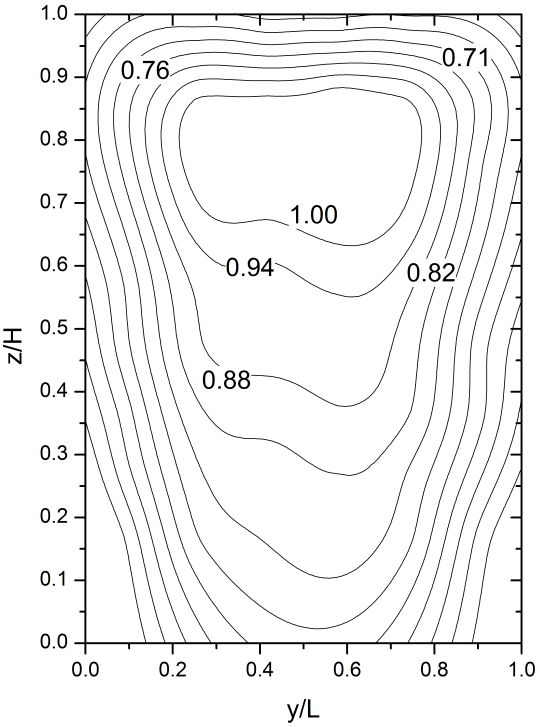
(a) View A. $R^2 = 0.979, SSE = 0.012$.



(b) View B. $R^2 = 0.980, SSE = 0.013$.



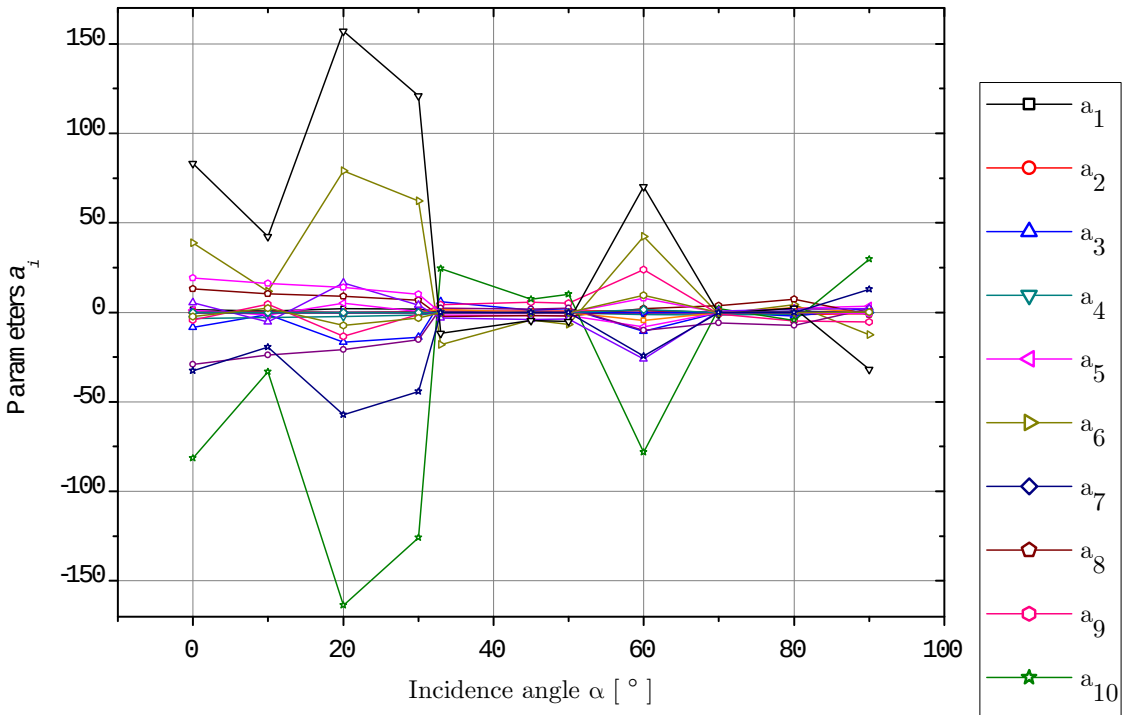
(c) View C. $R^2 = 0.965, SSE = 0.005$.



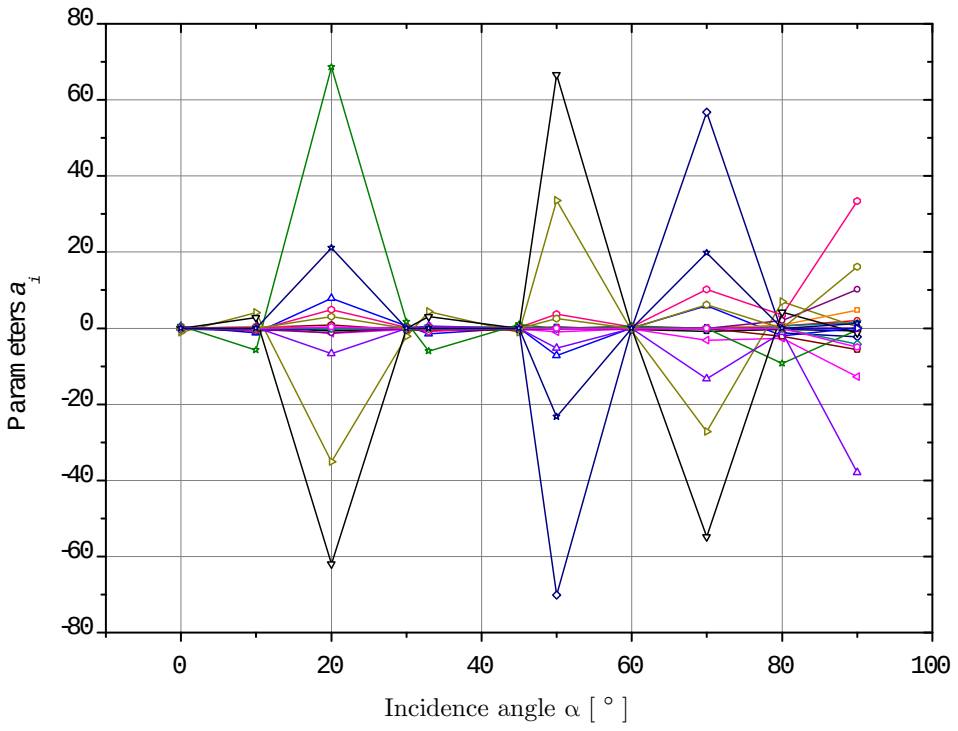
(d) View D. $R^2 = 0.996, SSE = 0.006$.

Figure A.10: Distribution of pressure coefficient c_p for an inflow velocity of $u_{10} = 4.7$ m/s and an incidence angle of $\alpha = 90°$.

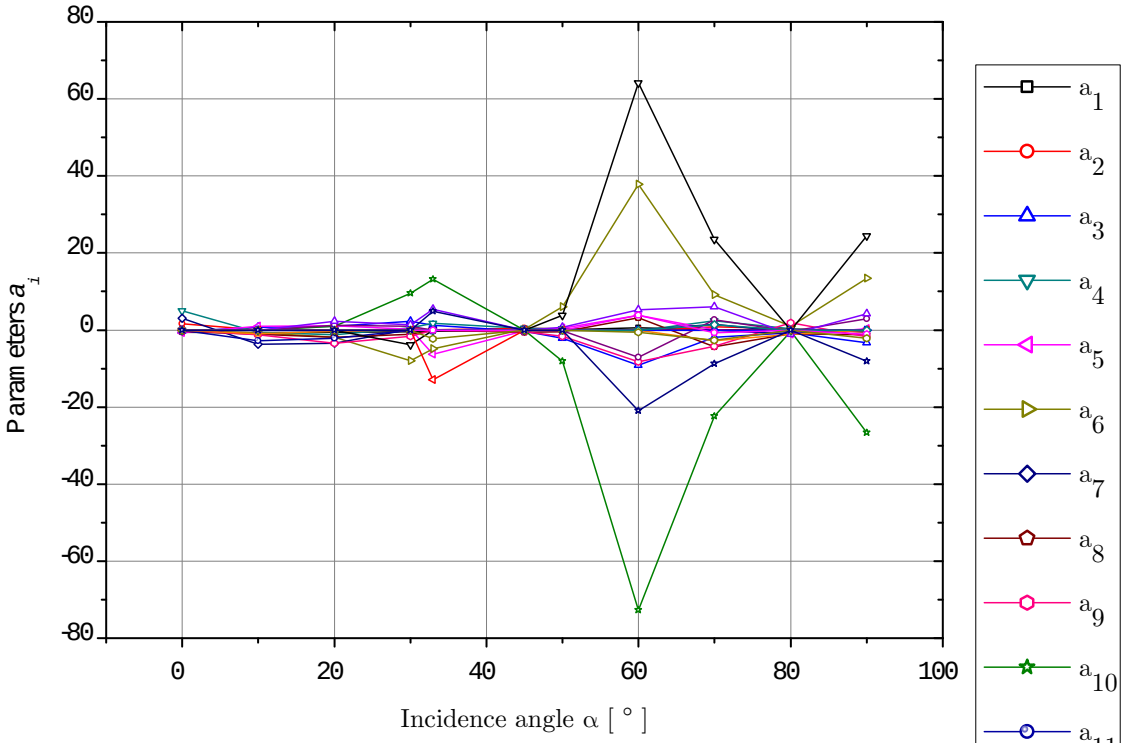
A.2 Distribution of the parameters a_i of the multi-dimensional polynomial function of the pressure distribution


150
100
50
0
-50
-100
-150
Parameters a_i
0
20
40
60
80
100
Incidence angle α [°]
a_1
a_2
a_3
a_4
a_5
a_6
a_7
a_8
a_9
a_{10}
a_{11}
a_{12}
a_{13}
a_{14}
a_{15}
a_{16}
a_{17}
a_{18}
a_{19}
a_{20}
a_{21}

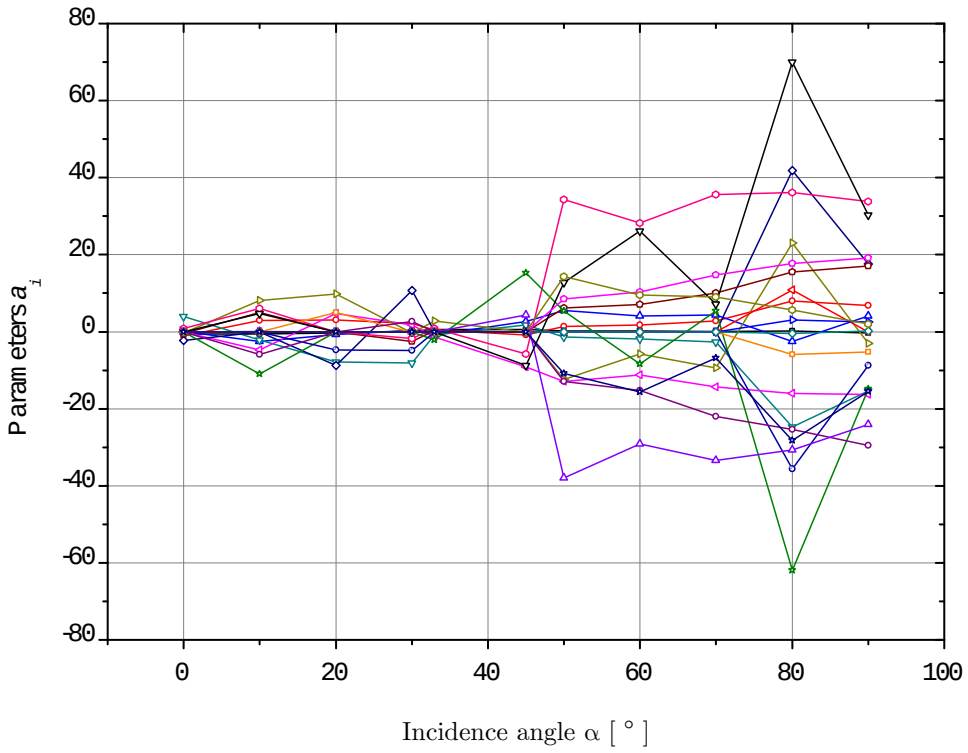
(a)


80
60
40
20
0
-20
-40
-60
-80
Parameters a_i
0
20
40
60
80
100
Incidence angle α [°]

(b)



(c)



(d)

Figure A.11: Distribution of the parameters a_1 to a_{21} for the multidimensional polynomial function in Eq. (3.10) for (a) the windward wall (view A), (b) the leeward wall (view B), (c) the left wall (view C), and (d) the right wall (view D) for $u_{10} = 2.8$ m/s.

Appendix B

Heat flux table

		Areas	0.1284	0.1524	0.1284	0.1524	Sum 0.5616	[m²]			Room volume	0.081534	[m³]									
Wind velocity [m/s]	ΔT [K]	Wind direction α	Heat flux through the building walls [W/m²]				A	B	C	D	A	B	C	D								
			A	B	C	D	$T_{w,i}$ [K]	$T_{w,i}$ [K]	$T_{w,i}$ [K]	$T_{w,i}$ [K]	$T_{w,a}$ [K]	$T_{w,a}$ [K]	$T_{w,a}$ [K]	$T_{w,a}$ [K]	T_i [K]	T_0 [K]	α_i [W/m²K]	α_a [W/m²K]	k [W/m²K]	p_0 [Pa]	P_{el} [W]
3.6	2	-40°	-0.124	0.004	-2.667	-2.997	22.676	22.650	22.266	22.361	21.064	21.113	21.115	21.038	23.048	21.012	**2.036**	**38.383**	**0.712**	97000	4.651
		-20°	-0.522	-0.090	-2.916	-3.091	22.776	22.724	22.388	22.446	21.147	21.192	21.200	21.147	23.144	21.092	**2.468**	**23.785**	**0.804**	97000	6.575
		0°	-0.538	-0.369	-3.165	-3.008	22.806	22.765	22.427	22.463	21.253	21.278	21.275	21.246	23.145	21.122	**2.831**	**12.831**	**0.871**	97000	4.587
		20°	-0.130	-0.400	-2.971	-3.412	22.869	22.826	22.491	22.534	21.401	21.366	21.353	21.310	23.234	21.106	**2.584**	**7.813**	**0.819**	97000	4.665
		40°	-0.647	-0.713	-2.908	-3.683	22.900	22.867	22.530	22.554	21.532	21.468	21.449	21.362	23.233	21.212	**3.390**	**10.692**	**0.992**	97000	6.605
		60°	-0.458	-0.774	-2.652	-3.549	22.960	22.903	22.572	22.575	21.654	21.558	21.548	21.415	23.233	21.337	**3.404**	**16.449**	**0.994**	97000	6.457
		80°	-0.618	-1.126	-2.585	-3.573	23.109	23.064	22.734	22.738	21.669	21.550	21.616	21.455	23.452	21.393	**3.378**	**20.691**	**0.975**	97000	4.955
		90°	-0.759	-1.390	-2.845	-3.750	23.105	23.068	22.722	22.705	21.737	21.597	21.685	21.504	23.405	21.412	**4.108**	**15.949**	**1.113**	97000	4.670
	4	-40°	-4.006	-4.184	-6.883	-7.826	25.205	25.128	24.434	24.653	22.101	22.061	22.117	22.093	25.683	21.711	**7.285**	**15.011**	**1.447**	96200	7.913
		-20°	-4.327	-3.246	-8.010	-7.772	25.289	25.235	24.581	24.740	22.126	22.132	22.076	22.146	25.816	21.746	**6.835**	**15.708**	**1.428**	96200	7.236
		0°	-4.610	-4.277	-7.037	-8.002	25.302	25.233	24.585	24.726	22.168	22.203	22.181	22.176	25.730	21.724	**8.362**	**13.128**	**1.496**	96200	6.828
		20°	-4.355	-3.661	-6.793	-7.851	25.281	25.230	24.595	24.709	22.157	22.208	22.217	22.192	25.784	21.671	**7.064**	**10.831**	**1.379**	96200	8.610
		40°	-4.062	-4.929	-6.984	-8.326	25.333	25.305	24.694	24.767	22.259	22.228	22.312	22.227	25.845	21.768	**7.779**	**12.665**	**1.502**	96200	6.123
		60°	-3.772	-5.086	-6.948	-8.299	25.360	25.342	24.692	24.757	22.328	22.255	22.376	22.237	25.805	21.834	**8.489**	**13.559**	**1.532**	96200	8.527
		80°	-3.636	-4.749	-6.786	-8.117	25.322	25.305	24.695	24.736	22.416	22.262	22.391	22.253	25.789	21.928	**7.955**	**15.700**	**1.522**	96200	6.753
		90°	-3.826	-4.819	-6.923	-8.224	25.460	25.460	24.820	24.871	22.447	22.296	22.421	22.270	25.996	21.877	**7.405**	**13.231**	**1.456**	96200	7.031
	6	-40°	-6.755	-7.724	-10.453	-12.824	26.734	26.722	25.660	26.044	21.844	21.804	21.952	21.968	27.423	21.363	**9.114**	**17.753**	**1.569**	97300	12.339
		-20°	-6.451	-5.690	-11.872	-12.623	26.626	26.647	25.672	25.982	21.762	21.822	21.784	21.947	27.332	21.383	**8.521**	**20.234**	**1.540**	97300	12.565
		0°	-5.741	-5.562	-11.564	-12.401	26.458	26.483	25.645	25.882	21.665	21.733	21.928	21.841	27.183	21.319	**8.274**	**18.226**	**1.506**	97300	13.126
		20°	-5.143	-3.816	-10.881	-12.088	26.334	26.406	25.602	25.843	21.566	21.628	21.883	21.782	27.177	21.175	**6.775**	**14.211**	**1.329**	96900	13.106
		40°	-3.773	-3.675	-10.899	-12.439	26.067	26.170	25.453	25.672	21.563	21.515	21.801	21.654	26.960	21.146	**6.502**	**15.224**	**1.329**	96900	14.021
		60°	-7.188	-7.420	-11.179	-12.791	27.055	27.068	26.184	26.317	22.367	22.287	22.517	22.339	27.775	21.717	**9.117**	**14.831**	**1.599**	96900	11.753
		80°	-6.572	-7.279	-10.808	-12.496	27.055	27.082	26.137	26.284	22.468	22.281	22.485	22.343	27.726	21.825	**9.218**	**16.946**	**1.583**	96900	12.317
		90°	-6.316	-7.171	-10.771	-12.599	27.095	27.157	26.225	26.414	22.368	22.241	22.408	22.281	27.904	21.680	**8.155**	**14.636**	**1.490**	96900	14.018
	8	-40°	-6.969	-7.387	-13.858	-15.916	28.296	28.331	27.093	27.657	21.959	21.907	22.197	22.228	29.274	21.456	**7.876**	**17.469**	**1.418**	97300	17.510
		-20°	-7.987	-6.743	-15.668	-16.423	28.539	28.563	27.393	27.842	22.082	22.112	22.093	22.360	29.513	21.495	**8.157**	**17.222**	**1.459**	97300	16.321
		0°	-8.680	-8.707	-13.904	-16.995	28.615	28.632	27.451	27.805	22.167	22.223	22.373	22.389	29.500	21.507	**9.238**	**15.201**	**1.518**	97300	17.831
		20°	-9.289	-7.352	-14.196	-16.499	28.672	28.695	27.547	27.865	22.151	22.297	22.515	22.486	29.607	21.499	**8.603**	**13.491**	**1.461**	97300	20.456
		40°	-8.349	-10.252	-14.673	-17.074	28.628	28.721	27.580	27.882	22.295	22.293	22.637	22.522	29.559	21.575	**9.829**	**14.582**	**1.588**	97300	17.399
		60°	-8.104	-10.679	-14.972	-17.434	28.726	28.762	27.632	27.914	22.349	22.298	22.698	22.514	29.609	21.655	**10.044**	**15.970**	**1.622**	97300	15.467
		80°	-8.088	-9.982	-14.907	-17.012	27.676	27.963	27.255	27.659	21.049	20.954	21.361	21.299	29.622	20.812	**6.374**	**42.501**	**1.428**	97300	34.021
		90°	-7.061	-7.231	-14.732	-16.896	27.798	27.869	26.774	27.134	21.608	21.500	21.797	21.749	28.789	21.034	**8.206**	**17.865**	**1.487**	97600	18.523
5.1	2	-40°	-2.030	-2.104	-3.510	-4.162	23.665	23.600	23.178	23.255	22.012	22.036	22.003	21.936	23.925	21.823	**6.308**	**19.644**	**1.412**	97600	3.695
		-20°	-1.996	-1.537	-3.219	-3.680	23.630	23.579	23.190	23.241	21.985	22.024	21.971	21.926	23.921	21.830	**5.260**	**20.731**	**1.247**	97600	4.309
		0°	-2.492	-1.617	-3.411	-3.333	23.424	23.361	22.996	23.002	21.951	21.971	21.901	21.857	23.617	21.719	**7.399**	**15.061**	**1.419**	97600	3.237
		20°	-1.941	-1.357	-3.410	-3.519	23.380	23.312	22.993	22.991	21.929	21.911	21.862	21.786	23.658	21.599	**5.264**	**10.598**	**1.237**	97600	2.927
		40°	-1.792	-1.377	-3.470	-3.780	23.338	23.297	22.986	22.971	21.950	21.890	21.870	21.761	23.629	21.600	**5.326**	**11.775**	**1.282**	97600	3.478
		60°	-1.306	-1.143	-3.370	-3.807	23.394	23.342	23.020	23.021	21.944	21.847	21.849	21.709	23.707	21.592	**4.427**	**13.879**	**1.140**	97600	5.100
		80°	-0.961	-1.028	-2.909	-3.501	23.290	23.235	22.908	22.890	21.911	21.780	21.833	21.798	23.537	21.698	**4.335**	**18.943**	**1.149**	97600	3.873
		90°	-0.809	-1.211	-2.926	-3.640	23.166	23.104	22.801	22.767	21.835	21.700	21.767	21.592	23.427	21.536	**4.291**	**23.052**	**1.148**	97600	3.835
	4	-40°	-2.655	-2.974	-6.483	-8.007	24.769	24.713	24.058	24.306	21.500	21.512	21.560	21.542	25.322	21.312	**5.736**	**22.722**	**1.264**	96900	9.722
		-20°	-2.345	-1.774	-7.096	-7.535	24.613	24.557	24.021	24.160	21.397	21.432	21.446	21.466	25.180	21.245	**5.124**	**23.473**	**1.191**	96900	9.100
		0°	-2.110	-1.882	-6.816	-7.533	24.512	24.463	23.948	24.096	21.280	21.295	21.397	21.340	25.106	21.112	**4.979**	**20.036**	**1.151**	96900	8.977
		20°	-5.768	-4.319	-7.685	-8.125	25.556	25.554	24.904	24.969	22.355	22.395	22.418	22.337	26.057	21.906	**8.514**	**13.896**	**1.555**	96400	6.248
		40°	-5.558	-4.946	-7.724	-8.440	25.471	25.525	24.863	24.893	22.419	22.371	22.450	22.327	25.970	21.944	**9.288**	**15.291**	**1.657**	96400	7.968
		60°	-4.901	-5.087	-7.887	-8.892	25.720	25.735	25.109	25.155	22.455	22.372	22.483	22.332	26.257	21.989	**8.492**	**16.693**	**1.574**	96400	6.632
		80°	-4.341	-4.891	-7.289	-8.441	25.522	25.553	24.902	24.939	22.545	22.373	22.459	22.328	25.986	22.089	**8.929**	**20.967**	**1.611**	96400	8.827
		90°	-4.160	-4.941	-7.746	-8.956	25.568	25.557	24.967	25.005	22.489	22.354	22.439	22.313	26.083	21.979	**8.238**	**16.562**	**1.582**	96400	6.065
	6	-40°	-5.324	-5.550	-10.973	-12.501	26.754	26.717	25.744	26.130	21.919	21.869	21.982	22.009	27.493	21.534	**7.507**	**20.413**	**1.447**	96900	12.920
		-20°	-5.993	-4.695	-12.594	-12.405	26.857	26.822	25.920	26.194	21.985	21.984	21.949	22.077	27.593	21.614	**7.641**	**22.999**	**1.487**	96900	13.503
		0°	-6.549	-6.356	-10.741	-12.831	26.906	26.856	25.961	26.235	22.004	22.028	22.082	22.069	27.603	21.538	**8.497**	**17.811**	**1.510**	96900	13.502
		20°	-6.798	-5.613	-10.736	-12.501	26.902	26.858	25.992	26.224	21.991	22.069	22.173	22.133	27.617	21.518	**8.123**	**15.312**	**1.463**	96900	13.446
		40°	-6.225	-7.547	-11.026	-13.028	26.907	26.939	26.040	26.241	22.117	22.082	22.264	22.156	27.612	21.637	**9.248**	**18.388**	**1.595**	96900	13.095
		60°	-5.755	-7.574	-10.966	-12.847	26.929	26.907	26.064	26.209	22.167	22.102	22.314	22.170	27.613	21.697	**8.938**	**19.318**	**1.583**	96900	12.267
		80°	-5.700	-7.126	-10.864	-12.566	26.959	26.979	26.135	26.291	22.346	22.164	22.341	22.240	27.683	21.846	**8.603**	**22.358**	**1.564**	96900	12.742
		90°	-6.122	-7.207	-11.278	-13.116	26.987	27.039	26.186	26.346	22.352	22.216	22.344	22.252	27.778	21.767	**8.526**	**18.539**	**1.579**	96900	12.140
	8	-40°	-9.078	-10.435	-14.531	-17.239	28.977	29.026	27.553	28.108	22.443	22.301	22.471	22.521	29.828	21.886	**10.153**	**23.588**	**1.625**	97600	16.986
		-20°	-8.887	-8.292	-15.969	-16.726	28.845	28.898	27.663	28.051	22.329	22.336	22.208	22.455	29.778	21.841	**9.089**	**26.070**	**1.571**	97600	17.039
		0°	-8.574	-9.172	-15.459	-16.827	28.622	28.681	27.579	27.906	22.175	22.244	22.404	22.296	29.573	21.665	**9.367**	**20.178**	**1.587**	97600	15.989
		20°	-10.055	-7.409	-14.917	-16.392	28.407	28.536	27.460	27.751	21.962	22.076	22.314	22.244	29.469	21.483	**8.604**	**18.126**	**1.524**	97600	16.422
		40°	-9.891	-8.555	-15.120	-17.309	28.256	28.495	27.401	27.750	21.870	21.821	22.164	22.022	29.403	21.372	**9.098**	**21.285**	**1.586**	97600	16.989
		60°	-8.716	-8.891	-14.847	-17.202	28.296	28.396	27.283	27.610	21.798	21.729	22.069	21.934	29.319	21.339	**8.964**	**23.024**	**1.563**	97600	18.521
		80°	-8.088	-8.562	-14.657	-16.778	28.261	28.377	27.237	27.570	21.945	21.719	21.944	21.904	29.261	21.409	**8.822**	**26.431**	**1.538**	97600	17.290
		90°	-7.798	-8.068	-15.278	-17.495	28.012	28.088	27.042	27.370	21.780	21.658	21.845	21.822	28.999	21.236	**8.910**	**22.327**	**1.573**	97600	15.902

Table B1: Measured heat flux for each wall of the single room model in 1:10 scale, under different velocity, wind and temperature conditions, and therefrom calculated heat transfer coefficients.